ILIAN ALEXANDROV BONEV

GEOMETRIC ANALYSIS OF PARALLEL MECHANISMS

Thèse
présentée
à la Faculté des études supérieures
de l'Université Laval
pour l'obtention
du grade de Philosophiae Doctor (Ph.D.)

Département de génie mécanique
FACULTÉ DES SCIENCES ET DE GÉNIE
UNIVERSITÉ LAVAL
QUÉBEC

NOVEMBRE 2002

Abstract

The primary objective of this dissertation is to demonstrate the incontestable effectiveness of geometric methods to the design and analysis of parallel mechanisms. To this end, it is shown how geometry brings deep insight into the principles of motion, much better than algebraic or numerical methods. Furthermore, this thesis is expected to prove that geometry develops creativity and intuition, abilities much needed for the proper synthesis and study of complex mechanisms.

The extensive use of basic geometry in this thesis uncovers the unseen properties of well-known parallel mechanisms. In addition, common misconceptions are examined and refuted. Through detailed comparisons and explanations, it is attempted to foster the reliance on the geometric approach. Finally, two promising research directions are identified and recommended.

This thesis is divided into three main parts. While the progress through these parts goes from the plane to three and then six degrees of freedom in space, the complexity does not follow the same advance. On the other hand, the focus goes from the general survey of all 3-DOF planar parallel mechanisms, to the analysis of a class of 3-DOF spatial parallel mechanisms, to the study of a single architecture of a 6-DOF parallel mechanism.

Firstly, the singularities of all 3-DOF planar parallel mechanisms are fully analysed. The velocity equations are derived by using both screw theory and differentiation with respect to time. For this purpose, a considerable attention is paid to explaining the not-so-well-known use of screw theory in the plane. Once these velocity equations are set up, an exhaustive study on the various types of singularities of these mechanisms

is performed. Several new designs are identified, having few or no singularities at all. Finally, a new research path emerges through an in-depth discussion on the problem of workspace segmentation, working modes, and assembly modes.

Next, the investigation leaves the plane and starts with a comprehensive discourse on the complex issue of orientation representation via the relatively unknown Tilt & Torsion angles. Numerous advantages of these angles are shown. Then, using the Tilt & Torsion angles, several 3-DOF spatial parallel mechanisms with one translational and two rotational degrees of freedom are analysed. The relationships between the three constrained and three feasible degrees of freedom are derived and it is shown clearly that the mechanisms belong to a special class of constrained mechanisms that have zero torsion of the platform.

Finally, the focus is shifted to the kinematic analysis of 6-DOF six-legged spatial parallel mechanisms with base-mounted revolute actuators and fixed-length struts. In the first section, a geometric method for the computation of the edges of the constant-orientation workspace is elaborated. In the second section, another geometric algorithm is described for the computation of the constant-orientation workspace. This new algorithm computes not only the edges of the workspace but its cross-sections as well. In the last section, the study is limited to a special parallel mechanism of this class, with pair-wise coincident spherical joints and six centres of the universal joints moving along the same circular track. This particular design allows the illustration in the spatial case of the problem of workspace segmentation by working modes. Geometric algorithms are proposed for the computation of the horizontal cross-sections of the singularity surface and constant-orientation workspace.

Ilian Alexandrov Bonev

Clément M. Gosselin

Résumé

Le principal objectif de cette dissertation est de démontrer l'efficacité incontestable des méthodes géométriques pour la conception et l'analyse des mécanismes parallèles à plusieurs degrés de liberté (ddl). Dans ce but, ce travail montre comment la géométrie permet d'analyser en profondeur les principes du mouvement, bien mieux que les méthodes algébriques ou numériques. En outre, cette thèse montre que l'utilisation de la géométrie développe la créativité et l'intuition, des aptitudes nécessaires pour la synthèse appropriée et l'étude des mécanismes complexes.

L'utilisation des outils géométriques de base dans cet ouvrage nous fait découvrir de nouvelles propriétés sur des mécanismes parallèles pourtant bien connus. En outre, de fausses idées sont examinées et réfutées. Par des comparaisons et des explications, le choix de l'approche géométrique est renforcé. Finalement, deux directions prometteuses de recherche sont identifiées et recommandées.

Cette thèse est divisée en trois parties principales, couvrant d'abord l'analyse de mécanismes plans, puis de mécanismes spatiaux à trois et six ddl. Il est à noter que la complexité de l'étude ne suit pas nécessairement le même ordre que la complexité des mécanismes. D'autre part, l'attention va de l'étude générale de tous les mécanismes parallèles plans à 3 ddl, à l'analyse d'une classe des mécanismes parallèles spatiaux à 3 ddl, à une architecture simple d'un mécanisme parallèle à 6 ddl.

Premièrement, l'ensemble des singularités de tous les mécanismes parallèles plans à 3 ddl sont analysées. Les équations de vitesse sont dérivées en employant la théorie des visseurs et la différentiation par rapport au temps. À cette fin, l'utilisation de la théorie des visseurs dans le plan est expliquée de façon approfondie. Une fois les équations de

vitesse dérivées, une étude approfondie est réalisée sur les divers types de singularités de ces mécanismes. Plusieurs nouvelles géometries ayant peu ou aucune singularité sont identifiées. Finalement, une nouvelle direction de recherche est identifiée à travers une discussion sur les problèmes de segmentation de l'espace de travail, des modes de fonctionnement et des modes d'assemblage.

Par la suite, la recherche sort du plan et commence par une revue complète sur la question de représentation de l'orientation avec les angles relativement inconnus *Tilt & Torsion*. De nombreux avantages de ces angles sont montrés. Puis, en utilisant les angles *Tilt & Torsion*, plusieurs mécanismes parallèles spatiaux avec un degré de liberté en translation et deux en rotation sont analysés. Les relations entre les trois degrés de liberté contraints et les trois degrés de liberté non-contraints sont dérivées et il est clairement montré que ces mécanismes appartiennent à une classe spéciale des mécanismes contraints qui ont une torsion nulle.

Finalement, l'étude est portée sur l'analyse cinématique des mécanismes parallèles spatiaux à 6 ddl avec six pattes et des actionneurs rotoïdes montés sur la base. Dans la première section, une méthode géométrique pour le calcul des arêtes de l'espace de travail à orientation constante est élaborée. Dans la deuxième section, un autre algorithme géométrique est décrit pour le calcul de l'espace de travail à orientation constante. Ce nouvel algorithme calcule non seulement les arêtes de l'espace de travail mais également les coupes. Dans la dernière section, l'étude est consacrée à un mécanisme parallèle spécial de cette classe, dont les liaisons rotules sont coïncidentes par paires et les six centres des joints de cardans se déplacent le long de la même voie circulaire. Cette géometrie particulière permet d'illustrer, dans le cas spatial, le problème de segmentation de l'espace de travail en modes de fonctionnement. Des algorithmes géométriques sont proposés pour le calcul des coupes horizontales de la surface de singularité et de l'espace de travail à orientation constante.

Ilian Alexandrov Bonev

Clément M. Gosselin

Foreword

I am very much obliged to my research supervisor Prof. Clément Gosselin for his tremendous support and his unquestionable confidence in me. With his comprehensive expertise in kinematics, he has been a great source of ideas. His quiet leadership based on the perfect balance between providing direction and encouraging independence has been a guiding inspiration for all of his students.

I am also grateful to Dr. Dimiter Zlatanov for his significant help during the various stages of my research. He has contributed to virtually every part of my dissertation through long hours of discussion and careful review of my thesis. Without him, I wouldn't have dared to use screws in my work or delve into the complex singularities of various mechanisms.

Special thanks are also due to the members of the Laval University Robotics Lab for their various technical contributions but mostly for creating the most pleasing working environment that a researcher may hope for. I will certainly miss the regular luncheon discussions and Friday's poutine...

I also wish to express my gratitude to my thesis defence committee and especially to Profs. Manfred Husty and Paul Zsombor-Murray. Their detailed remarks and valuable suggestions ensured that this manuscript is geometrically sound.

Last, but not least, I would like to thank my parents for their financial support and for their encouragement during my years of study around the world.

To my parents

Contents

List of Tables

List of Figures

Chapter 1

Introduction

1.1 Kinematic Geometry of Mechanisms

The publication of Lagrange's masterwork *Mécanique Analytique* in 1788 marked a new *analytic* era in dynamics. Indeed, his revolutionary achievement was to transform the study of rigid body movement into a branch of calculus. Prior to that, due to the rudimentary development of analytic tools, mechanics was, perforce, a geometric art.

> *On ne trouvera point de figures dans cet ouvrage. Les méthodes que j'y expose ne demandent ni constructions, ni raisonnements géométriques ou mécaniques, mais seulement des opérations algébriques, assujetties à une marche régulière et uniforme.*[1]

[1] The reader will find no figures in this work. The methods which I set forth do not require either constructions or geometrical or mechanical reasonings: but only algebraic operations, subject to a regular and uniform rule of procedure. (Excerpt from *Mécanique Analytique* by J.L. Lagrange, 1788)

Basic geometry was developed by the ancient Greeks and Euclid's *Elements* was written as early as 300 BC. The foundations of algebra as we know it, on the other hand, were laid down much later—in the third century AD—and it was only after the development of calculus in the 17th century that the analytical study of mechanics became possible. The arguable preference of the algebraic over the geometric approach is not an issue of the past. The recent advent of the computer brought a revolution in mechanical design. While certainly the computer proved to be of great assistance to the engineer, it has also had negative effects on the readiness to seek deeper understanding of the principles of mechanical motion. This trend was quickly noticed and eloquently described by the two most famous advocates of kinematic geometry:

> With a computer at his elbow an engineer is often tempted to pay little if any attention to principles, but rather plunge into a particular problem of synthesis without considering either the fundamental theory or the criteria that limit the performance of the devices he aims to produce. [...] But more importantly [...] the geometric principles reveal a map of a terrain, regions within which can then be explored in greater detail by analytical or graphical methods... If the map shows that there are inaccessible regions on the terrain, if it warns of hazards and dangerous frontiers, and if it can guide the explorer along safe paths by which he can reach his goal quickly with simple transport, then it should have some value. (Hunt, 1978)

> The digital computer demands on the part of its machine-designing users a ruthless competence in the algebraic processes needed for the manipulation of mechanical information and its numerical analysis. It is accordingly fashionable just now in the field of the theory of machines not so much to denigrate as simply to ignore the main bases in actual mechanical motion from which these algebraic processes grow. The main bases are essentially pictorial, geometrical. They arise from natural philosophy. Students in the mechanical sciences are becoming increasingly unable to contemplate a piece of ordinary reality in machinery accordingly, and to extract from that reality the geometric essence of it. It is of course true that without algebra there can be no programme, no numerical data, and no numerical result; but without an underlying geometry of the reality there can be no applicable algebra. Without a diagram we cannot write an equation. But without geometry we cannot even begin to draw. (Phillips, 1984)

So well have Profs. Kenneth Hunt and Jack Phillips warned against the treacherous trend of over-dependence on computer-based solutions. However, it was only recently that the advances in computer algebra systems such as *Maple*™ and *Mathematica*™ has critically worsened the situation. Students and even researchers are relying entirely on such mathematical packages without even mastering these tricky systems. While the powerful programs for symbolic computations are undoubtedly helpful in design, they should be used only with complete understanding of their limitations (e.g., when dealing with trigonometric expressions).

Paradoxically, it is exactly the development of the computer that has made geometry important again. As computers and automatic control algorithms have become more powerful, designs of increasingly complicated mechanisms have become practical. If prior to that, analytic methods were sufficient for the study of mechanisms, this was because these mechanisms were of outstanding simplicity. However, the complex spatial machines of nowadays can no longer be completely analysed by purely analytic or numerical methods. While most researchers were occupied developing or using computer-aided engineering tools, the two Australian professors, Kenneth Hunt and Jack Phillips, were among the few who realised the need for a revival of the geometric methods.

Kinematic geometry is the first and simplest segment of kinematics that deals exclusively with displacements (Hunt, 1978). Time, as a variable, is usually not required to be brought into account. Indeed, the use of screw theory eliminates that need completely. Yet for convenience, velocity may sometimes be introduced in the study of the special, so-called singular, configurations of mechanisms. The main subject of this thesis is the displacements of parallel mechanisms or the geometry of two relatively moving bodies connected by a multitude of kinematic chains.

1.2 Preliminaries

The geometric approach used in this thesis as well as many of the results in it have a wide application. Apart from parallel mechanisms, some results may also be applied to the study of serial robots or biomechanical systems, to computer animation, and to many other fields. However, we are addressing chiefly a specialised audience which is already acquainted with the basic principles of parallel mechanisms. Therefore, one will not find here any of the often seen pro/con comparisons between serial and parallel

robots, nor a vague attempt for extensive literature review on parallel robots in general, nor the commonly seen photos of flight simulators. The field of parallel robots, despite the scarcity of specialised textbooks, is already too advanced to allow us to review it on a couple of pages. If the reader is, however, looking for a quick free overview of the field, we suggest a visit to the on-line *Parallel Mechanisms Information Center* at http://www.parallemic.org.

What we are obliged to do is to present a brief overview of the terminology and nomenclature used in this thesis together with the corresponding definitions. This is because, unfortunately, there exist no well-established terminology in the field of parallel mechanisms. Or, should we say *parallel robots*?

The most controversial term relates to the very focus of our thesis—the *parallel mechanism*. A plethora of loose synonyms may be found in the literature such as *Stewart platform*, *Gough platform*, *hexapod*, *parallel robot*, *parallel manipulator*, or *closed-loop kinematic chain*. Sometimes, these terms are properly used based on their connotations, but most frequently, they are not. For example, according to the terminology for the Theory of Machines and Mechanisms defined by IFToMM, a *robot* is a *mechanical system under automatic control that performs operations such as handling and automation*, while a *kinematic chain* is simply an *assemblage of links and joints*. This thesis studies parallel kinematic chains which are sometimes actuated (as in Chapters 2 and 4), sometimes not (as in Chapter 3). However, we are always exclusively interested in the relative motion between the mobile platform and the base. Hence, the use of the term *parallel mechanism* throughout this thesis.

An n-DOF (n-degree-of-freedom) *fully-parallel mechanism* is composed of n independent *legs* connecting the mobile platform to the base. Each of these legs is a serial kinematic chain that hosts one and only one motor which actuates, directly or indirectly, one of the joints. The variables that describe the actuated joints will be referred to as the *input variables* or also as the *active joint variables*. Other authors refer to the same variables as *articular coordinates*. On the other hand, the variables that describe fully the *pose* of the *mobile platform* (the *end-effector*) will be referred to as *output variables*. In other works, the same variables are referred to as *generalised coordinates*.

In our thesis, we will deal mainly with fully-parallel mechanisms, each having identical legs. Our investigation will cover 3-DOF planar fully-parallel mechanisms, 3-DOF parallel mechanisms, and 6-DOF spatial fully-parallel mechanisms. Most of the results may be extended to other parallel mechanisms as well. For example, in Chapter 3, we

do not even mention actuators—all results remain valid even if two actuators are used per leg. In fact, a mechanism which is not covered by the above definition of fully-parallel mechanism is sometimes called a *hybrid mechanism*. Anyway, we will loosely use the term *parallel mechanism* to refer mostly to fully-parallel mechanisms but, in some cases, to hybrid mechanisms as well.

The *configuration* of an n-DOF parallel mechanism is not simply defined by the pose of its mobile platform. In general, for a given pose, i.e., for a given set of output variables, there are several valid sets of input variables. The task of computing the input variables out of the output variables will be referred to as the *inverse kinematic problem* (IKP). The (typically) two solutions to the inverse kinematics of a single chain will be identified by a *branch index*. The solutions to the inverse kinematics of the whole parallel mechanism will be called the *working modes* (Chablat and Wenger, 1998) or *branch sets*. When the inverse kinematic problem of a chain degenerates, we will talk about a *Type 1 singularity* (Gosselin and Angeles, 1990). These singularities are also referred to as *Redundant Input (RI)* singularities (Zlatanov et al., 1994b).

The configuration of an n-DOF parallel mechanism is not defined by its input variables either. The task of finding the valid set of output variables corresponding to a set of input variables, referred to as the *direct kinematic problem*, has usually a multitude of solutions, referred to as *assembly modes*. In fact, some mechanisms allow an infinite number of solutions to their direct kinematics—a situation referred to as *self motion* (Karger and Husty, 1996). More precisely, self motion means a finite mobility from some points of the workspace, whereas the confusingly similar term *architecture singularity* refers to a singularity in every point of the workspace (Ma and Angeles, 1992). When two, or more, of the assembly modes are coinciding, we say that there is a *Type 2 singularity* (Gosselin and Angeles, 1990). These are also referred to as *Redundant Output (RO)* singularities (Zlatanov et al., 1994b).

The configuration of an n-DOF parallel mechanism is not even defined by both the input and output variables. Indeed, some mechanisms exist which will allow passive motion even when the motors and the mobile platform are fixed. Such particular singularities are called *Redundant Passive Motion (RPM) singularities* (Zlatanov et al., 1994b). The configuration of a parallel mechanism is defined by all its *joint variables*. The set of all feasible sets of joint variable values will be referred to as the *configuration space*. When a singularity exists in the configuration space of a parallel mechanism, an *Increased Instantaneous Mobility (IIM)* occurs (Zlatanov et al., 1994b). If the increased mobility involves the platform, a *constraint singularity* appears (Zlatanov et al., 2002a).

Most frequently, however, the user and the designer of a parallel mechanism will be interested only in the set of feasible output variables which we will refer to as the *complete workspace*. The complete workspace of a 6-DOF parallel manipulator is a six-dimensional highly coupled entity which is practically impossible to visualise. Therefore, the complete workspace of such mechanisms is studied only through its different subsets. Most of these are also defined for parallel mechanisms with less than six degrees of freedom.

The most common subset of the complete workspace is the *constant-orientation workspace* (Merlet, 1994) which is the set of permissible positions for the centre of the mobile platform while the platform is kept at a constant orientation. Conversely, the *orientation workspace* is the set of permissible orientations of the mobile platform, while the platform centre is held fixed.

We will use the standard character-based notation for the different architectures of n-DOF fully-parallel mechanisms with identical legs. We will use the letters R, P, U, and S to denote respectively revolute, prismatic, universal, and spherical joints. When a joint is actuated, its corresponding letter will be underlined. Thus, the chain of letters (one of which is underlined) designating the joints in a leg, ordered consecutively from the base to the mobile platform, will be used to denote the leg. The sequence of characters, preceded by "$n-$," will be used to denote the architecture of an n-DOF fully-parallel mechanism with n such legs.

Finally, Oxy or $Oxyz$ will denote the *base frame* in a parallel mechanism, i.e., the coordinate frame which is attached to the base. Similarly, $Cx'y'$ or $Cx'y'z'$ will always be the *mobile frame* in a parallel mechanism, i.e., the coordinate frame which is attached to the mobile platform. Further, we will usually denote the centres of the joints (in the case of R, U, or S joints), by O_i, A_i, and B_i, starting from the base, where i will denote the leg. In this thesis, $i = 1, 2, 3$, in Chapters 2 and 3, and $i = 1, 2, \ldots, 6$, in Chapter 4. Finally, we will often use the notation $\mathbf{r}_{AB}$ to denote the vector connecting a point A to a point B.

1.3 Objectives and Contributions of the Thesis

The principal goal of this thesis is to show how a geometric approach to the study of the kinematics of well-known parallel mechanisms can reveal and correctly explain numerous previously unknown properties. Our investigation was propelled by the desire

to foster the reliance on such geometric methods. As we go through the kinematic analysis of parallel mechanisms, we show how geometry brings an in-depth insight into the very principles of motion, much better than the study of a mystifying algebraic equation. If, after reading this thesis, a researcher starts visualising circles, spheres, and tori, where earlier he or she saw nothing but quadratic or quartic equations, our first goal would have been achieved.

Geometry develops creativity. It is not through the use of a computer algebra system that one will come up with a new design or architecture. It is unlikely that a genetic algorithm will automatically generate an innovative optimal design. It is intuition and a confident grasp of the principles of motion that will lead to ingenious mechanical solutions.

In trying to convert the reader to a more geometry-aware approach, we also show concern for the weary readers of lengthy scientific papers. Numerous are the examples of papers with arrays of lengthy equations or obscure graphical results, struggling with the width limits of the common double-column format. The ancient Chinese proverb that *"a picture is worth a thousand words"* is very true in the field of mechanical design. Who would argue that a Bohemian dome is best understood through its geometric definition and an intelligent cutaway drawing (Fig. 4.26, page 151) rather than via studying its complicated algebraic equation? Who would dispute the advantage of a nicely-shaped closed surface (Fig. 3.3, page 82) over a dispersed cloud of points for the interpretation of the orientation workspace of a mechanism? It is geometry that allows for the most compact description and interpretation of results.

The second objective of this thesis is to uncover the hidden properties of well-known parallel mechanisms. Thus, our intention is to assist the numerous designers and users of these popular architectures. It should be noted that the mechanisms that we analyse were not specially chosen. We simply selected all 3-DOF planar parallel mechanisms, several popular 3-DOF spatial parallel mechanisms with mixed degrees of freedom, and the least-studied yet popular 6-DOF parallel mechanism with revolute actuators. Dozens of prototypes exist for nearly all of the mechanisms that we study, many of which are even commercially available.

While the revelations of our investigation would certainly not lead to product recalls, they will help better understand and explain the properties of these mechanisms, and, therefore, allow the optimal use of existing devices and the creation of new and improved designs. For example, manufacturers can stop saying that their mechanisms have pitch

and roll capabilities but instead simply state that there is no torsion. They can improve their control systems in order to make better use of the already small workspace of a parallel mechanism. They can adopt new designs with few or no singularities at all.

Our last aim is to suggest topics and avenues of further research. Two particular directions are identified in this thesis and detailed in the last chapter. While these directions call for a sophisticated immersion in the theory of kinematic geometry, the fruits of the research will not only be of theoretical but also of practical value.

1.4 Overview of the Results

Our work is presented in three main parts—Chapters 2, 3, and 4. While the progress through the chapters leads us from the planar movement to three, and then six degrees of freedom in space, the complexity does not necessarily follow the same progression. In fact, it is probably Chapter 3 that is easiest to read and understand. On the other hand, we go from the general study of all 3-DOF planar parallel mechanisms, to the analysis of a class of 3-DOF spatial parallel mechanisms, to a single architecture of a 6-DOF parallel mechanism.

In Chapter 2, we analyse the singularities of all 3-DOF planar parallel mechanisms. The velocity equations for all mechanisms are derived by using both screw theory and the conventional approach of differentiating with respect to time the constraint equations governing the motion of the mechanism. Therefore, a substantial part of the chapter is dedicated to explaining the use of screw theory in the plane. Once these velocity equations are set up, an exhaustive study on the various types of singularities of these mechanisms is performed. Several new designs are identified that have few or no singularities at all. Chapter 2 ends with a detailed discussion on one of the proposed directions for research—the problem of workspace segmentation, working modes, and assembly modes. Several examples are given to illustrate these intricate concepts.

In Chapter 3, we leave the plane and start with a discussion on the problem of orientation representation. We present a concise treatise on the relatively unknown Tilt & Torsion angles to demonstrate their numerous advantages. Then, using these angles, we analyse several 3-DOF spatial parallel mechanisms with one translational and two rotational degrees of freedom. We derive the relationships between the three constrained and three feasible degrees of freedom and show clearly that these mechanisms belong to a special class of mechanisms with zero torsion of the mobile platform.

In Chapter 4, we limit our investigation to the general 6-DOF 6-$\underline{R}US$ parallel mechanism. In the first part of the chapter, we set up a geometric method for the computation of the edges of the constant-orientation workspace. Our method takes into account the mechanical limits on the U joints. In the second part, we ignore those limits and describe another geometric algorithm for the computation of the constant-orientation workspace. This time, however, instead of computing only the edges, we also compute the cross-sections of the workspace. In the final part of Chapter 4, we limit our study to the special 6-$\underline{R}US$ parallel mechanism with pair-wise coincident S joints and all six centres of the U joints moving on the same circle. The *Rotobot*, as it is dubbed, allows us to demonstrate once more the issue of workspace segmentation by working modes. We propose geometric methods for the computation and representation of the horizontal cross-sections of the singularity loci and constant-orientation workspace. One interesting point relates to the astonishing geometric model of the constraint on the circular order of the U joints.

Chapter 2

Singularity Analysis of 3-DOF Planar Parallel Mechanisms

This chapter deals in an exhaustive way with the singularity analysis of all possible 3-DOF planar parallel mechanisms with identical legs. The velocity equations are derived in both the conventional manner, through differentiation of the inverse kinematic equations, and via screw theory. For this purpose, planar screw theory is introduced in a rigorous manner.

For each mechanism, polynomial expressions for the singularities in the Cartesian space are derived from the corresponding velocity equations. Then, for different designs, a plot is produced of the singularity loci for a constant orientation of the mobile platform. Detailed analyses of those loci are performed and numerous important observations are made.

Finally, some remarks are made, particularly on planar parallel mechanisms with mixed legs, the missing "Type 3" singularities, and on planar parallel mechanisms with parallelograms. To conclude the chapter, a greater attention is paid to workspace segmentation in the presence of assembly modes and kinematically different working modes.

2.1 Introduction

The direct kinematic problem has been studied in detail for all 3-DOF planar parallel mechanisms (PPMs) (Merlet, 1996; Hayes, 1999). In a similar fashion, the singularity configurations of all 3-DOF PPMs have been studied by Mohammadi Daniali et al. (1995). However, the authors have only presented a general approach for setting up the velocity equations and identifying all singular configurations, by dividing all PPMs into two classes. This chapter, on the other hand, provides a detailed investigation of the singular configurations and the singularity loci of each and every PPM. Such a detailed study yields valuable theoretical insight into the kinematics of PPMs. In practice, the presented results can be very useful in the selection of the optimal architecture for a given task. Furthermore, we point out several novel designs with valuable properties.

Since we are interested only in 3-DOF *fully-parallel* planar mechanisms, each of the three legs will be composed of one active and two passive joints. There are 21 3-DOF serial chains (legs) in total (Table 2.1). Three of them (marked with $^{\times}$) cannot yield 3-DOF PPMs since they lead to mechanisms with only one controllable DOF. There are also eight pairs of symmetrical chains, where each pair leads to two kinematically equivalent PPMs. Therefore, we can eliminate eight more chains (the ones marked with $^{\sim}$) which leaves us with only ten architectures to examine (Fig. 2.1).

$\underline{R}RR$	$\underline{R}PR$	$\underline{R}PP^{\times}$	$\underline{P}RR$	$\underline{P}RP$	$\underline{P}PR$	$\underline{R}RP$
$R\underline{R}R$	$R\underline{P}R$	$R\underline{P}P$	$P\underline{R}R$	$P\underline{R}P^{\times}$	$P\underline{P}R^{\sim}$	$R\underline{R}P^{\sim}$
$RR\underline{R}^{\sim}$	$RP\underline{R}^{\sim}$	$RP\underline{P}^{\sim}$	$PR\underline{R}^{\sim}$	$PR\underline{P}^{\sim}$	$PP\underline{R}^{\times}$	$RR\underline{P}^{\sim}$

Table 2.1: All possible 3-DOF serial chains (legs).

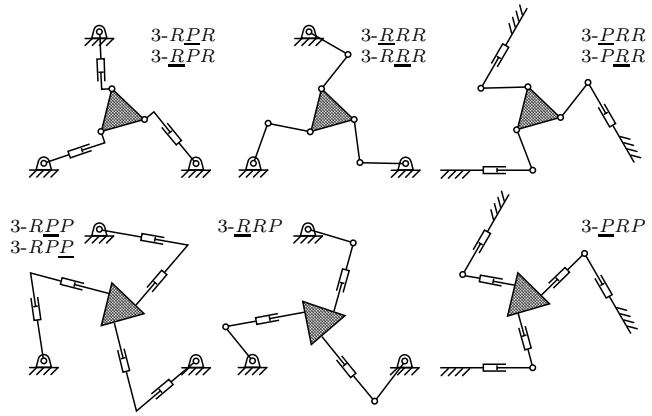

Figure 2.1: The basic 3-DOF PPMs with identical legs.

2.2 Planar Instantaneous Kinematics via Screw Theory

The conventional process of deriving the input-output velocity equation for a parallel mechanism consists of differentiating the inverse kinematic equation. Generally, the process is tedious and leads to possible parameterisation errors. A much better approach is the use of reciprocal screws. They provide a better geometrical insight into the problem and allow the precise and complete description of singularity types.

2.2.1 Screw Methods

Singularity analysis using reciprocal screws has already been described in the literature (Mohammed and Duffy, 1984; Kumar, 1992; Tsai, 1999; Zlatanov et al., 1994b). There are, however, two subtler aspects of the method that are not widely known, but are relevant to the analysis of planar parallel mechanisms.

Firstly, any screw-based approach needs to be modified when applied to mechanisms with $n < 6$ DOFs. In such cases, it is desirable to treat the *twists* (instantaneous motions) and *wrenches* (forces and moments) involved in the velocity and singularity analysis as n-dimensional so that the matrices involved are $n \times n$ (Zlatanov et al., 1994b; Hunt, 2000). Velocity analysis in such cases amounts to an n-dimensional version of screw calculus. However, screws and reciprocal screws (i.e., twists and wrenches) have different sets of n coordinates. Unlike the general 6-DOF case, screws and reciprocal screws can no longer be thought of as elements of the same vector space. Three-dimensional planar screws will be the focus of Section 2.2.2.

Secondly, for the analysis to remain valid in all configurations, it is important to always find a maximal set of (independent) reciprocal screws. Otherwise, the method can misinterpret or even fail to detect certain singularities (Zlatanov et al., 1994b). That issue will be discussed in Section 2.3.1.

2.2.2 Planar Twists and Wrenches

We assume that for all admissible reference frames the origin as well as the x and y axes are in the chosen plane of motion. For every given Cartesian frame in space we associate a standard basis, $\{\boldsymbol{\varrho}_x, \boldsymbol{\varrho}_y, \boldsymbol{\varrho}_z, \boldsymbol{\tau}_x, \boldsymbol{\tau}_y, \boldsymbol{\tau}_z\}$, in the six-dimensional space of twists, $\mathcal{S}$. The elements of this basis are the three rotations about and three translations

along the frame axes. The elements of $\mathcal{S}$ can be also interpreted as wrenches, the basis vectors being the pure forces along and the moments about the coordinate axes. In fact, wrenches comprise the dual vector space $\mathcal{S}^*$, i.e., they are linear forms defined on $\mathcal{S}$. The action of a wrench on a twist is the instantaneous work rate contributed by the wrench during the motion along the twist and defines the *reciprocal screw product* of the underlying elements of $\mathcal{S}$. When a wrench applies no power on a twist, their reciprocal product is zero, and it is said that the two are reciprocal.

The coordinates of a twist in the standard basis will be denoted by $\boldsymbol{\xi} = [\boldsymbol{\omega}^T, \mathbf{v}^T]^T = [\omega_x, \omega_y, \omega_z, v_x, v_y, v_z]^T$. When an element of $\mathcal{S}$ is seen as a wrench, its coordinates in the standard basis are given by $\boldsymbol{\zeta} = [\mathbf{f}^T, \mathbf{m}^T] = [f_x, f_y, f_z, m_x, m_y, m_z]^T$. As is customary in the literature, we will use the term *screw* to refer to a normalised[1] element of $\mathcal{S}$, twist or wrench (Hunt, 1978).

For planar mechanisms, all instantaneous motions (or twists) are part of the three-dimensional screw system of instantaneous planar motion. The planar screw system is, in fact, $\mathcal{E} = \text{Span}\,(\boldsymbol{\varrho}_z, \boldsymbol{\tau}_x, \boldsymbol{\tau}_y)$. A planar twist will always have three of its coordinates, ω_x, ω_y, v_z, equal to zero. Hence, we will write the planar twists as three-dimensional vectors, $\boldsymbol{\xi} = [\omega_z, v_x, v_y]^T$.

The *reciprocal screws* used in singularity analysis are reciprocal to some but not all joint twists. Physically, they represent wrenches which, when applied to the output link can be resisted by (i.e., do no work on) the mechanism at certain conditions (when some active joints are locked), but not always. In other words, these screws never belong to the reciprocal system of the screw system of the mechanism twists. Indeed, screws reciprocal to *all* mechanism twists would be of no interest. For planar mechanisms, the reciprocal system, $\mathcal{E}^\perp$, is identical to $\mathcal{E}$ itself. Therefore, we can assume that the reciprocal screws are all in a 3-system complementary to $\mathcal{E}$, for example, in $\mathcal{W} = \text{Span}\,(\boldsymbol{\varrho}_x, \boldsymbol{\varrho}_y, \boldsymbol{\tau}_z)$. The elements of $\mathcal{W}$ are pure forces in the xy plane as well as the pure moment about the z axis. Hence, we will write the wrenches as three-dimensional vectors, $\boldsymbol{\zeta} = [f_x, f_y, m_z]^T$.

Thus, the reciprocal product of a wrench $\boldsymbol{\zeta} = [\mathbf{f}^T, m]^T = [f_x, f_y, m]^T$ and a twist $\boldsymbol{\xi} = [\omega, \mathbf{v}^T]^T = [\omega, v_x, v_y]^T$ is defined as:

$$\boldsymbol{\zeta} \circ \boldsymbol{\xi} = m\omega + \mathbf{f}^T\mathbf{v} = m\omega + f_x v_x + f_y v_y \,. \tag{2.1}$$

[1] A twist (or wrench) is normalised when its $\boldsymbol{\omega}$ (or $\mathbf{f}$) component is either (1) a unit vector or (2) a zero vector while the $\mathbf{v}$ (or $\mathbf{m}$) component is a unit vector.

2.3 Planar Instantaneous Kinematics of PPMs

We will use the characters O, A, and B as superscripts to label the three joints in the i-th leg ($i = 1, 2, 3$) starting from the base. When a joint is revolute, its character index, with a subscript i, will also be used to denote the centre point of that joint, O_i, A_i or B_i (see Figs. 2.3(a), 2.5(a), 2.8(a), 2.9(a), etc.). In addition, let Oxy and $Cx'y'$ be the base and platform frames, respectively.

2.3.1 The Input-Output Velocity Equation

The relationship between the instantaneous motion of the platform, the *output twist* $\boldsymbol{\xi} = [\omega, v_x, v_y]^T$, and the nine joint rates $\dot{\theta}_i^J$ ($J = O,\ A,\ B$; $i = 1,\ 2,\ 3$) is given by the twist equations of the legs

$$\boldsymbol{\xi} = \dot{\theta}_i^O \boldsymbol{\xi}_i^O + \dot{\theta}_i^A \boldsymbol{\xi}_i^A + \dot{\theta}_i^B \boldsymbol{\xi}_i^B \ , \ i = 1, 2, 3. \tag{2.2}$$

Equation (2.2) is a necessary and sufficient condition for the twist $\boldsymbol{\xi}$ and the joint velocities $\dot{\theta}_i^J$ about the joint screws $\boldsymbol{\xi}_i^J$ to be feasible at a given configuration.

To eliminate the passive joint velocities from Eq. (2.2) and obtain an input-output velocity equation each of the three twist equations in Eq. (2.2) is multiplied (via the reciprocal screw product) with a screw, $\boldsymbol{\zeta}_i$, reciprocal to all passive joint twists in the i-th leg. This is a wrench which, if applied to the platform, can be resisted using only the actuator of the leg. As a result, three scalar equations are obtained:

$$\boldsymbol{\zeta}_i \circ \boldsymbol{\xi} = \boldsymbol{\zeta}_i \circ \boldsymbol{\xi}_i^a \ \ \dot{\theta}_i^a \ , \quad i = 1, 2, 3, \tag{2.3}$$

where the superscript $a \in \{O, A, B\}$ denotes the active joint.

Equations (2.3) are equivalent to Eqs. (2.2) only if each three-dimensional reciprocal wrench, $\boldsymbol{\zeta}_i$, is unique, i.e., if there are no other wrenches reciprocal to both passive-joint screws in the i-th leg (Zlatanov et al., 1994b). This is so if, and only if, the two passive-joint screws are linearly independent. If they are linearly dependent, there will be two reciprocal wrenches, $\boldsymbol{\zeta}_i'$ and $\boldsymbol{\zeta}_i''$, and the corresponding input-output velocity relationship in Eqs. (2.3) obtained from $\boldsymbol{\zeta}_i$ will need to be replaced by two equations:

$$\begin{aligned} \boldsymbol{\zeta}_i' \circ \boldsymbol{\xi} \ &= \ \boldsymbol{\zeta}_i' \circ \boldsymbol{\xi}_i^a \ \ \dot{\theta}_i^a \\ \boldsymbol{\zeta}_i'' \circ \boldsymbol{\xi} \ &= \ \boldsymbol{\zeta}_i'' \circ \boldsymbol{\xi}_i^a \ \ \dot{\theta}_i^a \ , \end{aligned} \tag{2.4}$$

which the input and output velocities must satisfy in addition to Eqs. (2.3) for the remaining values of i. An accurate velocity and singularity analysis must take Eqs. (2.4) into account.

Thus, for each of the PPMs, we expect to derive an input-output velocity equation of the type

$$\begin{bmatrix} \boldsymbol{\zeta}_1\circ \\ \boldsymbol{\zeta}_2\circ \\ \boldsymbol{\zeta}_3\circ \end{bmatrix} \begin{bmatrix} \omega \\ v_x \\ v_y \end{bmatrix} = \begin{bmatrix} \boldsymbol{\zeta}_1 \circ \boldsymbol{\xi}_1^a & 0 & 0 \\ 0 & \boldsymbol{\zeta}_2 \circ \boldsymbol{\xi}_2^a & 0 \\ 0 & 0 & \boldsymbol{\zeta}_3 \circ \boldsymbol{\xi}_3^a \end{bmatrix} \begin{bmatrix} \dot{\theta}_1^a \\ \dot{\theta}_2^a \\ \dot{\theta}_3^a \end{bmatrix}, \tag{2.5}$$

where $\boldsymbol{\zeta}\circ$ is a shorthand for the row vector obtained from $\boldsymbol{\zeta}$ by writing the moment before the force coordinates, $\boldsymbol{\zeta}\circ = [m, f_x, f_y]$. For some PPMs there will be configurations where one or more of the equations will need to be replaced by pairs of equations like Eqs. (2.4) in order to accurately describe the relationships between the input and output velocities.

We will denote the matrices multiplying the platform twist and the active joint rates with $\mathbf{Z}$ and $\boldsymbol{\Lambda}$, respectively. Thus, for every configuration of every PPM, there is an equation

$$\mathbf{Z}\boldsymbol{\xi} = \boldsymbol{\Lambda}\dot{\boldsymbol{\theta}}\,, \tag{2.6}$$

which completely describes the velocity kinematics of the mechanism. These two matrices are usually referred to as *Jacobian matrices* although this is not correct in the strictest mathematical sense. The matrices are 3×3 almost everywhere in the configuration space, but for some PPMs there are configurations where these matrices become rectangular.

2.3.2 Possible Reciprocal Screws for PPMs

Let us consider the nature of the reciprocal screws $\boldsymbol{\zeta}_i$ for the different PPMs. The screw $\boldsymbol{\zeta}_i$ will depend on the two passive joint screws in the i-th leg. We will also examine in what cases there can be configurations where the reciprocal screws for the leg form a 2-system, Span $(\boldsymbol{\zeta}_i', \boldsymbol{\zeta}_i'')$.

If the two passive joints are revolute, the reciprocal screw is a *zero-pitch screw* (i.e., a pure force) with an axis lying in the xy plane and intersecting the centres of the two

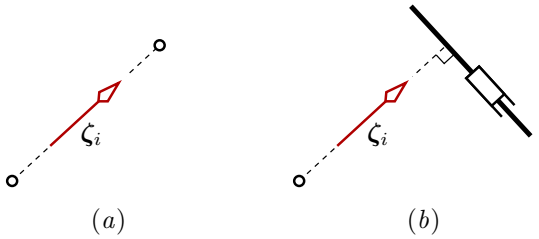

Figure 2.2: Reciprocal screw for (a) two passive R joints and (b) one passive R joint and one passive P joint.

passive R joints (Fig. 2.2). The two R-joint screws can become linearly dependent only when the passive joints are the extremal joints of the leg (i.e., joint A is active) and the constant link parameters have special values allowing the two joint centres to coincide. More precisely, in an $R\underline{R}R$ chain this will mean that the distal and proximal links must have equal lengths, while for an $R\underline{P}R$ leg a zero offset between the two R joints will be needed. If the passive joint centres do coincide, there is a 2-system of reciprocal screws, namely a planar pencil of zero-pitch screws lying in the xy plane and passing through the common centre of the coinciding joints. As a result, the leg will generate two scalar input-output equations, and the two reciprocal screws $\boldsymbol{\zeta}_i'$ and $\boldsymbol{\zeta}_i''$ can be taken as any two different forces through the common joint centre.

When one of the passive joints is revolute and the other is prismatic, they will always remain linearly independent and the uniquely defined reciprocal screw is a pure force passing through the R-joint centre and perpendicular to the direction of the P joint (Fig. 2.2).

Finally, let us consider the possibility of two passive prismatic joints. The active remaining joint must be revolute since a planar PPP chain would have only 2 DOFs and cannot be used as a leg of a 3-DOF PPM. Let us assume that the leg is nonsingular and hence the two passive-joint translations are distinct. Then, the unique reciprocal screw is the pure moment about the z axis, i.e., $\boldsymbol{\tau}_z$. Note that this wrench does not depend on the actual configuration or the link parameters. Therefore, if all three legs are with two passive P joints, then the three reciprocal screws $\boldsymbol{\zeta}_i$ will be identical. This means that the left-hand sides of the three Eqs. (2.3) will be identical and all three rows of the matrix multiplying the output twist in Eq. (2.5) will be $[1, 0, 0]$. Hence, the linear velocity of the platform can be arbitrary and cannot be controlled by the actuators. If only two legs have a pair of passive P joints there will still be a pair of equations which will not contain linear velocity terms and therefore there will be an uncontrollable translation of the end-effector. We can conclude that PPMs with two

passive prismatic joints in each of at least two legs cannot provide controlled 3-DOF planar motion.

However, a PPM can have a single leg with two passive P joints and one active R joint, since the linear motion will be controlled by the other two legs. If the leg is $P\underline{R}P$, it can become singular when the translations in the P joints become parallel. Then, there will be a 2-system which, apart from $\boldsymbol{\tau}_z$, includes all pure forces with axes perpendicular to the common direction of the P joints. A brief discussion of mechanisms with one $R\underline{P}R$ chain appears in Section 2.5.2.

Since our main attention is directed to PPMs with identical joint sequences in all legs, we can conclude that at least one of the passive joints in a leg is revolute and therefore that the reciprocal screws $\boldsymbol{\zeta}_i$ are all pure forces in the plane of motion as shown in Fig. 2.2.

2.3.3 Obtaining the Velocity Equation for Each PPM

When analysing a specific PPM one needs to find the reciprocal screws $\boldsymbol{\zeta}_i$ as expressions of the chosen joint and link parameters and substitute them in Eq. (2.5). Matrix $\mathbf{Z}$ will depend on the choice of the reference frame. However, $\boldsymbol{\Lambda}$ will be coordinate invariant due to the invariance of the reciprocal product.

Since all reciprocal screws are pure forces, their coordinates will be of the type $[\mathbf{f}_i^T, m_i]^T$, where $\mathbf{f}_i = [f_{xi}, f_{yi}]^T$ is a unit vector parallel to the force and m_i is the moment of the force axis about the platform centre. These quantities will be expressed as functions of the chosen parameters. Namely, in this chapter, we will use as parameters the position of the platform centre C defined by vector $\mathbf{p} = [x, y]^T$, and the orientation of the platform ϕ which will be assumed to be constant for the description of the singularity loci. These functions will be continuous everywhere except in those special configurations, where two passive joint screws become linearly dependent. For those configurations, the input-output velocity equation needs to be defined separately with four (or more) equations rather than three. The two reciprocal wrenches corresponding to the leg with coinciding passive revolute joints can be taken as the two forces parallel to the x and y axes and passing through the coinciding joint centre O_i, (x_{OO_i}, y_{OO_i}):

$$\boldsymbol{\zeta}_i' = [1,\, 0,\, -y_{CB_i}]^T\,, \quad \boldsymbol{\zeta}_i'' = [0,\, 1,\, x_{CB_i}]^T\,, \tag{2.7}$$

where x_{CB_i} and y_{CB_i} are the coordinates of the platform revolute joints in an instantaneous frame with origin at the mobile platform frame centre and axes parallel to those of the base frame.

The reciprocal products on the diagonal of $\mathbf{\Lambda}$ will be:

$$\boldsymbol{\zeta}_i \circ \boldsymbol{\xi}_i^a = \lambda_i = \begin{cases} (\mathbf{r}_i^a \times \mathbf{f}_i)_z & \text{if joint } a \text{ is revolute} \\ \mathbf{f}_i^T \boldsymbol{\pi}_i^a & \text{if joint } a \text{ is prismatic} \end{cases} \tag{2.8}$$

where $\mathbf{r}_i^a$ is any vector originating at the centre of the active R joint and ending on the axis of $\boldsymbol{\zeta}_i$, and $\boldsymbol{\pi}_i^a$ is the unit vector defining the direction of the active P joint. When the active joint is revolute, the scalar λ_i is the moment of the reciprocal force with respect to the centre of the active R joint. When the actuator is prismatic, λ_i is the projection of the force onto the direction of the actuated translation. The expression $(\cdot)_z$ stands for the z component of the vector argument.

Thus, to write the input-output Eq. (2.6) for any configuration we need to express the quantities f_{xi}, f_{yi}, m_i, and λ_i as functions of x and y and the design parameters.

2.3.4 Types of Singularities

Equation (2.6), where the matrices $\mathbf{Z}$ and $\mathbf{\Lambda}$ are occasionally non-square, completely describes the instantaneous kinematics of a parallel manipulator and hence can be used to fully describe and classify the singular configurations of the mechanism (Zlatanov et al., 1994b).

An input-output velocity equation was first used for the purposes of singularity classification of parallel mechanisms by Gosselin and Angeles (1990). In that paper, two main singularity types were defined. The first, or Type 1, occurs when matrix $\mathbf{\Lambda}$ is singular, while Type 2 corresponds to configurations where $\mathbf{Z}$ is singular.

Later, Zlatanov et al. (1994a) introduced a more detailed classification (for arbitrary mechanisms), based on six singularity types. The six types are: Redundant/Impossible Input/Output (RI, II, RO, IO); Redundant Passive Motion (RPM); and Increased Instantaneous Mobility (IIM). As it was shown in (Zlatanov et al., 1994b) (Theorems 2 and 3), the two basic types described in (Gosselin and Angeles, 1990) are, in fact, the types RI and RO. Namely, $\mathbf{Z}$ is rank deficient (Type 2) if, and only if, there is Redundant Output, i.e., an uncontrollable motion of the mobile platform when the

actuators are locked; and matrix $\mathbf{\Lambda}$ is rank deficient (Type 1) if, and only if, there is Redundant Input, i.e., a non-zero instantaneous motion in the active joints when the mobile platform is fixed.

If we consider only "usual" configurations, where the matrices $\mathbf{Z}$ and $\mathbf{\Lambda}$ are square, Type 1 singularities are identical with Impossible Output (IO) singularities, i.e., configurations where the platform loses a degree of freedom because the serial chain of one of the legs is singular (the three joint screws in the leg are linearly dependent).

In the special configurations where $\mathbf{Z}$ and $\mathbf{\Lambda}$ are not square, a leg is always singular and IO (reduced freedom of the platform) is always present. However, this is not necessarily accompanied by the rank deficiency of the rectangular matrix $\mathbf{\Lambda}$ or (equivalently) by a Redundant Input motion. Instead, in such configurations, there always exists a Redundant Passive Motion (RPM), i.e., a motion of the mechanism involving only the passive joints and leaving the platform fixed. Moreover, RPM singularities will usually be Impossible Input (II) singularities as well, which means that the input velocities cannot be chosen independently.

For all configurations, a Type 2 (or RO) singularity, where an uncontrollable motion of the platform occurs, is present if, and only if, the reciprocal screws $\boldsymbol{\zeta}_i$, possibly including $\boldsymbol{\zeta}'_i$ and $\boldsymbol{\zeta}''_i$ for some i, span at most a two-system rather than the whole wrench space $\mathcal{W} = \text{Span}\,(\boldsymbol{\varrho}_x, \boldsymbol{\varrho}_y, \boldsymbol{\tau}_z)$.

Any redundant motion (RO, RI, or RPM) can be either *infinitesimal* or *finite*. In the latter case, it is said that there is a (finite) *self motion* of the manipulator (Karger and Husty, 1996). When, the singularity is of Type 2 (RO), it is usually referred to as an *architecture singularity* (Ma and Angeles, 1992). In general, whether the motion is infinitesimal or finite cannot be detected by studying only Eq. (2.6) for a single given configuration.

2.4 Singularity Analysis of PPMs

This section presents the principal part of the present chapter, namely, the results from the singularity analysis of all ten PPMs. These results are obtained both by using the powerful tools of planar screw theory described in the last two sections and through a conventional approach. Two are the main contributions of the present section.

Firstly, we derive the expressions for $\mathbf{f}_i$, m_i, and λ_i as functions of x, y and the design parameters. As we will see, this task is not always trivial. The derivation of these expressions, in essence, amounts to solving the IKP. However, we do not always need to explicitly obtain the IKP solution. In fact, for some PPMs with active P joints, we will not even define the active joint variables.

Our second contribution is the study of the singularities for each PPM. The singularity loci of Type 1 and Type 2 are determined for a constant orientation of the mobile platform. Note that the derivation of the minimal-degree polynomial corresponding to Type 2 singularity loci for some PPMs is a delicate task. Those derivations cannot be performed simply by using a brute force approach with a computer algebra system such as Maple. The most difficult derivation is for 3-$\underline{R}RR$ PPMs and was already presented in a conference paper (Bonev and Gosselin, 2001). The singularity loci of Type 2 are generally obtained by a discretisation method.

2.4.1 Singularity Analysis of 3-$R\underline{P}R$ PPMs

As a so-to-speak planar equivalent of the Stewart platform (a 6-$U\underline{P}S$ parallel mechanism), the 3-$R\underline{P}R$ PPM is expected to share the same popularity. Yet, it is neither the PPM with the simplest kinematics, as we will see later, nor the most practical mechanism. Only a few 3-$R\underline{P}R$ PPMs have been constructed, and most usually, with a linear base and platform (Satya et al., 1995; Du Plesssis et al., 2000). The reason is that the mobile part of the manipulator hosts the heavy and cumbersome actuators which increases the inertia of the mechanism and the link interference.

Referring to Fig. 2.3(a), we denote with O_i and B_i the centres of the base and platform R joints, respectively. Point A_i is at the intersection of a line through O_i with the direction of the P joint, and a line through B_i and perpendicular to the first line. The *directed distance* between O_i and A_i along the direction of prismatic actuator i is ρ_i, which is the active joint variable, and the length of A_iB_i is ℓ, which is referred to as the *offset*. As mentioned before, the components of the vectors $\mathbf{r}_{OO_i}$ along OO_i (which are constant) and $\mathbf{r}_{CB_i}$ along CB_i (which are constant for a constant orientation) in the base frame are (x_{OO_i}, y_{OO_i}) and (x_{CB_i}, y_{CB_i}), respectively. Without loss of generality, we set $x_{OO_1} = y_{OO_1} = x_{CB_1} = y_{CB_1} = y_{OO_2} = 0$. Finally, as defined before, the vector along OC is designated by $\mathbf{p}$, where $\mathbf{p} = [x, y]^T$.

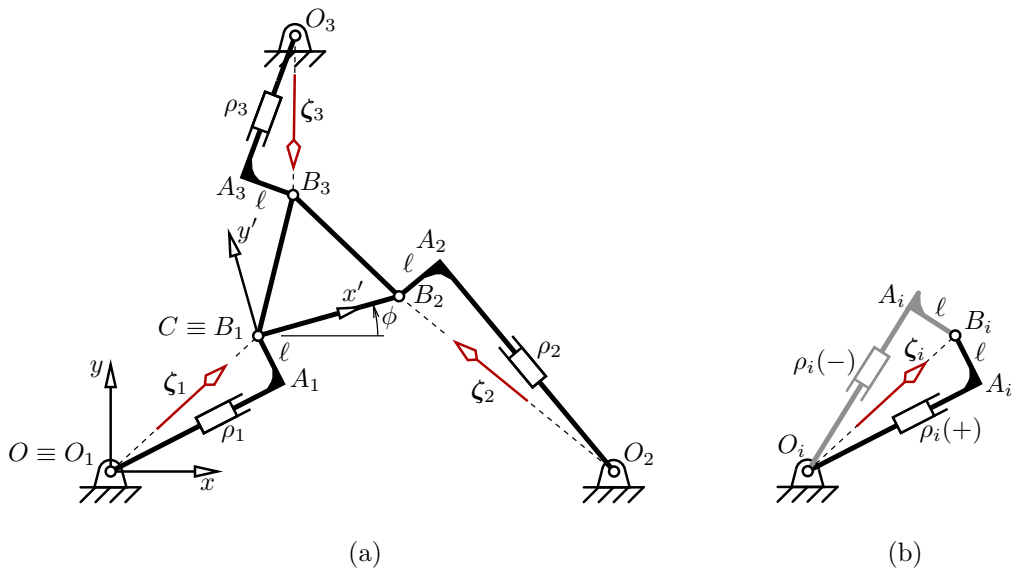

Figure 2.3: (a) A 3-DOF PPM of type 3-$R\underline{P}R$ and (b) the two branches of a leg.

2.4.1.1 Solving the Inverse Kinematic Problem

We will first consider the task of computing the input variables (ρ_1, ρ_2, ρ_3) from the set of output variables (x, y, ϕ), i.e., solve the inverse kinematic problem. Geometrically, for the i-th leg, the problem can be seen as the one of finding the distance between points O_i and B_i, and then computing the resultant value of ρ_i^A. We have

$$\mathbf{r}_{O_iB_i} = \mathbf{p} + \mathbf{r}_{CB_i} - \mathbf{r}_{OO_i}. \tag{2.9}$$

Squaring both sides of the above equation gives us:

$$\varrho_i^2 = \mathbf{r}_{O_iB_i}^T(\mathbf{p} + \mathbf{r}_{CB_i} - \mathbf{r}_{OO_i}) = \bar{x}_i^2 + \bar{y}_i^2, \tag{2.10}$$

where ϱ_i is the distance between points O_i and B_i and

$$\bar{x}_i = x + x_{CB_i} - x_{OO_i},\ \bar{y}_i = y + y_{CB_i} - y_{OO_i}. \tag{2.11}$$

On the other hand, from the rectangular triangle $O_iA_iB_i$, we finally have:

$$\rho_i = \delta_i\sqrt{\varrho_i^2 - \ell^2} = \delta_i\sqrt{\bar{x}_i^2 + \bar{y}_i^2 - \ell^2} \tag{2.12}$$

where $\delta_i = \pm 1$ is the so-called *branch index*. Indeed, as shown schematically on Fig. 2.3(b), there are two solutions for the IKP of each leg—one with a positive and one with a negative ρ_i. Hence, there is a total of eight solutions to the IKP of a 3-$P\underline{R}P$ planar parallel mechanism. Each of these solutions is called a *branch set* or a *working mode* (Chablat and Wenger, 1998). As we will see in this chapter and in Chapter 4, the issue of working modes is of great importance. Yet, there have been only a few works on this problem.

2.4.1.2 Obtaining the Velocity Equation

(a) Using differentiation

Differentiating Eq. (2.10) with respect to time, leads to

$$\varrho_i \dot{\varrho}_i = \mathbf{r}_{O_iB_i}^T (\mathbf{v} + \omega \mathbf{r}_{CB_i}^{\perp}), \tag{2.13}$$

where $\omega = \dot{\phi}$ is the angular velocity of the mobile platform, $\mathbf{v} = [\dot{x}, \dot{y}]^T$ is its linear velocity, and $\mathbf{r}_{CB_i}^{\perp} = [-y_{CB_i}, x_{CB_i}]^T$. Substituting in the above equation $\mathbf{r}_{O_iB_i} = \varrho_i \hat{\mathbf{f}}_i$, where $\hat{\mathbf{f}}_i$ is a unit vector, and $\varrho_i \dot{\varrho}_i = \rho_i \dot{\rho}_i$, we obtain:

$$\begin{bmatrix} \hat{\mathbf{f}}_i^T \mathbf{r}_{CB_i}^{\perp}, & \hat{\mathbf{f}}_i^T \end{bmatrix} \begin{bmatrix} \omega \\ \mathbf{v} \end{bmatrix} = \frac{\rho_i}{\varrho_i} \dot{\rho}_i. \tag{2.14}$$

Finally, we write the above equation in the $\mathbf{Z}\boldsymbol{\xi} = \boldsymbol{\Lambda}\dot{\boldsymbol{\rho}}$ matrix form:

$$\begin{bmatrix} \hat{\mathbf{f}}_1^T \mathbf{r}_{CB_1}^{\perp} & \hat{\mathbf{f}}_1^T \\ \hat{\mathbf{f}}_2^T \mathbf{r}_{CB_2}^{\perp} & \hat{\mathbf{f}}_2^T \\ \hat{\mathbf{f}}_3^T \mathbf{r}_{CB_3}^{\perp} & \hat{\mathbf{f}}_3^T \end{bmatrix} \boldsymbol{\xi} = \mathrm{diag}\left(\frac{\rho_1}{\varrho_1}, \frac{\rho_2}{\varrho_2}, \frac{\rho_3}{\varrho_3} \right) \dot{\boldsymbol{\rho}}. \tag{2.15}$$

(b) Using screw theory

If $O_i \not\equiv B_i$, the reciprocal screws $\boldsymbol{\zeta}_i$, $i = 1, 2, 3$, are the screws passing through the two R joints in each leg. Hence, their direction is along the already defined unit vector $\hat{\mathbf{f}}_i$, i.e., $\mathbf{f}_i = \hat{\mathbf{f}}_i$, and their moment m_i is:

$$m_i = (\mathbf{r}_{CB_i} \times \mathbf{f}_i)_z = \mathbf{f}_i^T \mathbf{r}_{CB_i}^{\perp}. \tag{2.16}$$

If, again, $O_i \not\equiv B_i$, the diagonal elements of $\boldsymbol{\Lambda}$ (see Eq. 2.8), are

$$\lambda_i = \mathbf{f}_i^T \boldsymbol{\pi}_i = \frac{\rho_i}{\varrho_i}, \tag{2.17}$$

where $\boldsymbol{\pi}_i$ is the unit vector along the direction of the active P joint. Note that this vector is always defined, even when $\rho_i = 0$.

The first studied mechanism, the 3-$R\underline{P}R$ PPM, does not clearly show the superiority of the reciprocal screw method as for the length of computations. However, it pinpoints one very common and representative mistake that is made when conventional procedures are used to obtain the velocity equations in the very common $\ell = 0$ case.

When $\ell = 0$, one usually writes the matrix velocity equation as in what one obtains by multiplying each side of Eq. (2.15) by the matrix $\mathrm{diag}(\rho_1, \rho_2, \rho_3)$. Therefore, one may wrongly assume that at $\rho_i = 0$, there is an ordinary Type 1 singularity. Sefrioui and Gosselin (1995) have done this, but have omitted to notice that at such configurations, their matrix $\mathbf{Z}$ will also be singular. So is this a Type 2 singularity as well? We will discuss this problem at the end of Section 2.4.1.3.

2.4.1.3 Obtaining the Singularity Loci

As we already mentioned, Eq. (2.12) represents the solution to the IKP and has real solutions only within the corresponding *vertex space* i which is the exterior of a circle of radius ℓ, centred at $(x_{OO_i} - x_{CB_i},\, y_{OO_i} - y_{CB_i})$. Vertex space i is defined as the area where the platform centre, C, is constrained to lie taking into account the kinematic constraint imposed by only leg i and the constant orientation of the platform. Hence, the form of each vertex space is constant for a given PPM, while its position changes as a function of the platform orientation. Note that the *constant-orientation workspace* (COW) is the intersection of all three vertex spaces.

Type 2 singularities occur when the three screw axes intersect or are parallel, i.e., when $\det \mathbf{Z} = 0$. This determinant consists of a fraction whose denominator is $\varrho_1\varrho_2\varrho_3$, while its numerator is the following quadratic polynomial:

$$\aleph(x, y) = q_1 x^2 + q_2 xy + q_3 y^2 + q_4 x + q_5 y, \tag{2.18}$$

where

$$\begin{aligned}
q_1 &= -y_{OO_3} y_{CB_2}, \\
q_2 &= -x_{OO_2} y_{CB_3} + y_{OO_3} x_{CB_2} + x_{OO_3} y_{CB_2}, \\
q_3 &= -x_{OO_3} x_{CB_2} + x_{OO_2} x_{CB_3}, \\
q_4 &= -y_{CB_2} \left(-x_{OO_2} y_{OO_3} - x_{OO_3} y_{CB_3} + y_{OO_3} x_{OO_3} + x_{OO_2} y_{CB_3}\right), \\
q_5 &= -x_{OO_3} \left(x_{OO_2} y_{CB_2} - x_{OO_2} y_{CB_3} + x_{CB_2} y_{CB_3}\right) \\
&\quad + x_{CB_3} \left(y_{OO_3} x_{CB_2} - x_{OO_2} y_{OO_3} + x_{OO_2} y_{CB_2}\right).
\end{aligned}$$

Note that the quadratic polynomial does not depend on ℓ. When $\ell \neq 0$, ϱ_i can never be zero and, hence, $\det \mathbf{Z} = 0$ exclusively along the entire conic defined by $\aleph(x, y)$, Eq. (2.18). The shape of that conic as function of the design parameters has been already studied in detail (Sefrioui and Gosselin, 1995). We would only add the interesting fact that the conic always passes through the three vertex space centres, i.e., $\aleph(x_{OO_i} - x_{CB_i}, y_{OO_i} - y_{CB_i}) = 0$. For some designs though, with congruent base and platform, there is an orientation at which the PPM is singular for any position. Thus, the singularity loci of Type 2 are those parts of the conic that are within all vertex spaces or the whole constant-orientation workspace.

An algebraic curve has little utility in the development of a CAD software for 3-$R\underline{P}R$ PPMs. The only way to plot such a curve is by time-consuming discretisation (Sefrioui and Gosselin, 1995). Fortunately, however, any quadratic (algebraic) curve can be written in parametric form—a fact that seems to be often ignored in robotics. A parametric curve can be quickly and accurately drawn. Our conic $\aleph(x, y)$, Eq. (2.18), may be written in parametric form as:

$$\begin{cases} x = -\dfrac{q_4 \cos\vartheta + q_5 \sin\vartheta}{q_1 \cos^2\vartheta + q_2 \cos\vartheta \sin\vartheta + q_3 \sin^2\vartheta} \cos\vartheta \\ y = -\dfrac{q_4 \cos\vartheta + q_5 \sin\vartheta}{q_1 \cos^2\vartheta + q_2 \cos\vartheta \sin\vartheta + q_3 \sin^2\vartheta} \sin\vartheta \end{cases} \qquad 0 \leq \vartheta \leq \pi. \tag{2.19}$$

To draw the above conic, one should not simply evaluate and plot x and y at equal increments of ϑ, but rather adjust each increment so that the distance between the new and old point is constant. Note, however, that points for sequential values of ϑ are not necessarily neighbouring and may even belong to different branches in the case of a hyperbola or two intersecting lines.

An example of the singularity loci of a 3-$R\underline{P}R$ PPM for which $\ell = 100$, $x_{OO_2} = -238.6$, $x_{CB_2} = -27.6$, $y_{CB_2} = 27.6$, $x_{OO_3} = -119.3$, $y_{OO_3} = -206.7$, $x_{CB_3} = -91.9$, and $y_{CB_3} = -18.4$ is presented in Fig. 2.4. Each of the vertex spaces is the exterior of a circle (drawn in black). The centres of those three circles are marked by the $\bullet$ symbol. The constant-orientation workspace is the intersection of those three vertex spaces. Hence, the Type 1 singularity loci are the parts (drawn in thick dash-dot line) of the the vertex space boundaries (the three circles) that are within the constant-orientation workspace. The conic corresponding to $\det \mathbf{Z} = 0$ in this example happens to be an ellipse (drawn in red). Similarly, the Type 2 singularity loci are those parts of the ellipse (drawn in thick solid line) that lie in the constant-orientation workspace.

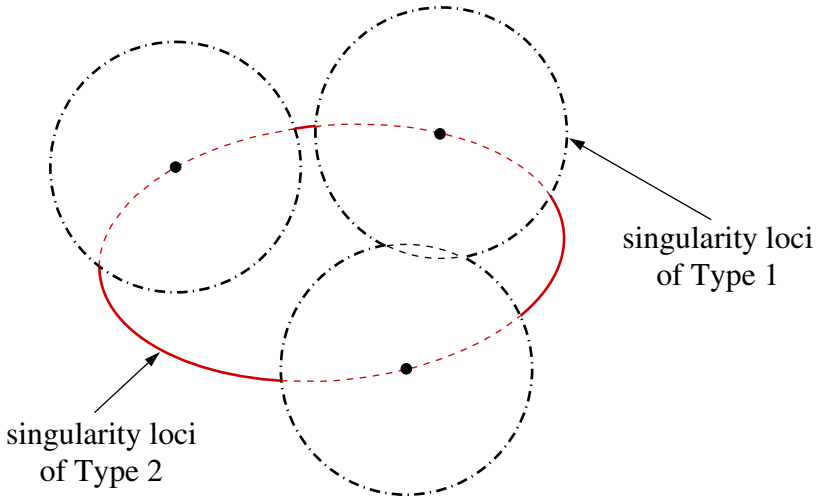

Figure 2.4: Example for the singularity loci of a 3-$R\underline{P}R$ PPM.

Now let us analyse the special case when $\ell = 0$. If $\ell = 0$, i.e. $O_i \equiv B_i$, there are two linearly independent reciprocal screws for the degenerate serial chain and $\mathbf{f}_i \neq \hat{\mathbf{f}}_i$. This singularity allows an *uncontrollable passive motion* (RPM type) and the three input velocities cannot be chosen independently (II type) (Zlatanov et al., 1994b). This redundant motion is *full-cycle* rather than infinitesimal. Note that, although there is a loss of a degree of freedom of the mobile platform (IO type), strictly speaking, this is *not* a Type 1 singularity since $\mathbf{\Lambda}$ is not singular.

For deeper analysis into the kinematics of $R\underline{P}R$ PPMs we refer the reader to the works of Husty (1996) and Hayes and Husty (2000) that treat the computation of the complete workspace, and the work of Husty et al. (1999) that focuses on the general singularity surface.

2.4.1.4 Summary

Since we have simple parametric equations for the singularity loci of a general 3-$R\underline{P}R$ PPM as a function of its design parameters and platform orientation, we may easily obtain the intersection between the singularity curves and plot only those sections that are inside the COW. We may thus plot the complete workspace as an array of horizontal cross-sections for the whole range of values of the platform orientation ϕ.

Let us also revisit the problem of working modes. We said that 3-$R\underline{P}R$ PPMs have eight working modes. Kinematically, however, they are all the same. In other words, no matter what working mode we choose, the singularities are all the same. It should only be noted that a working mode may be changed simply by passing over a Type 1 singularity (no disassembling is required).

Finally, here is a brief summary regarding the kinematics of 3-$R\underline{P}R$ PPMs:

- ✓ there are eight working modes, but they are all kinematically the same;
- ✓ for $\phi = const$, Type 1 singularity loci are 3 circles (or arcs) of radius ℓ;
- ✓ for $\phi = const$, Type 2 singularity loci are (parts of) a conic or the COW;
- ✓ the conic passes through the centres of the three circles;
- ✓ the conic does not depend on ℓ;
- ✓ when $\ell = 0$ and some $\rho_i = 0$, there is a full-cycle uncontrollable passive motion which is neither a Type 1 nor a Type 2 singularity;
- ✓ when $\Delta O_1O_2O_3$ and $\Delta B_1B_2B_3$ are congruent and $\rho_1 = \rho_2 = \rho_3$, there is a self-motion.

2.4.2 Singularity Analysis of 3-$\underline{\boldsymbol{R}}\boldsymbol{PR}$ PPMs

Referring to Fig. 2.5(a), we have exactly the same notation as the one used for the 3-$R\underline{P}R$ PPMs. The only new notation is for the active joint variables which in this case are the angles θ_i, defined as the angles between the x-axis and the direction of the P joint as shown in Fig. 2.5(b). As we are about to see, this new actuation scheme will render the kinematic analysis of the parallel mechanism much more complicated.

2.4.2.1 Solving the Inverse Kinematic Problem

We will first consider the task of computing the input variables (θ_1, θ_2, θ_3) from the set of output variables (x, y, ϕ). Let $\mathbf{r}_{O_iA_i}$ be the vector along O_iA_i and $\check{\mathbf{f}}_i$ be the unit vector along A_iB_i. Then we can write

$$\check{\mathbf{f}}_i = \frac{1}{\ell}\left(\mathbf{r}_{O_iB_i} - \mathbf{r}_{O_iA_i}\right) = \frac{1}{\ell}\begin{bmatrix} \bar{x}_i - \rho_i \cos\theta_i \\ \bar{y}_i - \rho_i \sin\theta_i \end{bmatrix}. \tag{2.20}$$

Now, note that $A_iB_i \perp O_iA_i$ and that according to the definition of the input variables θ_i the following is true for any branch:

$$\check{\mathbf{f}}_i = \begin{bmatrix} -\sin\theta_i \\ \cos\theta_i \end{bmatrix}. \tag{2.21}$$

Setting the right-hand sides of Eqs. (2.20) and (2.21) equal and solving, we obtain:

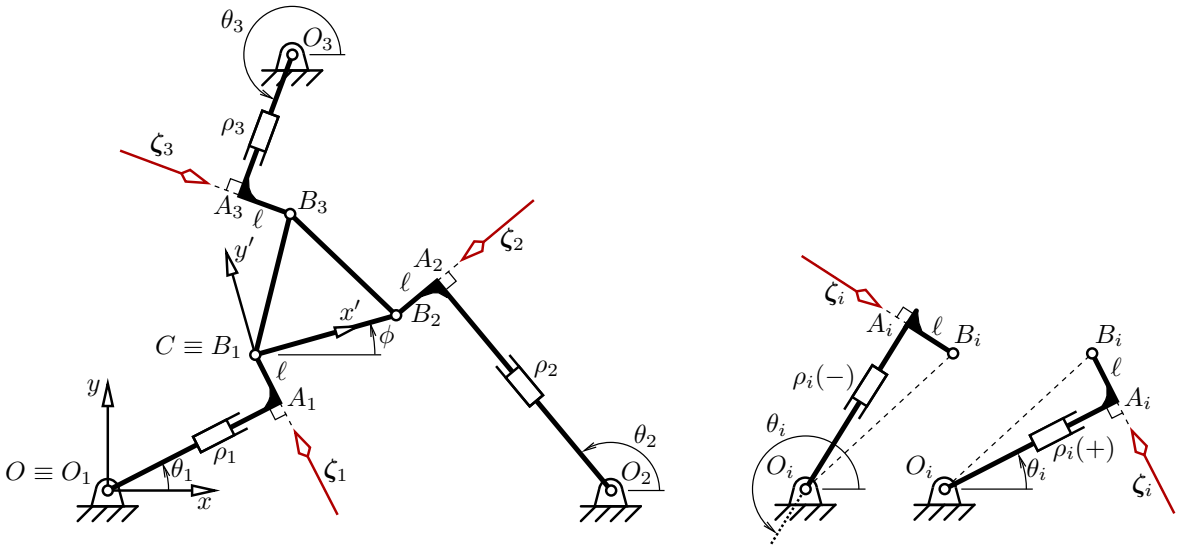

(a) (b)

Figure 2.5: (a) A 3-DOF PPM of type 3-$\underline{R}PR$ and (b) the two branches of a leg.

$$\cos\theta_i = \frac{1}{\rho_i^2 + \ell^2}(\ell\bar{y}_i + \rho_i\bar{x}_i), \quad \sin\theta_i = -\frac{1}{\rho_i^2 + \ell^2}(\ell\bar{x}_i - \rho_i\bar{y}_i) \tag{2.22}$$

which defines uniquely the solutions to the inverse kinematic problem. The two branches for each leg are defined by the same branch index as for 3-$R\underline{P}R$ PPMs. However, as we will see later, unless $\ell = 0$ the singularities of Type 2 for 3-$\underline{R}PR$ PPMs are strictly dependent on the particular working mode.

Finally, substituting the expressions from Eq. (2.22) into Eq. (2.21) yields:

$$\check{\mathbf{f}}_i = \frac{1}{\rho_i^2 + \ell^2}\begin{bmatrix} \ell\bar{x}_i - \rho_i\bar{y}_i \\ \ell\bar{y}_i + \rho_i\bar{x}_i \end{bmatrix}. \tag{2.23}$$

2.4.2.2 Obtaining the Velocity Equation

(a) Using differentiation

Multiplying the right-hand sides of Eqs. (2.21) and (2.20) and differentiating the result with respect to time yields

$$-\dot{\theta}_i\begin{bmatrix} \cos\theta_i \\ \sin\theta_i \end{bmatrix}^T\begin{bmatrix} \bar{x}_i - \rho_i\cos\theta_i \\ \bar{y}_i - \rho_i\sin\theta_i \end{bmatrix} + \begin{bmatrix} -\sin\theta_i \\ \cos\theta_i \end{bmatrix}^T\left(\begin{bmatrix} \dot{\bar{x}}_i \\ \dot{\bar{y}}_i \end{bmatrix} - \dot{\rho}_i\begin{bmatrix} \cos\theta_i \\ \sin\theta_i \end{bmatrix} - \rho_i\dot{\theta}_i\begin{bmatrix} -\sin\theta_i \\ \cos\theta_i \end{bmatrix}\right) = 0. \tag{2.24}$$

Expanding the above equation, noticing that the first and third terms are both equal to zero, and recalling that $\dot{\mathbf{r}}_{O_iB_i} = [\dot{\bar{x}}_i, \dot{\bar{y}}_i]^T = \mathbf{v} + \omega \mathbf{r}^{\perp}_{CB_i}$, we obtain

$$\check{\mathbf{f}}_i^T \left(\mathbf{v} + \omega \mathbf{r}^{\perp}_{CB_i} \right) = \rho_i \dot{\theta}_i. \tag{2.25}$$

Finally, we write the above equation in the $\mathbf{Z}\boldsymbol{\xi} = \boldsymbol{\Lambda}\dot{\boldsymbol{\theta}}$ matrix form:

$$\begin{bmatrix} \check{\mathbf{f}}_1^T \mathbf{r}^{\perp}_{CB_1} & \check{\mathbf{f}}_1^T \\ \check{\mathbf{f}}_2^T \mathbf{r}^{\perp}_{CB_2} & \check{\mathbf{f}}_2^T \\ \check{\mathbf{f}}_3^T \mathbf{r}^{\perp}_{CB_3} & \check{\mathbf{f}}_3^T \end{bmatrix} \boldsymbol{\xi} = \mathrm{diag}(\rho_1, \rho_2, \rho_3)\dot{\boldsymbol{\theta}}. \tag{2.26}$$

(b) Using screw theory

The reciprocal screws $\boldsymbol{\zeta}_i$, $i = 1, 2, 3$, are the screws passing through the platform R joints and normal to the direction of the corresponding P joint. Hence, their direction is along the already defined unit vector $\check{\mathbf{f}}_i$, i.e., $\mathbf{f}_i = \check{\mathbf{f}}_i$, and their moment m_i is the same as for 3-$R\underline{P}R$ PPMs defined in Eq. (2.16). Note, however, that if $\ell = 0$ and $O_i \equiv B_i$, Eq. (2.23) is not valid and $\mathbf{f}_i$ is defined by Eq. (2.21).

The diagonal elements of $\boldsymbol{\Lambda}$ (see Eq. 2.8), are

$$\lambda_i = (\mathbf{r}_{O_iA_i} \times \mathbf{f}_i)_z = \rho_i. \tag{2.27}$$

2.4.2.3 Obtaining the Singularity Loci

Type 1 singularities occur for the same configurations as in 3-$R\underline{P}R$ PPMs. For this mechanism, however, when $\rho_i = 0$ and $\ell = 0$ (i.e., $O_i \equiv B_i$), there is a generic Type 1 (RI) singularity, where the input velocities are indeterminate. This redundant input (RI) motion is full-cycle.

When $\ell = 0$, the determinant of $\mathbf{Z}$ consists of a fraction whose numerator is again a quadratic polynomial (generally a different one, though) and whose denominator is $\rho_1\rho_2\rho_3$. Again, the corresponding conic defining Type 2 singularities always passes through the centres of the vertex spaces. Those three centres, however, do not necessarily correspond to Type 2 singularities. The equation for the quadratic polynomial will not be given here since it may be easily obtained and since 3-$\underline{R}PR$ PPMs and not very useful in practice. We will present an example of the singularity loci for the same design parameters as the ones used for Fig. 2.4, except for $\ell = 0$. The result is presented in Fig. 2.6, where we see that the conic is a hyperbola.

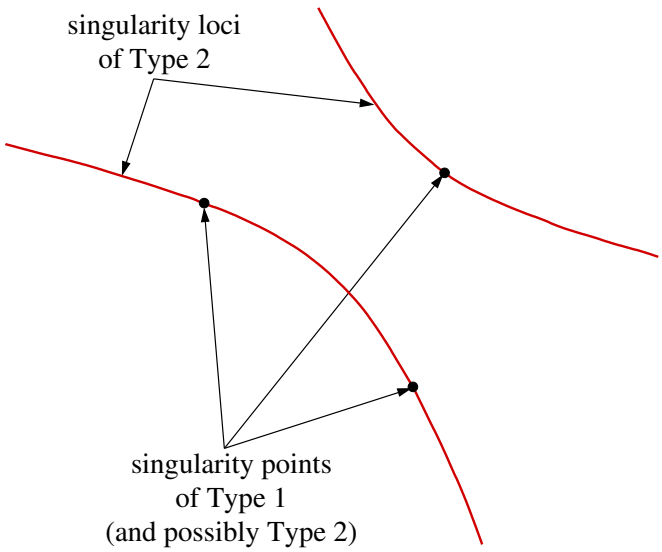

Figure 2.6: Example for the singularity loci of a 3-$\underline{R}PR$ PPM with $\ell = 0$.

While the Type 2 singularity loci for both 3-$R\underline{P}R$ and 3-$\underline{R}PR$ PPMs in the case $\ell = 0$ are the same for all working modes, they differ in the case of 3-$\underline{R}PR$ PPMs with $\ell \neq 0$. When $\ell \neq 0$, the singularities of Type 2 for 3-$\underline{R}PR$ PPMs are completely different from the case $\ell = 0$. The numerator of $\det \mathbf{Z}$ is no longer a polynomial but contains radicals (the variables ρ_i), and is, hence, dependent on the given working mode. If we manipulate properly that expression and raise it to square three times, we may obtain a polynomial of degree 16 in x and y. This polynomial will correspond to all working modes. The polynomial will not be presented here due to its huge coefficients nor shall we discuss in detail its derivation. A similar, yet much more intricate derivation will, however, be discussed in the case of 3-$\underline{R}RR$ PPMs in Section 2.4.4.

An example of the singularity loci for a 3-$\underline{R}PR$ PPM for all working modes is presented in Fig. 2.7. For this PPM $\ell = 50$, $x_{OO_1} = y_{OO_1} = x_{CB_1} = y_{CB_1} = 0$, $x_{OO_2} = -255.6$, $y_{OO_2} = 0$, $x_{CB_2} = -110.8$, $y_{CB_2} = 0$, $x_{OO_3} = -127.8$, $y_{OO_3} = -221.4$, $x_{CB_3} = -55.4$, and $y_{CB_3} = -95.9$. Note that this time the resulting curves are obtained through discretisation—the only way to obtain them. In fact, the "curve" for the Type 2 singularity loci, shown in the figure, corresponding to all working modes and defined by the polynomial of degree 16 is nothing but discrete points. To plot those points, we have swept a sufficiently large rectangular area, both horizontally and vertically, for each one of the eight working modes, and checked the determinant of $\mathbf{Z}$ at each point.

To illustrate the issue of working modes, we have plotted the Type 2 singularity curve portion for the $\{-,-,-\}$ branch set in green, while the portion for the $\{+,+,-\}$ branch set is in blue. The portions for the other six working modes are drawn in red.

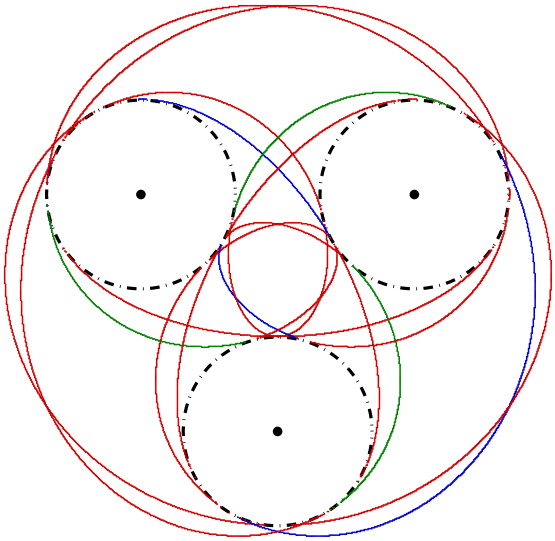

Figure 2.7: Example for the singularity loci of a 3-$\underline{R}PR$ PPM with $\ell \neq 0$.

2.4.2.4 Summary

As it may be seen from the last and other examples, each of the points of contact between the two types of singularity loci correspond to a change of branch index. Furthermore, the curve of degree 16 corresponds exactly to the Type 2 singularity loci for all working modes and is, hence, inside all vertex spaces. The reason for this fact is that the polynomial of degree 16 is directly obtained from the numerator of $\det \mathbf{Z}$ which is an expression containing the radicals ρ_i defined by Eq. (2.12). And this expression is obviously not defined outside the vertex spaces (recall that for 3-$R\underline{P}R$ and 3-$\underline{R}PR$ PPMs, each vertex space is defined by $\bar{x}_i^2 + \bar{y}_i > \ell^2$).

In fact, the same reasoning applies for all PPMs with branches and reciprocal screws dependent on the chosen branch. Their Type 2 singularity loci are usually within the *intersection* of all vertex spaces, i.e., within the constant-orientation workspace. However, Type 2 singularity loci are always within the *union* of the three vertex spaces.

Finally, here is a brief summary regarding the kinematics of 3-$\underline{R}PR$ PPMs:

Case 1: $\ell = 0$

✓ there are eight working modes, but they are all kinematically the same;

✓ for $\phi = const$, Type 1 singularity loci are three points;

✓ for $\phi = const$, Type 2 singularity loci are a conic or the COW;

✓ the conic passes through the three Type 1 singularity points;

✓ the three points correspond to *generic* Type 1 (RI) singularities but not necessarily to Type 2 singularities.

Case 2: $\ell \neq 0$

- ✓ there are eight working modes that are all kinematically different;
- ✓ for $\phi = const$, Type 1 singularity loci are three circles (or arcs) of radius ℓ;
- ✓ the Type 2 singularity loci for all working modes is a curve of order 16;
- ✓ the Type 2 singularity curve is inside all vertex spaces;
- ✓ the Type 2 singularity curve is segmented into portions corresponding to the eight working modes at the points of contact between the curve and the three circles.

2.4.3 Singularity Analysis of 3-*RRR* PPMs

Referring to Fig. 2.8(a), we denote with O_i, A_i, and B_i the centres of the base, intermediate, and platform R joints, respectively. The links attached to the base will be referred to as the *proximal links* and the links attached to the mobile platform will be called the *distal links*. The lengths of the proximal and distal links will be denoted by ℓ_1 and ℓ_2, respectively. Active joint variable i is denoted by θ_i^A and defined as the angle, measured counter-clockwise, between the proximal and distal links in leg i, as shown in Fig. 2.3(b). For convenience, θ_i^A will be defined in the range $[-\pi, \pi]$. All other notations and assumptions remain the same as for the two previous manipulators.

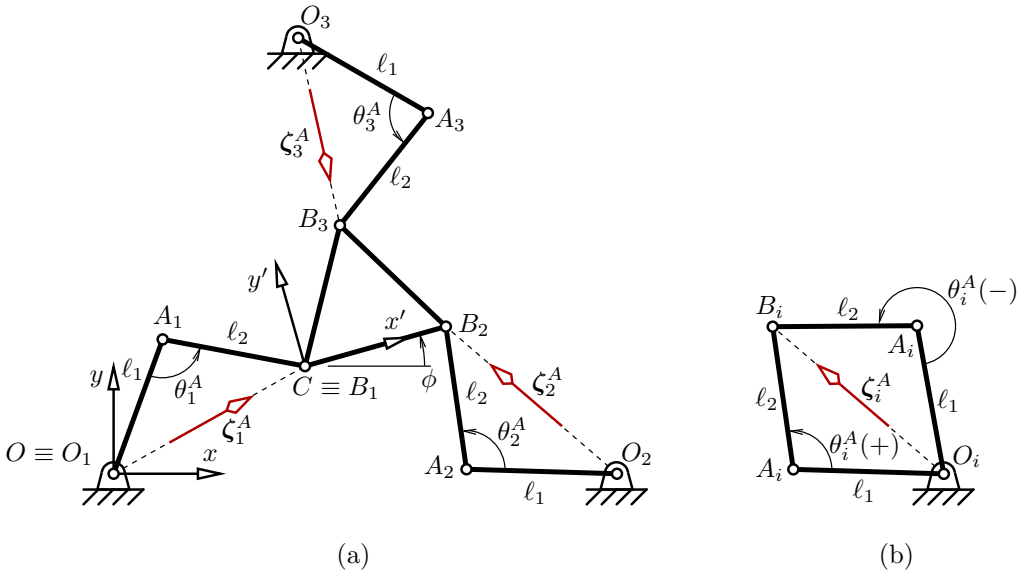

Figure 2.8: (a) A 3-DOF PPM of type 3-$R\underline{R}R$ and (b) the two branches of a leg.

2.4.3.1 Solving the Inverse Kinematic Problem

Obviously, 3-$R\underline{R}R$ PPMs are almost kinematically identical to 3-$R\underline{P}R$ PPMs with zero offset ($\ell = 0$). Thus, if ϱ_i is the distance between O_i and B_i, i.e., $\varrho_i = \sqrt{\bar{x}_i^2 + \bar{y}_i^2}$, the angle between the proximal and distal links can be uniquely defined. In other words, as long as a leg is not fully stretched or fully folded, in both PPMs we simply drive in a direct manner the distance between the base and platform R joint centres. Applying the *law of cosines* for the triangle $O_iA_iB_i$ we have

$$\varrho_i^2 = \ell_1^2 + \ell_2^2 - 2\ell_1\ell_2 \cos\theta_i^A. \tag{2.28}$$

Solving the above equation gives us the two values of θ_i^A as:

$$\theta_i^A = \delta_i \cos^{-1}\left(\frac{\ell_1^2 + \ell_2^2 - \varrho_i^2}{2\ell_1\ell_2}\right), \tag{2.29}$$

where again $\delta_i = \pm 1$ is the branch index that defines the branch of the leg as shown in Fig. 2.8(b).

2.4.3.2 Obtaining the Velocity Equation

(a) Using differentiation

The first part of the derivation process should be the same as the one presented in Section 2.4.1.2 for 3-$R\underline{P}R$ PPMs but simplified by setting $\rho_i = \varrho_i$. Hence, we may directly rewrite Eq. (2.15) as

$$\begin{bmatrix} \hat{\mathbf{f}}_1^T \mathbf{r}_{CB_1}^{\perp} & \hat{\mathbf{f}}_1^T \\ \hat{\mathbf{f}}_2^T \mathbf{r}_{CB_2}^{\perp} & \hat{\mathbf{f}}_2^T \\ \hat{\mathbf{f}}_3^T \mathbf{r}_{CB_3}^{\perp} & \hat{\mathbf{f}}_3^T \end{bmatrix} \boldsymbol{\xi} = \dot{\boldsymbol{\varrho}}. \tag{2.30}$$

where again $\hat{\mathbf{f}}_i$ is the unit vector along O_iB_i.

Differentiating Eq. (2.28) with respect to time leads us to

$$\dot{\varrho}_i = \frac{\ell_1\ell_2 \sin\theta_i^A}{\varrho_i}\dot{\theta}_i^A = \frac{\delta_i\ell_1\ell_2|\sin\theta_i^A|}{\varrho_i}\dot{\theta}_i^A = \frac{\delta_i 2\Upsilon_i}{\varrho_i}\dot{\theta}_i^A, \tag{2.31}$$

where $\Upsilon_i = \ell_1\ell_2|\sin\theta_i^A|/2$ is the area of the triangle $O_iA_iB_i$. We may now make use of that old formula taught in school, called the *Heron's formula*, which after some trivial manipulation, states that

$$\Upsilon_i = \frac{1}{4}\sqrt{(\varrho_i + \ell_1 + \ell_2)(\varrho_i - \ell_1 + \ell_2)(\varrho_i + \ell_1 - \ell_2)(-\varrho_i + \ell_1 + \ell_2)}. \tag{2.32}$$

Therefore, the final matrix velocity equation for 3-$R\underline{R}R$ PPMs is

$$\begin{bmatrix} \hat{\mathbf{f}}_1^T \mathbf{r}_{CB_1}^{\perp} & \hat{\mathbf{f}}_1^T \\ \hat{\mathbf{f}}_2^T \mathbf{r}_{CB_2}^{\perp} & \hat{\mathbf{f}}_2^T \\ \hat{\mathbf{f}}_3^T \mathbf{r}_{CB_3}^{\perp} & \hat{\mathbf{f}}_3^T \end{bmatrix} \boldsymbol{\xi} = \mathrm{diag}\left(\frac{2\delta_1 \Upsilon_1}{\varrho_1}, \frac{2\delta_2 \Upsilon_2}{\varrho_2}, \frac{2\delta_3 \Upsilon_3}{\varrho_3} \right) \dot{\boldsymbol{\theta}}. \tag{2.33}$$

(b) Using screw theory

If $O_i \not\equiv B_i$, the reciprocal screws $\boldsymbol{\zeta}_i$, $i = 1, 2, 3$, are the screws passing through the two passive R joints in each leg. Hence, their direction is along the already defined unit vector $\hat{\mathbf{f}}_i$, i.e., $\mathbf{f}_i = \hat{\mathbf{f}}_i$. Their moment m_i is also the same as for 3-$R\underline{P}R$ PPMs defined in Eq. (2.16).

If, again, $O_i \not\equiv B_i$, the diagonal elements of $\boldsymbol{\Lambda}$ (see Eq. 2.8), are the moments of the reciprocal forces with respect to the centre of the corresponding active R joints. Therefore, $|\lambda_i|$ is equal to the *altitude* of the triangle $A_iO_iB_i$ to the side O_iB_i, i.e., $|\lambda_i| = 2\Upsilon_i/\varrho_i$. Noticing in Fig. 2.8(b) that this moment has the same sign as the branch index δ_i, we may write without any computations:

$$\lambda_i = \frac{2\delta_i \Upsilon_i}{\varrho_i}. \tag{2.34}$$

2.4.3.3 Obtaining the Singularity Loci

As we already suggested, and as clearly seen from the velocity equations of 3-$R\underline{P}R$ and 3-$R\underline{R}R$ PPMs, i.e., Eqs. (2.15) and (2.33), respectively, the Type 2 singularities of those two PPMs are the same. Type 1 singularities, on the other hand, occur when the area of the triangle $A_iO_iB_i$ is zero, or in other words, when the proximal and distal links in a leg are *aligned*. Therefore, the Type 1 singularity loci for a constant orientation correspond to pairs of concentric circles of radius $|\ell_1 \pm \ell_2|$, centred at $(x_{OO_i} - x_{CB_i}, y_{OO_i} - y_{CB_i})$. The area between a pair od circles is vertex space i and is defined by the inequality $|\ell_1 - \ell_2| \geq \varrho_i \geq \ell_1 + \ell_2$.

When the links are of equal lengths ($\ell_1 = \ell_2$) and are overlapping, i.e., $O_i \equiv B_i$, there is a singularity of the same class (RPM, II, IO) as in 3-$R\underline{P}R$ PPMs and *not* a Type 1 singularity.

2.4.3.4 Summary

Note that a 3-$R\underline{R}R$ PPM has eight working modes, but its singularities do not depend on the particular working mode unlike a 3-$\underline{R}RR$ PPM, as we will see next. And once again, its Type 1 and Type 2 singularity loci are independent except for the fact that the conic, whose portions are the Type 1 singularity loci, pass through the three vertex space centres.

Finally, here is a brief summary regarding the kinematics of 3-$R\underline{R}R$ PPMs:

- ✓ there are eight working modes, but they are all kinematically the same;
- ✓ for $\phi = const$, Type 1 singularity loci are 3 pairs of concentric circles (or arcs) of radii $|\ell_1 \pm \ell_2|$;
- ✓ vertex space i is the area between the two corresponding concentric circles;
- ✓ for $\phi = const$, Type 2 singularity loci are (parts of) a conic or the COW;
- ✓ the conic passes through the centres of the three vertex spaces;
- ✓ the conic does not depend on ℓ_1 and ℓ_2;
- ✓ when $\ell = 0$ and some $\varrho_i = 0$, there is a full-cycle uncontrollable passive motion which is neither a Type 1 nor a Type 2 singularity.

2.4.4 Singularity Analysis of 3-$\underline{R}RR$ PPMs

Undoubtedly, the most common architecture for a 3-DOF PPM is the 3-$\underline{R}RR$ one. The reason is mostly practical—these PPMs are easiest to build. Even more than a decade ago, a 100 μm-link 3-$\underline{R}RR$ PPM was possible to build (Behi et al., 1990). The fact that the actuators are fixed to the base allows the use of inexpensive DC drives and reduces the weight of the mobile equipment. In addition, the links can be made of thin rods and even be curved (Schönherr, 1998) to decrease significantly link interference. Finally, revolute joints have virtually no mechanical limits which, together with the previously mentioned feature, maximises considerably the workspace of 3-$\underline{R}RR$ PPMs.

Referring to Fig. 2.9(a), we have exactly the same notation as the one used for the 3-$R\underline{R}R$ PPMs. The only new notation is for the active joint variables which in this case are the angles θ_i^O, defined as the angles between the x-axis and the proximal link as shown in Fig. 2.9(b). As we are about to see, this new actuation scheme will render the kinematic analysis of the parallel mechanism much more complicated.

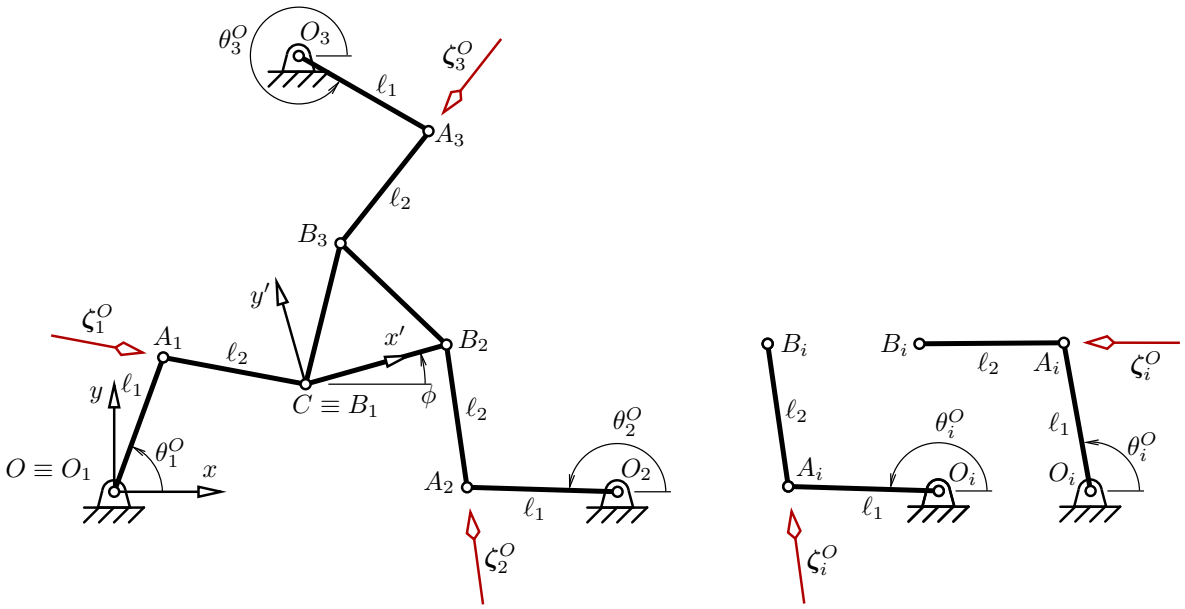

Figure 2.9: (a) A 3-DOF PPM of type 3-$\underline{R}RR$ and (b) the two branches of a leg.

2.4.4.1 Solving the Inverse Kinematic Problem

We will now consider the task of computing the set of input variables (θ_1^O, θ_2^O, θ_3^O) from the output variables (x, y, ϕ). Geometrically, for the i-th leg, the IKP can be seen as the problem of finding the intersection point(s) between a circle of radius ℓ_1 and centre O_i and a circle of radius ℓ_2 and centre B_i. Clearly, depending on the position of point B_i, this problem may have two real solutions, a single one, or none at all. If $\ell_1 = \ell_2$, the problem may even have an infinite number of solutions.

We may write the following equation for the distal link vector:

$$\mathbf{r}_{A_iB_i} = \mathbf{p} + \mathbf{r}_{CB_i} - \mathbf{r}_{O_iA_i} - \mathbf{r}_{OO_i}. \tag{2.35}$$

Squaring both sides of this equation gives us

$$\ell_2^2 = \mathbf{r}_{A_iB_i}^T \left(\mathbf{p} + \mathbf{r}_{CB_i} - \mathbf{r}_{O_iA_i} - \mathbf{r}_{OO_i}\right), \tag{2.36}$$

$$\ell_2^2 = \varrho_i^2 + \ell_1^2 - 2\mathbf{r}_{O_iB_i}^T \mathbf{r}_{OO_i}, \tag{2.37}$$

where ϱ_i is, as previously defined, the distance between O_i and B_i, i.e., $\varrho_i = ||\mathbf{r}_{O_iB_i}||$, and $\mathbf{r}_{O_iB_i} = [\bar{x}_i, \bar{y}_i]^T$. In addition, we obviously have $\mathbf{r}_{O_iA_i} = \ell_1[\cos\theta_i^O, \sin\theta_i^O]^T$. Therefore, Eq. (2.36) may be written as

$$\bar{x}_i \cos\theta_i^O + \bar{y}_i \sin\theta_i^O = \frac{\varrho_i^2 + \ell_1^2 - \ell_2^2}{2\ell_1} \equiv p_i = \varrho_i \cos\gamma_i. \tag{2.38}$$

where $\gamma_i = \angle A_iO_iB_i$. In order to have a real solution to the above equation, the following inequality should hold true:

$$\varrho_i^2 - p_i^2 = \varrho_i^2 \sin^2\gamma_i \equiv \Gamma_i \geq 0. \tag{2.39}$$

Therefore, $\sqrt{\Gamma_i}$ is the altitude of the triangle $A_iO_iB_i$ to the side O_iA_i. Unless $\Gamma_i = 0$, there exist two real solutions to Eq. (2.38), determined uniquely from:

$$\sin\theta_i^O = \frac{p_i\bar{y}_i + \bar{x}_i\delta_i\sqrt{\Gamma_i}}{\varrho_i^2}, \quad \cos\theta_i^O = \frac{p_i\bar{x}_i - \bar{y}_i\delta_i\sqrt{\Gamma_i}}{\varrho_i^2}, \tag{2.40}$$

where δ_i is the same branch index as the one for 3-$R\underline{R}R$ PPMs. Note that Eq. (2.40) is not valid when $\varrho_i = 0$, which may occur only if $\ell_1 = \ell_2$ and $B_i \equiv O_i$.

2.4.4.2 Obtaining the Velocity Equation

(a) Using differentiation

Having resolved the inverse kinematic problem, we may now proceed to obtaining the velocity equation by differentiating Eq. (2.36) with respect to time, leading to

$$\ell_2\check{\mathbf{f}}_i^T\left(\mathbf{v} + \omega\mathbf{r}_{CB_i}^{\perp} - \ell_1\dot{\theta}_i^O\begin{bmatrix} -\sin\theta_i^O \\ \cos\theta_i^O \end{bmatrix}\right) = 0, \tag{2.41}$$

where $\check{\mathbf{f}}_i = \mathbf{r}_{A_iB_i}/\ell_2$. The above equation may be written in the following vector form:

$$\begin{bmatrix}\check{\mathbf{f}}_i^T\mathbf{r}_{CB_i}^{\perp}, & \check{\mathbf{f}}_i^T\end{bmatrix}\begin{bmatrix}\omega \\ \mathbf{v}\end{bmatrix} = \ell_1\check{\mathbf{f}}_i^T\begin{bmatrix} -\sin\theta_i^O \\ \cos\theta_i^O \end{bmatrix}\dot{\theta}_i^O, \tag{2.42}$$

where

$$\check{\mathbf{f}}_i = \frac{1}{\ell_2}\begin{bmatrix}\bar{x}_i - \ell_1\cos\theta_i^O \\ \bar{y}_i - \ell_1\sin\theta_i^O\end{bmatrix}. \tag{2.43}$$

Using that equality and the expressions from Eq. (2.40), Eq. (2.42) is simplified to

$$\left[\check{\mathbf{f}}_i^T\mathbf{r}_{\overline{CB}_i}^{\perp},\ \ \check{\mathbf{f}}_i^T\right]\begin{bmatrix}\omega\\ \mathbf{v}\end{bmatrix} = -\frac{\ell_1}{\ell_2}\delta_i\sqrt{\Gamma_i}\dot{\theta}_i^O. \tag{2.44}$$

Finally, the above equation may be written in the $\mathbf{Z}\boldsymbol{\xi} = \boldsymbol{\Lambda}\dot{\boldsymbol{\theta}}$ matrix form:

$$\begin{bmatrix}\check{\mathbf{f}}_1^T\mathbf{r}_{\overline{CB}_1}^{\perp},\ \ \check{\mathbf{f}}_1^T\\ \check{\mathbf{f}}_2^T\mathbf{r}_{\overline{CB}_2}^{\perp},\ \ \check{\mathbf{f}}_2^T\\ \check{\mathbf{f}}_3^T\mathbf{r}_{\overline{CB}_3}^{\perp},\ \ \check{\mathbf{f}}_3^T\end{bmatrix}\boldsymbol{\xi} = -\frac{\ell_1}{\ell_2}\mathrm{diag}\Big(\delta_1\sqrt{\Gamma_1},\delta_2\sqrt{\Gamma_2},\delta_3\sqrt{\Gamma_3}\Big)\dot{\boldsymbol{\theta}}. \tag{2.45}$$

(b) Using screw theory

The reciprocal screws $\boldsymbol{\zeta}_i$, are the screws passing through the two passive R joints in each leg. Hence, their direction is along the already defined unit vector $\check{\mathbf{f}}_i$, i.e., $\mathbf{f}_i = \check{\mathbf{f}}_i$. Their moment m_i is also the same as for 3-$R\underline{P}R$ PPMs defined in Eq. (2.16).

The diagonal elements of $\boldsymbol{\Lambda}$ (see Eq. 2.8), are the moments of the reciprocal forces with respect to the centre of the corresponding active R joints. Therefore, $|\lambda_i|$ is equal to the *altitude* of the triangle $A_iO_iB_i$ to the side A_iB_i, and λ_i is negative for the positive branch index, and positive for the negative branch index. Hence,

$$\lambda_i = -\frac{2\delta_i\Upsilon_i}{\ell_2} = -\frac{\delta_i\left(\ell_1\sqrt{\Gamma_i}\right)}{\ell_2} = -\frac{\ell_1}{\ell_2}\delta_i\sqrt{\Gamma_i}. \tag{2.46}$$

Note that the conventional approach does not require any geometric interpretation but pure algebraic computations. On the other hand, the reciprocal screw method calls for a complete understanding of the geometry of the mechanism. Such an understanding does not only reduces the chances for errors but also brings an insight into the kinematics of the mechanism.

2.4.4.3 Obtaining the Singularity Loci

The singularity loci of Type 1 and, hence, the vertex spaces and the constant-orientation workspace of 3-$\underline{R}RR$ PPMs are the same as for 3-$R\underline{R}R$ PPMs. The only difference is that when $\ell_1 = \ell_2$ and $B_i = O_i$, there is a Type 1 singularity.

Type 2 singularity loci are, however, much more complicated to determine due to the existence of the terms $\sqrt{\Gamma_i}$ in $\det\mathbf{Z}$. To our best knowledge, the first attempt to resolve this problem has been reported in (Gosselin and Wang, 1997). In that work, the authors have concluded that the resulting polynomial is of degree 64 in y and 48 in x even though they have only considered a simplified 3-$\underline{R}RR$ PPM design with collinear

base and platform joints. Their remark that the reason for the high degree is the fact that the singularity loci are for all working modes and not only for a single one as well as the high degree itself has motivated our research in that area. Subsequently, we have recently reported our results (Bonev and Gosselin, 2001).

If the fact that the actual degree of the polynomial is 42 is not of great immediate importance, the process of derivation of this minimum polynomial reveals essential facts. The most significant of these facts is that no polynomial exists that corresponds to only a single working mode. Indeed, to eliminate all radicals in the equation $\det \mathbf{Z}$, the latter should be rearranged and squared three times. The equation resulting after each such operation loses the information for a branch index.

We will now outline the procedure used for obtaining the minimal polynomial of degree 42 that corresponds to the singularity loci of Type 2 for all working modes. Two cases will be investigated depending on the relationship between ℓ_1 and ℓ_2.

(a) Special case: proximal and distal links of equal lengths

Let us first consider the special case when $\ell_1 = \ell_2$. The reason is that in this case, we may obtain the polynomial in symbolic form. We render our problem dimensionless and set $\ell_1 = \ell_2 = 1$. Once the matrix $\mathbf{Z}$ is expressed in the variables x, y, and the parameters x_{OO_i}, y_{OO_i}, x_{CB_i}, y_{CB_i}, and ϱ_i, we follow the procedure described below:

S1 Substitute the expressions $\delta_i\sqrt{\Gamma_i}$ with the parameters Δ_i.

S2 Obtain $\det \mathbf{Z}$. The denominator of this determinant is $8\varrho_1\varrho_2\varrho_3$. Indeed, $\mathbf{Z}$ is not defined when $B_i \equiv O_i$, i.e., when $\varrho_i = 0$. Eliminating these possibilities, we consider further only the numerator, $\mathcal{E}$. This numerator is a function of x and y that cannot be generally factored and contains the three radicals $\delta_i\sqrt{\Gamma_i}$ (actually the parameters Δ_i) and the parameters ϱ_i. Note, that this is the only expression that corresponds to the singularity loci for the given working mode.

S3 Eliminate the radical in $\sqrt{\Gamma_1}$. Rewrite $\mathcal{E}$ in the form $\mathcal{C}_1\Delta_1 = \mathcal{C}_2$, where $\mathcal{C}_1$ and $\mathcal{C}_2$ do not contain Δ_i. Next, raise to square leading to $\mathcal{C}_1^2\Gamma_1 = \mathcal{C}_2^2$. Both Γ_1 and $\mathcal{C}_2^2$ are multiples of ϱ_1 which can be cancelled. Our new expression, $\mathcal{E}_1 = \mathcal{C}_1^2(\Gamma_1/\rho_1) - \mathcal{C}_2^2/\rho_1$, does not contain δ_1 and, hence, corresponds to two working modes.

S4 Split $\mathcal{E}_1$ and substitute the terms Δ_2^2 and Δ_3^2 with respectively Γ_2 and Γ_3. Note, that if we attempt to perform this substitution directly in $\mathcal{E}_1$, the resulting expression becomes too large to allow to be handled symbolically. Thus, $\mathcal{E}_1$ is written in parts:

$$\mathcal{E}_1 = \mathcal{E}_{1,1} + \mathcal{E}_{1,2}\Delta_3 + \mathcal{E}_{1,3}\Delta_2 + \mathcal{E}_{1,4}\Delta_2\Delta_3 + \mathcal{E}_{1,5} + \mathcal{E}_{1,6} + \mathcal{E}_{1,7}\Delta_2 + \mathcal{E}_{1,8}\Delta_3 + \mathcal{E}_{1,9}$$

$$\begin{array}{lll} \mathcal{E}_{1,1} = \mathcal{C}_{0,0}/(\varrho_2\varrho_3) & \mathcal{E}_{1,4} = \mathcal{C}_{1,1}/(\varrho_2\varrho_3) & \mathcal{E}_{1,7} = \big(\mathcal{C}_{1,2}/\varrho_2\big)(\Gamma_3/\varrho_3) \\ \mathcal{E}_{1,2} = \mathcal{C}_{0,1}/(\rho_2\rho_3) & \mathcal{E}_{1,5} = \big(\mathcal{C}_{0,2}/\varrho_2\big)\Gamma_3/\varrho_3 & \mathcal{E}_{1,8} = \big(\mathcal{C}_{2,1}/\varrho_3\big)(\Gamma_2/\varrho_2) \\ \mathcal{E}_{1,3} = \mathcal{C}_{1,0}/(\varrho_2\varrho_3) & \mathcal{E}_{1,6} = \big(\mathcal{C}_{2,0}/\varrho_3\big)\Gamma_2/\varrho_2 & \mathcal{E}_{1,9} = \mathcal{C}_{2,2}(\Gamma_2/\varrho_2)(\Gamma_3/\varrho_3) \end{array}$$

where $\mathcal{C}_{j,k}$ $(j,k = 0,1,2)$ are coefficients that contain neither Δ_2 nor Δ_3. Furthermore, all the divisions can be performed exactly.

S5 Eliminate the radical in $\sqrt{\Gamma_2}$:

$$\mathcal{E}_2 = \mathcal{E}_{2,1}^2\Gamma_2 + \mathcal{E}_{2,2}^2\Gamma_2\Gamma_3 + 2\mathcal{E}_{2,1}\mathcal{E}_{2,2}\Gamma_2\Delta_3 - \mathcal{E}_{2,3}^2 - \mathcal{E}_{2,4}^2\Gamma_3 - 2\mathcal{E}_{2,3}\mathcal{E}_{2,4}\Delta_3$$

$$\mathcal{E}_{2,1} = \mathcal{E}_{1,3} + \mathcal{E}_{1,7},\ \ \mathcal{E}_{2,2} = \mathcal{E}_{1,4},\ \ \mathcal{E}_{2,3} = \mathcal{E}_{1,1} + \mathcal{E}_{1,5} + \mathcal{E}_{1,6} + \mathcal{E}_{1,9},\ \ \mathcal{E}_{2,4} = \mathcal{E}_{1,2} + \mathcal{E}_{1,8}$$

The new expression $\mathcal{E}_2$ does not contain δ_1 or δ_2 and, hence, corresponds to the singularity loci of four working modes.

S6 Eliminate the radical in $\sqrt{\Gamma_3}$:

$$\mathcal{E}_3 = (2\mathcal{E}_{2,1}\mathcal{E}_{2,2}\Gamma_2 - 2\mathcal{E}_{2,3}\mathcal{E}_{2,4})^2\Gamma_3 - (\mathcal{E}_{2,1}^2\Gamma_2 + \mathcal{E}_{2,2}^2\Gamma_2\Gamma_3 - \mathcal{E}_{2,3}^2 - \mathcal{E}_{2,4}^2\Gamma_3)^2$$

Finally, we substitute the expressions for ϱ_i in $\mathcal{E}_3$, which becomes a polynomial in the variables x and y but cannot be expanded in symbolic form. However, it can quickly be verified to be of degree 48 using the Maple command `coeff(`$\mathcal{E}_3$`,(x,y))`. Furthermore, if we use the same command to extract and simplify all the coefficients of $\mathcal{E}_3$ corresponding to the terms of degree greater than 42, we can observe that they are all zero. In addition, the coefficients of the terms of degree less than 8 are also zero which makes $\mathcal{E}_3$ a *fewnomial* of degree 42.

Fig. 2.10 shows an example of the singularity loci of a 3-$\underline{R}RR$ PPM with proximal and distal links of equal length. The mechanism parameters are $\ell_1 = \ell_2 = 1$, $x_{OO_2} = 1.741$, $x_{CB_2} = 0.889$, $y_{CB_2} = 0$, $x_{OO_3} = 0.870$, $y_{OO_3} = 1.508$, $x_{CB_3} = 0.444$, and $y_{CB_3} = 0.770$. The Type 2 singularity loci for all eight working modes are drawn in red. Once again, all branch index changes are done at the vertex space boundaries, i.e., at Type 1 singularities. Hence the Type 2 singularity loci for all branches pass through the vertex space centres. Note, however, that those centres are Type 1 singularities, but not necessarily Type 2 singularities. This is because, at these three points, the configuration of the PPM is not uniquely determined by the pose of its mobile platform.

(b) General case

In the case when $\ell_1 \neq \ell_2$, we set only $\ell_1 = 1$ and follow a much simplified procedure. Firstly, we assign *random integer values* to the coefficients x_{OO_i}, y_{OO_i}, x_{CB_i}, y_{CB_i} since

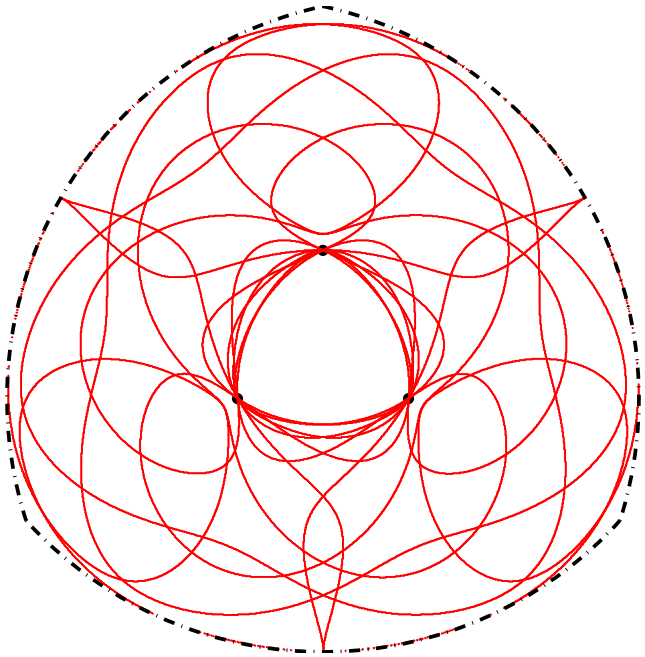

Figure 2.10: Example for the singularity loci of a 3-$\underline{R}RR$ PPM with $\ell_1 = \ell_2$.

the procedure *cannot be performed symbolically*. Then, we eliminate the radical in $\sqrt{\Gamma_1}$ and divide the resulting expression $\mathcal{E}_1$ by ϱ_1. Note that in this case Γ_i is not a multiple of ϱ_i. Next, we substitute the terms Δ_2^2 and Δ_3^2 with respectively Γ_2 and Γ_3. Then, we eliminate the radical in $\sqrt{\Gamma_2}$, divide the resulting expression $\mathcal{E}_2$ by ϱ_2^2, and substitute Δ_3^2 with Γ_3. Finally, we eliminate the radical in $\sqrt{\Gamma_3}$ and divide the resulting expression $\mathcal{E}_3$ by ϱ_3^4. The polynomial $\mathcal{E}_3$ is again of degree 42, but this time the coefficients of all possible terms are generally non-zero (except for the odd-power terms of degree 42).

Fig. 2.11 shows an example of the singularity loci of a general 3-$\underline{R}RR$ PPM. The mechanism parameters for this example are $\ell_1 = 1$, $\ell_2 = 1.350$, $x_{OO_2} = 2.350$, $x_{CB_2} = 1.200$, $y_{CB_2} = 0$, $x_{OO_3} = 1.175$, $y_{OO_3} = 2.035$, $x_{CB_3} = 0.600$, and $y_{CB_3} = 1.039$. Again, the Type 2 singularity loci for all working modes are drawn in red.

2.4.4.4 3-$\underline{R}RR$ PPMs with Two Coincident Platform Joints

In general, the polynomial $\mathcal{E}_3$ cannot be factored. Special designs such as base and platform being equilateral triangles or collinear do not lead to simplified results. One particular case, however, simplifies greatly that polynomial and allows the singularity loci to be geometrically described. This case also brings insight into the complex relationship between branches and singularity loci. It shows the clear superiority of the geometrical methods for finding the singularity loci without even having to set up the velocity equations.

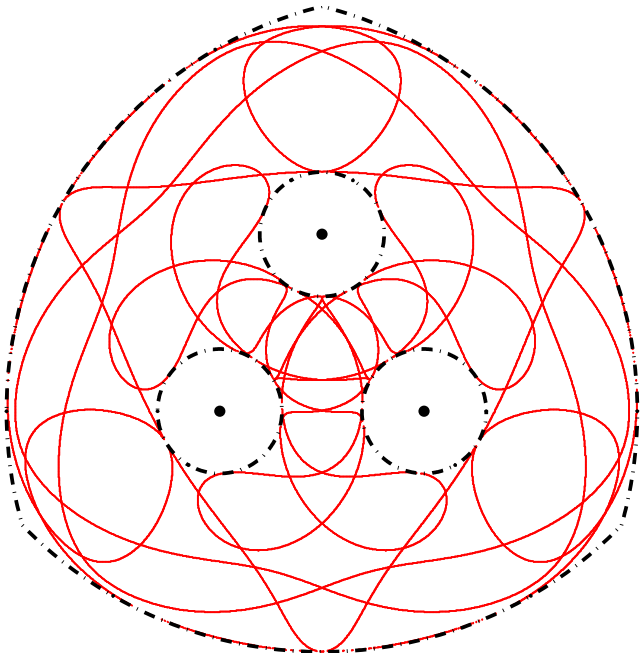

Figure 2.11: Example for the singularity loci of a 3-$\underline{R}RR$ PPM with $\ell_1 \neq \ell_2$.

The particular case of interest occurs simply when two platform joints are coincident, e.g., when $B_1 \equiv B_2$ (Fig. 2.12). Using the parameterisation introduced previously, this case implies that $x_{OO_1} = y_{OO_1} = x_{CB_1} = y_{CB_1} = y_{OO_1} = x_{CB_2} = y_{CB_2} = 0$. Now, we can either use the algebraic approach described in the last section or observe the following and use a geometrical approach. As mentioned before, singularities of Type 2 occur when the lines associated with the distal links intersect at one point or are all parallel. Since two of the lines always intersect at point C, we have only two possible cases leading to singularities of Type 2:

Case 1: Points C, B_3, and A_3 are collinear.

This condition implies that $\mathbf{f}_3 = \pm[-\sin\phi, \cos\phi]^T$. Hence, the corresponding singularity loci consist of two circles of radius ℓ_1 and centres at $\mathbf{r}_{OO_3} + \mathbf{f}_3(\ell_2 + ||\mathbf{r}_{CB_3}||)$:

$$\left(x + x_{CB_3} - x_{OO_3} \pm \frac{\ell_2 x_{CB_3}}{\sqrt{x_{CB_3}^2 + y_{CB_3}^2}}\right)^2 + \left(y + y_{CB_3} - y_{OO_3} \pm \frac{\ell_2 y_{CB_3}}{\sqrt{x_{CB_3}^2 + y_{CB_3}^2}}\right)^2 = \ell_1^2. \tag{2.47}$$

Note that each of the two circles is separated by lines parallel to $\mathbf{f}_3$ into semicircles corresponding to the two possible branches of the third leg.

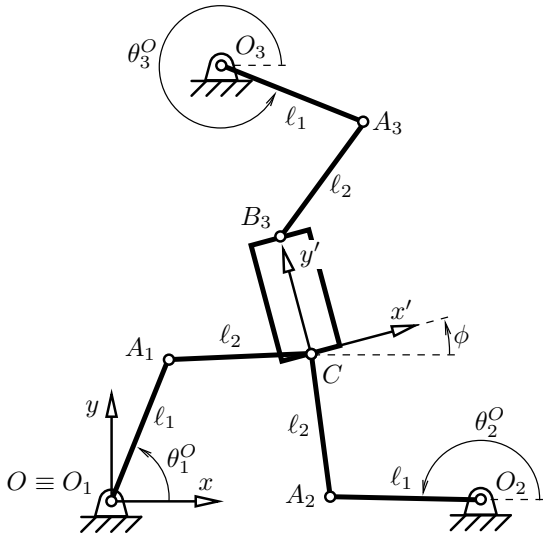

Figure 2.12: A special 3-$\underline{R}RR$ PPM with two coincident platform joints.

Case 2: Points A_1, C, and A_2 are collinear.

This case has two sub-cases. In the first one, points A_1 and A_2 coincide which may occur at two locations symmetric with respect to line O_1O_2. Thus, the corresponding singularity loci are two circles:

$$(x - x_{OO_2}/2)^2 + \left(y \pm \sqrt{\ell_1^2 - x_{OO_2}^2/4}\right)^2 = \ell_2^2. \tag{2.48}$$

Again, each of the circles is divided into two semicircles by lines O_1A_1 and O_2A_2 distinguished respectively by the branch indices δ_1 and δ_2. Thus, each circle is divided into four arcs corresponding to four different pairs of working modes.

The second sub-case requires that $A_1 \not\equiv A_2$. Thus, the singularity loci correspond to the coupler curve of the four-bar mechanism $O_1A_1A_2O_2$, where $A_1A_2 = 2\ell_2$ is the coupler, defined by the following sextic (Hunt, 1978):

$$\begin{gathered}(x + x_{OO_2}/2)^2(x^2 + x_{OO_2}x + \ell_2^2 - \ell_1^2 + y^2)^2 \\ +y^2(x^2 + x_{OO_2}x + x_{OO_2}^2/2 + \ell_2^2 - \ell_1^2 + y^2)^2 - \ell_2^2 x_{OO_2}^2 y^2 = 0.\end{gathered} \tag{2.49}$$

This sextic, will also be divided in four parts, each corresponding to two working modes defined by δ_1 and δ_2. Note that the sextic is symmetric with respect to the y-axis and the line $x = -x_{OO_2}/2$. Indeed, the sextic can be represented by the following parametric equation:

$$\begin{cases} x &= \pm\varrho\cos\vartheta - x_{OO_2}/2 \\ y &= \pm\varrho\sin\vartheta \end{cases} \qquad 0 \leq \vartheta \leq \pi/2 \tag{2.50}$$

where

$$\varrho = \frac{1}{2}\sqrt{4(\ell_1^2 - \ell_2^2) - x_{OO_2}^2(1 - 2\cos^2\vartheta) \pm 2x_{OO_2}\sin\vartheta\sqrt{4\ell_2^2 - x_{OO_2}^2\cos^2\vartheta}}, \tag{2.51}$$

where ϱ is the distance between point C and the centre of line O_1O_2, referred to as point O_c, and ϑ is the angle between the x-axis and the line O_cC.

Note, however, that the sextic described by Eq. (2.49) *always* passes through the point $(x_{OO_2}/2,\ 0)$, which in some cases may be an isolated point that is actually outside the constant-orientation workspace, while *if* Eq. (2.51) has this point as a solution, the point is *not* isolated.

In conclusion, for a given working mode, we have two semi-circles defined by δ_3, and a pair (symmetric with respect to line O_1O_2) of circular arcs and arcs from a sextic defined by δ_1 and δ_2. The first two semi-circles, of radius ℓ_1, depend on the orientation of the mobile platform, while the other circular arcs and arcs from a sextic are the same for any platform orientation. All of these geometrical curves are parts of geometric objects defined by parametric equations and constrained by limits on the parameters that can easily be computed. Therefore, these curves can be promptly represented.

Note how well this example illustrates the advantage of the geometrical approach to studying the kinematics of a mechanism. If we were to simply compute the determinant of the matrix $\mathbf{Z}$, we would have probably come to the same result but without any understanding of the nature of these curves. Not to mention, that if we were simply given the algebraic equation of the sextic, it would have not been obvious to find the corresponding parametric equation.

The kinematic analysis of this simplified 3-$\underline{R}RR$ PPM is a perfect candidate for a problem of the exam of a robot kinematics course. The PPM is also ideal for helping understand the kinematics of PPMs as it allows the use of simple geometrical models for representing its singularities.

Finally, Fig. 2.13 illustrates the singularity loci of a 3-$\underline{R}RR$ PPM with two coincident platform joints. For this PPM, $\ell_1 = 40$, $\ell_2 = 30$, $x_{OO_2} = 50$, $x_{CB_3} = 13$, $y_{CB_3} = 17$,

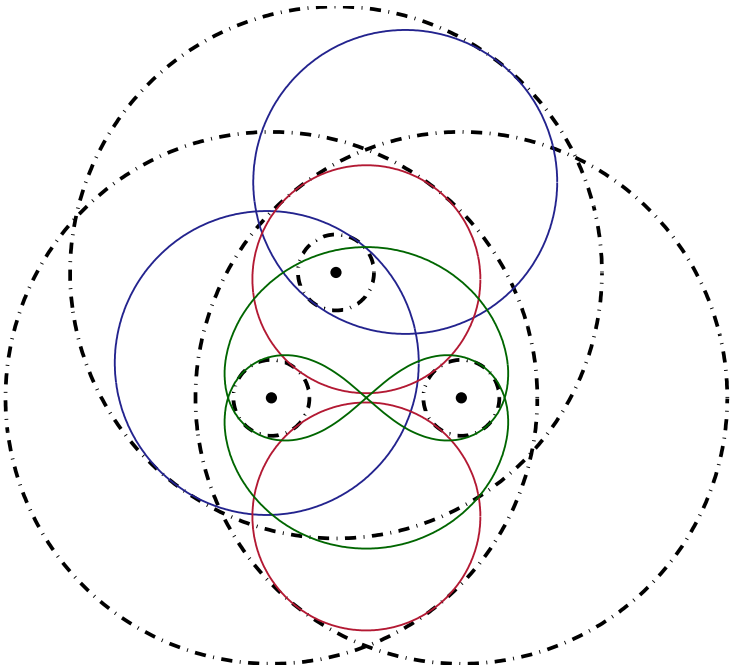

Figure 2.13: Example for the singularity loci of a 3-$\underline{R}RR$ PPM with $B_1 \equiv B_2$.

$x_{OO_3} = 30$, and $y_{OO_3} = 50$. The two circles corresponding to the first case are drawn in blue, the other two are in red, and the sextic is in green. Each of these curves is separated into portions corresponding to different (groups of) working modes at the points of tangency with the boundaries of the vertex spaces.

In addition, each curve is entirely enclosed within only the vertex space(s) corresponding to the leg on which the curve depends. For example, the two circles from the first case are always within the third vertex space, while the other two circles and the sextic are always within the intersection of the first and second vertex spaces. This fact is obvious from the geometric method with which the singularity curves were obtained. Algebraically, this means that $\det \mathbf{Z}$ can be factored into two—one part that contains only $\sqrt{\Gamma_3}$ and another that contains both $\sqrt{\Gamma_1}$ and $\sqrt{\Gamma_2}$.

2.4.4.5 Summary

Further examples of the singularity loci of 3-$\underline{R}RR$ PPM may be seen online at http://www.parallemic.org/Reviews/Review001.html. A *JavaScript*™ module allows the user to see interactively the singularity loci for each one of the eight working modes—individually and all together—as well as a schematic of the particular design.

Based on the detailed study of examples such as the ones presented herein and on the procedure for obtaining the polynomial of degree 42, we may summarise the following

list of observations for the singularity loci of 3-$\underline{R}RR$ planar parallel mechanisms for a constant orientation:

- ✓ there are eight working modes that are all kinematically different;
- ✓ for $\phi = const$, Type 1 singularity loci are three pairs of concentric circles (or arcs) of radii $|\ell_1 \pm \ell_2|$;
- ✓ vertex space i is the area between the two corresponding concentric circles;
- ✓ for $\phi = const$, Type 2 singularity loci are a curve of order 42 or the COW;
- ✓ when $\ell = 0$ and some $B_i \equiv O_i$, the three vertex space centres correspond to generic Type 1 (RI) singularities and may or may not be Type 2 singularities too;
- ✓ no polynomial exists for the singularity loci of Type 2 for a single working mode;
- ✓ the singularity loci of Type 2 are inside the vertex spaces;
- ✓ at the points of contact, a change of a branch index occurs when the Type 2 singularity loci are inside the COW;
- ✓ if the singularity loci of Type 2 extend outside the COW, then there is a factorisation in the polynomial of degree 42;
- ✓ the singularity loci of Type 2 for a given working mode divide the COW into separate regions, i.e., they are either closed curves or end at the COW boundaries.

2.4.5 Singularity Analysis of 3-$\underline{P}RR$ PPMs

The 3-$\underline{P}RR$ architecture (Fig. 2.4.5) was proposed in (Gosselin et al., 1996). A very simplified design was also patented for machining applications (Zirn et al., 1999). For that design, all three intermediate R joints move along the same line and two of the platform R joints coincide. Finally, a micro-assembly robot with pseudo-elastic flexure notch hinges has been recently developed by Hesselbach and Raatz (2000).

Let in each leg, the *directed line* through the intermediate R joint and along the active translation be defined by its moment μ_i about the base frame centre, and its angle α_i measured from the x axis. Let also points O_i (not shown) be fixed somewhere along the above-mentioned directed lines, and ρ_i be defined as the directed distance between O_i and A_i. Without loss of generality, we assume that $\mu_1 = 0$ and $\alpha_1 = 0$. 3-$\underline{R}RR$ and 3-$\underline{P}RR$ planar parallel mechanisms, have exactly the same mobile part but in the first, points A_i are driven on a circle, while in the second one, these points are driven along a line.

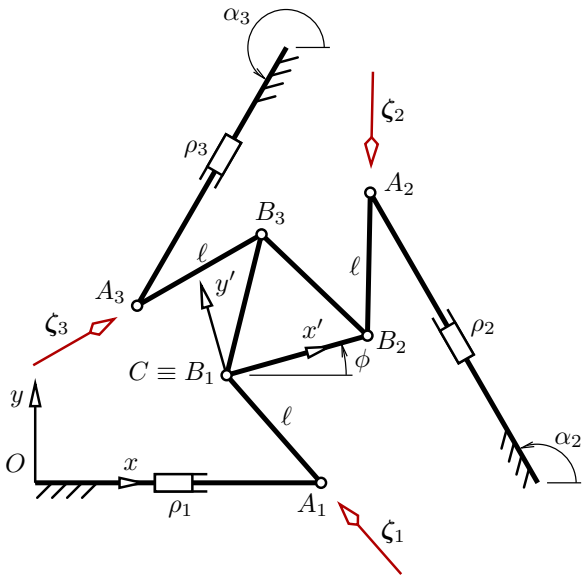

Figure 2.14: A 3-DOF PPM of type 3-$\underline{P}RR$.

2.4.5.1 Solving the Inverse Kinematic Problem

Geometrically, the inverse kinematic problem for a $\underline{P}RR$ chain can be seen as the problem of finding the points of intersection between a circle of radius ℓ and centre B_i and the directed line i. Let, π_i be the unit vector along that directed line. By definition,

$$(\mathbf{r}_{OA_i} \times \boldsymbol{\pi}_i)_z = -\mathbf{r}_{OA_i}^T \boldsymbol{\pi}_i^\perp = -(\mathbf{r}_{OB_i} - \mathbf{r}_{A_iB_i})^T \boldsymbol{\pi}_i^\perp = \mu_i. \tag{2.52}$$

Substituting with the expressions $\mathbf{r}_{OB_i} = [x+x_{CB_i}, y+y_{CB_i}]^T$, and $\boldsymbol{\pi}_i^\perp = [-\sin\alpha_i, \cos\alpha_i]^T$ in the above equation and rearranging, we obtain

$$\ell \hat{\mathbf{f}}_i^T \begin{bmatrix} -\sin\alpha_i \\ \cos\alpha_i \end{bmatrix} = \mu_i - (x + x_{CB_i})\sin\alpha_i + (y + y_{CB_i})\cos\alpha_i \equiv \eta_i, \tag{2.53}$$

where $\hat{\mathbf{f}}_i = \mathbf{r}_{A_iB_i}/\ell$ is the unit vector along A_iB_i. The new variable p_i is the moment of $\boldsymbol{\pi}_i$ about B_i, or in other words, η_i is the distance from B_i to directed line i.

The solution to Eq. (2.53) is

$$\hat{\mathbf{f}}_i = \frac{1}{\ell} \begin{bmatrix} -\sin\alpha_i\eta_i + \cos\alpha_i\delta_i\sqrt{\Gamma_i} \\ \cos\alpha_i\eta_i + \sin\alpha_i\delta_i\sqrt{\Gamma_i} \end{bmatrix}, \tag{2.54}$$

where $\Gamma_i = \ell^2 - \eta_i^2$ and $\delta_i = \pm 1$ is the branch index. Finally, as we already know the position of point A_i, $\mathbf{r}_{OA_i} = \mathbf{r}_{OB_i} - \ell\hat{\mathbf{f}}_i$, ρ_i is readily available.

2.4.5.2 Obtaining the Velocity Equation

(a) Using differentiation

Let us write the vector equation for $\mathbf{r}_{A_iB_i}$:

$$\mathbf{p} + \mathbf{r}_{CB_i} - \mathbf{r}_{OO_i} - \mathbf{r}_{O_iA_i} = \mathbf{r}_{A_iB_i}. \tag{2.55}$$

Squaring this equation gives us

$$\mathbf{r}_{A_iB_i}^T(\mathbf{p} + \mathbf{r}_{CB_i} - \mathbf{r}_{OO_i} - \mathbf{r}_{O_iA_i}) = \ell^2. \tag{2.56}$$

Differentiating Eq. (2.56) with respect to time leads to

$$\mathbf{r}_{A_iB_i}^T(\mathbf{v} + \omega\mathbf{r}_{CB_i}^{\perp} - \dot{\rho}_i\boldsymbol{\pi}_i) = 0. \tag{2.57}$$

Substituting $\mathbf{r}_{A_iB_i} = \ell\hat{\mathbf{f}}_i$ in the above equation and writing in vector format, we obtain:

$$\begin{bmatrix} \hat{\mathbf{f}}_i^T\mathbf{r}_{CB_i}^{\perp}, & \hat{\mathbf{f}}_i^T \end{bmatrix} \begin{bmatrix} \omega \\ \mathbf{v} \end{bmatrix} = \dot{\rho}_i\hat{\mathbf{f}}_i^T\boldsymbol{\pi}_i. \tag{2.58}$$

Substituting the expression for $\hat{\mathbf{f}}_i$ from Eq. (2.54) in the right-hand side of Eq. (2.58), one obtains easily

$$\hat{\mathbf{f}}_i^T\boldsymbol{\pi}_i = \frac{1}{\ell}\delta_i\sqrt{\Gamma_i}, \tag{2.59}$$

which is, in fact, the cosine of the angle between directed line i and link i. Finally, we write Eq. (2.58) in the $\mathbf{Z}\boldsymbol{\xi} = \boldsymbol{\Lambda}\dot{\boldsymbol{\rho}}$ matrix form:

$$\begin{bmatrix} \hat{\mathbf{f}}_1^T\mathbf{r}_{CB_1}^{\perp} & \hat{\mathbf{f}}_1^T \\ \hat{\mathbf{f}}_2^T\mathbf{r}_{CB_2}^{\perp} & \hat{\mathbf{f}}_2^T \\ \hat{\mathbf{f}}_3^T\mathbf{r}_{CB_3}^{\perp} & \hat{\mathbf{f}}_3^T \end{bmatrix} \boldsymbol{\xi} = \frac{1}{\ell}\mathrm{diag}\Big(\delta_1\sqrt{\Gamma_1}, \delta_2\sqrt{\Gamma_2}, \delta_3\sqrt{\Gamma_3}\Big)\dot{\boldsymbol{\rho}}. \tag{2.60}$$

(b) Using screw theory

The reciprocal screws $\boldsymbol{\zeta}_i$, $i = 1, 2, 3$, are the screws passing through the two passive R joints in each leg. Hence, their direction is along the already defined unit vector $\hat{\mathbf{f}}_i$, i.e., $\mathbf{f}_i = \hat{\mathbf{f}}_i$. Their moment m_i is also the same as for 3-$R\underline{P}R$ PPMs defined in Eq. (2.16).

The diagonal elements of $\boldsymbol{\Lambda}$ (see Eq. 2.8), are

$$\lambda_i = \mathbf{f}_i^T\boldsymbol{\pi}_i = \frac{1}{\ell}\delta_i\sqrt{\Gamma_i}. \tag{2.61}$$

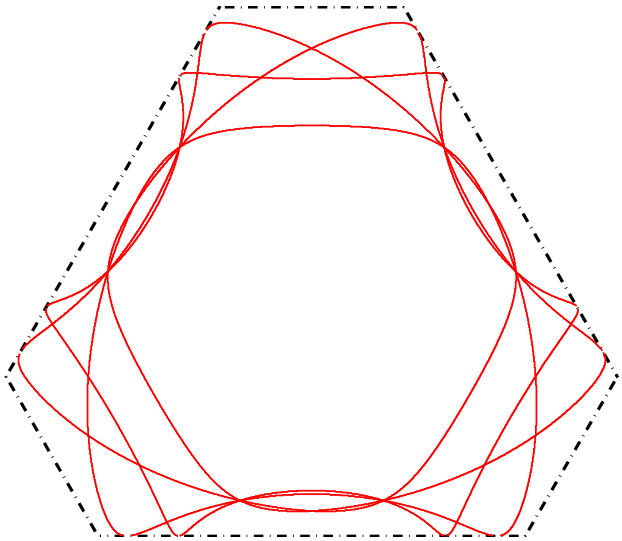

Figure 2.15: Example for the singularity loci of a 3-$\underline{P}RR$ PPM.

2.4.5.3 Obtaining the Singularity Loci

The inequality $\Gamma_i \geq 0$ defines each vertex space which is the area between a pair of lines parallel to the direction of P joint i and separated by a distance of 2ℓ. Indeed, Type 1 singularities occur when a link is normal to the P joint in a leg.

The Type 2 singularity loci for a constant orientation of the platform form a curve of degree 20 that corresponds to all working modes. That curve is obtained symbolically in a way similar to the one used for 3-$\underline{R}RR$ PPMs and described in detail in Section 2.4.4.3. For that purpose, it is assumed, without loss of generality, that $\ell = 1$, $\alpha_1 = 0$, $\mu_1 = 0$, $x_{CB_1} = 0$, and $y_{CB_1} = 0$. With that assumption, the polynomial is actually of degree 16 in x, but of degree 20 in y and as a whole.

Fig. 2.15 shows an example of the singularity loci of a general 3-$\underline{P}RR$ PPM. The mechanism parameters are $\ell = 130$, $\alpha_1 = 0$, $\alpha_2 = 2\pi/3$, $\alpha_3 = -2\pi/3$, $\mu_1 = \mu_3 = 0$, $\mu_2 = -147.6$, $x_{CB_1} = y_{CB_1} = y_{CB_2} = 0$, $x_{CB_2} = -110.8$, $x_{CB_3} = -55.4$, and $y_{CB_3} = -95.9$. In this figure, the Type 2 singularity loci for all eight working modes are drawn in red. Once again, all branch index changes are done at the vertex space boundaries, i.e., at Type 1 singularities.

Even in the very simplified case, when the three directed lines are parallel, $\alpha_1 = \alpha_2 = \alpha_3 = 0$, the polynomial, which in this case is in y only, is still of degree 18. The same is true even if the three lines coincide, $\mu_1 = \mu_2 = \mu_3 = 0$. This means, that the singularity loci of Type 2 may be up to 18 lines parallel to the directed lines. If the three platform R joint centres are collinear, the polynomial is decreased to degree 16.

If, however, two of the platform R joint centres coincide, the singularity loci become suddenly quite simplified. Following the same geometrical approach as the one described in Section 2.4.4.4, one may easily obtain that the corresponding loci of Type 2, for all working modes, will be two parallel line segments, one (arc of a) circle, and one (portion of an) ellipse (or a circle or a line). If the example with the simplified 3-$\underline{R}RR$ planar parallel mechanism was too complicated for an exam problem, due to the sextic, but simple enough for a homework assignment, the simplified 3-$\underline{R}RR$ planar parallel mechanism is ideal for an exam.

2.4.5.4 Summary

Based on the detailed study of examples like the one presented herein and on the procedure for obtaining the polynomial of degree 20, we may summarise the following list of observations for the singularity loci of 3-$\underline{P}RR$ planar parallel mechanisms for a constant orientation:

- ✓ there are eight working modes that are all kinematically different;
- ✓ for $\phi = const$, Type 1 singularity loci are 3 pairs of parallel lines distanced at 2ℓ;
- ✓ vertex space i is the area between the two corresponding parallel lines;
- ✓ for $\phi = const$, the Type 2 singularity loci correspond to a curve of order 20 or up to 18 parallel lines;
- ✓ for $\phi = const$ and if two of the platform joints coincide, the Type 2 singularity loci correspond to two line segments, one arc of a circle, and one portion of an ellipse (or a circle or a line).
- ✓ no polynomial exists for the singularity loci of Type 2 for a single working mode (in general);
- ✓ the singularity loci of Type 2 are inside the vertex spaces;
- ✓ if the singularity loci of Type 2 extend outside the COW, then there is a factorisation in the polynomial of degree 20;
- ✓ at the points of contact, a change of a branch index occurs when the Type 2 singularities are inside the COW;
- ✓ the singularity loci of Type 2 for a given working mode divide the COW into separate regions, i.e., the loci are either closed curves or end at the COW boundaries.

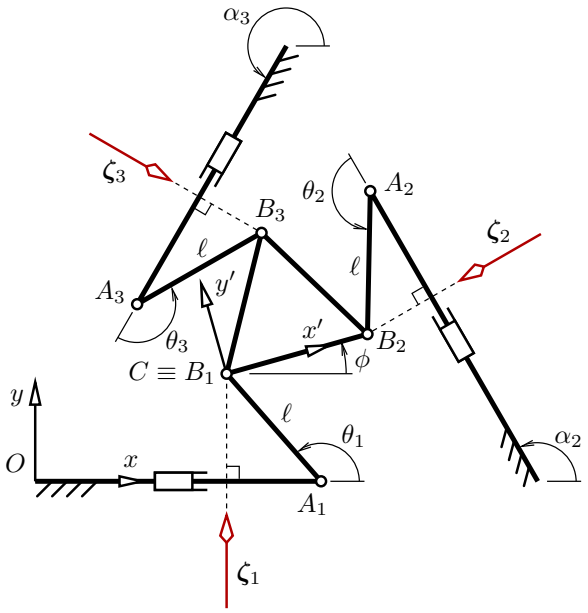

Figure 2.16: A 3-DOF PPM of type 3-$P\underline{R}R$.

2.4.6 Singularity Analysis of 3-$P\underline{R}R$ PPMs

Referring to Fig. 2.16, we denote by θ_i the active joint variables, which in this case are the angles between the directed lines and the corresponding links. As we will see, while this manipulator is probably not of great practical use, its kinematics is very simple. This is especially true after having in hand the results from the analysis of 3-$\underline{P}RR$ PPMs from the last section.

2.4.6.1 Solving the Inverse Kinematic Problem

Let us imagine a right-hand reference frame attached at A_i such that its x axis is along the directed line. From Eq. (2.54), we see that the unit vector along the link A_iB_i expressed in the above mentioned reference frame is $[\delta_i\sqrt{\Gamma_i},\ \eta_i]^T$. Therefore,

$$\theta_i = \text{atan2}\left(\delta_i\sqrt{\Gamma_i},\ \eta_i\right). \tag{2.62}$$

2.4.6.2 Obtaining the Velocity Equation

(a) Using differentiation

Let $\check{\mathbf{f}}_i$ be the unit vector obtained by rotating the directed line vector $\boldsymbol{\pi}_i$ at 90°, i.e., $\check{\mathbf{f}}_i = \boldsymbol{\pi}_i^{\perp}$. The following is then true

$$\check{\mathbf{f}}_i^T \mathbf{r}_{O_iA_i} = \check{\mathbf{f}}_i^T (\mathbf{r}_{OB_i} - \mathbf{r}_{A_iB_i} - \mathbf{r}_{OA_i}) = 0. \tag{2.63}$$

Differentiating the above equation with respect to time leads to

$$\check{\mathbf{f}}_i^T (\mathbf{v} - \omega \mathbf{r}_{A_iB_i}^{\perp} - \dot{\theta}_i \mathbf{r}_{OA_i}^{\perp}) = 0, \tag{2.64}$$

which after substituting $\check{\mathbf{f}}_i^T \mathbf{r}_{OA_i}^{\perp} = \boldsymbol{\pi}^T \mathbf{r}_{OA_i} = \ell \cos\theta_i = \delta_i \sqrt{\Gamma_i}$, rearranging and writing in matrix form gives

$$\begin{bmatrix} \hat{\mathbf{f}}_i^T \mathbf{r}_{CB_i}^{\perp}, & \hat{\mathbf{f}}_i^T \end{bmatrix} \begin{bmatrix} \omega \\ \mathbf{v} \end{bmatrix} = \delta_i \sqrt{\Gamma_i}. \tag{2.65}$$

Note, that the same could have been obtained directly by differentiating the relationship $\ell \sin\theta_i = \eta_i$. Finally, we write Eq. (2.65) in the $\mathbf{Z}\boldsymbol{\xi} = \boldsymbol{\Lambda}\dot{\boldsymbol{\rho}}$ matrix form:

$$\begin{bmatrix} \hat{\mathbf{f}}_1^T \mathbf{r}_{CB_1}^{\perp} & \hat{\mathbf{f}}_1^T \\ \hat{\mathbf{f}}_2^T \mathbf{r}_{CB_2}^{\perp} & \hat{\mathbf{f}}_2^T \\ \hat{\mathbf{f}}_3^T \mathbf{r}_{CB_3}^{\perp} & \hat{\mathbf{f}}_3^T \end{bmatrix} \boldsymbol{\xi} = \mathrm{diag}\Big(\delta_1 \sqrt{\Gamma_1}, \delta_2 \sqrt{\Gamma_2}, \delta_3 \sqrt{\Gamma_3}\Big) \dot{\boldsymbol{\theta}}. \tag{2.66}$$

(b) Using screw theory

The reciprocal screws $\boldsymbol{\zeta}_i$, $i = 1, 2, 3$, are the screws passing through the passive R joint in each leg and normal to the direction of the corresponding P joint. Hence, their direction is along the already defined unit vector $\check{\mathbf{f}}_i$, i.e., $\mathbf{f}_i = \hat{\mathbf{f}}_i = \boldsymbol{\pi}_i^{\perp}$, which is a constant vector. Their moment m_i is also the same as for 3-$R\underline{P}R$ planar parallel mechanisms defined in Eq. (2.16).

The diagonal elements of $\boldsymbol{\Lambda}$ (see Eq. 2.8), are

$$\lambda_i = (\mathbf{r}_{A_iB_i} \times \mathbf{f}_i)_z = \boldsymbol{\pi}_i^T \mathbf{r}_{A_iB_i} = \ell \cos\theta_i = \delta_i \sqrt{\Gamma_i}. \tag{2.67}$$

2.4.6.3 Obtaining the Singularity Loci

The constant-orientation workspace, the vertex spaces, and the singularity loci of Type 1 for 3-$P\underline{R}R$ PPMs are of course the same as for 3-$\underline{P}RR$ PPMs. As for the Type 2 singularities, we saw that the reciprocal screws for 3-$P\underline{R}R$ PPMs are constant, in the mobile frame, for a constant orientation of the mobile platform. Therefore, for a given orientation, a 3-$P\underline{R}R$ PPM is either at a Type 2 singularity for all positions or has no Type 2 singularities at all.

Indeed, let us write out the coordinates of vectors r_{CB_i} as functions of the platform orientation angle ϕ:

$$x_{CB_i} = x'_{CB_i}\cos\phi - y'_{CB_i}\sin\phi, \tag{2.68}$$
$$y_{CB_i} = x'_{CB_i}\sin\phi + y'_{CB_i}\cos\phi, \tag{2.69}$$

where x'_{CB_i} and y'_{CB_i} are the coordinates of vector r_{CB_i} as expressed in the mobile frame. Without loss of generality, we assume that $\alpha_1 = 0$, and $x_{CB_1} = y_{CB_1} = y_{CB_2} = 0$. Substituting the above expressions in the equation $\det \mathbf{Z} = 0$ and solving, gives the following *pair of distinct orientations*:

$$\phi = \begin{cases} -\tan^{-1}\left(\dfrac{x_\phi}{y_\phi}\right) + k\pi & \text{if } y_\phi \neq 0 \\ -\dfrac{\pi}{2} + k\pi & \text{if } y_\phi = 0 \end{cases} \tag{2.70}$$

where $k = 0, 1$ and

$$x_\phi = y'_{CB_3}\sin\alpha_2\sin\alpha_3 + x'_{CB_3}\sin\alpha_2\cos\alpha_3 - x'_{CB_2}\sin\alpha_3\cos\alpha_2,$$
$$y_\phi = \sin\alpha_2(x'_{CB_3}\sin\alpha_3 - y'_{CB_3}\cos\alpha_3 - x'_{CB_2}\sin\alpha_3).$$

Similarly to 3-$R\underline{R}R$ planar parallel mechanisms, the choice of working mode does not influence the singularity loci of Type 2.

2.4.6.4 Summary

We summarise the following observations for the singularity loci of 3-$P\underline{R}R$ planar parallel mechanisms:

- ✓ there are eight working modes, but they are all kinematically the same;
- ✓ for $\phi = const$, Type 1 singularity loci correspond to three pairs of parallel lines distanced at 2ℓ;
- ✓ vertex space i is the area between the two corresponding parallel lines;
- ✓ there are four orientations at which there are Type 2 singularities, and they happen to be the whole COW.

2.4.7 Singularity Analysis of 3-$RP\underline{P}$ and 3-$R\underline{P}P$ PPMs

In this section, 3-$RP\underline{P}$ and 3-$R\underline{P}P$ planar parallel mechanisms (Fig. 2.4.7) will be studied together due to their nearly identical kinematics. For that purpose, the notation will be a bit more complicated. We denote by α_i^A and α_i^B the angles between the directed lines along respectively the intermediate and platform P joints. Naturally, $\alpha_i^A \neq \alpha_i^B$. The unit vectors defining these directed lines will be respectively denoted by $\boldsymbol{\pi}_i^A$ and $\boldsymbol{\pi}_i^B$, i.e., $\boldsymbol{\pi}_i^A = [\cos\alpha_i^A,\ \sin\alpha_i^A]^T$, and $\boldsymbol{\pi}_i^B = [\cos\alpha_i^B,\ \sin\alpha_i^B]^T$. The angle between the each two corresponding directed lines will be denoted by γ_i, so that $\gamma_i = \alpha_i^B - \alpha_i^A + \pi$.

Obviously, the angles α_i^A and α_i^B are directly dependent on the orientation of the mobile platform, ϕ. In fact, we may write $\alpha_i^A = \phi + \beta_i^A$ and $\alpha_i^B = \phi + \beta_i^B$, where β_i^A and β_i^B are some constant offset angles, set by the design of the planar parallel mechanism.

Let points B_i be arbitrary points on the mobile platform (not shown). Let points A_i denote the intersection of the two corresponding directed lines passing through points O_i and B_i. Let ρ_i^A and ρ_i^B denote the distances along the directed lines between respectively O_i and A_i, and A_i and B_i. All of these notations are not shown on Fig. 2.4.7, because, as we will see later, none of them plays any role in the determination of the singularities of these two planar parallel mechanisms.

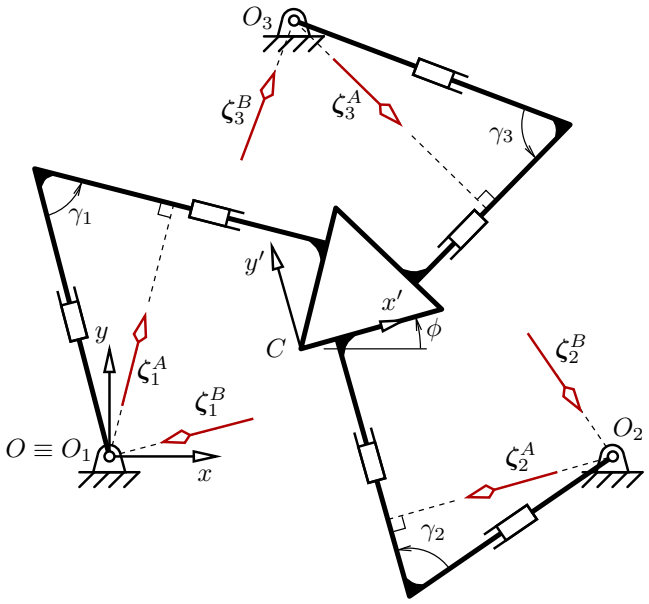

Figure 2.17: A 3-DOF PPM of type 3-$RP\underline{P}$ or 3-$R\underline{P}P$.

2.4.7.1 Solving the Inverse Kinematic Problem

For a given pose of the mobile platform, we know the positions of points B_i and the direction lines. Hence, points A_i can be obtained in a unique manner. Once, points A_i are obtained, the active joint variables ρ_i^A or ρ_i^B are readily obtainable. The straightforward procedure will not be, however, presented herein since the values of the active joint variables will not be of interest to us for our purposes. Note that 3-$RP\underline{P}$ and 3-$R\underline{P}P$ PPMs are the only PPMs that have only one working mode.

2.4.7.2 Obtaining the Velocity Equation

(a) Using differentiation

These two PPMs provide the best example of the superiority of the reciprocal screw method. Not only is the "conventional way" unobvious and tedious, but it also requires the definition of numerous variables that disappear in the final result—the velocity equation. The derivation procedure is identical for both PPMs. Hence, we will only present it for the 3-$RP\underline{P}$ case.

Let $(\boldsymbol{\pi}_i^B)^\perp$ be the unit vector obtained by rotating the direction vector $\boldsymbol{\pi}_i^B$ at 90°. The following equation can, therefore, be written down:

$$(\mathbf{r}_{O_iC} + \mathbf{r}_{CB_i} - \mathbf{r}_{O_iA_i})^T(\boldsymbol{\pi}_i^B)^\perp = 0. \tag{2.71}$$

Differentiating the above equation leads to

$$-\omega(\mathbf{r}_{O_iC} + \mathbf{r}_{CB_i} - \mathbf{r}_{O_iA_i})^T\boldsymbol{\pi}_i^B + \left(\mathbf{v} + \omega\mathbf{r}_{CB_i}^\perp - \dot{\rho}_i^A\boldsymbol{\pi}_i^A - \rho_i^A\omega(\boldsymbol{\pi}_i^A)^\perp\right)^T(\boldsymbol{\pi}_i^B)^\perp = 0. \tag{2.72}$$

Expanding the above expression and using the identities $\mathbf{a}^T\mathbf{b}^\perp = -\mathbf{b}^T\mathbf{a}^\perp$ and $(\mathbf{a}^\perp)^T\mathbf{b}^\perp = \mathbf{a}^T\mathbf{b}$ where $\mathbf{a}$ and $\mathbf{b}$ are vectors, we obtain

$$\begin{aligned} &-\omega(\mathbf{r}_{O_iC}^\perp)^T(\boldsymbol{\pi}_i^B)^\perp - \omega(\mathbf{r}_{CB_i}^\perp)^T(\boldsymbol{\pi}_i^B)^\perp + \omega\rho_i^B(\boldsymbol{\pi}_i^A)^T\boldsymbol{\pi}_i^B \\ &+\mathbf{v}^T(\boldsymbol{\pi}_i^B)^\perp + \omega(\mathbf{r}_{CB_i}^\perp)^T(\boldsymbol{\pi}_i^B)^\perp - \dot{\rho}_i^A(\boldsymbol{\pi}_i^A)^T(\boldsymbol{\pi}_i^B)^\perp - \omega\rho_i^A(\boldsymbol{\pi}_i^A)^T\boldsymbol{\pi}_i^B = 0. \end{aligned} \tag{2.73}$$

After cancelling the identical terms, substituting $(\boldsymbol{\pi}_i^A)^T(\boldsymbol{\pi}_i^B)^\perp = -\sin\gamma_i$, and rearranging, the above is summed up to

$$\hat{\mathbf{f}}_i^T\left(\mathbf{v} - \omega\mathbf{r}_{O_iC}^\perp\right) = -\sin\gamma_i\,\dot{\rho}_i^A. \tag{2.74}$$

where $\hat{\mathbf{f}}_i = (\boldsymbol{\pi}_i^B)^{\perp}$. Finally, we write the above equation in the $\mathbf{Z}\boldsymbol{\xi} = \boldsymbol{\Lambda}\dot{\boldsymbol{\rho}}$ matrix form:

$$\begin{bmatrix} -\hat{\mathbf{f}}_1^T \mathbf{r}_{O_1C}^{\perp} & \hat{\mathbf{f}}_1^T \\ -\hat{\mathbf{f}}_2^T \mathbf{r}_{O_2C}^{\perp} & \hat{\mathbf{f}}_2^T \\ -\hat{\mathbf{f}}_3^T \mathbf{r}_{O_3C}^{\perp} & \hat{\mathbf{f}}_3^T \end{bmatrix} \boldsymbol{\xi} = -\mathrm{diag}(\sin\gamma_1, \sin\gamma_2, \sin\gamma_3)\dot{\boldsymbol{\rho}}. \tag{2.75}$$

In the case of a 3-$R\underline{P}PP$ planar parallel mechanism, the velocity equation has the same form, but the right-hand side has a positive sign rather than negative and $\hat{\mathbf{f}}_i = (\boldsymbol{\pi}_i^A)^{\perp}$.

(b) Using screw theory

The reciprocal screws $\boldsymbol{\zeta}_i$, $i = 1, 2, 3$, are the screws passing through the passive R joint in each leg and normal to the direction of the corresponding passive P joint. Hence, their direction is along the already defined unit vector $\check{\mathbf{f}}_i$, i.e.,

$$\mathbf{f}_i = \begin{cases} \begin{bmatrix} -\sin\alpha_i^A \\ \cos\alpha_i^A \end{bmatrix}, & \text{for 3-}R\underline{P}PP\text{ PPMs} \\ \begin{bmatrix} -\sin\alpha_i^B \\ \cos\alpha_i^B \end{bmatrix}, & \text{for 3-}RP\underline{P}\text{ PPMs} \end{cases} \tag{2.76}$$

Their moment m_i of $\mathbf{f}_i$ about C is defined as

$$m_i = -\mathbf{f}_i^T \mathbf{r}_{O_iC}^{\perp} = \begin{cases} -(x - x_{OO_i})\cos\alpha_i^A - (y - y_{OO_i})\sin\alpha_i^A, & \text{for 3-}R\underline{P}PP\text{ PPMs} \\ -(x - x_{OO_i})\cos\alpha_i^B - (y - y_{OO_i})\sin\alpha_i^B, & \text{for 3-}RP\underline{P}\text{ PPMs} \end{cases} \tag{2.77}$$

The diagonal elements of $\boldsymbol{\Lambda}$ (see Eq. 2.8), are

$$\lambda_i = \begin{cases} \sin\gamma_i, & \text{for 3-}R\underline{P}PP\text{ PPMs} \\ -\sin\gamma_i, & \text{for 3-}RP\underline{P}\text{ PPMs} \end{cases} \tag{2.78}$$

2.4.7.3 Obtaining the Singularity Loci

Among all ten planar parallel mechanism designs, the 3-$RP\underline{P}$ and 3-$R\underline{P}P$ ones are the only two that have no Type 1 singularities. Thus, their constant-orientation workspace is the whole plane. Furthermore, the reciprocal screws for both the 3-$RP\underline{P}$ and 3-$R\underline{P}P$ planar parallel mechanisms depend only on the orientation of the mobile platform. Therefore, for a given orientation, a 3-$RP\underline{P}$ or 3-$R\underline{P}P$ planar parallel mechanism is either at a Type 2 singular configuration for all positions in the plane or has no Type 2 singularities at all.

Indeed, solving $\det \mathbf{Z} = 0$, gives the following *pair of distinct orientations*:

$$\phi = \begin{cases} -\tan^{-1}\left(\dfrac{x_\phi}{y_\phi}\right) + k\pi & \text{if } y_\phi \neq 0 \\ -\dfrac{\pi}{2} + k\pi & \text{if } y_\phi = 0 \end{cases} \tag{2.79}$$

where $k = 0, 1$ and

$$\begin{aligned} x_\phi &= -x_{OO_3} \sin\beta_2 \cos\beta_3 - y_{OO_3} \sin\beta_2 \sin\beta_3 + x_{OO_2} \cos\beta_2 \sin\beta_3, \\ y_\phi &= \sin\beta_2 (x_{OO_3} \sin\beta_3 - y_{OO_3} \cos\beta_3 - x_{OO_2} \sin\beta_3). \end{aligned}$$

In the above expressions, $\beta_i = \beta_i^A$ for 3-$R\underline{P}P$ planar parallel mechanisms and $\beta_i = \beta_i^B$ for 3-$RP\underline{P}$ planar parallel mechanisms, where we have assumed without loss of generality that $\beta_1 = 0$.

Therefore, the complete workspace of 3-$RP\underline{P}$ and 3-$R\underline{P}P$ planar parallel mechanisms is unrestricted with the exception of the two planes $\phi = const$ defined by Eq. (2.79).

2.4.7.4 Summary

We may summarise the following list of observations for the singularity loci of 3-$RP\underline{P}$ and 3-$R\underline{P}P$ planar parallel mechanisms:

- ✓ there is only one working mode;
- ✓ there are no Type 1 singularities;
- ✓ there are only four orientations at which there are Type 2 singularities, and they happen to be the whole plane.

2.4.8 Singularity Analysis of 3-$\underline{R}RP$ PPMs

Referring to Fig. 2.4.8, we denote by θ_i the active joint variables, which in this case are the angles between the x axis and the proximal links O_iA_i. The length of the proximal links is ℓ. The angles defining the directed lines parallel to the directions of the P joint are denoted, as usual, by α_i, while the unit vectors along these lines are referred to as $\boldsymbol{\pi}_i$. Furthermore, the directed lines passing through points A_i are defined by their moments μ_i about the platform centre C.

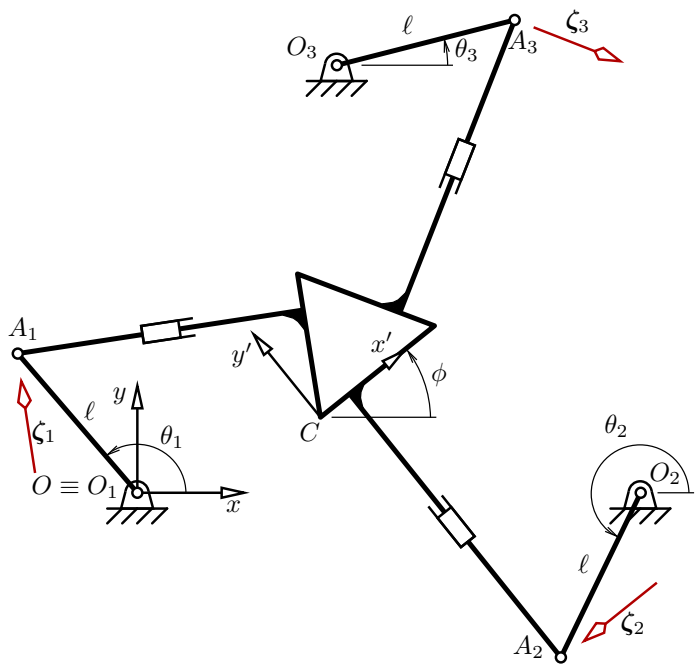

Figure 2.18: A 3-DOF PPM of type 3-$\underline{R}RP$.

2.4.8.1 Solving the Inverse Kinematic Problem

Geometrically, the inverse kinematic problem for a $\underline{P}RR$ chain can be seen as the problem of finding the points of intersection between a circle of radius ℓ and centre O_i and the directed line i. By definition,

$$\begin{aligned}(\boldsymbol{\pi}_i \times \mathbf{r}_{A_iC})_z &= \mathbf{r}_{A_iC}^T \boldsymbol{\pi}_i^{\perp} = (\mathbf{r}_{O_iC} - \mathbf{r}_{O_iA})^T \begin{bmatrix} -\sin\alpha_i \\ \cos\alpha_i \end{bmatrix} \\ &= \left(\begin{bmatrix} x - x_{OO_i} \\ y - y_{OO_i} \end{bmatrix} - \ell \begin{bmatrix} \cos\theta_i \\ \sin\theta_i \end{bmatrix} \right)^T \begin{bmatrix} -\sin\alpha_i \\ \cos\alpha_i \end{bmatrix} = \mu_i. \end{aligned} \tag{2.80}$$

Expanding Eq. (2.80) and rearranging leads to

$$\ell \sin\alpha_i \cos\theta_i - \ell \cos\alpha_i \sin\theta_i = \mu_i + (x - x_{OO_i}) \sin\alpha_i - (y - y_{OO_i}) \cos\alpha_i \equiv p_i, \tag{2.81}$$

where p_i is the moment of $\boldsymbol{\pi}_i$ about O_i. Solving Eq. (2.81) gives us

$$\sin\theta_i = \frac{-p_i \cos\alpha_i + \delta_i \sin\alpha_i \sqrt{\Gamma_i}}{\ell}, \quad \cos\theta_i = \frac{p_i \sin\alpha_i + \delta_i \cos\alpha_i \sqrt{\Gamma_i}}{\ell}, \tag{2.82}$$

where $\delta_i = \pm 1$ is a branch index and $\Gamma_i = \ell^2 - p_i^2$.

2.4.8.2 Obtaining the Velocity Equation

(a) Using differentiation

Differentiating Eq. (2.80) with respect to time leads to

$$\left(\mathbf{v} - \dot{\theta}_i \mathbf{r}^{\perp}_{O_iA}\right)^T \boldsymbol{\pi}_i^{\perp} + \mathbf{r}^T_{A_iC}(-\boldsymbol{\pi}_i)\omega = 0. \tag{2.83}$$

Let $\hat{\mathbf{f}}_i = \boldsymbol{\pi}_i^{\perp} = [-\sin\alpha_i, \cos\alpha_i]^T$. Therefore, we can write

$$\hat{\mathbf{f}}_i^T \mathbf{v} - \hat{\mathbf{f}}_i^T \mathbf{r}^{\perp}_{A_iC}\omega = \hat{\mathbf{f}}_i^T \mathbf{r}^{\perp}_{O_iA}\dot{\theta}_i. \tag{2.84}$$

Using the identity $\sin\alpha_i \sin\theta_i + \cos\alpha_i \cos\theta_i = \delta_i\sqrt{\Gamma_i}/\ell$ we obtain

$$-\hat{\mathbf{f}}_i^T \mathbf{r}^{\perp}_{A_iC} = -\boldsymbol{\pi}_i^T \mathbf{r}_{A_iC} = -(x - x_{OO_i})\cos\alpha_i - (y - y_{OO_i})\sin\alpha_i + \delta_i\sqrt{\Gamma_i}, \tag{2.85}$$

and

$$\hat{\mathbf{f}}_i^T \mathbf{r}^{\perp}_{O_iA} = \delta_i\sqrt{\Gamma_i}. \tag{2.86}$$

Finally, we write the above velocity equation in the $\mathbf{Z}\boldsymbol{\xi} = \boldsymbol{\Lambda}\dot{\boldsymbol{\theta}}$ matrix form:

$$\begin{bmatrix} -\hat{\mathbf{f}}_1^T \mathbf{r}^{\perp}_{A_1C} & \hat{\mathbf{f}}_1^T \\ -\hat{\mathbf{f}}_2^T \mathbf{r}^{\perp}_{A_2C} & \hat{\mathbf{f}}_2^T \\ -\hat{\mathbf{f}}_3^T \mathbf{r}^{\perp}_{A_3C} & \hat{\mathbf{f}}_3^T \end{bmatrix} \boldsymbol{\xi} = \operatorname{diag}\left(\delta_1\sqrt{\Gamma_1}, \delta_2\sqrt{\Gamma_2}, \delta_3\sqrt{\Gamma_3}\right)\dot{\boldsymbol{\theta}}. \tag{2.87}$$

(b) Using screw theory

The reciprocal screws $\boldsymbol{\zeta}_i$ are the screws passing through the passive R joint in each leg and normal to the direction of the corresponding passive P joint. Hence, their direction is along the already defined unit vector $\hat{\mathbf{f}}_i$, i.e., $\mathbf{f}_i = \hat{\mathbf{f}}_i = \boldsymbol{\pi}_i^{\perp}$. Their moment about the platform centre C is defined as

$$\begin{aligned} m_i &= (\mathbf{f}_i \times \mathbf{r}_{A_iC})_z = -\mathbf{r}^T_{A_iC}\boldsymbol{\pi}_i = \left(\begin{bmatrix} x - x_{OO_i} \\ y - y_{OO_i} \end{bmatrix} - \ell \begin{bmatrix} \cos\theta_i \\ \sin\theta_i \end{bmatrix}\right)^T \begin{bmatrix} -\cos\alpha_i \\ -\sin\alpha_i \end{bmatrix} \\ &= -(x - x_{OO_i})\cos\alpha_i - (y - y_{OO_i})\sin\alpha_i + \delta_i\sqrt{\Gamma_i}. \end{aligned} \tag{2.88}$$

The diagonal elements of Λ are

$$\lambda_i = (\mathbf{r}_{O_iA_i} \times \mathbf{f}_i)_z = \mathbf{f}_i^T \mathbf{r}^{\perp}_{O_iA_i} = \delta_i\sqrt{\Gamma_i}. \tag{2.89}$$

2.4.8.3 Obtaining the Singularity Loci

Type 1 singularities of 3-$\underline{R}RP$ PPMs occur when a proximal link is normal to the direction of its corresponding P joint, i.e., when $\Gamma_i = 0$. For a constant orientation of the mobile platform, Type 1 singularities are, therefore, a pair of parallel lines at a distance 2ℓ. The vertex space of 3-$\underline{R}RP$ PPMs is the area between these two lines, just like in 3-$\underline{P}RR$ and 3-$P\underline{R}R$ PPMs.

Type 2 singularities, on the other hand, are more complicated and depend on the working mode of the mechanism. Let us assume without loss of generality that $\ell = 1$, $\alpha_1 = 0$, $\mu_1 = 0$, $\mu_2 = 0$, $x_{OO_1} = 0$, $y_{OO_1} = 0$, and $y_{OO_2} = 0$. Then, Type 2 singularities are defined by the following expression

$$\begin{aligned} \det \mathbf{Z} = \sin\alpha_2 \cos\alpha_3 x_{OO_3} - \sin\alpha_3 \cos\alpha_2 x_{OO_2} + \sin\alpha_2 \sin\alpha_3 y_{OO_3} \\ + \sin(\alpha_3 - \alpha_2)\delta_1\sqrt{\Gamma_1} - \sin\alpha_3\delta_2\sqrt{\Gamma_2} + \sin\alpha_2\delta_3\sqrt{\Gamma_3} = 0. \end{aligned} \tag{2.90}$$

The Type 2 singularity loci for a constant orientation of the platform form a curve of degree 6 that corresponds to all working modes. In fact, the polynomial is of degree 4 in y, but of degree 6 in x and as a whole. The expression, however, is enormous and will not be presented here. It is obtained symbolically by rearranging and raising to square the above expression in a way similar to the one used for 3-$\underline{R}RR$ PPMs.

Fig. 2.19 shows an example of the singularity loci of a general 3-$\underline{R}RP$ PPM. The mechanism parameters are $\ell = 130$, $\alpha_1 = 0$, $\alpha_2 = 2\pi/3$, $\alpha_3 = -2\pi/3$, $\mu_1 = \mu_2 = \mu_3 = 0$, $x_{OO_1} = y_{OO_1} = y_{OO_2} = 0$, $x_{OO_2} = -76.7$, $x_{OO_3} = -38.3$, and $y_{OO_3} = -66.4$. In this figure, the Type 2 singularity loci for all eight working modes are drawn in red. Once again, all branch index changes are done at the vertex space boundaries, i.e., at Type 1 singularities.

By inspecting the expression in Eq. (2.90) more carefully, we reach to the conclusion that it can never be factored by separating one of the $\delta_i\sqrt{\Gamma_i}$ terms. Therefore, the Type 2 singularities are always inside all vertex spaces, i.e., inside the constant-orientation workspace. Furthermore, there is no polynomial that corresponds to a single working mode. However, one of the $\delta_i\sqrt{\Gamma_i}$ terms can easily disappear if two of the directed line angles are equal, i.e., if $\alpha_2 = \alpha_1 = 0$, or $\alpha_3 = \alpha_1 = 0$, or $\alpha_2 = \alpha_3$.

Instead of studying this interesting case algebraically, let us immediately analyse it geometrically. The directions of the reciprocal screws in the mobile frame are fixed by the design of the mechanism. If we build two of the P joints so that their directions

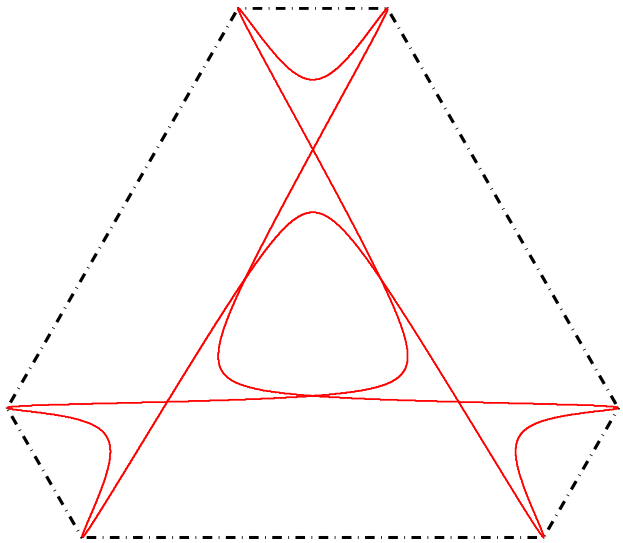

Figure 2.19: Example for the singularity loci of a 3-$\underline{R}RP$ PPM.

are parallel they will always stay parallel. The third P joint should not, however, be parallel to the first two. Therefore, the three reciprocal screws will never be dependent except if the two screws with parallel axes coincide.

Such a simplified PPM will obviously be free of Type 2 singularities, as long as the intermediate R joints in the legs with parallel P joints do not coincide. Or, in other words, the distance between the base R joints in the legs with parallel P joints should be greater that 2ℓ. An example of such a simplified Type 2 singularity-free planar parallel mechanism is shown in Fig. 2.20.

Note that Type 2 singularities may be eliminated in the same way for 3-$RP\underline{P}$, 3-$R\underline{P}P$, and 3-$\underline{P}RP$ planar parallel mechanisms.

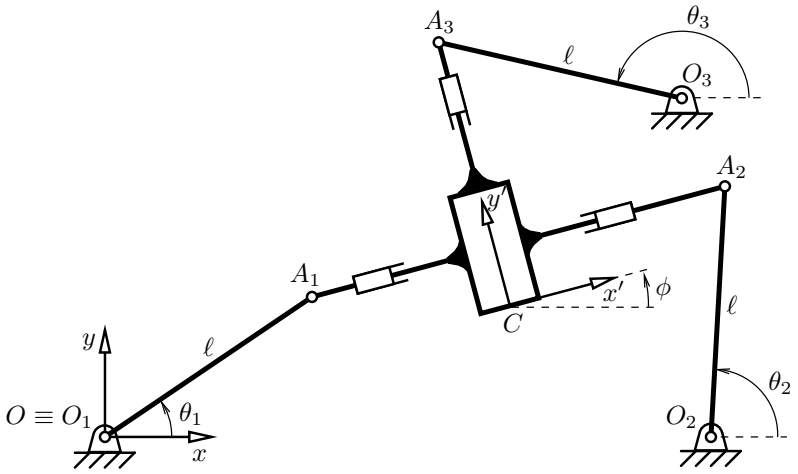

Figure 2.20: A special 3-$\underline{R}RP$ PPM with two parallel P joints.

2.4.8.4 Summary

We may summarise the following observations for the singularities of 3-$\underline{R}RRP$ planar parallel mechanisms:

- ✓ there are eight working modes that are all kinematically different;
- ✓ for $\phi = const$, Type 1 singularity loci are 3 pairs of parallel lines distanced at 2ℓ;
- ✓ vertex space i is the area between the two corresponding parallel lines;
- ✓ for $\phi = const$, Type 2 singularity loci are curve of order 6;
- ✓ the singularity loci of Type 2 are inside the COW;
- ✓ at the points of contact, a change of a branch index occurs;
- ✓ if (only) two P joints are parallel, and the distance between the corresponding two base R joints is greater than 2ℓ, there are no Type 2 singularities.

2.4.9 Singularity Analysis of 3-$\underline{P}RRP$ PPMs

A design of this type was proposed in (Daniali et al., 1993) under the name *double-triangular manipulator*. In addition, a 3-$\underline{P}RP$ *alignment stage*, based on the just previously mentioned singularity-free design concept is commercially available by the Japanese company *Hephaist Seiko* (http://www.hephaist.co.jp).

Referring to Fig. 2.4.9, we denote by ρ_i^O the active joint variables. Let in each leg, the directed line through the R joint and along the active (passive) translation be defined by its moment μ_i^O (μ_i^B) about the base (platform) frame centre, O (C), and its angle α_i^O (α_i^B) measured from the base x axis. As usual, the unit vectors along the active (passive) translation will be denoted by $\boldsymbol{\pi}_i^O$ ($\boldsymbol{\pi}_i^B$).

2.4.9.1 Solving the Inverse Kinematic Problem

By definition,

$$(\boldsymbol{\pi}_i^B \times \mathbf{r}_{A_iC})_z = \mathbf{r}_{A_iC}^T (\boldsymbol{\pi}_i^B)^\perp = \mathbf{r}_{A_iC}^T \begin{bmatrix} -\sin\alpha_i^B \\ \cos\alpha_i^B \end{bmatrix} = \mu_i^B, \tag{2.91}$$

and

$$(\boldsymbol{\pi}_i^O \times \mathbf{r}_{A_iO})_z = (\mathbf{r}_{A_iC} - \mathbf{p})^T (\boldsymbol{\pi}_i^O)^\perp = (\mathbf{r}_{A_iC} - \mathbf{p})^T \begin{bmatrix} -\sin\alpha_i^O \\ \cos\alpha_i^O \end{bmatrix} = \mu_i^O. \tag{2.92}$$

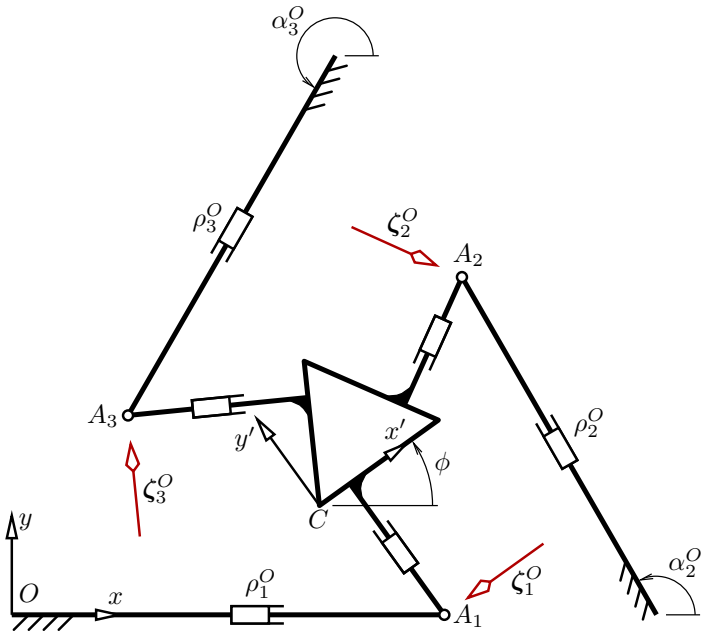

Figure 2.21: A 3-DOF PPM of type 3-*PRP*.

Solving Eqs. (2.91) and (2.92) gives

$$\mathbf{r}_{A_iC} = \frac{1}{\sin(\alpha_i^O - \alpha_i^B)} \begin{bmatrix} \cos\alpha_i^B \sin\alpha_i^O x - \cos\alpha_i^B \cos\alpha_i^O y - \cos\alpha_i^B \mu_i^O + \cos\alpha_i^O \mu_i^B \\ \sin\alpha_i^B \sin\alpha_i^O x - \sin\alpha_i^B \cos\alpha_i^O y - \sin\alpha_i^B \mu_i^O + \sin\alpha_i^O \mu_i^B \end{bmatrix}. \tag{2.93}$$

On the other hand,

$$\mathbf{r}_{A_iC} = \mathbf{p} - \mathbf{r}_{OO_i} - \rho_i^O \boldsymbol{\pi}_i^O, \tag{2.94}$$

where point O_i is fixed to the base somewhere on the directed line passing through A_i. It is clear that a *unique solution* for ρ_i^O can be easily found by solving Eqs. (2.93) and (2.94).

Note, however, that when $\sin(\alpha_i^O - \alpha_i^B) = 0$, i.e., when the directions of both P joints in a leg are parallel, Eq. (2.93) is no longer valid, and ρ_i^O cannot be uniquely defined.

2.4.9.2 Obtaining the Velocity Equation

(a) Using differentiation

Differentiating Eq. (2.91) with respect to time leads to

$$(\mathbf{v} - \dot{\rho}_i^O \boldsymbol{\pi}_i^O)^T (\boldsymbol{\pi}_i^B)^\perp - \mathbf{r}_{A_iC}^T \boldsymbol{\pi}_i^B \omega = (\mathbf{v} - \dot{\rho}_i^O \boldsymbol{\pi}_i^O)^T (\boldsymbol{\pi}_i^B)^\perp - (\mathbf{r}_{A_iC}^\perp)^T (\boldsymbol{\pi}_i^B)^\perp \omega = 0. \quad (2.95)$$

Setting $\hat{\mathbf{f}}_i = (\boldsymbol{\pi}_i^B)^\perp$ and writing the above equation in matrix form gives us

$$\begin{bmatrix} -\hat{\mathbf{f}}_i^T \mathbf{r}_{A_iC}^\perp & \hat{\mathbf{f}}_i^T \end{bmatrix} \begin{bmatrix} \omega \\ \mathbf{v} \end{bmatrix} = \left(\hat{\mathbf{f}}_i^T \boldsymbol{\pi}_i^O \right) \dot{\rho}_i^O. \quad (2.96)$$

If we use the expression found for $\mathbf{r}_{A_iC}$, we have

$$\hat{\mathbf{f}}_i^T \mathbf{r}_{A_iC} = -\frac{\mu_i^O - \sin\alpha_i^O x + \cos\alpha_i^O y - \cos(\alpha_i^O - \alpha_i^B)\mu_i^B}{\sin(\alpha_i^O - \alpha_i^B)} \quad (2.97)$$

and

$$\hat{\mathbf{f}}_i^T \boldsymbol{\pi}_i^O = \begin{bmatrix} -\sin\alpha_i^B \\ \cos\alpha_i^B \end{bmatrix}^T \begin{bmatrix} \cos\alpha_i^O \\ \sin\alpha_i^O \end{bmatrix} = \sin(\alpha_i^O - \alpha_i^B). \quad (2.98)$$

Finally, we write the above velocity equation in the $\mathbf{Z}\boldsymbol{\xi} = \boldsymbol{\Lambda}\dot{\boldsymbol{\theta}}$ matrix form:

$$\begin{bmatrix} -\hat{\mathbf{f}}_1^T \mathbf{r}_{A_1C}^\perp & \hat{\mathbf{f}}_1^T \\ -\hat{\mathbf{f}}_2^T \mathbf{r}_{A_2C}^\perp & \hat{\mathbf{f}}_2^T \\ -\hat{\mathbf{f}}_3^T \mathbf{r}_{A_3C}^\perp & \hat{\mathbf{f}}_3^T \end{bmatrix} \boldsymbol{\xi} = \mathrm{diag}\big(\sin(\alpha_1^O - \alpha_1^B), \sin(\alpha_2^O - \alpha_2^B), \sin(\alpha_3^O - \alpha_3^B)\big)\dot{\boldsymbol{\theta}}. \quad (2.99)$$

(b) Using screw theory

The reciprocal screws $\boldsymbol{\zeta}_i$ are the screws passing through the passive R joint in each leg and normal to the direction of the corresponding passive P joint. Hence, their direction is along the already defined unit vector $\hat{\mathbf{f}}_i$, i.e., $\mathbf{f}_i = \hat{\mathbf{f}}_i$. Their moment about the platform centre C is defined as

$$m_i = (\mathbf{f}_i \times \mathbf{r}_{A_iC})_z - \mathbf{f}_i^T \mathbf{r}_{A_iC} = \frac{\mu_i^O - \sin\alpha_i^O x + \cos\alpha_i^O y - \cos(\alpha_i^O - \alpha_i^B)\mu_i^B}{\sin(\alpha_i^O - \alpha_i^B)}. \quad (2.100)$$

where $\mathbf{r}_{A_iC}$ is defined by Eq. (2.93), if the directions of both P joints in leg i are not parallel, or otherwise by Eq. (2.94).

As for the diagonal elements of Λ, they are

$$\lambda_i = \mathbf{f}_i^T \boldsymbol{\pi}_i^O = \sin(\alpha_i^O - \alpha_i^B). \tag{2.101}$$

2.4.9.3 Obtaining the Singularity Loci

As we already mentioned, the 3-$\underline{P}RP$ PPM has only one working mode. Hence, the vertex space and the COW for a given orientation are the whole plane. Yet, the 3-$\underline{P}RP$ PPM is not free of Type 1 singularities. Such a singularity occurs when the directions of both P joints in a leg coincide. Obviously, there are at most six orientations at which this may occur. In other words, there are at most six lines corresponding to Type 1 singularities in the complete three-dimensional workspace. *This refutes the common misconception that Type 1 singularities are always the boundaries of the workspace.*

The expression for the determinant of $\mathbf{Z}$ is a fraction of which the denominator is $\sin(\alpha_1^O - \alpha_1^B)\sin(\alpha_2^O - \alpha_2^B)\sin(\alpha_3^O - \alpha_3^B)$. Thus, let us first study the case when this denominator is non-zero, i.e., when there is no Type 1 singularity. The numerator of $\det \mathbf{Z}$ is a linear polynomial in x and y whose coefficients are dependent on the orientation of the mobile platform. Hence, in general, the Type 2 singularity loci for a constant orientation of the platform correspond to a line.

If, however, $\alpha_i^B = \alpha_i^O + \phi$ for $i = 1, 2, 3$, as in the *double-triangular manipulator* (Daniali et al., 1993), shown in Fig. 2.22, then the numerator of $\det \mathbf{Z}$ is dependent only on the platform orientation (does not contain x and y terms). In fact, in this case, there are only two orientations at which the parallel mechanism is in a Type 2 singularity whatever its position:

$$\phi = \pm \cos\left(\frac{\mu_1^O \sin(\alpha_2^O - \alpha_3^O) + \mu_2^O \sin(\alpha_3^O - \alpha_1^O) + \mu_3^O \sin(\alpha_1^O - \alpha_2^O)}{\mu_1^B \sin(\alpha_2^O - \alpha_3^O) + \mu_2^B \sin(\alpha_3^O - \alpha_1^O) + \mu_3^B \sin(\alpha_1^O - \alpha_2^O)}\right). \tag{2.102}$$

From the above expression, we may conclude that one possible way to eliminate Type 2 singularities is to make the directed lines for the passive P joints pass through one point. Choosing C to coincide with that point, translates to $\mu_1^B = \mu_2^B = \mu_3^B = 0$.

Another way to eliminate Type 2 singularities was already proposed at the end of Section 2.4.8.3. To do this, it suffice to design the mechanism, so that two, and only two, of the directed lines of the passive P joints be parallel.

Now, let us see what happens when leg i is in a Type 1 singularity. If the mechanism is not constructed in the way just mentioned, then at a Type 1 singularity (and at any

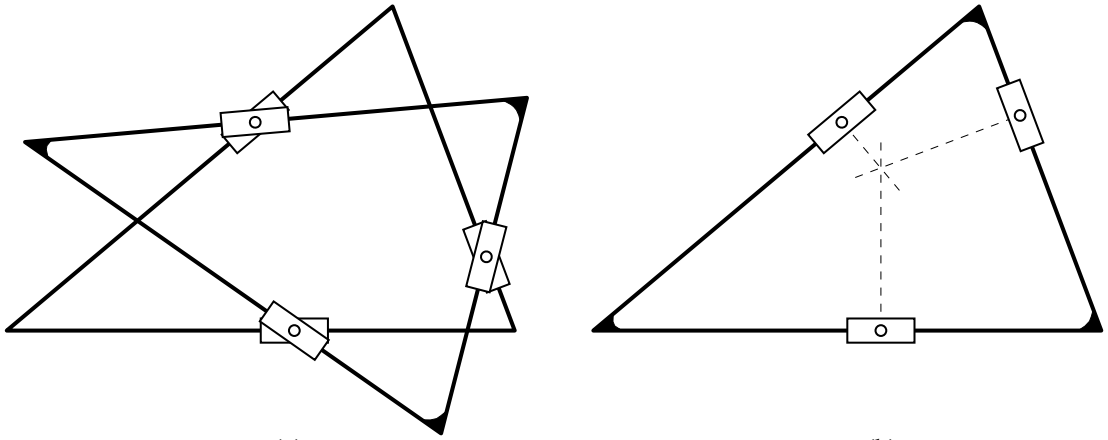

Figure 2.22: The double triangular manipulator (a) at a nonsingular configuration and (b) at a combined Type 1 and Type 2 singularity.

other configuration, in fact), the screw axes for the remaining two (non-singular) legs intersect at one point. Since moving the actuator of the singular leg does not produce any change in the pose of the mechanism but translates screw axis i, the latter can be adjusted to pass through the intersection point of the other two screw axes. Therefore, all Type 1 singularity loci may also correspond to Type 2 singularities (if Type 2 singularities exist at all).

Finally, note, that in a mechanism for which $\alpha_i^B = \alpha_i^O + \phi$ for $i = 1, 2, 3$, if it is physically possible to have one leg in a Type 1 singularity, then the other two legs will also be singular. (This may easily occur in the double-triangular manipulator, for example.) Once such a mechanism enters a Type 1 singularity, the platform becomes *jammed* and can no longer get away with the aid of the three actuators. What is more, even external action cannot remove the platform from this pose unless the actuators are arranged in such a way as to provoke a Type 2 singularity (Fig. 2.22).

2.4.9.4 Summary

We may summarise the following observations for the singularities of 3-$\underline{P}RP$ PPMs:

- ✓ there is only one working mode;
- ✓ at only six orientations, there are Type 1 singularity loci corresponding to a line;
- ✓ Type 1 singularity loci may also, in general, correspond to Type 2 singularities;
- ✓ in general, for $\phi = const$, Type 2 singularity loci form a line;
- ✓ if the directed lines of the passive P joints are intersecting at one point, there are only two orientations at which the PPM is at a Type 2 singularity everywhere.

2.5 Further Remarks

Through the complete set of all possible planar parallel mechanisms with revolute and/or prismatic joints, we have been able to show the beauty of the reciprocal screw method. The velocity kinematic analysis of planar parallel mechanisms based on screw theory is rigorous, compact, intuitive, and brings an insight into the robot kinematics. This powerful geometric tool allows a designer to promptly identify ways of simplifying the mechanical design in order to reduce or even eliminate singularities. The method provides solid means for explaining some rather particular singular configurations, which have otherwise been often wrongly described by other researchers.

However, the contribution of this chapter is not limited to the advocacy of the use of reciprocal screws. Numerous important results have been outlined up to here. Namely, new designs of planar parallel mechanisms with few or even no singularities have been identified. It has been shown that Type 1 singularities do not always correspond to the workspace boundaries. The issue of singularities in the presence of working modes (branch sets) has been directly addressed. It has been shown how for some architectures the singularities for all working modes correspond to one or several curves. These singularity curves were shown to be separated by points of contact with the Type 1 singularity loci into segments corresponding to different working modes.

In addition to all that, we will comment next in greater detail on some of the issues that were not fully explored up to here. Yet, some of these points will not be fully investigated here either. Instead, we will lay the paths to new unexplored areas that deserve the serious attention of detailed devoted studies.

2.5.1 Parameterisation and Polynomial Derivation

In this chapter, we have used the minimal and most intuitive parameterisation for all ten planar parallel architectures. In the case of base and/or platform R joints, we used the coordinates of vectors $\mathbf{r}_{OO_i}$ and $\mathbf{r}_{CB_i}$ expressed in the base frame, (x_{OO_i}, y_{OO_i}) and (x_{CB_i}, y_{CB_i}), respectively. In the case of base and/or platform P joints, we used the angle between the base x axis and the direction of the P joint, α_i, and the moment, μ_i, of the line directed along the P joint and through the neighbouring R joint about the base and platform centres, respectively. In addition, we assumed without loss of generality that some of the parameters are zeros.

The described parameterisation was very useful for the elegant derivation of the matrices $\mathbf{Z}$ and $\mathbf{\Lambda}$. In most cases, we did not even have to define exactly the active joint variables, when the active joints were prismatic. Consequently, we did not need to present the complete solution to the inverse kinematic problem.

However, a slightly different parameterisation may be more convenient for the derivation of the polynomial representing the Type 2 singularity loci of a planar parallel mechanism with multiple working modes. For example, for 3-$\underline{R}RR$ planar parallel mechanisms, instead of using x_{OO_i} and y_{OO_i} as parameters, $x_{CB_i} - x_{OO_i}$ and $y_{CB_i} - y_{OO_i}$ have been used (Bonev and Gosselin, 2001). The latter is essential in order to reduce the number of terms in the final polynomial.

2.5.2 PPMs with Mixed Legs

Firstly, let us consider the case of a planar parallel mechanism with any combination of three legs from the ten different studied previously. For such a mechanism, one should simply write the scalar velocity equation for each leg as given before and then combine all three to obtain the matrices $\mathbf{Z}$ and $\mathbf{\Lambda}$. Note that one can easily reverse the order of the joints (e.g., use an $\underline{R}RR$ chain and an $RR\underline{R}$ one) and still use our equations. To obtain the singularity loci of Type 2, one should simply compute $\det \mathbf{Z}$ in order to obtain a polynomial in x and y.

Secondly, let us consider the case of a planar parallel mechanism with a leg having two passive P joints and one active R joint ($\underline{R}PP$, $P\underline{R}P$, $PP\underline{R}$) and any combination of two legs from the ten different studied previously. As we already mentioned in Section 2.3.2, the reciprocal screw of the leg with the two passive P joints is the moment about the z axis. Hence, for the planar parallel mechanism to be in a Type 2 singular configuration, the reciprocal screws of the two other legs, which are forces in the xy plane, should be linearly dependent. So, we only need to obtain the expressions for $\mathbf{f}_2$ and $\mathbf{f}_3$, and check when their vector product vanishes.

In both cases, the corresponding Type 1 singular configurations can be deduced directly from the diagonal elements of the matrix $\mathbf{\Lambda}$. However, the singularity loci can be determined in a much easier manner by a simple geometric method—the same algorithm as the one used for the computation of the constant-orientation workspace of the planar parallel mechanisms.

2.5.3 The Missing "Type 3" Singularities

Some readers might ask why we have omitted the so-called Type 3 singularities. This type was introduced in (Gosselin and Angeles, 1990) in conjunction with Type 1 and Type 2 singularities. It was defined as the type of singularity configurations at which matrices $\mathbf{Z}$ and $\mathbf{\Lambda}$ are both singular. Then, the type was erroneously associated with architecture singularities. It was later claimed that Type 3 singularities are only a subset of architecture singularities (Ma and Angeles, 1992). This inaccurate definition may even be found in a recent textbook on robotics (Tsai, 1999). As we show, architecture singularities, or finite self motions, are *not related* to the simultaneous degeneracy of matrices $\mathbf{Z}$ and $\mathbf{\Lambda}$.

Indeed, for a parallel mechanism, the singularity loci of Type 2 generally intersect the vertex space boundary, i.e., the singularity loci of Type 1 and no special design conditions are required for that. One obvious example is a 3-$R\underline{P}R$ planar parallel mechanism, where, for a constant orientation, the intersection points of the Type 2 singularity loci (a conic) and Type 1 singularity loci (three circles) always exist for any design with $\ell \neq 0$. We have observed that configurations at which both matrices $\mathbf{Z}$ and $\mathbf{\Lambda}$ are singular exist for the general designs of most 3-DOF planar parallel mechanisms. However, generally, there is no finite uncontrollable motion in these configurations. In conclusion, those special configurations (*i*) do not occur for particular designs only and (*ii*) do not necessarily correspond to self motions.

2.5.4 PPMs with Parallelograms

A *parallelogram* is a four-bar mechanism whose opposing links are of equal length (Fig. 2.23a). It has the property that at least a pair of opposing links remains parallel at all times. The parallelogram is sometimes used in the construction of mechanisms as a 1-DOF pair (denoted as $P\!a$) in combination with P and R joints. However, we would like to stress that *the parallelogram is not a distinct kinematic pair* in the strictest sense.

Indeed, an exhaustive study of 3-DOF chains based on one passive/active $P\!a$ joint and any combination of P or R joints, placed in any order, shows that any such chain has a kinematically equivalent serial 3-DOF chain with only three P and/or R joints. In particular, for any 3-DOF planar parallel mechanism with identical legs that have $P\!a$ joints, there is a *kinematically equivalent* 3-DOF planar parallel mechanism with legs of type $\underline{R}RR$, $R\underline{R}R$, $P\underline{R}R$, or $\underline{P}RR$. By kinematically equivalent planar parallel

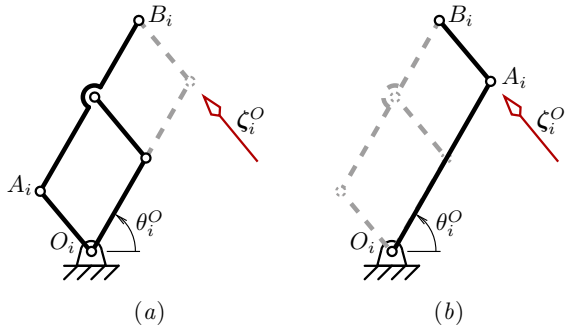

Figure 2.23: An example showing (a) a $\underline{R}PaR$ serial chain and (b) its kinematically equivalent $\underline{R}RR$ chain.

mechanism, we mean a mechanism that has the same input-output velocity equation and the same singularities. For example, the 3-DOF 3-$\underline{R}PaR$ mechanism whose leg is shown in Fig. 2.23 is kinematically equivalent to a 3-DOF 3-$\underline{R}RR$ planar parallel mechanism. Basically, in all cases, the Pa joint is substituted by an R joint, but the order of the three joints does not always remain the same (e.g., 3-$\underline{Pa}PR$ planar parallel mechanisms are kinematically equivalent to 3-$P\underline{R}R$ mechanisms). This is an interesting fact, since, instantaneously, a Pa joint is equivalent to a translation.

Hence, the main reasons for using parallelograms in practice may be to avoid link interference and to achieve static or even dynamic balancing, e.g., (Chung et al., 2001). Of course, parallelograms are also ideal if legs with two actuators are needed, in which case, both drives can be placed at the base.

2.5.5 Workspace Segmentation, Working Modes, and Assembly Modes

We saw that the singularities of Type 2 for some planar parallel mechanisms (and this also applies to some spatial parallel mechanisms) depend on the given working mode of the parallel mechanism. We also observed that the Type 2 singularity loci divide the workspace into segments. Typically, each of these segments corresponds to a different assembly mode. Since Type 2 singularities should be avoided, the *usable* workspace of such a parallel mechanism is limited to only one of these segments which also determines the preferred assembly mode.

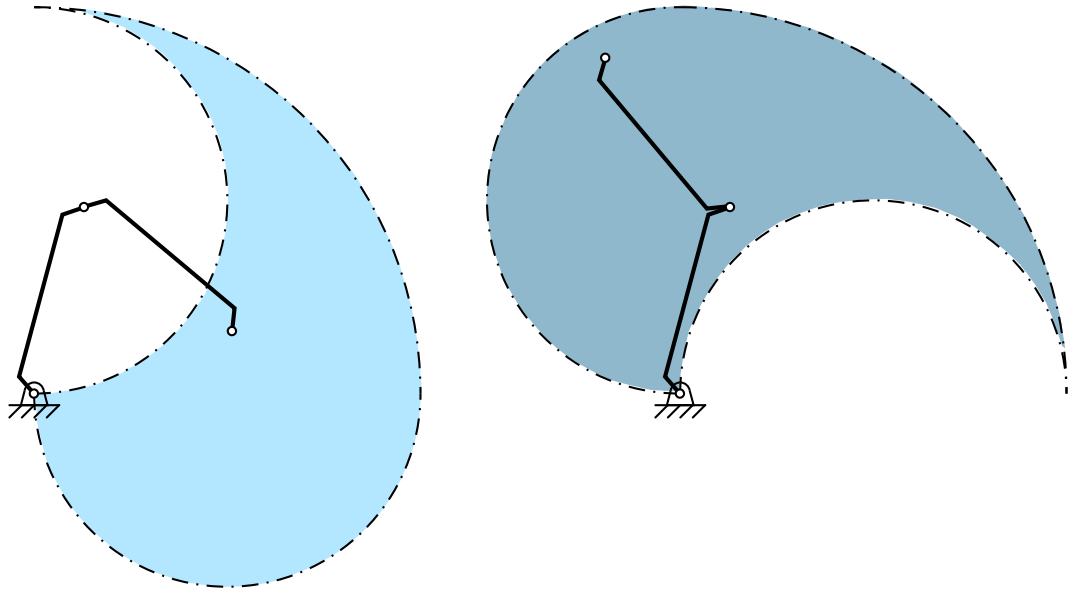

Figure 2.24: Workspace segmentation by working modes in case of mechanical limits on the active joints.

2.5.5.1 Workspace Segmentation Upon Mechanical Limits

In practice, the range of revolute and, especially, prismatic actuators is limited. Therefore, the actual vertex space for a given leg may differ in form and shape. For example, Fig. 2.24 shows the different vertex spaces for each working mode for an $\underline{R}RR$ chain for which the range of the active R joint is only 90°.

Similarly, in practice, mechanical interference may cause further limitation and segmentation of the workspace. For example, Fig. 2.25 shows a particular 3-$\underline{R}RR$ planar parallel mechanism with proximal and distal links of length ℓ, three coinciding base R joints, and two coinciding platform R joints. For clarity, the proximal links are not shown, but instead the common circular track on which all three intermediate R joints move is drawn in green dashed line. The initial assembly of the mechanism imposes that the three intermediate R joints (1, 2, 3) be arranged in a counter-clockwise circular order. The centre of the mobile platform is represented by the diamond symbol. For the zero orientation, we have drawn the two vertex spaces, which are the large dash-dot circles of radius ℓ. Their centres are represented, as usual, by the dot symbol.

The two blue dash-dot-dot circles of radius ℓ correspond to the loci where two adjacent intermediate R joints (1 and 3, or 2 and 3) coincide. The red circle or, rather, parts of it represent the Type 2 singularity loci. The filled region, composed of five subregions, is the part of the workspace where the counter-clockwise order of the

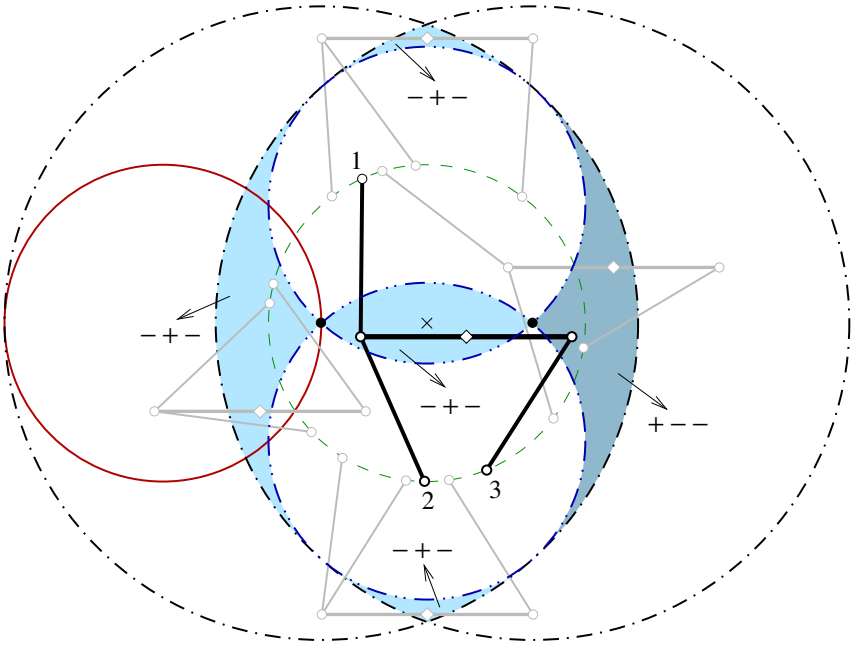

Figure 2.25: Workspace segmentation by working modes for a special 3-$\underline{R}RR$ PPM.

intermediate R joints is preserved. Close inspection reveals that the four left regions correspond to the $\{-,+,-\}$ working mode, while the right-most region corresponds to the $\{+,-,+\}$ branch set.

Note that the constant-orientation workspace, and everything else, for a different orientation ϕ of the mobile platform will be exactly the same as that for $\phi = 0$ but rotated about the centre of the base R-joints (marked with an "$\times$") at an angle ϕ. Therefore, the complete 3D workspace is separated into five disconnected volumes, one of which corresponds to a different working mode.

Thus, in order to augment the *usable* workspace of some parallel mechanisms, without changing the design parameters, we should be able to operate the mechanism in more than one working mode.

2.5.5.2 Optimising Trajectory Through Change of Working Mode

To change the working mode, the mechanism should *pass through* or *bounce off* a Type 1 singularity. Indeed, without attempting to set any formal definition, *passing* through a Type 1 singularity may occur when the centre of the platform R joint of a $\underline{R}PR$ or $\underline{R}RR$ leg passes through the interior vertex space boundary. An example of such a trajectory is presented for an $\underline{R}RR$ chain in Fig. 2.26. (Note that the proximal and distal links may be of different lengths.) For such a trajectory, changing the branch

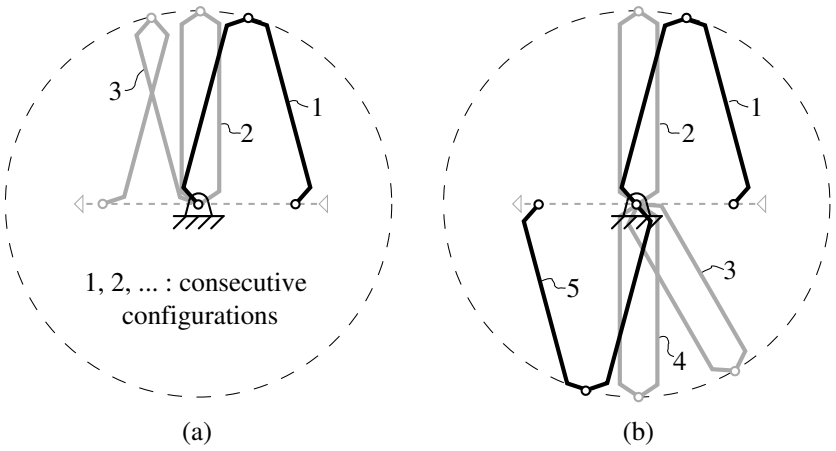

Figure 2.26: Passing through a Type 1 singularity by (a) changing or (b) keeping the branch index.

index of the leg ensures the *minimum-energy* sequence. In fact, for a given platform motion, it may even be impossible to keep the branch index due to power limits in the actuators. The same is true for some point-to-point trajectories, where passing through a Type 1 singularity and changing a branch index is not obligatory but ensures the optimal path. This provides yet another pro for changing working modes.

2.5.5.3 Practical Implications of Changing a Working Mode

In practice, though, changing a branch index in an automated manner is not a trivial task. In fact, in some cases it is not even mechanically feasible due to the limited range of the passive joints (e.g., the U joint in a 6-$\underline{R}US$ parallel mechanism). In planar parallel mechanisms, however, we may assume that this problem does not exist, since passive R joints with no mechanical limits can be easily built. Thus, the main problem is how to switch between two branch indices.

This problem has two implications: (1) how to mechanically force the leg to change its configuration, and (2) how to control the mechanism while at or even close to a Type 1 singularity. And all this should be done at a minimum cost. Thus, the straightforward solution of installing extra actuators at the passive joints is unacceptable. Rather, the solution should be based on a mechanical principle such as the installation of a mechanical device (e.g., a spring) or making use of inertia (Hesselbach et al., 2002). To the best of our knowledge, however, no parallel mechanism that can automatically switch working modes has yet been built.

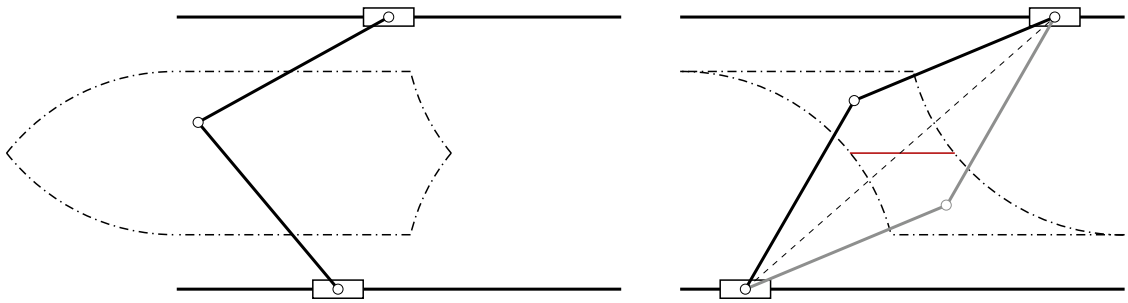

Figure 2.27: Workspace of a $\underline{P}RRR\underline{P}$ PPM in (a) $\{+,-\}$ and (b) $\{-,-\}$ working modes.

2.5.5.4 Changing Working Modes Leads to Type 2 Singularities?

At a recent conference, Hesselbach et al. (2002) reported what seemed to be the first practical implementation of a parallel mechanism that can *indirectly* switch working modes in an automated manner. Their excellent example deserves a close look to conclude our section on workspace segmentation. Yet, this example will only widen the open questions left so far.

Hesselbach et al. (2002) constructed a 2-DOF $\underline{P}RRR\underline{P}$ PPM such as the one shown in Fig. 2.27. For this parallel mechanism, the axes of the P joints are parallel and the ranges of the same are, naturally, limited. The mechanism has four working modes and for each working mode, the workspace and the Type 2 singularity loci are different. Figure 2.27 shows the workspace boundaries, i.e., the Type 1 singularities (in dash-dot line), and the Type 2 singularity loci (in red solid line) for two of the working modes. For the other two working modes, all entities are mirror images.

Note that Type 2 singularities (when the links are aligned) exist in only two of the working modes ($\{+,+\}$ and $\{-,-\}$). In these two working modes, the Type 2 singularity loci, a line segment, separates the workspace into two parts. Each of this parts corresponds to one of the two assembly modes of the mechanism (Fig. 2.27b).

In order to make use of the complete workspace of this mechanism, one should be able to switch among its working modes. In fact, it will be sufficient and necessary to be able to operate in the $\{+,-\}$ and $\{-,+\}$ working modes. Indeed, being able to operate in any other combination of up to three modes excluding the possibility of having both the $\{+,-\}$ and $\{-,+\}$ ones does not lead to any important workspace augmentation. Close inspection reveals, however, that it would be impossible to move from the $\{+,-\}$ to the $\{-,+\}$ working modes without passing through a Type 2 singularity...

This controversial condition is probably a requirement for many other planar parallel mechanisms. We started the section stating that working mode change is advantageous since Type 2 singularity loci are also changed and thus can be avoided for certain trajectories. But now we conclude that to do this change, a Type 2 singularity should be confronted... Of course, we also saw that there are a plethora of other obvious advantages in the ability to switch working modes. But after all, is this possible at all?

Well, Hesselbach et al. (2002) have done it. And instead of changing branch index by branch index and in the process pass through a Type 2 singularity, they have adopted a completely different approach. Instead of fearing the Type 2 singularity, the authors confront it directly using the inertia of the end-effector (at the middle R joint) to switch between ... assembly modes.

With this final example, we will conclude our discussion on working modes. This problematic is certainly of great theoretical and practical importance, yet it is largely unexplored. We saw that the geometric approach based on a local-coordinate formulation (x, y, ϕ) is very helpful for most situations. However, we should admit that a thorough systematic analysis of this problem should be approached by studying the configuration space of the parallel mechanism and relying on a more advanced mathematical techniques such as differential geometric analysis.

Chapter 3

Constraint Analysis of 3-DOF Spatial Parallel Mechanisms

An unorthodox set of rotation angles, referred to by us as the Tilt & Torsion (T&T) angles, has been independently proposed by several authors for use in human body modelling and parallel mechanism analysis. The T&T angles are similar to the ZYZ (ϕ, θ, ψ) Euler angles, except that a fourth clockwise rotation about Z at an angle ϕ is added. These new angles are easier to interpret geometrically and allow simple computation and representation of the 3D orientation workspace and the 2D projected orientation workspace.

This chapter begins by shedding light on the various advantages of these angles, as used in the analysis of spatial parallel mechanisms. Then, we show that the new angles greatly facilitate the geometric analysis of a special class of 3-DOF spatial parallel mechanisms with mixed DOFs: two rotations and one translation. We prove that for this class the last angle is always zero. Hence, using the new angles leads to the simplest kinematic model and reveals the exact type of rotational DOFs.

3.1 Introduction

The need for a geometric approach in the kinematic analysis of spatial parallel mechanisms is even more pronounced than for planar ones. The added dimension spurs an exponential increase in the complexity of the algebraic expressions that govern the motion of the mechanism. An in-depth geometric analysis can significantly reduce the size of these expressions. Furthermore, the essential geometric interpretation of the motion of a mechanism is almost impossible if based purely on the analysis of some algebraic expressions.

The complexity in the analysis of spatial motion is mainly due to the nature of rotations in space which not only requires two more parameters, but is coupled and non-Euclidean. Not surprisingly, then, we commence our endeavour to investigate spatial kinematic geometry with a study of orientation representation.

Representing the orientation of a body in space is a non-trivial problem that has intrigued scientists for centuries. According to Euler's Rotation Theorem, a rigid body can be guided into any orientation in space by a single rotation. The *variable* axis and angle of this rotation can be used to parameterise the possible body orientations—an idea that leads to the use of quaternions and Rodrigues parameters to describe orientation (Murray et al., 1994). However, it is often much more practical to generate the new orientation of the body using one or more rotations about *constant* axes, such as the reference frame axes. Then, we can describe body orientation by only specifying the angles of the rotations, in analogy to the single angle that describes the orientation of a shape in the plane.

In general, three rotations about some of the coordinate axes are needed to bring the body into an arbitrary orientation. The angles of these rotations are referred to as *Euler angles*, and since Leonard Euler first considered them in his *Theoria motus corporum solidorum*, these three parameters have provided the most popular description of rigid body orientation.

The coordinate transformation associated with a change of orientation is given by a 3×3 proper orthogonal rotation matrix, $\mathbf{R}$. If $\mathbf{p}$ is a vector whose coordinates are expressed in the fixed frame, $Oxyz$ (the *base frame*), and $\mathbf{p}'$ is the same vector expressed in the rotated body frame, $O'x'y'z'$ (the *mobile frame*), then $\mathbf{p} = \mathbf{R}\mathbf{p}'$. When $\mathbf{R}$ represents a rotation at an angle α about a coordinate axis it has a well known form:

$$\mathbf{R}_x(\alpha)=\begin{bmatrix}1 & 0 & 0\\ 0 & \cos\alpha & -\sin\alpha\\ 0 & \sin\alpha & \cos\alpha\end{bmatrix},\ \mathbf{R}_y(\alpha)=\begin{bmatrix}\cos\alpha & 0 & \sin\alpha\\ 0 & 1 & 0\\ -\sin\alpha & 0 & \cos\alpha\end{bmatrix},\ \mathbf{R}_z(\alpha)=\begin{bmatrix}\cos\alpha & -\sin\alpha & 0\\ \sin\alpha & \cos\alpha & 0\\ 0 & 0 & 1\end{bmatrix}.$$

To describe orientation via Euler angles is to perform a single arbitrary rotation as a pre-chosen sequence of coordinate-axis rotations, i.e., to express any $\mathbf{R}$ as an ordered product of three matrices of the above form. Since matrix multiplications do not commute, the order is important. There are twelve different sequences of the three rotations, and hence, there can be twelve Euler-angle conventions: *XYZ*, *XZY*, *YXZ*, *YZX*, *ZXY*, *ZYX*, *XYX*, *XZX*, *YXY*, *YZY*, *ZXZ*, and *ZYZ*.

For example, using the *XYZ* convention, $\mathbf{R}=\mathbf{R}_x(\alpha_x)\mathbf{R}_y(\alpha_y)\mathbf{R}_z(\alpha_z)$. In this expression, $\mathbf{R}$ is decomposed as an ordered product of three rotation matrices. However, there are multiple interpretations of the actual physical sequence of rotations that this product represents. When a product of two matrices is read *from right to left* the two rotations are performed, in that order, as if they are given in the base frame. Equivalently, the two factors can be performed *from left to right* but then they are rotations about axes in a frame attached to the body. For example, $\mathbf{R}$ can be achieved by executing the rotations about the fixed Oz, Oy, and Ox. Equivalently, the body can be rotated about its own *body frame* axes: first about the original Ox axis, next about the *new* Oy axis (now at an intermediate location y^*) and then about the final z' axis.

The numerous possible conventions and their multiple interpretations have led to a certain confusion in the use of the term "Euler angles." Different texts use different conventions, yet the authors often assume that their chosen variant is the "standard" one, and fail to clearly describe the axes used or the order of the rotations. Sometimes, other proper names are used to describe the parameters, such as *Fick angles* (*ZYX*) or *Helmholtz angles* (*YZX*), and to complicate things even further some authors use left-handed reference frames.

Fortunately, standard practices in the use of Euler angles have been established in the different fields. For example, most physics textbooks use the *ZXZ* convention and refer to the corresponding three angles as *precession*, *nutation*, and *spin*. Aeronautical engineers generally use the *XYZ* convention and refer to the three angles as *bank*, *attitude*,, and *heading*, or, more commonly, *roll*, *pitch*, and *yaw*. The same convention is also used in the automotive and machine tool industries. In robotics, the term "Euler angles" usually refers to the *ZYZ* convention.

The use of different conventions to model different problems is not (entirely) a matter of personal preference or arbitrary choice. It is determined by the type of coordinate frame used in the field and the nature of a typical displacement in the studied system. Conventions of the roll-pitch-yaw type, with three different axes, are suitable when small rotations occur frequently, while the use of only two axes (as in precession-nutation-spin conventions) gives a clearer geometric picture of an orientation defined by an arbitrary set of Euler angles.

Parallel kinematic machine (PKM) terminology and notation is usually borrowed from the robotics and machine tool industries. However, neither the ZYZ nor the roll-pitch-yaw angles used in the two fields are suitable to become a standard for describing PKM platform orientation. In what follows, we make clear the important advantages of a relatively new, modified set of angles that cannot be classified into any of the above mentioned categories of orientation representation.

3.2 The Tilt-and-Torsion Angles

Various 6-DOF parallel mechanism applications do not require the rotational degree of freedom about the mobile z' axis. For example, hexapods used in telescope secondary mirrors or as satellite dish bases have an axisymmetric mobile platform. PKMs are also usually equipped with an axisymmetric tool along their mobile z'-axis, and so the rotation of the mobile platform about this axis is irrelevant. Furthermore, the mobile platform is usually shaped as an equilateral triangle, a semiregular hexagon, or another non-rectangular shape, and exhibits no particular symmetry about any pair of orthogonal axes that could be chosen as the mobile x' and y' axes.

Such observations have led to the idea of a modified set of orientation angles (Bonev and Ryu, 1999a), particularly well suited to the specific symmetries of some hexapods. These parameters were also introduced by Huang et al. (1999) and Wang (1999). In the process of editing this text, we ran across a thread that lead us to the much earlier origins of the angles. It turns out that the angles have been proposed by Korein (1984) in his Ph.D. dissertation under the name *halfplane-deviation-twist* angles. The author proposed the set due to its indisputable advantages in modelling the limits of human body joints. At present, the angles seem to be somewhat popular for computer animation of articulated bodies (Grassia, 1998; Baerlocher and Boulic, 2000), known as *swing-and-twist* representation.

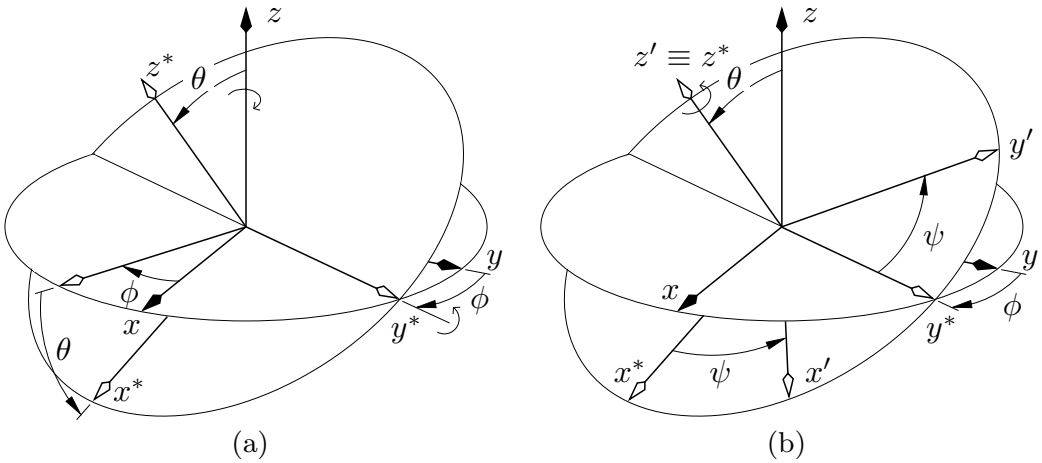

Figure 3.1: The successive rotations that define the ZYZ Euler angles: (a) precession and nutation, (b) spin.

The new angles were arrived at by a modification of a classic two-axis precession-nutation-spin convention, such as *ZYZ*. In *ZYZ*, the three Euler-angle rotations are defined as follows. First, rotate about Oz until the vertical Oxz plane incorporates Oz'. Then, with a nutation about the new Oy axis, guide Oz into Oz', Fig. 3.1(a). Finally, spin the body about its z' axis until the desired orientation is reached, Fig. 3.1(b). The angles of these three coordinate-axis rotations are ϕ, θ, and ψ, respectively, precession, nutation, and spin.

One can observe that the process, as described in the previous paragraph, has two distinct stages. First, make Oz coincide with Oz'. Then, spin to the final orientation. The newly proposed parameterisation uses the same two stages. However, unlike the classic convention, the goal of the first stage, i.e. the guiding of Oz into Oz', is achieved directly, *by a single rotation* about a horizontal axis, a, Fig. 3.2(a). In other words, Oz is *tilted* to its final location by the shortest path, and this movement is not preceded by a precession.

Two points should be well understood. First, the tilt axis, a, *is not* a body coordinate axis, at any time. Secondly, at the end of the tilt, when the Oz axis reaches its final destination Oz', the body will be oriented differently as compared to the end of the classic precession-nutation sequence. Therefore, the final spin, σ, needed to achieve the desired $Ox'y'z'$ orientation (Fig. 3.1b) will differ from the spin, ψ in the conventional *ZYZ* Euler sequence. For this reason, we must use a different name and notation for the angle of this final rotation: we can call it the *endspin* and will denote it by σ as opposed to the (most) common ψ for the classic *spin* angle. More conventionally, we can refer

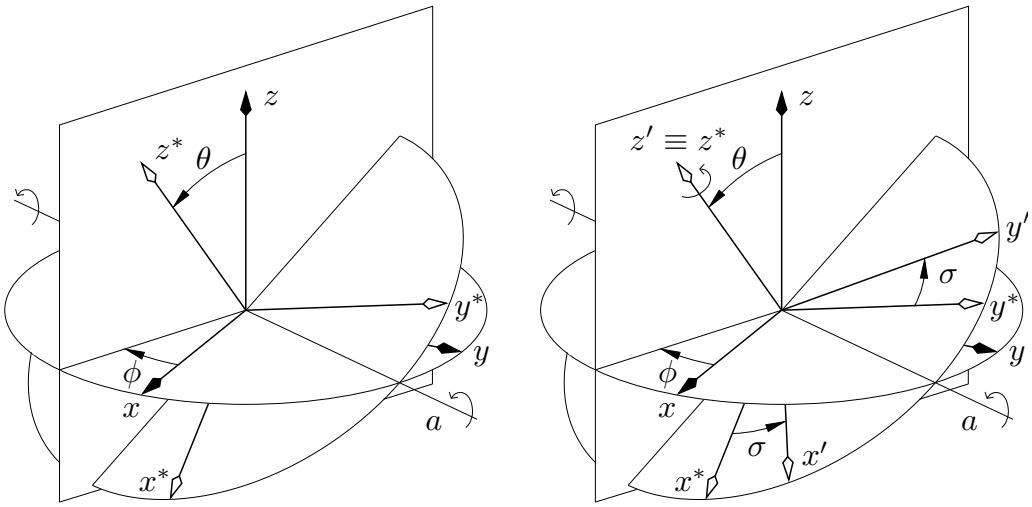

Figure 3.2: The successive rotations that define the T&T angles: (a) tilt, (b) torsion.

to the endspin as the *torsion*. This last term describes well the physical effect of σ on a PKM's configuration and we will use it throughout this thesis. However, this word should be handled with caution since, in the literature, "torsion" is used extensively and with a variety of meanings.

Rather than decompose the rotation matrix $\mathbf{R}$ into three coordinate-axis rotations, $\mathbf{R} = \mathbf{R}_z(\phi)\mathbf{R}_y(\theta)\mathbf{R}_z(\psi)$, we have used *two* rotations, $\mathbf{R} = \mathbf{R}_a(\theta)\mathbf{R}_z(\sigma)$. The axis of the first is a variable horizontal axis, and we need an angle, ϕ, to locate it. This angle will have the same value as the precession angle in the *ZYZ* convention. However, it has a different geometrical interpretation. It is no longer the angle of one of the performed rotations, but rather an indicator of the location of the tilt axis a. More precisely, ϕ is the angle between Ox and the projection of Oz' in Oxy, i.e., it defines the vertical *tilt plane* (perpendicular to a, Fig. 3.2a) in which Oz must move to merge with Oz'. In view of its new role we will refer to ϕ as the *azimuth*. The angle θ, between Oz and Oz', will be denoted as the *tilt* (and is equal to the classic nutation angle). Thus, the new orientation angles are azimuth, tilt and torsion, (ϕ, θ, σ), and we will refer to this parameterisation as the *Tilt-and-Torsion* (T&T) angles.

As we pointed out, the tilt rotation is not the same as precession-and-nutation, $\mathbf{R}_a(\theta) \neq \mathbf{R}_z(\phi)\mathbf{R}_y(\theta)$. However, it can be seen that $\mathbf{R}_a(\theta) = \mathbf{R}_z(\phi)\mathbf{R}_y(\theta)\mathbf{R}_z(-\phi)$, i.e., to achieve the tilt $\mathbf{R}_a(\theta)$ one needs to spin back at $-\phi$ after the precession and nutation are completed. Therefore,

$$\mathbf{R} = \mathbf{R}_a(\theta)\mathbf{R}_z(\sigma) = \mathbf{R}_z(\phi)\mathbf{R}_y(\theta)\mathbf{R}_z(-\phi)\mathbf{R}_z(\sigma) = \mathbf{R}_z(\phi)\mathbf{R}_y(\theta)\mathbf{R}_z(\sigma - \phi). \tag{3.1}$$

Thus,

$$\mathbf{R}(\phi,\theta,\sigma) = \begin{bmatrix} c_\phi c_\theta c_{\sigma-\phi} - s_\phi s_{\sigma-\phi} & -c_\phi c_\theta s_{\sigma-\phi} - s_\phi c_{\sigma-\phi} & c_\phi s_\theta \\ s_\phi c_\theta c_{\sigma-\phi} + c_\phi s_{\sigma-\phi} & -s_\phi c_\theta s_{\sigma-\phi} + c_\phi c_{\sigma-\phi} & s_\phi s_\theta \\ -s_\theta c_{\sigma-\phi} & s_\theta c_{\sigma-\phi} & c_\theta \end{bmatrix} \tag{3.2}$$

where $c_\phi \equiv \cos\phi$, $s_\phi \equiv \sin\phi$, etc.

From the above, we see that the T&T angles (ϕ,θ,σ) are equivalent to the ZYZ Euler angles $(\phi,\theta,\sigma-\phi)$, i.e., the spin angle ψ has been replaced with $\sigma-\phi$. We will see later that this seemingly slight change leads to significant simplifications in the study of some spatial parallel mechanisms.

One of the characteristics of Euler angles, in any definition, is that any orientation can be represented by at least two triplets of angles. To avoid this, we set the ranges of the azimuth, tilt, and torsion as $\phi \in (-\pi,\,\pi]$, $\theta \in [0,\,\pi)$, and $\sigma \in (-\pi,\,\pi]$, respectively.

3.3 Representations of the Orientation Workspace

The *orientation workspace* of a parallel mechanism is the set of all practically feasible orientations of the mobile platform, for a given position. When the parallel mechanism has three rotational freedoms, the graphical representation of the orientation workspace becomes problematic due to the coupled and non-Euclidean nature of rotation as well as the inherent singularity of any 3-dimensional parameterisation of orientation. However, the T&T representation allows for a very intuitive and compact visualisation.

In the case of T&T angles as well as ZYZ Euler angles, there is a singularity at $\theta = 0$. Indeed, for such orientations, the choice of ϕ is arbitrary. However, at such a singularity, the orientation of the mobile frame is defined by $\phi+\psi$ in the ZYZ convention, while if using T&T angles, it is measured simply by σ. Similarly, for both sets of angles, there is a singularity at $\theta = \pi$. At this singularity, the orientation of the mobile frame is defined by $\phi-\sigma$ in the ZYZ convention, while if using T&T angles, it is measured by $2\phi-\sigma$. However, for most applications $\theta = \pi$ is beyond the feasible range of motion.

The $\theta = 0$ T&T representational singularity is of the same nature as the singularity of a system of cylindrical coordinates (r,ϕ,h) occurring for zero-radius $(r = 0)$. For this reason, it is convenient to map the T&T parameters using such a cylindrical system

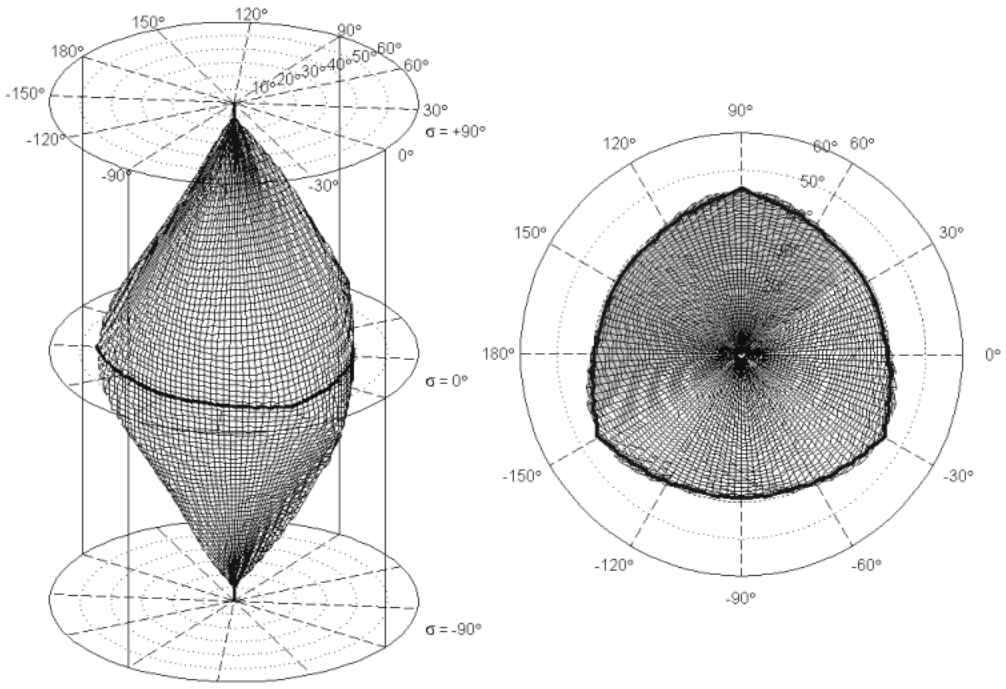

Figure 3.3: Example for the orientation workspace of a 6-$\underline{P}US$ parallel manipulator.

while identifying the tilt θ with the radius r and the torsion σ with the height h. This yields a bijective map of the orientation workspace into a vertical cylinder in 3-dimensional space. This representation was introduced in (Bonev and Ryu, 1999a).

The feasible orientations of many existing parallel mechanisms have an inherent symmetry about zero torsion. It is for this fundamental reason that the image of the cylindrical mapping is typically a compact almond-shaped *single* volume giving a very intuitive and faithful representation of the size and symmetry of the orientation workspace. An example of this workspace is given in Fig. 3.3.

For many PKM applications, we are interested only in the set of all feasible directions of the mobile z'-axis, i.e., the set of all attainable pairs of azimuth and tilt. This set was defined in (Bonev and Ryu, 1999a) as the *projected orientation workspace* due to the fact that in the cylindrical coordinate system of our choice, this 2D workspace is simply the projection of the 3D orientation workspace onto a horizontal plane. When using T&T angles, the projected orientation workspace can be obtained with relative ease using a computationally intensive discretisation method (Bonev and Ryu, 1999a; Wang, 1999). However, with only a fraction of this computational cost one can obtain a cross-section of the 3D orientation workspace for a given σ (Bonev and Ryu, 1999a; Huang et al., 1999). Due to symmetry, the cross-section $\sigma = 0$ gives a particularly

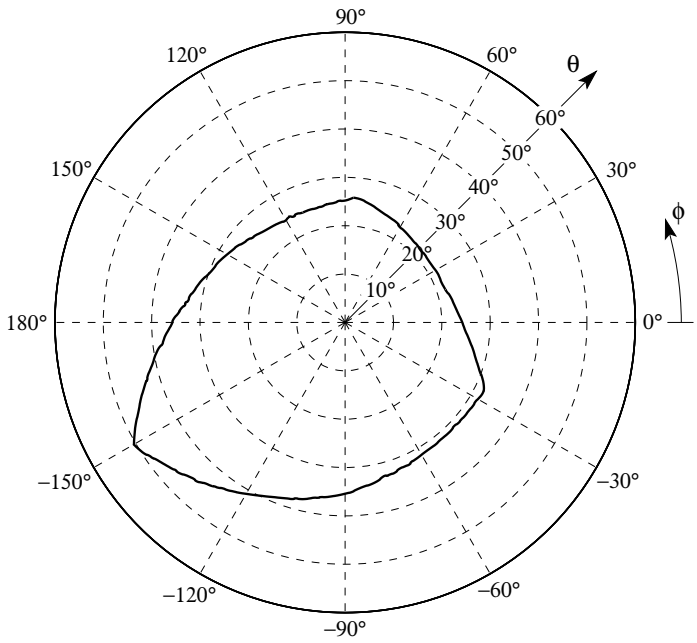

Figure 3.4: Example for the approximated projected orientation workspace.

good approximation of the total projected orientation workspace, although not necessarily exact as pointed out in (Bonev and Ryu, 1999a). As a spin-off benefit, this fact provides a straightforward solution to the redundancy problem of hexapods with axisymmetric tools, namely, eliminate the redundant rotational freedom by fixing $\sigma = 0$, with minimal loss of workspace.

An example of the *approximated* projected orientation workspace is shown in Fig. 3.4. Not only can this workspace be computed quickly but it can also be shown in a very intuitive representation that may be easily displayed on the low-resolution LCD panel of a PKM or any other hexapod device.

These highly accurate workspace representations are in stark contrast to current practices of hexapod manufacturers, for example. Most existing specifications list ambiguous "±" ranges for the roll, pitch, and yaw as if these angles always have the same (decoupled) symmetrical ranges for every configuration. Instead, when using the T&T angles, one needs only specify a typical value of the maximal tilt angle and, if necessary, a typical torsion range.

Not surprisingly, these angles are used for computer animation of human bodies for exactly the same important reason—the angles represent the range of motion in the most natural manner. Astonishingly, however, the analogue between the human body and some spatial parallel mechanisms goes even further...

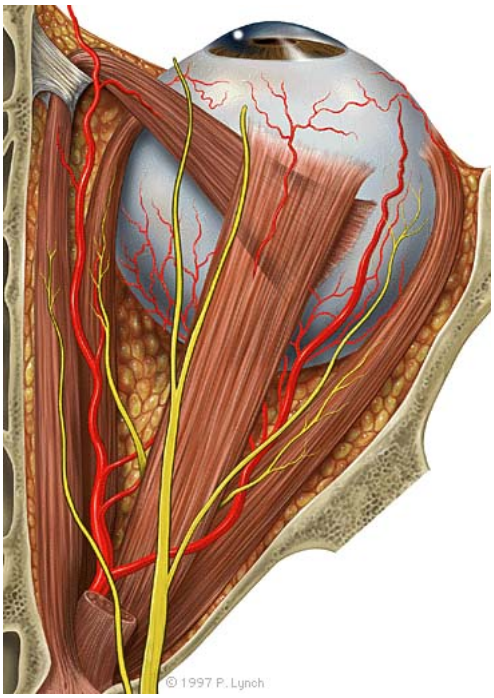

Figure 3.5: The human eye is a zero-torsion spherical parallel mechanism actuated by tendons (illustration courtesy of Patrick J. Lynch, Yale University School of Medicine).

3.4 Zero-Torsion 3-DOF Spatial Parallel Mechanisms

As we pointed out in the previous section, parallel mechanisms with full rotational capability (3 rotational DOFs), tend to exhibit a natural symmetry with respect to zero-torsion. It is, therefore, not very surprising that many parallel mechanism designs with restricted rotational freedoms (two rotational DOFs) are, in fact, with zero torsion for all configurations.

One such "mechanism" is the *human eye* (Fig. 3.5). According to Listing's Law (Helmholtz, 1867), known in ophthalmology since the 19th century, all possible orientations of a *healthy* eyeball can be obtained from the primary gaze by a single tilt, i.e., a rotation whose axis is in a plane (the Listing plane) normal to the primary gaze. In other words, ocular motions preserve zero torsion, $\sigma = 0$, in the T&T convention. Please be warned, that the term "ocular torsion" is often used in the medical literature as the twisting of the eye as *perceived* during a frontal examination (which is not always zero), although some authors do use the term as a synonym of the T&T endspin, σ. (Confusion in rotation terminology is not restricted to the engineering domains.)

The human eye is essentially a 3-DOF parallel mechanism actuated by tendons (muscles). It is constrained to rotate with zero-torsion by the (healthy) brain, i.e., by its "controller." However, there are other human joints that are mechanically constrained to rotate with zero torsion. One such zero-torsion "mechanism" is the *sterno-clavicular joint* which articulates the clavicle by its proximal end onto the sternum (Korein, 1984). This is the joint that is used to shrug the shoulders. We should point out, however, that the sterno-clavicular joint is not always modelled as a zero-torsion mechanism. For example, in a recent publication (Lenarčič et al., 2002), the authors have modelled the human shoulder complex as a 4-DOF parallel mechanism allowing all three rotations and one translation. Another zero-torsion "parallel mechanism" is the *human wrist* (Canfield et al., 1996) which will be studied in Section 3.4.1, as the first member of the class of zero-torsion mechanisms.

Back to engineering, there are multiple examples of constrained spatial parallel mechanisms with three identical legs, each with 5 DOFs, and only 3 DOFs of the platform. In many cases, the platform has one translational and two rotational freedoms, and very frequently the allowed orientations are such that the torsion of the platform remains zero.

Due to the use of traditional orientation parameterisations, these mechanisms have not yet been recognised as a separate class, and their common properties have not been investigated. A better known subclass of the zero-torsion family consists of the so-called *constant-velocity couplings* of intersecting shafts. The work of Hunt (1973) provides an in-depth theory of such constant-velocity transmissions.

Below, we outline the analysis of three popular zero-torsion parallel mechanisms, of which the first is a constant-velocity coupling. A fourth example can be found in (Zlatanov et al., 2002b). Once again, Hunt (1983) was the first to propose these three designs for use as parallel manipulators. While multiple other works on the three mechanisms have already been published, this is the first time when these parallel mechanisms are recognised as members of the same $\sigma = 0$ class and studied via a common methodology. Moreover, we obtain explicit relationships of the platform centre coordinates and the two independent orientation parameters (ϕ, θ). The further kinematic analysis of these mechanisms is much simplified due to the particularly straightforward position-orientation relationships. These expressions become much more complicated when obtained with another Euler-angle convention.

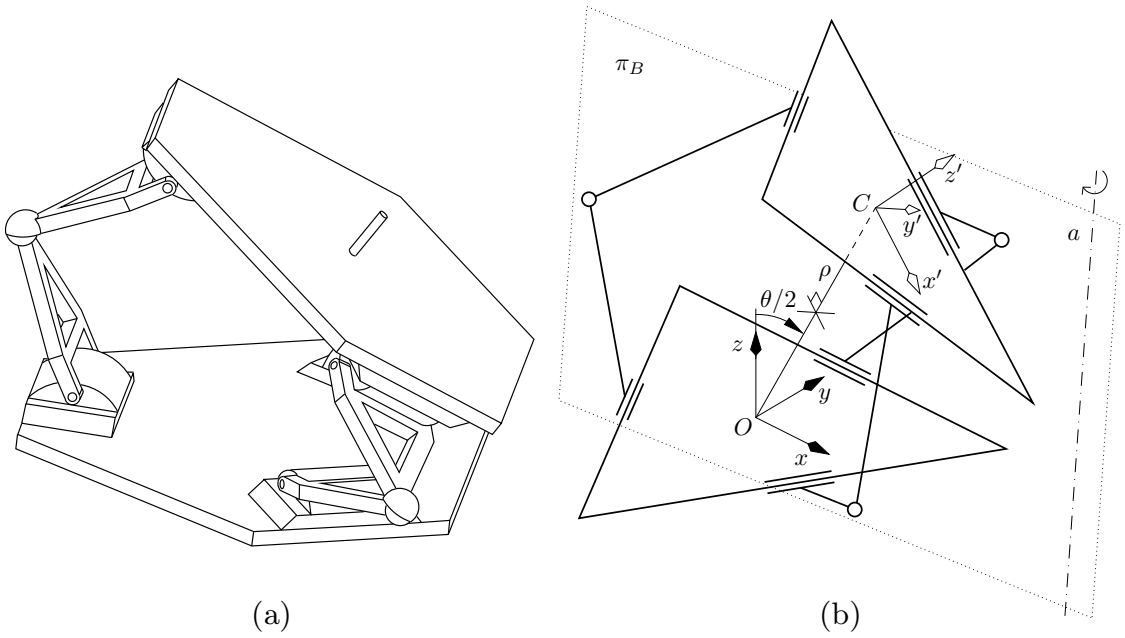

Figure 3.6: (a) A 3-*RSR* 3-DOF spatial symmetrical parallel mechanism and (b) its kinematic geometry.

3.4.1 3-*RSR* 3-DOF Spatial Parallel Mechanisms

Our simplest example is the earliest constant-velocity coupling, known as *Clemens joint* or *reflected tripod* (Hunt, 1973). It is composed of two bodies connected by three *RSR* chains, so that, at any moment, the mechanism exhibits complete symmetry with respect to the plane, π_B, passing through the S joints, the *bisecting plane*, (Fig. 3.6).

The reflected tripod in its actuated form, i.e., the 3-$\underline{R}SR$ parallel mechanism, has been studied extensively in the literature (Peruzzini et al., 1995; Canfield et al., 1996; Dunlop and Jones, 1997; Hertz and Hughes, 1998). The mechanism, with slight modifications, has been used as a haptic device (Peruzzini et al., 1995), a robotic wrist (Canfield et al., 1996), and a satellite tracking mechanism (Dunlop and Jones, 1996), and even patented (Lambert, 1987; Canfield et al., 1997). Yet the physical nature of the feasible orientations is not revealed in any of these publications.

The kinematic geometry of the reflected tripod is trivial. In any configuration, π_B intersects the planes Oxy and $Cx'y'$ at a common line (Fig. 3.6b). Let us choose a directed axis a along this line, with a positive moment about both Oz and Cz'. Let the angle between Ox and a be $\phi + \pi/2$. Due to symmetry, the orientation of the mobile frame is such that it could be obtained by rotating the base frame about the a axis at some angle θ. It is easy to conclude that the orientation of the mobile platform is

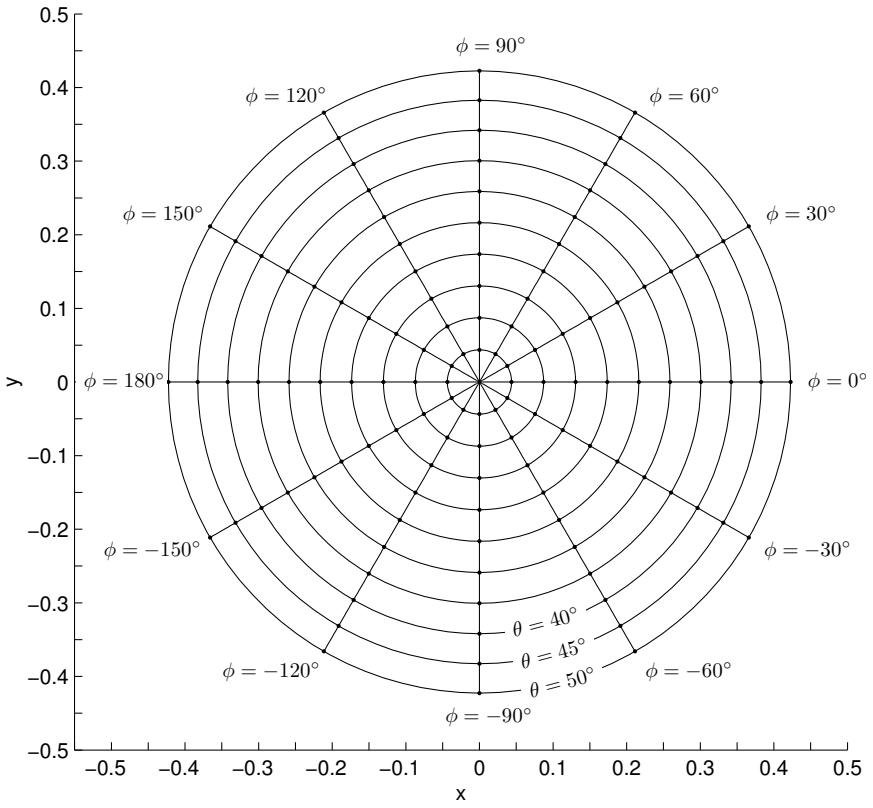

Figure 3.7: Horizontal offset as function of orientation for 3-*RSR* mechanisms.

described by the angles ϕ and θ which happen to be exactly the azimuth and tilt angles of the T&T convention, while the torsion σ is obviously zero.

The plunging motion (the translational freedom) of the mobile platform, for any given orientation is parallel to the segment OC, whose length is denoted by ρ. The pose of the mobile platform is completely defined by ϕ, θ, and ρ. The orientation is (ϕ, θ, $\sigma = 0$), and for the centre C, we have:

$$x = \rho \cos\phi \, \sin\theta/2, \tag{3.3}$$

$$y = \rho \sin\phi \, \sin\theta/2, \tag{3.4}$$

$$z = \rho \cos\theta/2. \tag{3.5}$$

To clearly understand the coupling between the position and orientation of the mobile platform, Fig. 3.7 shows the curves for x and y for constant ϕ or θ, and $\rho = 1$.

Note how elegantly T&T angles describe the kinematics of the 3-*RSR* parallel mechanism. Any other set of Euler angles would have led to larger expressions. Moreover, the T&T angles put into evidence the exact geometric nature of the DOFs.

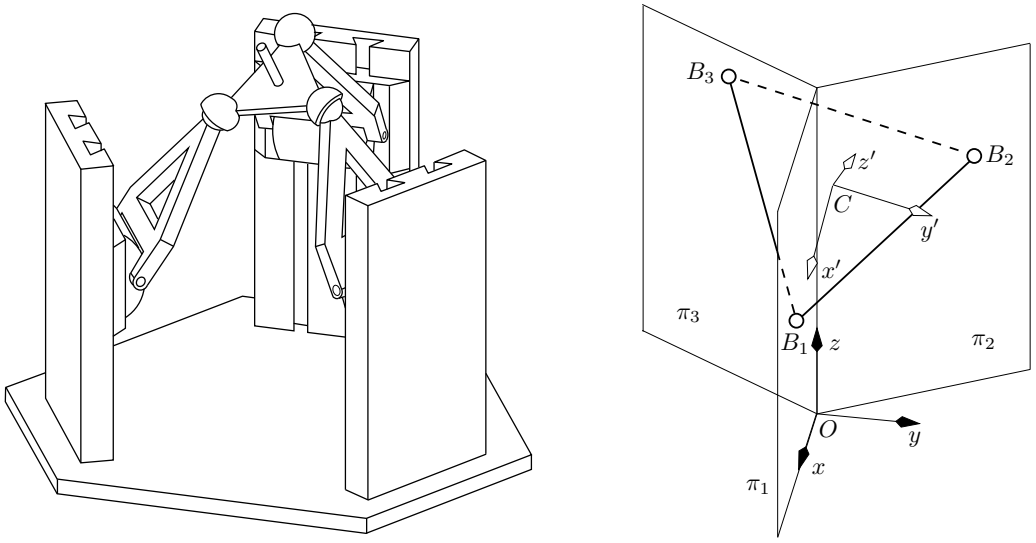

Figure 3.8: (a) A 3-$\underline{P}RS$ 3-DOF spatial parallel mechanism and (b) the kinematic geometry of a general 3-*[PP]S* parallel mechanism.

3.4.2 3-*[PP]S* 3-DOF Spatial Parallel Mechanisms

Undoubtedly, the most popular examples of zero-torsion parallel mechanisms belong to this group. Each leg of these mechanisms has a 2-DOF chain, equivalent to two coplanar translations, followed by an S joint. The vertical planes in which the three equidistant S joints move are intersecting at a common line at 120° angles (Fig. 3.8).

There is abundant literature on this group of mechanisms. The 3-$R\underline{P}S$ architecture has been analysed in (Lee and Shah, 1988; Buruncuk and Tokad, 1999; Huang and Wang, 2000), two different designs of 3-$\underline{P}RS$ robots have been studied in, respectively, (Carretero et al., 2000) used for telescope focusing, and (Chang et al., 2000) used as a machine tool—a design, best known through the patented *Z3 Head* by DS Technologie (Wahl, 2000), Fig. 3.8(a)—, and finally a 3-$\underline{R}RS$ manipulator has been investigated in (Li et al., 2001). Of all these publications, only one, (Buruncuk and Tokad, 1999), seems to identify the exact nature of the interdependence of the orientation parameters and its geometric significance.

Let the three equidistant S joint centres, denoted by B_i (not shown), lie on a circle of radius 1, i.e.,

$$\mathbf{r}'_{CB_1} = \begin{bmatrix} 1 \\ 0 \\ 0 \end{bmatrix}, \quad \mathbf{r}'_{CB_2} = \begin{bmatrix} \cos(2\pi/3) \\ \sin(2\pi/3) \\ 0 \end{bmatrix}, \quad \mathbf{r}'_{CB_3} = \begin{bmatrix} \cos(4\pi/3) \\ \sin(4\pi/3) \\ 0 \end{bmatrix}, \tag{3.6}$$

where $\mathbf{r}'_{CB_i}$ are the vectors along CB_i expressed in the mobile frame. We, then, express the coordinates of these three points in terms of the coordinates of the platform centre, x, y, z, and the three T&T angles:

$$\mathbf{r}_{OB_i} = \mathbf{R}\mathbf{r}'_{CB_i} + \begin{bmatrix} x \\ y \\ z \end{bmatrix} \equiv \begin{bmatrix} x_{OB_i} \\ y_{OB_i} \\ z_{OB_i} \end{bmatrix}, \tag{3.7}$$

for $i = 1, 2, 3$, where $\mathbf{R}$ is the rotation matrix defined by Eq. (3.2). Then, we write the three linear equations that constrain the S joint centres in the three vertical planes (Fig. 3.8b):

$$y_{OB_1} = 0, \tag{3.8}$$

$$\cos(2\pi/3)y_{OB_2} - \sin(2\pi/3)x_{OB_2} = 0, \tag{3.9}$$

$$\cos(4\pi/3)y_{OB_3} - \sin(4\pi/3)x_{OB_3} = 0. \tag{3.10}$$

Since z is obviously an independent coordinate, it is of no surprise that, after substitution of y_{OB_1}, x_{OB_2}, y_{OB_2}, x_{OB_3}, and y_{OB_3} from Eqs. 3.7, none of the above three equations contains that variable:

$$y + q_{1,3} = 0, \tag{3.11}$$

$$-\frac{\sqrt{3}}{2}x - \frac{1}{2}y + q_{2,3} = 0, \tag{3.12}$$

$$\frac{\sqrt{3}}{2}x - \frac{1}{2}y + q_{3,3} = 0, \tag{3.13}$$

where $q_{1,3}$, $q_{2,3}$, and $q_{3,3}$ are functions of the three T&T angles. Therefore, in order to have a solution for x and y, the three linear equations must be linearly dependent. Obviously, any two of these equations are linearly independent. Hence, for any feasible orientation of the mobile platform, there is a unique solution for (x, y).

Let $\mathbf{Q}$ be the coefficient matrix for the above three equations, i.e.,

$$\mathbf{Q} = \begin{bmatrix} 0 & 1 & q_{1,3} \\ -\frac{\sqrt{3}}{2} & -\frac{1}{2} & q_{2,3} \\ \frac{\sqrt{3}}{2} & -\frac{1}{2} & q_{3,3} \end{bmatrix}. \tag{3.14}$$

For these equations to be linearly dependent, the matrix $\mathbf{Q}$ should be singular, i.e.,

$$\det \mathbf{Q} = \frac{3\sqrt{3}}{4} \sin\sigma(\cos\theta + 1) = 0. \tag{3.15}$$

From the above, we conclude that as long as $\theta = \pi$, i.e., the mobile platform is upside down, the parallel mechanism can be assembled. If we substitute $\theta = \pi$ in Eqs. (3.11–3.13) and solve any two of them, we obtain the following for the feasible motion of the mobile platform centre:

$$x = -\cos(2\phi - \sigma), \tag{3.16}$$

$$y = \sin(2\phi - \sigma). \tag{3.17}$$

Indeed, as we already mentioned, the T&T angles have a singularity at $\theta = \pi$ at which the orientation of the mobile platform is defined by $2\phi - \sigma$. Thus, when $\theta = \pi$, the mobile platform acquires a new degree of freedom. Figure 3.9 shows the horizontal upside down mobile platform. Simple geometrical analysis shows that the three normals to the points B_i intersect at one point, H. The feasible poses of the platform in every horizontal plane form a one-parameter set obtained by rolling the circle, c_m, drawn around the platform triangle, on the inside of a fixed circle, c_f, twice the radius of c_m and centred at the point of intersection of the three planes π_i and the mobile platform plane. Hence, for one complete counter-clockwise tour of point C along the inner circle of radius 1, the mobile platform makes exactly one clockwise rotation. This planar motion is the so-called *Cardanic movement* (Hunt, 1978).

In other words, in general, the redundant motion with locked actuators will be a screw motion, more precisely, a linear combination of a rotation through H and the vertical translation (Zlatanov et al., 2002a).

Configurations like this were recently identified as a new type of singularity, associated with constrained parallel mechanisms, named *constraint singularity* (Zlatanov et al., 2002a). At such a singular configuration of a n-DOF mechanism ($n < 6$), both the mechanism as a whole and the mobile platform have at least $n + 1$ DOFs. And we are pleased to note that constraint singularities were found and analysed due to

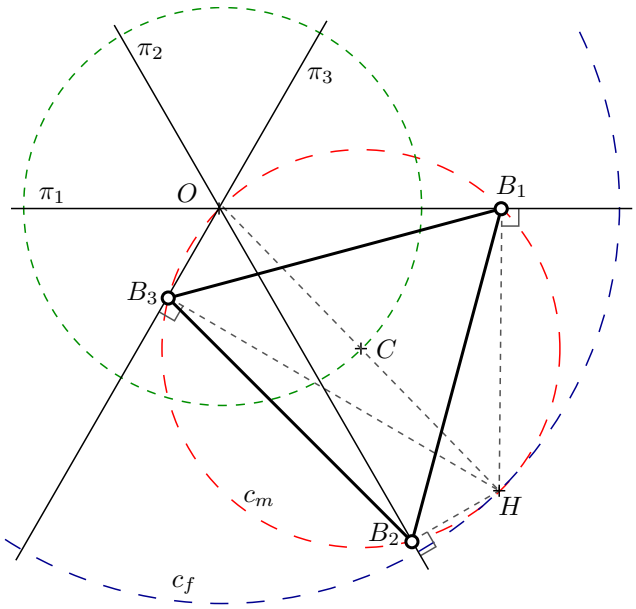

Figure 3.9: Constraint singularities of a 3-*[PP]S* parallel mechanism.

the application of the powerful geometric method of screw theory and basic geometric constructions such as the one shown in Fig. 3.9.

Now, disregarding the not-so-practical case of $\theta = \pi$, Eq. (3.15) leads us to the only remaining possibility: $\sigma = 0$ or $\sigma = \pi$. If, again, we substitute $\sigma = 0$ or $\sigma = \pi$ in Eqs. (3.11–3.13), and solve any two of them, we obtain the following for the feasible motion of the mobile platform centre:

$$x = \eth \frac{1}{2} \cos 2\phi (\cos\theta - 1), \tag{3.18}$$

$$y = -\eth \frac{1}{2} \sin 2\phi (\cos\theta - 1), \tag{3.19}$$

where $\eth = 1$ for $\sigma = 0$ and $\eth = -1$ for $\sigma = \pi$. These two modes of operation are *separated* by the constraint singularity $\theta = \pi$. Indeed, as shown in (Zlatanov et al., 2002a), constraint singularities generally separate the different modes of operation of constrained parallel mechanisms. While both modes exist in theory, in practice the tilt angle θ will be quite limited, and the actual prototype will be confined to operate in only one of the modes. Whether this mode corresponds to $\sigma = 0$ or $\sigma = \pi$ is only a matter of mobile reference frame choice. Since, normally, the mobile and base frames are selected to coincide at $\theta = 0$, we are automatically in the $\sigma = 0$ mode.

In industry, zero-torsion parallel mechanisms are used as *plunge-and-tilt* mechanisms with axisymmetric tools. Thus, the lack of knowledge that some torsion angle

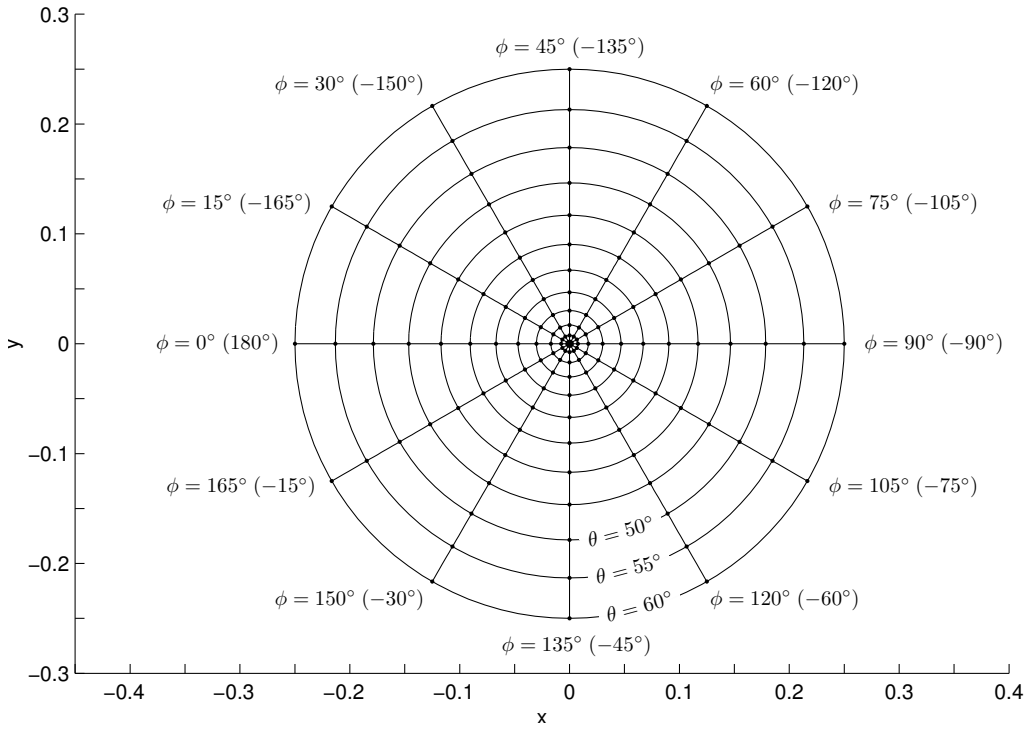

Figure 3.10: Horizontal offset as function of orientation for 3-*[PP]S* mechanisms.

remains zero does not prevent from successfully operating the mechanism. However, the knowledge of the exact motion of these mechanisms is undoubtedly essential at the design stage and certainly helpful for the development of the control algorithms, since expressions would be more compact. The fact that the centre of the mobile platform does not always lie on the central z axis is considered as unwanted motion and should be compensated (through an XY stage). This unwanted motion should, therefore, be well understood.

Parallel mechanisms of type 3-*[PP]S* have an offset, υ, from the central axis that is entirely dependent on the tilt of the mobile platform:

$$\upsilon = \frac{1}{2}(1 - \cos\theta). \tag{3.20}$$

Recall that for the previous class of zero-torsion parallel mechanisms, constant-velocity joints, the offset was also dependent on the distance between the base and platform centres, ρ, and was equal to $\rho \sin(\theta/2)$. Furthermore, if the centre of constant-velocity-joint-like parallel mechanisms goes in the direction of the tilt, the situation is slightly more complicated for 3-*[PP]S* parallel mechanisms.

To understand more clearly the coupling between position and orientation, we have

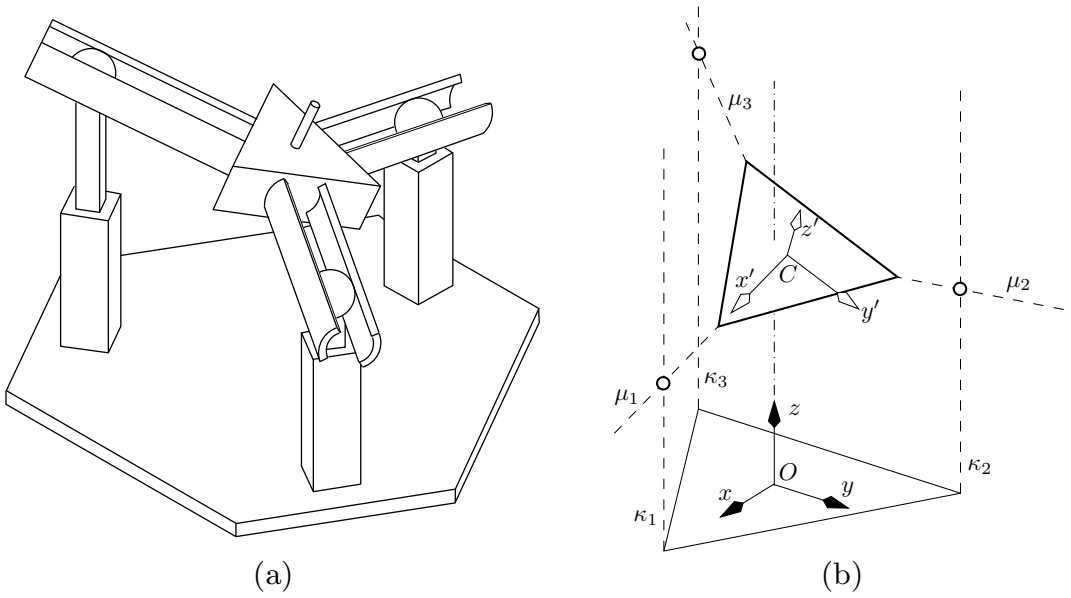

Figure 3.11: (a) A 3-*PSP* 3-DOF spatial parallel mechanism and (b) its kinematic geometry.

shown in Fig. 3.10 the curves for x and y for constant ϕ or θ (they are independent of z). It should be noted, that in contrast to the 3-*RSR* mechanism, here, for any position of the mobile platform, there are two (rather than only one) orientations. Their tilts are the same but the azimuths are offset by 180°. In other words, while for the 3-*RSR* parallel mechanism, the platform centre moves away from the z axis in the direction in which the platform tilts, for the group of mechanisms presented in this section, the platform centre moves *away* from the z axis in a direction normal to the tilt plane.

3.4.3 3-*PSP* 3-DOF Spatial Parallel Mechanisms

The last and most complex example is the so-called *Tripode* joint, used in automotive transmissions. The latter is a 3-*PSP* parallel mechanism (Fig. 3.11) for which the fixed axes κ_i, along which the S joints slide, are parallel and equidistant, while the axes μ_i, traced by the S joints on the platform, are coplanar and intersecting at 120° angles.

The 3-*PSP* mechanism was studied in detail by Durum (1975). Its actuated implementation, the 3-*PSP* mechanism, was later analysed by Tischler et al. (1998) for use as a robot finger. Yet, Stefanini et al. (1999), who have found an interesting biomedical application by actuating only two of the base P joints and blocking the third one, could not interpret exactly the feasible orientations of their platform.

Let the distance from the z axis to any κ_i axis be equal to 1. The unit vectors $\mathbf{m}'_i$ along μ_i, expressed in the mobile frame, are

$$\mathbf{m}'_1 = \begin{bmatrix} 1 \\ 0 \\ 0 \end{bmatrix}, \quad \mathbf{m}'_2 = \begin{bmatrix} \cos(2\pi/3) \\ \sin(2\pi/3) \\ 0 \end{bmatrix}, \quad \mathbf{m}'_3 = \begin{bmatrix} \cos(4\pi/3) \\ \sin(4\pi/3) \\ 0 \end{bmatrix}, \tag{3.21}$$

We, then, express the coordinates of these three unit vectors, expressed in the base frame, in terms of the three T&T angles:

$$\mathbf{m}_i = \mathbf{R}\mathbf{m}'_i, \tag{3.22}$$

for $i = 1, 2, 3$, where $\mathbf{R}$ is the rotation matrix defined by Eq. (3.2). Then, we express the vectors $\mathbf{n}_i$ from the platform centre C (x, y, z) to three points chosen on the vertical axes κ_i (e.g., the intersection points with the base xy plane):

$$\mathbf{n}_1 = \begin{bmatrix} x-1 \\ y \\ z \end{bmatrix}, \quad \mathbf{n}_2 = \begin{bmatrix} x-\cos(2\pi/3) \\ y-\sin(2\pi/3) \\ z \end{bmatrix}, \quad \mathbf{n}_3 = \begin{bmatrix} x-\cos(4\pi/3) \\ y-\sin(4\pi/3) \\ z \end{bmatrix}. \tag{3.23}$$

Let $\mathbf{k}$ be the unit vector along z. Since μ_i should intersect κ_i, vectors $\mathbf{n}_i$, $\mathbf{m}_i$, and $\mathbf{k}$ should be coplanar, for all i. This gives us three linear equations in x, y, and z whose coefficients are functions of the three T&T angles:

$$\det[\mathbf{n}_1, \mathbf{m}_1, \mathbf{k}] = 0, \tag{3.24}$$

$$\det[\mathbf{n}_2, \mathbf{m}_2, \mathbf{k}] = 0, \tag{3.25}$$

$$\det[\mathbf{n}_3, \mathbf{m}_3, \mathbf{k}] = 0. \tag{3.26}$$

Since z is obviously an independent coordinate, none of the above three equations contains that variable, after simplification. Therefore, in order to have a solution for x and y, the three linear equations should be linearly dependent. This time, the coefficient matrix $\mathbf{Q}$ of the constraint equations, Eqs. (3.24–3.26), has all its entries as functions of the three T&T angles. For the three equations to be linearly dependent, the coefficient matrix should be singular, i.e.,

$$\det \mathbf{Q} = -\frac{3\sqrt{3}}{4} \sin\sigma \cos\theta(\cos\theta + 1) = 0. \tag{3.27}$$

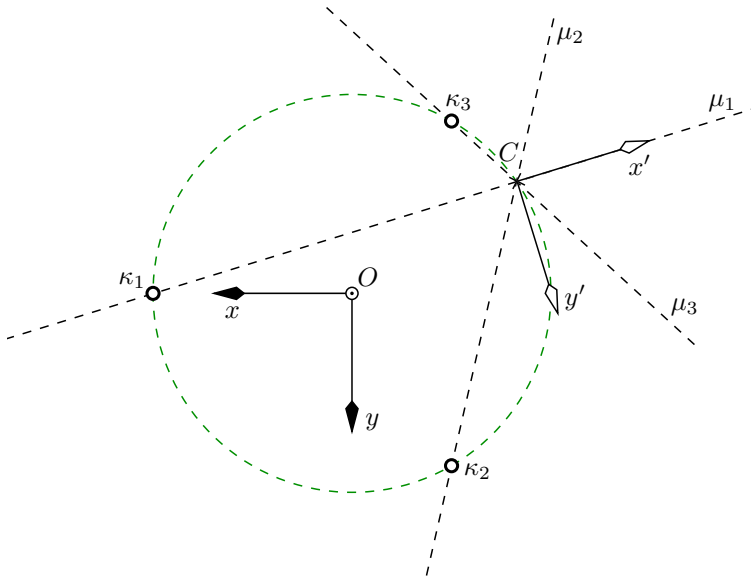

Figure 3.12: Constraint singularities of a 3-*PSP* parallel mechanism.

Note that Eq. (3.27) is only a necessary, but not a sufficient condition. Indeed, if $\theta = \pm\pi/2$, the mobile platform obviously can not be assembled. Substituting $\theta = \pm\pi/2$ in Eqs. (3.24–3.26), reveals that the systems of equations has no solution.

The next solution that satisfies the necessary condition set by Eq. (3.27) is $\theta = \pi$. The resulting situation is similar to the one that happens in *[PP]S* mechanisms when $\theta = \pi$. In other words, the *PSP* mechanism is at a constraint singularity when its mobile platform is upside down. At such a tilt angle, the centre of the mobile platform moves again along a horizontal unit circle, centred at the z axis, as a function of the platform orientation, which is again defined by $2\phi - \psi$ (Fig. 3.12). However, this time, for one complete counter-clockwise tour of point C along the circle of radius 1, the mobile platform makes only *half* a turn in the *same* counter-clockwise direction:

$$x = -\cos(4\phi - 2\sigma) \tag{3.28}$$

$$y = -\sin(4\phi - 2\sigma). \tag{3.29}$$

Disregarding the impractical case $\theta = \pi$, Eq. (3.15) leads us to the only remaining possibility: $\sigma = 0$ or $\sigma = \pi$. If, again, we substitute $\sigma = 0$ or $\sigma = \pi$ in Eqs. (3.24–3.26) and solve them, we obtain the following for the feasible motion of the platform centre:

$$x = \frac{\cos\theta - 1}{4\cos\theta}\big(\cos 4\phi(\cos\theta - 1) + \cos 2\phi(\cos\theta + 1)\big), \tag{3.30}$$

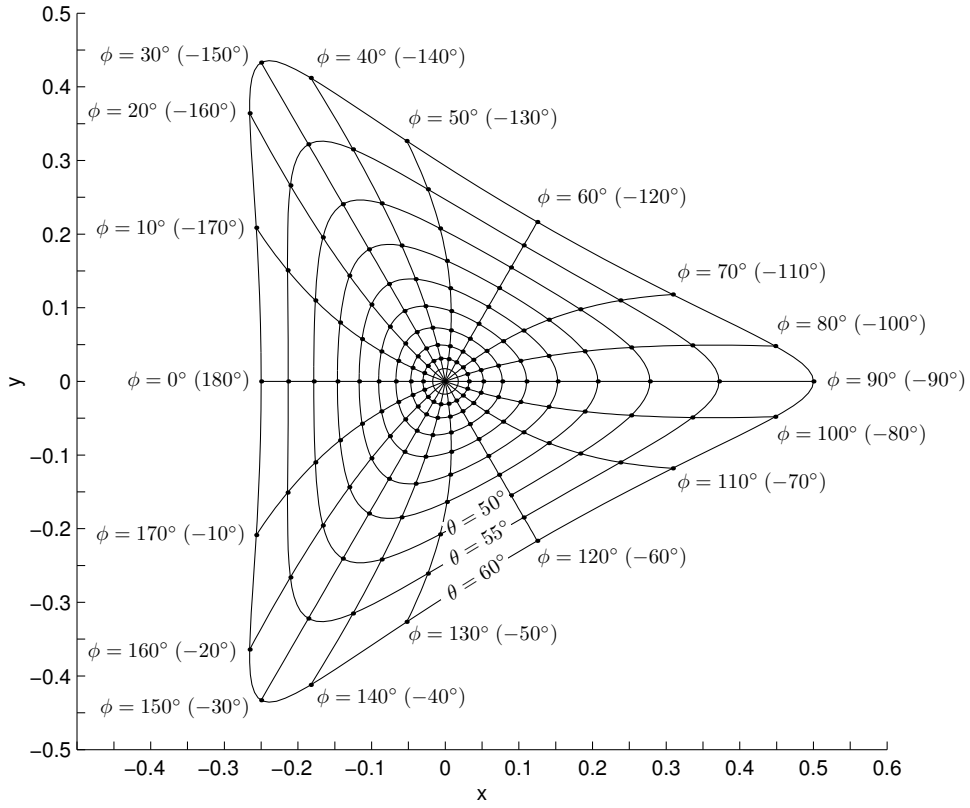

Figure 3.13: Horizontal offset as function of orientation for 3-*PSP* mechanisms.

$$y = \frac{\cos\theta - 1}{4\cos\theta}\big(\sin 4\phi(\cos\theta - 1) - \sin 2\phi(\cos\theta + 1)\big). \tag{3.31}$$

for both $\sigma = 0$ and $\sigma = \pi$. However, for *PSP* parallel mechanisms, it is impossible to pass from one mode of operation to the other without disassembling the mechanism. Again since, normally, the mobile and base frames are selected to coincide at $\theta = 0$, we are automatically in the $\sigma = 0$ mode.

Parallel mechanisms of type 3-*[PP]S* have an offset from the central axis that is dependent not only on the tilt but also on the azimuth of the mobile platform:

$$\upsilon = \frac{1 - \cos\theta}{4\cos\theta}\sqrt{\cos 2\theta\cos 6\phi - \cos 6\phi + \cos 2\theta + 3}. \tag{3.32}$$

From the above, we may conclude that the minimum and maximum offsets depend only on the tilt angle and are respectively:

$$\upsilon_{min} = \frac{\cos\theta - 1}{2},\ \ \upsilon_{max} = \frac{\cos\theta - 1}{2|\cos\theta|}. \tag{3.33}$$

To understand more clearly the coupling between position and orientation, we have shown in Fig. 3.13 the curves for x and y for constant ϕ or θ (they are independent of z). Once again, for every position of the mobile platform, there are two orientations with the same tilt, and azimuths offset by 180°.

With this final example, we conclude our study of orientation representation and constraint analysis of 3-DOF spatial parallel mechanisms. It is left no doubt that, the use of the Tilt-and-Torsion (T&T) angles provides the fittest tool for the geometric analysis of a plethora of parallel mechanisms. Furthermore, attention is drawn on the newly-defined class of 3-DOF zero-torsion spatial parallel mechanisms which shows a great potential for various industrial applications. It remains, however, to identify all members of this zero-torsion family—a task that may be accomplished only by relying on screw theory.

Chapter 4

Kinematic Analysis of 6-DOF 6-$\underline{R}US$ Parallel Mechanisms

In this chapter, we study the kinematic geometry of general 6-$\underline{R}US$ parallel mechanisms as well as of a very particular design of the same class, called the *Rotobot*. For the general case, we describe a geometrical method for the computation and representation of the constant-orientation workspace. Firstly, we compute only the edges of the workspace by taking into account the physical limits of the U joints. Then we ignore those limits, and calculate the horizontal cross-sections of the constant-orientation workspace. We do the same for the *Rotobot* but, in addition, we calculate the Type 2 singularity loci. The geometric study of the *Rotobot* reveals an interesting phenomenon related to working modes and workspace segmentation.

The geometric analysis of these spatial mechanisms involve the manipulations of tori, cyclides, Bohemian domes, and bicircular quartics. Toric surfaces are intersected by circles or planes, toric sections are intersected by other toric sections and then polygonised.

4.1 Introduction

It is well known that parallel mechanisms have a rather limited and complex workspace. At the same time, the size and shape of the workspace is probably one of the main design criteria. As the complete workspace of a 6-DOF parallel mechanism is a six-dimensional entity which is practically impossible to visualise, algorithms for the calculation and representation of various workspace subsets have been proposed. Apart from the brute-force approach—the discretisation algorithms—all other computational schemes are strictly dependent on the particular architecture. Thus, in general, each research on workspace analysis can be virtually situated in a 3D array whose axes are the type of workspace subset, the type of algorithm (geometrical, numerical, analytical), and the type of mechanism architecture.

In the area of 6-DOF parallel mechanisms, most of the research has been particularly aimed at the simplest and most popular architecture, namely the 6-$U\underline{P}S$ parallel mechanism, commonly known as the *Stewart-Gough platform*. Indeed, almost all existing 6-DOF *motion bases*, used in entertainment or motion (particularly flight) simulation, are based on the 6-$U\underline{P}S$ architecture. (An exhaustive list of links to the web sites of manufacturers of motion bases or complete motion simulators, may be found at http://www.parallemic.org/WhosWho/CompSims.html.) Motion simulators, generally, manipulate excessive loads of up to tens of tons. Furthermore, the mechanical part, i.e., the motion base, is often only a small fraction of the cost of a high-tech flight simulator. Hence, a 6-$U\underline{P}S$ parallel mechanism is no doubt an excellent choice for these applications, as it is the stiffest of all 6-DOF architectures (only axial loads in the legs) and allows the use of powerful (yet expensive and messy) hydraulic actuators.

The second most common, yet much less studied, 6-DOF architecture is undoubtedly the 6-$\underline{R}US$ one. Often the U joints in the legs are replaced by S joints. This leads to a redundant DOF in each distal link (the one connecting the mobile platform) which, however, does not alter the properties of 6-$\underline{R}US$ parallel mechanisms. Similarly, the U and S joints in each leg may be interchanged without any change in the mechanism characteristics. Therefore, in what follows, we will make no difference between legs of type $\underline{R}US$, $\underline{R}SS$, or $\underline{R}SU$ and refer to them simply as $\underline{R}US$.

An example of 6-$\underline{R}US$ parallel kinematic machine (PKM), actually a 6-$\underline{R}SS$ one, is presented in Fig. 4.1. Undoubtedly, however, the most popular member of the 6-$\underline{R}US$ class is the *Hexa* robot (Pierrot et al., 1990), of which various versions are already available. The first to propose this architecture, however, was Hunt (1983).

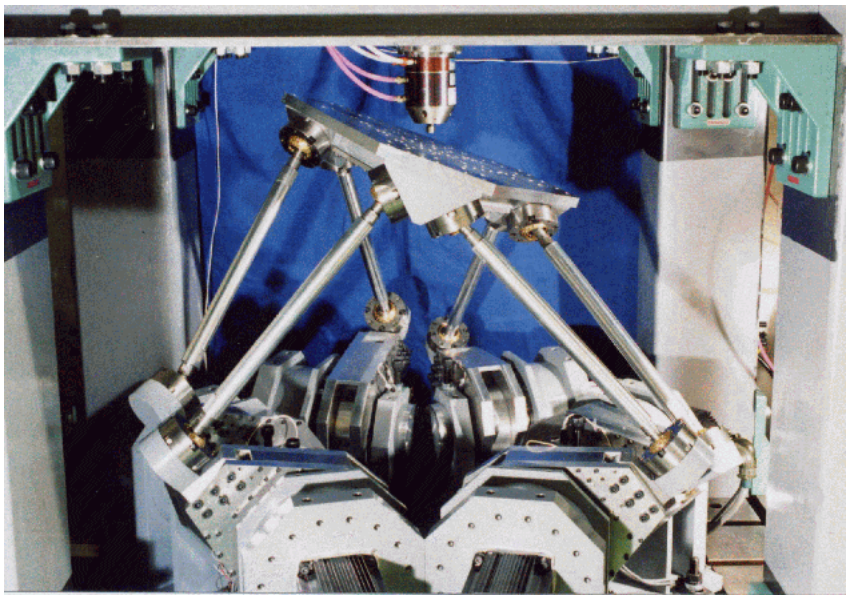

Figure 4.1: An example of a 6-$\underline{R}US$ parallel kinematic machine (photo courtesy of Prof. Yukio Takeda, Tokyo Institute of Technology).

Some other prototypes have been constructed by Takeda et al. (1997), by Zabalza et al. (1999), and by Benea (1996). The latter has even performed a detailed set of analyses on this type of mechanism. Three other designs, one of which is shown in Fig. 4.2, are also commercially available from *Servos & Simulation, Inc.*, as motion simulation systems (http://www.servos.com). A similar design is also available as part of the newly developed low-cost flight simulator by *Fidelity Flight Simulation, Inc.* (http://www.flightmotion.com). Finally, a more peculiar design has been introduced by Hexel Corporation (http://www.hexel.com), dubbed *Rotobot*^{TM} (Chi, 1999). The kinematic geometry of the *Rotobot* will be the subject of our study in Section 4.4.

The main advantages of 6-$\underline{R}US$ parallel mechanisms are (1) their light mobile part, as the heavy motors are mounted on the base, and (2) the possibility for use of lower-cost electric motors. Certainly, the ability to use thin rods for the distal links and thus reduce the risk for link interference is beneficial too. Finally, these mechanisms can be statically balanced, as shown in (Wang and Gosselin, 1998). The main disadvantages of these mechanisms are (1) the presence of bending moments in the proximal links and, as we will see, (2) their highly complicated kinematic analysis. To overcome the first of this disadvantages, designers have built their prototypes with solid proximal links, as it may be seen in Fig. 4.1, or replaced these links with sliders moving on base-mounted circular guides, as in the *Rotobot* (Fig. 4.22). To alleviate the second of

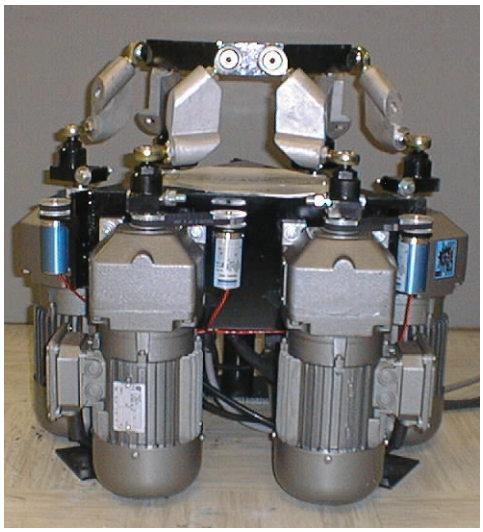

Figure 4.2: An example of a 6-$\underline{R}US$ personal motion system (photo courtesy of Servos & Simulation, Inc.).

these drawbacks, designers have oriented the axis of the R joints in only two ways: all coplanar or all parallel. Our contribution serves to alleviate this same shortcoming, while giving freedom to designers to place arbitrarily the axes of the R joints. Namely, in this chapter we examine in depth the kinematic geometry of the 6-$\underline{R}US$ parallel architecture and provide tools for the optimal design of these mechanisms.

Despite the relative popularity of the 6-$\underline{R}US$ parallel architecture, few researchers have analysed in detail its workspace. What is more, as we just emphasised, all of the existing prototypes have rather particular designs which facilitate their workspace analyses. Benea (1996) has studied two subsets of the complete workspace: the constant-orientation workspace and the orientation workspace. A *discretisation* algorithm has been used for this purpose. The philosophy of such an algorithm is rather simple and consists roughly in discretising the three-dimensional space, solving the inverse kinematic problem at each point, and verifying the constraints that limit the workspace.

Such discretisation algorithms are used by most researchers and can be applied to any type of architecture. They are clearly computationally intensive and require large amounts of disk space for storing the computed point cloud. A more advanced approach for the computation of the constant-orientation workspace is based on the geometric description of all constraints that limit the workspace. Unlike the discretisation methods, the geometric methods are very fast and accurate. Furthermore, they bring insight into the problem and are very useful during the design stage.

It is for the class of 6-$U\underline{P}S$ parallel mechanisms, that such an approach was first introduced by Gosselin (1990) and then again, under a modified version, by Gosselin et al. (1992), considering only the limits of the actuators. In the first paper, horizontal cross-sections of the constant-orientation workspace have been determined, while in the second, the workspace edges have been defined directly. Merlet (1994) later extended this geometric approach by including the limited ranges of the passive joints and even the risk of link interference. For the class of 6-$\underline{P}US$ parallel mechanisms, Merlet and Gosselin (1991) applied the same philosophy to compute horizontal cross-sections of the workspace of their "active wrist." Recently, a more general and detailed workspace analysis following the same approach was performed by Bonev and Ryu (1999b), where the constant-orientation workspace was directly computed and represented as a solid model in the CAD/CAM system CATIA$^{\text{TM}}$.

To the best of our knowledge, a geometric algorithm has never been applied to the general 6-$\underline{R}US$ parallel mechanism. Yet, only a moderate change in the program code used in Bonev and Ryu (1999b) would have been sufficient to produce a similar program for 6-$\underline{R}US$ parallel mechanisms. Besides, a similar implementation has also been carried out by Chrisp and Gindy (1999) in Pro/ENGINEER$^{\text{TM}}$ for a 6-$U\underline{P}S$ parallel mechanism. However, while the use of CATIA or Pro/ENGINEER results in an excellent visualisation of the workspace, common experience shows the obvious disadvantages of this approach. Firstly, the two CAD/CAM systems, although quite popular, are not necessarily available to all users of parallel mechanisms. Secondly, the natural trend in industry is to develop large integrated programs that perform various types of analyses and not just compute the constant-orientation workspace (Mayer St-Onge and Gosselin, 2001; Astanin et al., 2002; Podzorov and Bushuev, 2002). That is why, in the first part of this chapter, we propose an algorithm inspired by the one presented in (Gosselin et al., 1992) for computing and representing the edges of the constant-orientation workspace of 6-$\underline{R}US$ parallel mechanisms. This algorithm can be easily implemented and requires no special programming libraries. Later on, we ignore all joint limits and present briefly the procedure for computing the horizontal cross-sections of the constant-orientation workspace of general 6-$\underline{R}US$ parallel mechanisms.

Finally, in Section 4.4, we examine the simplified but intriguing design of the *Rotobot*. Its geometric analysis revealed a couple of new interesting phenomena which are not present in general 6-$\underline{R}US$ parallel mechanisms. The complete geometric analysis of the *Rotobot*, emphasised once again the major open problem concerning working modes.

In particular, we present the procedure for computing and representing its constant-orientation workspace and Type 2 singularity surface as horizontal cross-sections. While mechanical joint limits are ignored, we take into account the obvious constraint on the circular order of the centres of the U joints (slider interference constraint). Astonishingly, this constraint can be modelled by a so-called *Bohemian dome* which fits nicely into the vertex spaces of the mechanism. Thus, in each horizontal plane, the constant-orientation workspace consists of one or more complex shapes with circular arc boundaries, while the singularity loci of Type 2 are given by both the workspace boundary and a bisymmetric bicircular quartic. Inevitably, the most interesting discussion appears, once again, on the topic of working modes.

All the algorithms presented in this chapter were implemented in Matlab$^{\text{TM}}$ R12 under Linux and run on a PC with 512 Mb RAM and 1.8 GHz Intel Pentium CPU.

4.2 Computing the Edges of the Constant-Orientation Workspace of General 6-$\underline{R}US$ Parallel Mechanisms

Following our established notation pattern, we select a fixed reference frame, called the *base frame* with centre O and axes x, y, and z. Then, we also select a *mobile frame* that is fixed to the mobile platform, with centre C and axes x', y', and z' (Fig. 4.3). We denote the centres of the U joints by A_i and the centres of the S joints attached at the mobile platform by B_i (in this chapter, $i = 1, \ldots, 6$). Each point A_i moves along a circular trajectory referred to as *track* i whose centre is denoted by O_i. We assume that each actuated revolute joint can rotate fully, without any restriction imposed by the joint itself. Let the lengths of all proximal links be equal and denoted by ℓ_1 and the lengths of all distal links be equal and denoted by ℓ_2.

Next, we select a local frame with centre at point O_i and axes $x^{(i)}$, $y^{(i)}$, and $z^{(i)}$, so that $z^{(i)}$ coincides with the axis of actuated revolute joint i. We will refer to that frame as *track frame* i. The constant matrix $\mathbf{R}_i$ defines the orientation of track frame i with respect to the base frame. Finally, let us denote the angle between the $x^{(i)}$ axis and the line O_iA_i by θ_i. This angle is the i-th input variable.

We select also a moving frame that is fixed to proximal link i, with centre at point A_i and axes $x^{(A_i)}$, $y^{(A_i)}$, and $z^{(A_i)}$, so that the $z^{(A_i)}$ axis is always parallel to the track

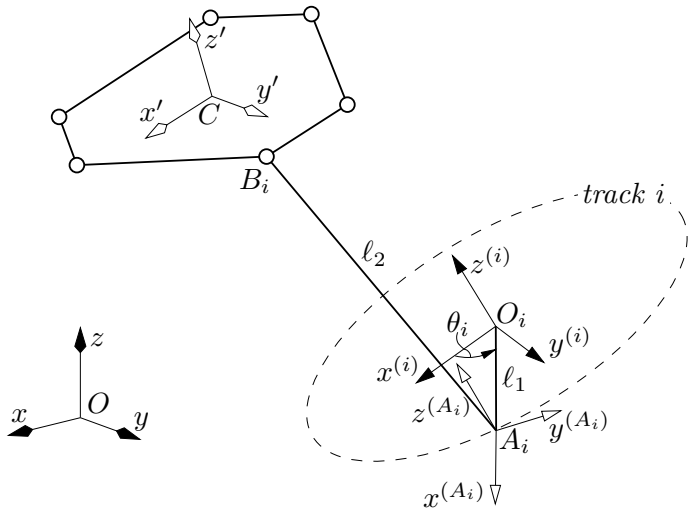

Figure 4.3: Leg i of a 6-$\underline{R}US$ parallel mechanism.

frame's $z^{(i)}$ axis, and the $x^{(A_i)}$ axis is always along line O_iA_i, pointing away from O_i. We will call this frame *proximal link frame* i. The rotation matrix that transforms coordinates from proximal link frame i to track frame i is a function of θ_i only and will be designated by $\mathbf{R}_{A_i}$.

The mobile platform's position is defined by vector $\mathbf{p}$, while its orientation is described by a rotation matrix $\mathbf{R}$ that is defined by the three T&T angles defined in the previous chapter. Once again, given two points in space, e.g., A and B, we will denote by $\mathbf{r}_{AB}$ the vector along the directed line connecting point A to point B.

Finally, we will add the superscript $'$ to a vector when the latter is expressed in the mobile frame, the superscript $^{(i)}$ when the vector is expressed in track frame i, and the superscript $^{(A_i)}$ when the vector is expressed in proximal link frame i. No superscript will mean that the vector is expressed in the base frame.

4.2.1 Solving the Inverse Kinematic Problem

The solution to the inverse kinematic problem for 6-$\underline{R}US$ parallel mechanisms is very similar to the one for 3-$\underline{R}RR$ PPMs that we outlined in Chapter 2. Geometrically, for each leg, the problem can be regarded as the one of finding the intersection point(s) between a sphere of radius ℓ_2 and centre B_i and the track circle. Clearly, depending on the position of point B_i, this problem may have an infinite number of real solutions, two solutions, a single one, or none at all.

The first step in the computation process is to calculate the coordinates of each point B_i, first in the base frame, and then in track frame i:

$$\mathbf{r}_{OB_i} = \mathbf{p} + \mathbf{R}\,\mathbf{r}'_{CB_i}, \tag{4.1}$$

$$\mathbf{r}^{(i)}_{O_iB_i} = \mathbf{R}_i^T(\mathbf{r}_{OB_i} - \mathbf{r}_{OO_i}). \tag{4.2}$$

Now, by squaring $\mathbf{r}^{(i)}_{A_iB_i} = \mathbf{r}^{(i)}_{O_iB_i} - \mathbf{r}^{(i)}_{O_iA_i}$, we obtain the main equation constituting the inverse kinematic problem:

$$\ell_2^2 = \varrho_i^2 + \ell_1^2 - 2(\mathbf{r}^{(i)}_{O_iB_i})^T\mathbf{r}^{(i)}_{O_iA_i}. \tag{4.3}$$

where $\varrho_i = ||\mathbf{r}^{(i)}_{O_iB_i}||$. If $(\mathbf{r}^{(i)}_{O_iB_i})^T\mathbf{r}^{(i)}_{O_iA_i} = 0$, i.e., if point B_i lies on the $z^{(i)}$ axis, then Eq. (4.3) degenerates. That is to say, if, in addition, $\varrho_i^2 = \ell_2^2 - \ell_1^2$, then the inverse kinematic problem has an infinite number of solutions.

From the definition of input variable θ_i, we have that $\mathbf{r}^{(i)}_{O_iA_i} = \ell_1\,[\cos\theta_i, \sin\theta_i, 0]^T$. Let also the components of $\mathbf{r}^{(i)}_{O_iB_i}$ be $x^{(i)}_{B_i}$, $y^{(i)}_{B_i}$, and $z^{(i)}_{B_i}$. Then, Eq. (4.3) reduces to

$$x^{(i)}_{B_i}\cos\theta_i + y^{(i)}_{B_i}\sin\theta_i = \frac{\varrho_i^2 + \ell_1^2 - \ell_2^2}{2\ell_1} \equiv p_i. \tag{4.4}$$

Now, in order to have a real solution to this equation, the following inequality should hold true:

$$x^{(i)2}_{B_i} + y^{(i)2}_{B_i} - p_i^2 \equiv \Gamma_i \geq 0. \tag{4.5}$$

This inequality is equivalent to the distal link's length constraint that will be presented later on. Unless $p_i^2 = x^{(i)2}_{B_i} + y^{(i)2}_{B_i}$, there exist two real solutions to Eq. (4.4), determined uniquely from:

$$\sin\theta_i = \frac{p_i y^{(i)}_{B_i} + x^{(i)}_{B_i}\delta_i\sqrt{\Gamma_i}}{x^{(i)2}_{B_i} + y^{(i)2}_{B_i}} \equiv S_i, \quad \cos\theta_i = \frac{p_i x^{(i)}_{B_i} - y^{(i)}_{B_i}\delta_i\sqrt{\Gamma_i}}{x^{(i)2}_{B_i} + y^{(i)2}_{B_i}} \equiv C_i, \tag{4.6}$$

$$\theta_i = \mathrm{atan2}(S_i, C_i), \tag{4.7}$$

where $\theta_i \in [-\pi, \pi]$, and $\delta_i = \pm 1$ is the branch index. As we just mentioned, when the inequality represented by Eq. (4.5) turns into an equality, leg i is in a singular configuration.

At the end of Chapter 2, we discussed the issue of working modes and workspace segmentation. In this chapter, this issue will be readdressed in Section 4.4, where we

study the *Rotobot* and see that its workspace is strictly dependent on the working mode. For the general 6-$\underline{R}US$ parallel mechanism, this fact is also true. However, as we will see, a very simple and obvious design consideration may assure that the workspace is maximum for one of the eight working modes. Therefore, in Sections 4.2 and 4.3, we will assume that the mechanism is always in one working mode. In other words, once the mechanism is assembled, distal link i should never be allowed to lie in one plane with the $z^{(i)}$ axis.

In the remaining part of Section 4.2, we first describe the basic geometric algorithm for defining the constant-orientation workspace of a general 6-$\underline{R}US$ parallel mechanism. Then, we describe our main contribution for obtaining analytically the intersection points between a cyclide and a circle. This algorithm is the heart of the procedure for computing the edges of the constant-orientation workspace. Subsequently, we propose the general procedure for computing each vertex space, and then the procedure for tracing the edges of the constant-orientation workspace. We conclude the section with several examples and a brief discussion.

4.2.2 Geometric Modelling of the Constant-Orientation Workspace

In order to describe a geometric method for the computation of the constant-orientation workspace, it is necessary to establish geometric models for all the constraints that limit it. The basic idea is to first regard all legs as independent and only then consider their interdependence (Gosselin, 1990).

As defined earlier, for a constant orientation of the platform, the i-th *vertex space* is the volume that can be attained by vertex B_i from chain i, ignoring the constraints imposed by all other legs. The constraints that determine each vertex space are (i) the distal link's length, (ii) the leg singularity, (iii) the ranges of the base and platform joints, and (iv) the proximal link's length. However, we will explain later why the constraints on the mobile platform joints cannot be easily described geometrically in the determination of the vertex spaces. Also, as we already mentioned, we assume that the revolute actuators can fully rotate, i.e., there are no revolute joint limits. Next, we will investigate each constraint individually to finally construct vertex space i.

4.2.2.1 Distal Link's Length

In the proximal link's frame, the set of points reachable by B_i is a sphere $\mathcal{S}_i$ of radius ℓ_2 and centre A_i.

4.2.2.2 Leg Singularity

As we already outlined, an $\underline{R}US$ chain is at a singular configuration when a distal link is coplanar with the axis of the corresponding actuated R joint, but its vertex B_i does not lie on that axis. In this singularity, the two branches of the inverse kinematics of the leg meet and the mobile platform loses one degree of freedom. In addition, if vertex B_i lies on the axis of the actuated revolute joint, then the two branches degenerate to an infinite number of solutions.

The motion of each distal link will, therefore, be restricted so that the angle between vector $\mathbf{r}_{A_iB_i}$ and the proximal link frame's $y^{(A_i)}$ axis be always in only one of the two ranges $[0°, 90°)$ (corresponding to $\delta_i = -1$) or $(90°, 180°]$ (corresponding to $\delta_i = +1$). Hence, we split the sphere $\mathcal{S}_i$ by the $x^{(A_i)}z^{(A_i)}$ plane. Depending on the branch index, we take one of the two hemispheres. The great circle formed by the intersection of $\mathcal{S}_i$ with that plane will be denoted by $\mathcal{C}_{i,N}$.

4.2.2.3 Mechanical Limits on the Passive Joints

The physical constraints that limit the range of a base joint can be modelled by a general conical surface whose vertex is the centre of the joint. We already mentioned that the distal links are attached to the proximal links through U joints, but, in practice, spherical joints are often used instead. Thus, we choose to model the constraint imposed by the base joint as a circular cone, within which the corresponding distal link is restrained to stay, as shown in Fig. 4.4. If indeed, U joints are used, a better model would be a pyramid as used in (Merlet, 1994), which, however, will inevitably make the workspace analysis slightly more complicated.

Let α be the *maximum misalignment angle* of the base joints ($\alpha < 90°$) and let $\mathbf{j}_{A_i}^{(A_i)}$ be the unit vector along the axis of symmetry of the joint at point A_i, expressed in proximal link frame i. This vector is constant when expressed in that frame and depends only on the design of the parallel mechanism. Then, the allowable region for point B_i consists of a *spherical cap* of radius ℓ_2 and centre A_i. The *base circle* of that spherical cap will be designated by $\mathcal{C}_{i,A}$.

The same cone model could be used for the platform spherical joints. Let β be

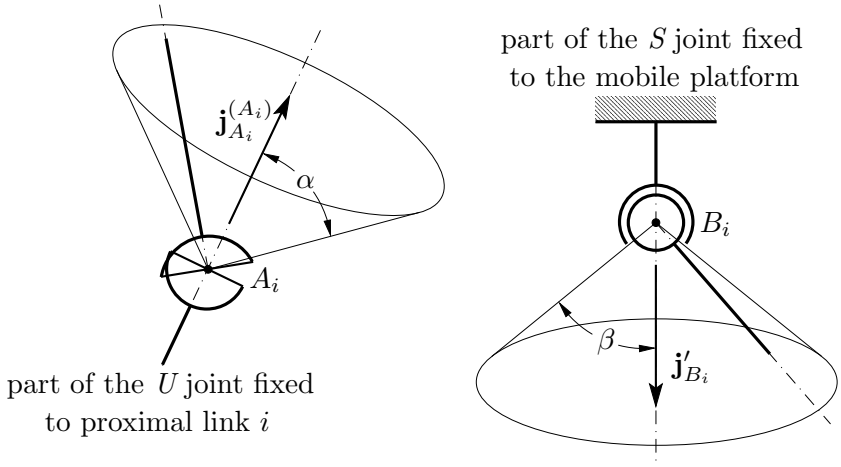

Figure 4.4: Ranges of motion of the passive joints.

the maximum misalignment angle of the platform joints ($\beta < 90°$) and let $\mathbf{j}'_{B_i}$ be the constant unit vector along the axis of symmetry of the spherical joint with centre B_i expressed in the mobile frame. Then, the allowable region for point A_i, referred to the mobile frame, consists of a spherical cap of radius ℓ_2 and centre B_i. Let $-\mathbf{j}_{B_i}^{(A_i)}$ be the opposite unit vector, expressed in the proximal link frame i, and defined as:

$$\mathbf{j}_{B_i}^{(A_i)} = \mathbf{R}_{A_i}^T \mathbf{R}_i^T \mathbf{R} \mathbf{j}'_{B_i}. \tag{4.8}$$

Thus, with respect to the proximal link frame, point B_i is located on an equivalent spherical cap of radius ℓ_2 but centre A_i.

For the 6-$\underline{P}US$ parallel mechanism (Bonev and Ryu, 1999b), the orientations of the proximal link frames are fixed with respect to the base frame. Thus, when point A_i moves along the linear track, the equivalent spherical cap representing the constraint on spherical joint i remains unchanged in proximal link frame i. This, however, is not true for the 6-$\underline{R}US$ parallel mechanisms, since $\mathbf{R}_{A_i}$ in Eq. (4.8) is not constant. Therefore, the spherical cap has a different orientation in proximal link frame i for each different position of point A_i on the circular track. This makes it practically impossible to construct and use a geometric model of the platform-joint constraint.

Fortunately, simulations performed on different designs have shown that the constraint imposed by the S joint ranges is much less frequently violated than the constraint on the U joints. Thus, we may ignore this constraint for the sake of describing geometrically the constant-orientation workspace. If this constraint is too tight to be neglected, then the use of a discretisation or a numerical method is the only alternative.

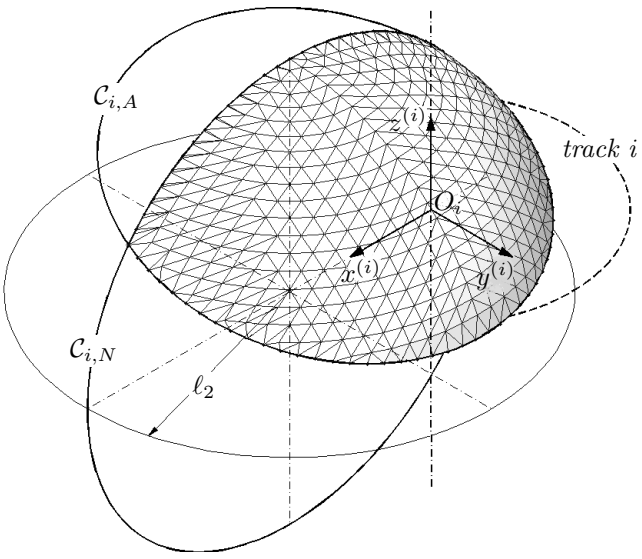

Figure 4.5: The allowable spherical region.

4.2.2.4 Proximal Link's Length

The *allowable spherical region* for point B_i in proximal link frame i is the intersection of the hemisphere defined in Section 4.2.2.2 and the spherical cap defined in Section 4.2.2.3 (Fig. 4.5). Now, in track frame i, the allowable spatial region for vertex B_i is the volume swept by the allowable spherical region by revolving it about the $z^{(i)}$ axis. Therefore, the allowable spatial region for the platform centre C, i.e., vertex space i (Fig. 4.6), is the allowable spatial region for vertex B_i translated along the vector $\mathbf{r}_{B_iC}$.

Note that *ignoring the constraints on the mobile platform joints makes the shape and orientation of each vertex space independent from the orientation of the mobile platform.* Thus, for a given design, we can store the data defining all vertex spaces and avoid computing them for each different orientation of the mobile platform.

For simplification purposes, once the platform orientation is set, we will offset the coordinates of each point O_i by vector $\mathbf{r}_{B_iC}$. Thus, for a given design we compute the vertex spaces at the original positions of points O_i, store the data, and then offset by $\mathbf{r}_{B_iC}$ when computing the constant-orientation workspace for a given orientation.

After all six vertex spaces have been defined, we must consider the fact that all points B_i are fixed to the mobile platform. This condition will be referred to as the *closure constraint*. Thus, the intersection of all six vertex spaces is the constant-orientation workspace of the parallel mechanism.

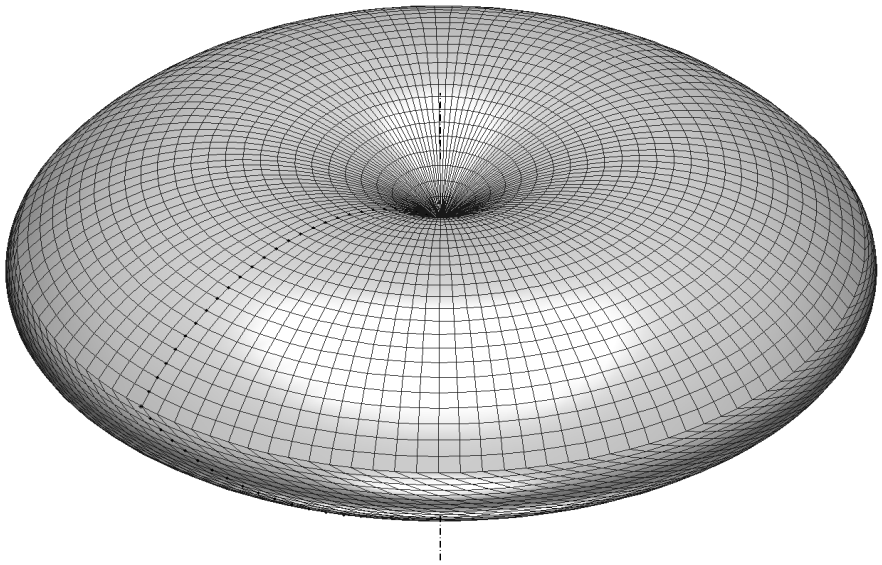

Figure 4.6: Vertex space i.

4.2.3 Intersecting a Cyclide with a Circle

As we just saw, the geometric model of the vertex space for an $\underline{R}US$ chain is not simply a torus. Rather, it is a surface of revolution that consists, in general, of two parts. One of these surfaces is part of the well-known *torus*—the part generated by the arc from $\mathcal{C}_{i,N}$. The surface traced by $\mathcal{C}_{i,A}$ is, however, part of a special *cyclide* (Segre, 1884), sometimes referred to as a generalised torus (Fichter and Hunt, 1975), which includes the (right circular) torus as a special case.

Therefore, in order to compute the edges of the constant-orientation workspace we need to have a procedure for computing the intersection curve between two cyclides (Fig. 4.7). In general, it is not possible to obtain directly analytic (parametric) expressions for the intersection curves. Thus, we proceed as in (Johnstone, 1993) and use *circle decomposition* to reduce the surface intersection problem to the problem of finding the intersection points between a cyclide and a circle. We do this by decomposing one of the surfaces into its *generator circles* (Fig. 4.9) and intersecting with them the other surface.

In what follows, we will define the equation of the special cyclide from vertex space i in track frame i (for brevity, we will omit the index $k = 1, 2$). Then, we will present our algorithm for obtaining the intersection points between that cyclide and a circle. Note that, to our best knowledge, no analytic solutions for this problem have been presented before.

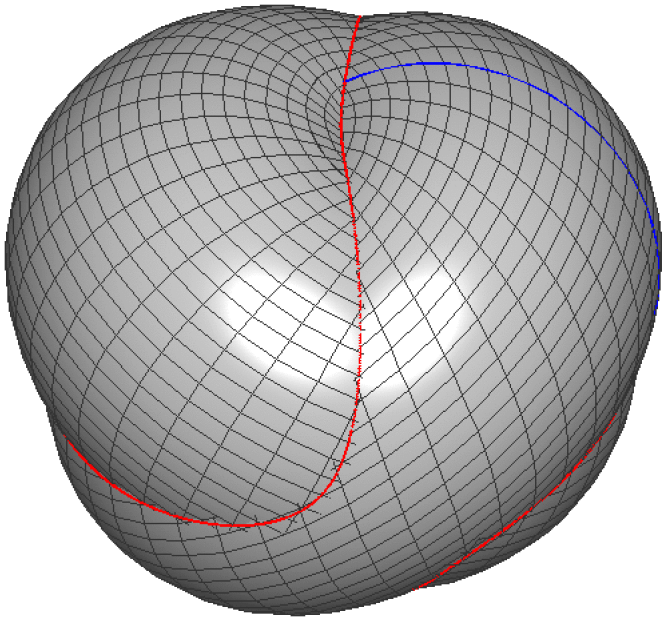

Figure 4.7: Intersection curve between two cyclides.

4.2.3.1 Algebraic Approach

A detailed study on our special cylide was made by Fichter and Hunt (1975) related to the design of spatial linkages. Indeed, our cyclide is the 2D locus of a point attached to a body that is joined back to the reference system through an RR kinematic chain as shown in Fig. 4.8(a). Its algebraic equation is:

$$\left(x^2 + y^2 + z^2 - a^2 - b^2 - f^2\right)^2 = 4a^2\left[b^2 - \left(\frac{z - f\cos\gamma}{\sin\gamma}\right)^2\right] \tag{4.9}$$

where for a torus, $f = 0$ and $\gamma = \pi/2$.

The cyclide is a quartic surface that contains the imaginary spherical circle twice, therefore having full *circularity* (Hunt, 1978). Consequently, its intersection curve with a plane is a *bicircular quartic*, including its diametral sections shown in Fig. 4.8(b). Thus, since a circle has circularity one, there may be at most four intersection points between a cyclide and a circle.

A circle in space can be defined as the system of two algebraic equations—one of a sphere and one of a plane. Those two equations and Eq. (4.9) can then be solved for the unknowns x, y, and z. In fact, we can even set up the algebraic equation for the other toroidal surface and then trace the intersection curves using some surface intersection algorithm for algebraic (implicit) surfaces. However, such an approach suffers from

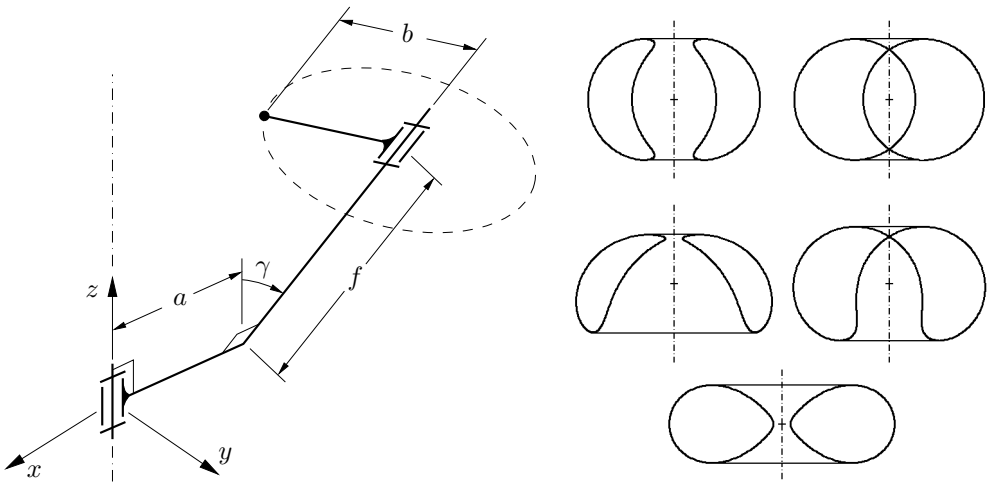

(a) (b)

Figure 4.8: (a) Tracing the cyclide and (b) several possible diametral sections.

disadvantages such as the necessity of determining starting points and the difficulties in tracing the different branches of the intersection curves (Patrikalakis and Prakash, 1990). Furthermore, in the area of mechanism design, a parametric approach is much more relevant and may suggest other applications than the one discussed here. It also allows to define directly the range of the toroidal surface and the circle—recall that we have to intersect a *portion* of a cyclide with an *arc* of a circle. Hence, our obvious decision to use the parametric approach.

4.2.3.2 Parametric Approach

A circle in space can be defined by its radius r, coordinates p_x, p_y, and p_z of its centre, and unit vector along the axis of symmetry defined by the angles ϑ and φ, such that its parametric equation is

$$\mathbf{C}^{(i)}(u_i) = \begin{bmatrix} \cos\varphi & -\sin\varphi & 0 \\ \sin\varphi & \cos\varphi & 0 \\ 0 & 0 & 1 \end{bmatrix} \begin{bmatrix} \cos\vartheta & 0 & \sin\vartheta \\ 0 & 1 & 0 \\ -\sin\vartheta & 0 & \cos\vartheta \end{bmatrix} \begin{bmatrix} r\cos u_i \\ r\sin u_i \\ 0 \end{bmatrix} + \begin{bmatrix} p_x \\ p_y \\ p_z \end{bmatrix} \tag{4.10}$$

where ϑ is the angle between the $z^{(i)}$ axis and the unit vector, and φ is the angle between the $x^{(i)}$ axis and the projection of the unit vector onto the $x^{(i)}y^{(i)}$ plane. Thus, for example, for circle $\mathcal{C}_{i,N}$, $r = \ell_2$, $p_x = r_A$, $p_y = p_z = 0$, and $\vartheta = \varphi = \pi/2$ in track frame i.

Each cyclide is generated by revolving the corresponding circle, whose equation was derived above, about the track's $z^{(i)}$ axis. Therefore, the parametric equation of the resulting cyclide with respect to track frame i is

$$\mathbf{T}^{(i)}(u_i, v_i) = \begin{bmatrix} \cos v_i & -\sin v_i & 0 \\ \sin v_i & \cos v_i & 0 \\ 0 & 0 & 1 \end{bmatrix} \mathbf{C}^{(i)}(u_i), \tag{4.11}$$

where $v_i \in [-\pi, +\pi]$.

The parametric equation for a cyclide, $\mathbf{T}^{(j)}(u_j, v_j)$, from vertex space j expressed in track frame j has exactly the same form as the one defined by Eq. (4.11). Setting v_j equal to a constant, $\mathbf{T}^{(j)}(u_j, v_j) \equiv \mathbf{C}^{(j)}(u_j)$ becomes the equation of a circle. Finally,

$$\mathbf{C}^{*(i)}(u_j) = \mathbf{r}_{OO_j} - \mathbf{r}_{OO_i} + \mathbf{R}_i^T \mathbf{R}_j \mathbf{C}^{(j)}(u_j) \tag{4.12}$$

will be the expression for that circle referred to track frame i, where vectors $\mathbf{r}_{OO_i}$ and $\mathbf{r}_{OO_j}$ are the modified positions of the origins of track frames i and j (recall the remarks at the end of Section 4.2.2.4).

Obviously, one can find equivalent values ϑ^*, φ^*, p_x^*, p_y^*, and p_z^*, such that $\mathbf{C}^{*(i)}(u_j)$ can be written in exactly the same form as in Eq. (4.10). Note, however, that due to the rotation defined by $\mathbf{R}_i^T \mathbf{R}_j$, the permissible range of the variable u_j should be modified by a certain offset, depending on $\mathbf{R}_i^T \mathbf{R}_j$ and the value of v_j. Hence, the matrix equation that needs to be solved is

$$\mathbf{T}^{(i)}(u_i, v_i) = \mathbf{C}^{*(i)}(u_j). \tag{4.13}$$

The above is a system of three coupled sine-cosine polynomial equations in the three unknowns u_i, v_i, and u_j. Now, the first part of the solution can be applied for the intersection of any surface of revolution with any spatial curve. The idea is that the distance from the origin to any point on the surface of revolution is dependent only on the parameter u_i. Thus, we can obtain an equation that does not contain v_i by writing

$$\|\mathbf{T}^{(i)}(u_i, v_i)\|^2 = \|\mathbf{C}^{*(i)}(u_j)\|^2 \tag{4.14}$$

where $\|\cdot\|$ is the Euclidean norm. In our case, the above equation is not only free of v_i but also has a rather simple form:

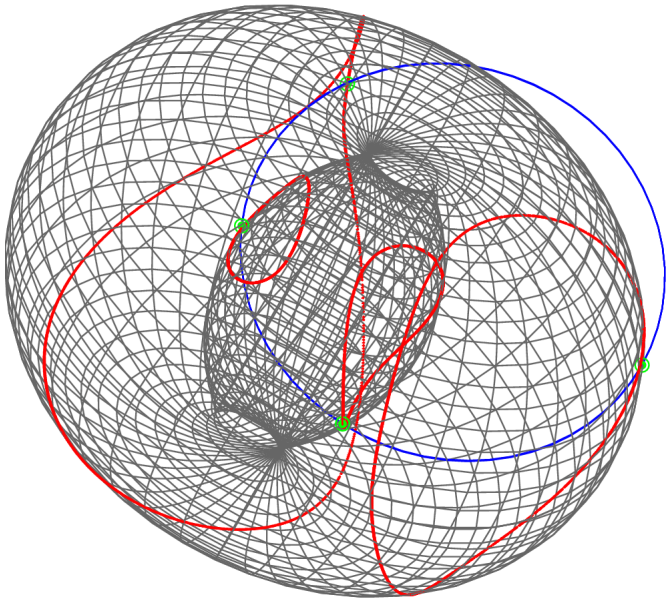

Figure 4.9: Intersection points between a cyclide and a circle.

$$A \sin u_i + B \cos u_i + C \sin u_j + D \cos u_j + E = 0 \tag{4.15}$$

where

$$\begin{aligned}
A &= 2r(p_y \cos\varphi - p_x \sin\varphi), \\
B &= 2r(p_x \cos\varphi \cos\vartheta - p_z \sin\vartheta + p_y \sin\varphi \cos\vartheta), \\
C &= -2r^*(p_y^* \cos\varphi^* - p_x^* \sin\varphi^*), \\
D &= -2r^*(p_x^* \cos\varphi^* \cos\vartheta^* - p_z^* \sin\theta^* + p_y^* \sin\varphi^* \cos\vartheta^*), \\
E &= p_x^2 + p_y^2 + p_z^2 + r^2 - (p_x^{*2} + p_y^{*2} + p_z^{*2} + r^{*2}).
\end{aligned}$$

The other equation that is also free of v_i is simply the last equation of the system of three equations (4.13). The z component of $\mathbf{T}^{(i)}(u_i, v_i)$ is clearly not dependent on v_i, since $z^{(i)}$ is the axis of revolution. Indeed, in our case, the equation is:

$$F \cos u_i + G \cos u_j + H = 0, \tag{4.16}$$

where

$$F = -r \sin\vartheta, \quad G = r^* \sin\vartheta, \quad H = p_z - p_z^*.$$

The second step of the solution process is to solve Eqs. (4.15) and (4.16) for $\sin u_i$ and $\cos u_i$ obtaining:

$$\sin u_i = \frac{(BG - DF)\cos u_j - CF \sin u_j + BH - EF}{AF}, \tag{4.17}$$

$$\cos u_i = -\frac{G \cos u_j + H}{F}. \tag{4.18}$$

Then, from the identity $\sin^2 u_i + \cos^2 u_i = 1$, we may obtain the following equation which is dependent only on u_j:

$$J \sin u_j + K \cos u_j + L \sin u_j \cos u_j + M \cos^2 u_j + N = 0 \tag{4.19}$$

where

$$\begin{aligned} J &= 2(CEF^2 - BCFH), \\ K &= 2(A^2GH + DEF^2 + B^2GH - BEFG - BDFH), \\ L &= 2(CDF^2 - BCFG), \\ M &= (DF - BG)^2 + (AG)^2 - (CF)^2, \\ N &= (BH - EF)^2 + (CF)^2 + (AH)^2 - (AF)^2. \end{aligned}$$

Next, we perform the tangent-half-angle substitution:

$$\sin u_j = \frac{2t_j}{1 + t_j^2}, \quad \cos u_j = \frac{1 - t_j^2}{1 + t_j^2}, \tag{4.20}$$

where $t_j = \tan(u_j/2)$. After substituting the above identities in Eq. (4.19), multiplying by $(1 + t_j^2)^2$, and rearranging, we obtain:

$$q_4 t_j^4 + q_3 t_j^3 + q_2 t_j^2 + q_1 t_j + q_0 = 0 \tag{4.21}$$

where

$$q_4 = M + N - K,\ q_3 = 2(J - L),\ q_2 = 2(N - M),\ q_1 = 2(J + L),\ q_0 = N + K + M.$$

The solutions for t_j may be found analytically by solving the polynomial of degree 4 in Eq. (4.21). Then, for each real solution for t_j, we obtain the corresponding value for u_j using $u_j = 2\tan^{-1}(t_j)$. Note that $\tan(u_j/2)$ is not defined at $u_j = \pi$, and indeed, if

the latter is a solution to Eq. (4.19), then $q_4 = 0$. Thus, if $q_4 = 0$, we add the solution $u_j = \pi$. Finally, we substitute the values for u_j into Eqs. (4.17) and (4.18) and solve for the unknown u_i.

The complete solution of the system of Eqs. (4.13) is an interesting problem involving a large number of degenerate cases. Indeed, this is exactly what should have been done if our task were the solution to the inverse kinematics of an *RRSR* kinematic chain. However, in our case we are not interested in the values of v_i, since we have assumed that there are no actuated limits. Hence, the only cases that need to considered are those that may prevent us from finding unique solutions for u_i and u_j.

In our particular problem, the generator circle of our special cyclide does not have an arbitrary position and orientation. Thus, some of the cases will drop out and should not be considered. Indeed, the constant $A = 2r(p_y \cos\varphi - p_x \sin\varphi)$ is equal to zero if and only if the axis of the generator circle intersects the $z^{(i)}$ axis. However, this could happen if and only if $\mathbf{j}_{A_i}^{(A_i)} = [\pm 1, 0, 0]^T$, in which case $B = 0$ and the cyclide degenerates to a *doubly-covered spherical ring* (or even a whole sphere).

Similarly, $F = -r \sin\vartheta$ is equal to zero if and only if $\mathbf{j}_{A_i}^{(A_i)} = [0, 0, \pm 1]^T$ in which case the cyclide degenerates to a *doubly-covered planar ring* or *annulus*. If also $G = r^* \sin\vartheta^*$ and $H = p_z - p_z^*$ are equal to zero, then the circle from vertex space j lies in the plane of the degenerated cyclide which could lead to having an arc as intersection rather than distinct points.

To simplify our task, we will eliminate the above degenerate cases by imposing the requirement that $\mathbf{j}_{A_i}^{(A_i)} \neq [\pm 1, 0, 0]^T$ and $\mathbf{j}_{A_i}^{(A_i)} \neq [0, 0, \pm 1]^T$. Indeed, installing the U joints in such a way that $\mathbf{j}_{A_i}^{(A_i)}$ is along the $x^{(A_i)}$ or $z^{(A_i)}$ axis is unlikely to lead to an optimal workspace.

Finally, it remains to consider the peculiar case $C = D = G = 0$ which geometrically corresponds to the circle from vertex space j lying in a plane parallel to the $x^{(i)}y^{(i)}$ plane and with centre on the $z^{(i)}$ axis. In this case, Eq. (4.19) degenerates to $N = 0$, so if it holds true, then the intersection we look for is the entire circle from vertex space j. If this happens, then we discretise the arc of the circle defined by the permissible range of u_j into a finite number of points.

Hence, in any case we end up with a finite number of intersection points (most frequently less than or equal to four) defined by the parameters u_j and u_i.

4.2.4 Implementation Procedure

Armed with the essential geometric tools previously described, we can now formulate the procedure for determining each vertex space (Section 4.2.4.1). The idea is to obtain explicitly the *contour* of the allowable spherical region and then to construct the boundary representation of the vertex space as the surface of revolution obtained by revolving that contour. After that, in Section 4.2.4.2, we consider the algorithm for obtaining the edges of the constant-orientation workspace.

4.2.4.1 Procedure for the Vertex Spaces

Each of the two circles $\mathcal{C}_{i,N}$ and $\mathcal{C}_{i,A}$ (recall Fig. 4.5), can be defined by a parametric equation, in which the parameter $u_{i,1}$ (respectively $u_{i,2}$) varies from $-\pi$ to $+\pi$. Then, for each vertex space, we calculate the intersection points between the two circles, storing the values of the parameter $u_{i,1}$ (respectively $u_{i,2}$) corresponding to each intersection point. Two different situations may occur depending on the value of $\xi = \cos^{-1}\left([0, -b_i, 0]\,\mathbf{j}_{A_i}^{(A_i)}\right)$.

Case 1: The number of intersection points is 0 or 1;
If $\xi \geq \pi/2 + \alpha$, then stop—vertex space i and, consequently, the constant-orientation workspace do not exist for the current orientation and design. Else, if $\xi \leq \pi/2 - \alpha$, then the contour of the allowable spherical region is the whole circle $\mathcal{C}_{i,A}$ and the vertex space constitutes a *cyclide*, i.e., $u_i \in [-\pi, \pi]$.

Case 2: The number of intersection points is 2;
If $\pi/2 + \alpha > \xi > \pi/2 - \alpha$, then there exist two distinct intersection points. For each circle, calculate the centre point of each of the two arcs connecting the intersection points. If the centre point lies on the hemisphere and on the spherical cap, then the arc belongs to the allowable spherical region. Store the arc's range as the ordered couple $\{u_{i,k}^s, u_{i,k}^e\}$, so that if $u_{i,k}^s < u_{i,k}^e$, then $u_{i,k} \in [u_{i,k}^s, u_{i,k}^e]$, else $u_{i,k} \in [u_{i,k}^s, +\pi] \cup (-\pi, u_{i,k}^e]$, where $k = 1, 2$. In this case, the vertex space has two distinct boundary surfaces, one of which is a portion of a torus, and the other is a portion of a special cyclide.

The number of boundary surfaces (1 or 2), the data for circle(s) $\mathcal{C}_{i,A}$ (and $\mathcal{C}_{i,N}$), and the range limits $\{u_{i,k}^s, u_{i,k}^e\}$ is all that needs to be saved for vertex space i. In addition, in Case 2, we also need to calculate and save the data for the two circles that define the edges of the vertex space. Finally, we modify vector $\mathbf{r}_{OO_i}$ that positions the origin of track frame i by adding to it vector $\mathbf{r}_{B_iC}$.

4.2.4.2 Procedure for the Constant-Orientation Workspace

Since each vertex space has up to two boundary surfaces, our problem can be decomposed into a finite number of intersections between surfaces. Each of the surfaces is a parametric toroidal surface depending on two parameters, $u_{i,k} \in [u^s_{i,k}, u^e_{i,k}]$ or $u_{i,k} \in [u^s_{i,k}, +\pi] \cup (-\pi, u^e_{i,k}]$, and $v_{i,k} \in [-\pi, +\pi]$, where i corresponds to the vertex space to which the surface belongs, and $k = 1, 2$.

We initialise as many lists as there are pairs of boundary surfaces. There may be up to 60 *inter-space pairs* (15 pairs of vertex spaces $\times$ 4 pairs of boundary surfaces, each pair coming from different vertex spaces) and 6 *intra-space pairs*, each pair coming from the same vertex space.

To compute the edges of the workspace, we take each inter-space pair of surfaces—one belonging to vertex space i and the other to vertex space j. Then, for the torus to which one of the boundary surfaces belongs, say from vertex space j, we start to increment the parameter v_j from $-\pi$ to π. For each discrete value of v_j, we find the intersection points, in terms of the parameters u_j and u_i, between the corresponding circle and the cyclide to which the other boundary surface belongs using the algorithm presented in the Section 4.2.3. The next step is to eliminate those solutions that are not within the permissible ranges of u_j and u_i.

Then, we simply calculate the Cartesian coordinates of each point corresponding to a solution for u_j. Each such point lies on the boundaries of vertex spaces i and j. Then, at this point, we solve the inverse kinematic problem for all legs except chains i and j, and check for all constraints. The point will lie inside the four vertex spaces if all constraints are satisfied. The remaining points belong to the edges of the constant-orientation workspace and are put into a corresponding list.

Finally, for each intra-space pair of boundary surfaces, say corresponding to chain i, we already know the two circles constituting the intersection curves. Then, we intersect each circle with the (maximum 5×2) boundary surfaces of all vertex spaces except vertex space i. This is done again by using the algorithm presented in Section 4.2.3. The intersection points divide each circle into a maximum number of 4×10 arcs. For each arc, we calculate its centre point, and at this point, we solve the inverse kinematics for the five legs. If all constraints are satisfied, then the corresponding arc is discretised and put into a corresponding list.

4.2.5 Examples and Discussion

To illustrate our geometric method, we take as an example a 6-$\underline{R}US$ parallel mechanism whose data is given in Table 4.2.5. In this table, $\mathbf{z}_i$ denotes the unit vector along the $z^{(i)}$ axis of track frame i, expressed in the base frame. In addition, $\ell_1 = 90$, $\ell_2 = 150$, $\alpha = 70°$, and $\delta_i = (-1)^{i+1}$ $(i = 1, \ldots, 6)$. In our implementation, we adopt the choice of *Tilt & Torsion angles* (Chapter 3) to represent the orientation of the platform.

Table 4.1: Geometry of the 6-$\underline{R}US$ parallel mechanism.

i	$\mathbf{r}_{OO_i}$	$\mathbf{z}_i$	$\mathbf{r}'_{CB_i}$	$\mathbf{j}_{A_i}^{(A_i)}$
1	$\begin{bmatrix} 100.000 \\ -173.205 \\ 0.000 \end{bmatrix}$	$\begin{bmatrix} -0.500 \\ 0.866 \\ 0.000 \end{bmatrix}$	$\begin{bmatrix} 70.707 \\ -84.265 \\ 50.000 \end{bmatrix}$	$\begin{bmatrix} 0.380 \\ -0.912 \\ 0.152 \end{bmatrix}$
2	$\begin{bmatrix} 200.000 \\ 0.000 \\ 0.000 \end{bmatrix}$	$\begin{bmatrix} -1.000 \\ 0.000 \\ 0.000 \end{bmatrix}$	$\begin{bmatrix} 108.329 \\ -19.101 \\ 50.000 \end{bmatrix}$	$\begin{bmatrix} 0.380 \\ 0.912 \\ 0.152 \end{bmatrix}$
3	$\begin{bmatrix} 100.000 \\ 173.205 \\ 0.000 \end{bmatrix}$	$\begin{bmatrix} -0.500 \\ -0.866 \\ 0.000 \end{bmatrix}$	$\begin{bmatrix} 37.622 \\ 103.366 \\ 50.000 \end{bmatrix}$	$\begin{bmatrix} 0.380 \\ -0.912 \\ 0.152 \end{bmatrix}$
4	$\begin{bmatrix} -100.000 \\ 173.205 \\ 0.000 \end{bmatrix}$	$\begin{bmatrix} 0.500 \\ -0.866 \\ 0.000 \end{bmatrix}$	$\begin{bmatrix} -37.622 \\ 103.366 \\ 50.000 \end{bmatrix}$	$\begin{bmatrix} 0.380 \\ 0.912 \\ 0.152 \end{bmatrix}$
5	$\begin{bmatrix} -200.000 \\ 0.000 \\ 0.000 \end{bmatrix}$	$\begin{bmatrix} 1.000 \\ 0.000 \\ 0.000 \end{bmatrix}$	$\begin{bmatrix} -108.329 \\ -19.101 \\ 50.000 \end{bmatrix}$	$\begin{bmatrix} 0.380 \\ -0.912 \\ 0.152 \end{bmatrix}$
6	$\begin{bmatrix} -100.000 \\ -173.205 \\ 0.000 \end{bmatrix}$	$\begin{bmatrix} 0.500 \\ 0.866 \\ 0.000 \end{bmatrix}$	$\begin{bmatrix} -70.707 \\ -84.265 \\ 50.000 \end{bmatrix}$	$\begin{bmatrix} 0.380 \\ 0.912 \\ 0.152 \end{bmatrix}$

The proposed methodology was implemented in Matlab 5 and take full advantage of the newly introduced data structures and cell arrays. Three examples of the constant-orientation workspace of the 6-$\underline{R}US$ parallel mechanism are presented here. The first one is at the *reference orientation* (Fig. 4.10), $\phi = \theta = \sigma = 0°$—a workspace measure

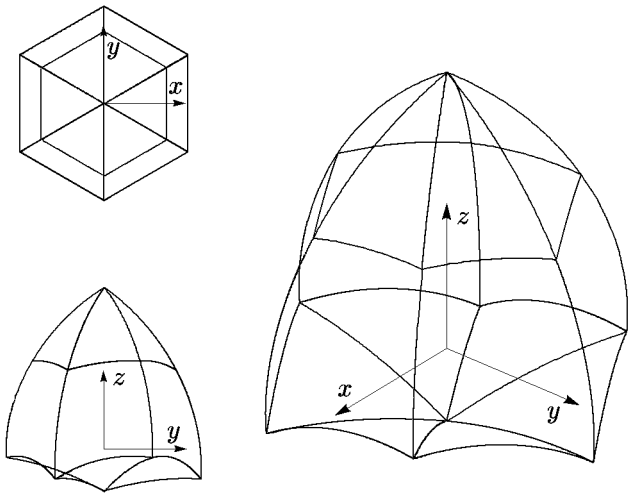

Figure 4.10: Constant-orientation workspace for the reference orientation.

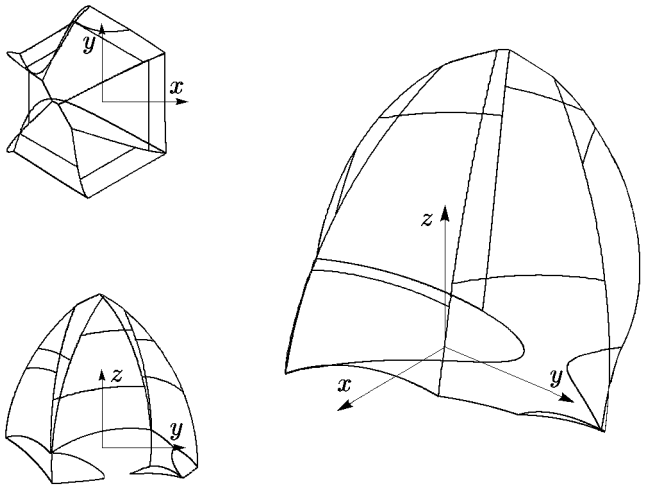

Figure 4.11: Constant-orientation workspace for $\phi = \sigma = 0^\circ$ and $\theta = 10^\circ$.

that is highly misleading if taken solely at this orientation. The second example is at a slightly tilted orientation (Fig. 4.11), $\phi = \sigma = 0^\circ$ and $\theta = 10^\circ$ already showing some substantial decrease in the workspace. The final example shows clearly how a slightly greater tilt of $\theta = 25^\circ$ at $\phi = 50^\circ$ plus a very small twist of $\sigma = 10^\circ$ reduces, distorts, and offsets the workspace significantly (Fig. 4.12).

These three examples demonstrate that computing and drawing the edges of the constant-orientation workspace provides a relatively intuitive representation. Naturally, these 2D projections are not sufficient, but in practice, they are to be displayed on a computer screen where the user can interactively manipulate the workspace wireframe and see it from any direction.

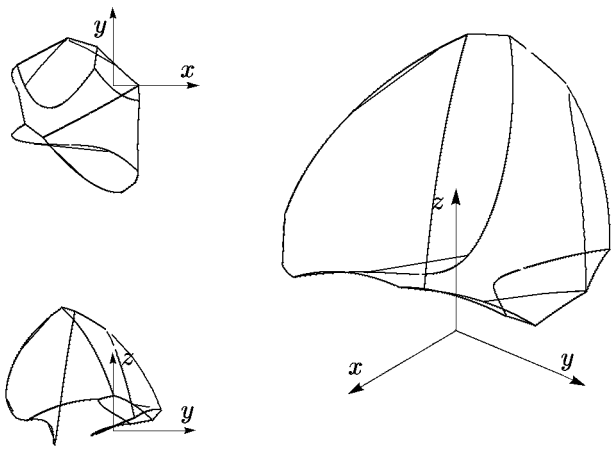

Figure 4.12: Constant-orientation workspace for $\phi = 50°$, $\theta = 25°$, and $\sigma = 10°$.

Our representation, however, has several faults. The biggest of all is that the workspace wireframe is not a set of curves or polylines but a "thin point cloud" of points. Indeed, it would be too time consuming to order the coordinates of these points. The core of this problem lies in the intersection between two cyclides (recall Figs. 4.7 and 4.9). In order to have the maximum four closed-loop intersection curves as polylines, a large number of checks should be performed.

The same cyclide/cyclide intersection procedure leads to another imperfection. Namely, the distances between the subsequent points representing a particular edge, generally, vary significantly. The latter is due to the fact that each cyclide has been sliced into generator circles of equiangular spacing. This shortcoming can be avoided by using some adaptive slicing which attempts to preserve the distance between successive points. However, unlike other similar problems, such a procedure would, in this case, be too complex and time consuming.

Regardless of these two unavoidable disadvantages, our method remains a better solution than a brute-force discretisation method. Our procedure for the wireframe representation can be easily implemented in the proprietary software of any commercial 6-$\underline{R}US$ parallel robot, despite its design. Alternatively, if the manufacturer or user has either a commercial CAD/CAM software such as CATIA or some Boolean algebra library, our method can be implemented even more easily. Indeed, we should admit that, from our previous experience, we know that a CAD/CAM software will generally produce the workspace as a wireframe and even solid, faster than a complex exact method as ours implemented in Matlab.

Our strongest contribution, however, is the geometric description of the constant-orientation workspace of a general 6-$\underline{R}US$ parallel mechanism. This is of great help to the designer in finding the optimal configuration from a workspace point of view. It provides insights to answer such questions as "How should the base U joints be mounted?" and "How should the axes of the motors be placed?". None of these questions can be answered correctly by simply using a numerical optimisation procedure since we are dealing not only with quantitative measures (i.e., workspace volume) but also with qualitative measures (i.e., workspace shape).

The reader may derive other benefits from our geometric method. Firstly, we describe the geometry of a special cyclide which is a surface that appears in the analysis of other serial and parallel mechanisms. Secondly, as we already mentioned, our solution to the problem of intersecting a circle with a cyclide is basically the solution to the inverse kinematics of a general $RSRR$ serial chain. Finally, we bring to light the circle decomposition method, which may be used to obtain the intersection curves between various *ringed surfaces*. Ringed surfaces are surfaces generated by sweeping a circle (with non constant radius) along a curve (Johnstone, 1993). Such surfaces obviously appear in most mechanisms with revolute joints.

4.3 Computing the Horizontal Cross-Sections of the Constant-Orientation Workspace of General 6-$\underline{R}US$ Parallel Mechanisms

An important disadvantage of computing and displaying only the edges of the constant-orientation workspace is that it is not possible to make any quantitative measure. For example, in an optimisation algorithm, we would need to know the (approximate) volume of the constant-orientation workspace for various key orientations. This information is readily available if we use a CAD/CAM software or a solid-geometry Boolean algebra library. However, in many cases these expensive packages are not available and alternative solutions to our problem are needed.

The most obvious way to enhance the representation of the constant-orientation workspace and computing the approximate workspace volume is to calculate and draw the horizontal cross-sections of the workspace in addition to the edges. This task is, however, too difficult if we decide to keep taking into account the mechanical constraints

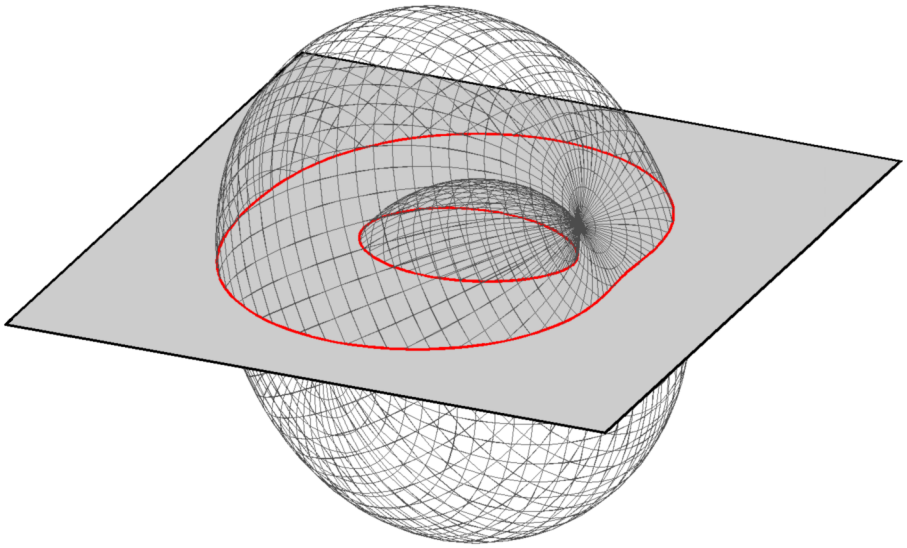

Figure 4.13: Cross-section of a torus.

on the U joints. Indeed, in an optimisation procedure, it is usual to ignore these joint limits and optimise the orientations of the joint limit cones, once the geometry of the mechanism is decided.

Therefore, in this section, we will deal only with six identical tori. The part needed for computing the edges of the constant-orientation workspace can be easily derived from the general procedure described in the previous section. Besides, if optimisation is our sole goal, we do not need to compute the edges of the workspace. Therefore, we will not describe the simplified procedure for computing the workspace wireframe of a 6-$\underline{R}US$ parallel mechanism with no joint limits. It should be noted, however, that we have implemented this procedure in our new Matlab program.

We may, therefore, concentrate directly on the problem of computing the horizontal slices of a torus in an arbitrary orientation (Fig. 4.13). We will first derive the equation of such a toric section, which is a bicircular quartic. Unfortunately, a toric section can only be represented by an algebraic equation and not a parametric one. Hence, the only way to draw it and further manipulate it is to discretise it to a polygon. Once we have the six polygonised toric sections it remains to intersect them and compute the area of the intersection. The process can be repeated at various altitudes, the areas integrated, and the approximate workspace volume found.

4.3.1 Algebraic Equation of a Toric Section

Referring to the algebraic equation of our cyclide represented by Eq. (4.9), we may directly write the equation for the surface of vertex space i, a torus, in track frame i:

$$\left(x^{(i)2} + y^{(i)2} + z^{(i)2} - \ell_1^2 - \ell_2^2\right)^2 = 4\ell_1^2\left(\ell_2^2 - z^{(i)2}\right). \tag{4.22}$$

To express the above equation in the base frame, we apply the following coordinate transformation:

$$\begin{bmatrix} x^{(i)} \\ y^{(i)} \\ z^{(i)} \end{bmatrix} = \begin{bmatrix} \cos\varphi_i\cos\vartheta_i & \sin\varphi_i\cos\vartheta_i & -\sin\vartheta_i \\ -\sin\varphi_i & \cos\varphi_i & 0 \\ \cos\varphi_i\sin\vartheta_i & \sin\varphi_i\sin\vartheta_i & \cos\vartheta_i \end{bmatrix} \begin{bmatrix} x - x_{OO_i} \\ y - y_{OO_i} \\ z - z_{OO_i} \end{bmatrix} \tag{4.23}$$

where ϑ_i is the angle between the $z^{(i)}$ axis and the base z axis, and φ_i is the angle between the base x axis and the projection of $z^{(i)}$ onto the the base xy plane. Substituting the above new expressions for $x^{(i)}$, $y^{(i)}$, and $z^{(i)}$ in Eq. (4.22) we obtain:

$$(x^2+y^2)(x^2+y^2+q_1x+q_2y) + q_3x^2 + q_4xy + q_5y^2 + q_6x + q_7y + q_8 = 0, \tag{4.24}$$

where the constant coefficients are

$$\begin{aligned}
q_1 &= -4x_{OO_i}, \\
q_2 &= -4y_{OO_i}, \\
q_3 &= 2(2\ell_1^2\cos^2\varphi_i\sin^2\vartheta_i + 2x_{OO_i}^2 + s_1), \\
q_4 &= 8(\ell_1^2\sin\varphi_i\cos\varphi_i\sin^2\vartheta_i + x_{OO_i}y_{OO_i}), \\
q_5 &= 2\left(-2\ell_1^2 s_3 + 2y_{OO_i}^2 + s_2\right), \\
q_6 &= 4(-x_{OO_i}s_1 - 2\ell_1^2 s_4\sin\vartheta_i\cos\varphi_i), \\
q_7 &= 4\big(-y_{OO_i}s_2 - 2\ell_1^2 x_{OO_i}\sin\varphi_i\cos\varphi_i\sin^2\vartheta_i + 2\ell_1^2 y_{OO_i}s_3 \\
&\quad -2\ell_1^2(z_{OO_i} - z)\sin\varphi_i\sin\vartheta_i\cos\vartheta_i\big), \\
q_8 &= s_1^2 - 4\ell_1^2(\ell_2^2 - s_4^2), \\
s_1 &= x_{OO_i}^2 + y_{OO_i}^2 + (z_{OO_i} - z)^2 - \ell_1^2 - \ell_2^2, \\
s_2 &= x_{OO_i}^2 + y_{OO_i}^2 + (z_{OO_i} - z)^2 + \ell_1^2 - \ell_2^2, \\
s_3 &= \cos^2\vartheta_i + \cos^2\varphi_i\sin^2\vartheta_i, \\
s_4 &= x_{OO_i}\cos\varphi_i\sin\vartheta_i + y_{OO_i}\sin\varphi_i\sin\vartheta_i + (z_{OO_i} - z)\cos\vartheta_i.
\end{aligned}$$

The bicircular quartic from Eq. (4.24) that represents a general *toric section* can be written in a much more compact form under the following coordinate transformation:

$$x = \hat{x}\cos\varphi_i - \hat{y}\sin\varphi_i + x_{OO_i}, \tag{4.25}$$
$$y = \hat{x}\sin\varphi_i + \hat{y}\cos\varphi_i + y_{OO_i}, \tag{4.26}$$
$$z = \hat{z} + z_{OO_i}. \tag{4.27}$$

In fact, the new frame $\hat{x}\hat{y}\hat{z}$ is simply obtained by rotating frame i at an angle $-\varphi_i$ about its $y^{(i)}$ axis. We say that in the new frame, our toric section is expressed in *canonical form* with the following simple equation:

$$(\hat{x}^2 + \hat{y}^2)^2 + \hat{q}_3\hat{x}^2 + \hat{q}_5\hat{y}^2 + \hat{q}_6\hat{x} + \hat{q}_8 = 0, \tag{4.28}$$

where

$$\begin{aligned}
\hat{q}_3 &= 4\ell_1^2\sin^2\vartheta_i + 2\hat{s}_1,\\
\hat{q}_5 &= 2\hat{s}_1,\\
\hat{q}_6 &= 8\ell_1 z\sin\vartheta_i\cos\vartheta_i,\\
\hat{q}_8 &= \hat{s}_1^2 - 4\ell_1^2(\ell_2^2 - z^2\cos^2\vartheta_i),\\
\hat{s}_1 &= z^2 - \ell_1^2 - \ell_2^2.
\end{aligned}$$

The toric section in canonical form is symmetric with respect to the $\hat{x}$ axis but takes a variety of different shapes, some of which were shown in Fig. 4.8(b). One of its simplest forms, the *spiric section* (occurring when $\vartheta = \pi/2$), has been studied as early as 150 BC by the Greek mathematician Perseus. Unfortunately, however, even this simplest form of the toric section cannot be written in polar form or with a parametric equation. Therefore, we are obliged to work with its algebraic equation and subsequently polygonise the toric section so that we may visualise it.

4.3.2 Intersection Between two Toric Sections

As we already mentioned, and as will be discussed in the next section, in order to compute the horizontal cross-sections of the constant-orientation workspace of 6-$\underline{R}US$ parallel mechanisms we will need to polygonise all toric sections. Therefore, if we only

need to compute a close estimate of the volume of the constant-orientation workspace, we do not need to know the exact intersection points between the toric sections.

However, if we wish to represent the constant-orientation workspace using both horizontal slices and edges we will need to know the exact locations of the intersection points between all pairs of toric sections. These points lie on the edges of the workspace and, therefore, may enhance the continuity of the (discretised) workspace edges. What is more, they need to be incorporated in the polygonised models of the toric sections, so that, as a result, the vertices of each horizontal cross-section lie exactly on the workspace edges.

In order to simplify the intersection problem, we will compute the intersection points in the natural frame of one of the quartics. Note, that under any planar coordinate transformation, the equation of the toric section remains in the general form represented by Eq. (4.24). Therefore, our algebraic problem is to find the solutions of two quartic equations, one of the form represented by Eq. (4.28) and one of the form given by Eq. (4.24):

$$(x^2+y^2)(x^2+y^2+p_1x+p_2y)+p_3x^2+p_4xy+p_5y^2+p_6x+p_7y+p_8=0, \quad (4.29)$$

$$(x^2+y^2)^2+q_3x^2+q_5y^2+q_6x+q_8=0. \quad (4.30)$$

Since both quartics have a circularity of 2, we may expect to have as much as eight solutions to such a problem. We will obtain them using *dialytic elimination* (Raghavan and Roth, 1995). If we suppress the variable y, then we obtain the following two quartics in x:

$$x^4+m_3x^3+m_2x^2+m_1x+m_0=0, \quad (4.31)$$

$$x^4+n_2x^2+n_1x+n_0=0, \quad (4.32)$$

where

$$m_3=p_1, \;\; m_2=2y^2+p_2y+p_3, \;\; m_1=p_1y^2+p_4y+p_6,$$
$$m_0=y^4+p_2y^3+p_5y^2+p_7y+p_8,$$
$$n_2=2y^2+q_3, \;\; n_1=q_6, \;\; n_0=y^4+q_5y^2+q_8.$$

The resultant of these two equations is

$$\mathbf{D} = \begin{bmatrix} 1 & m_3 & m_2 & m_1 & m_0 & 0 & 0 & 0 \\ 0 & 1 & m_3 & m_2 & m_1 & m_0 & 0 & 0 \\ 0 & 0 & 1 & m_3 & m_2 & m_1 & m_0 & 0 \\ 0 & 0 & 0 & 1 & m_3 & m_2 & m_1 & m_0 \\ 1 & 0 & n_2 & n_1 & n_0 & 0 & 0 & 0 \\ 0 & 1 & 0 & n_2 & n_1 & n_0 & 0 & 0 \\ 0 & 0 & 1 & 0 & n_2 & n_1 & n_0 & 0 \\ 0 & 0 & 0 & 1 & 0 & n_2 & n_1 & n_0 \end{bmatrix} \tag{4.33}$$

such that the system of two quartic equations, Eqs. (4.31) and (4.32), is equivalent to the following system of eight equations:

$$\mathbf{D}[x^7, x^6, x^5, x^4, x^3, x^2, x, 1]^T = \mathbf{0}. \tag{4.34}$$

Setting the determinant of the above resultant equal to zero gives us a univariate polynomial in y of degree eight. The expressions for all nine coefficients of this polynomial can be easily obtained using a computer algebra system such as Maple. Introducing several new variables, i.e., for $q_3 - p_3$, $q_6 - p_6$, $q_5 - p_5$, $q_8 - p_8$, $q_3 - p_3 - q_5 + p_5$, and $q_5 - q_3$, reduces the total of nine coefficients to about 260 lines (80 characters each). Naturally, these will not be shown on the pages of this thesis.

Next, the polynomial in y of degree eight is to be solved using a numerical procedure. Only the real and unique solutions are to be retained. Once these solutions are available, for each value of y, the corresponding (maximum four) value(s) of x should be found.

To do so, we rewrite the matrix equation (4.34) as follows:

$$\bar{\mathbf{D}}[x^7, x^6, x^5, x^4, x^3, x^2, x]^T = [0, 0, 0, -m_0, 0, 0, 0, -n_0]^T, \tag{4.35}$$

where the 8×7 matrix $\bar{\mathbf{D}}$ is obtained from matrix $\mathbf{D}$ by erasing its last column. We substitute the current value of y in $\bar{\mathbf{D}}$, which becomes numerical. Then we run all eight 7×7 submatrices of $\bar{\mathbf{D}}$, denoted by $\hat{\mathbf{D}}$, obtained by erasing one row and select the one that has highest condition number. If the number is sufficiently high, i.e., if matrix $\hat{\mathbf{D}}$ is not singular, we solve for the corresponding value of x by taking the last component of the vector $\hat{\mathbf{D}}^{-1}[0, 0, 0, -m_0, 0, 0, 0, -n_0]^T$.

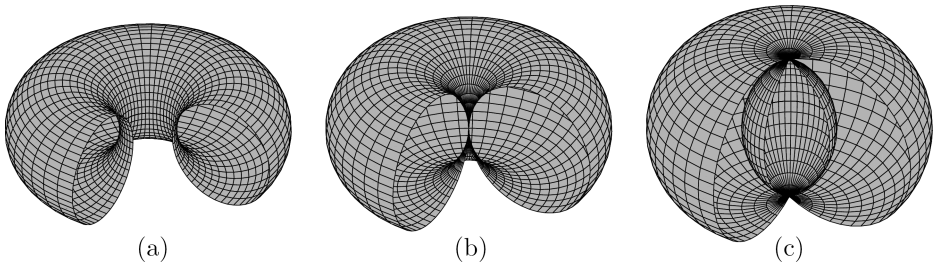

Figure 4.14: Cutaways of the three types of tori: (a) ring torus, (b) horn torus, and (c) spindle torus.

If, however, matrix $\hat{\mathbf{D}}$ is singular, then we have more than one solution for x. The simplest and most stable method to get all (maximum four) solutions for x is to substitute the value of y and to compute all four solutions of each of Eqs. (4.31) and (4.32), and then to retain only those solutions that satisfy both equations.

Following the above procedure, we find the intersection points between all fifteen pairs of toric sections. We create a two dimensional list for each of the six toric sections, and for each pair, we save the coordinates of the maximum eight intersection points to the lists of both toric sections. These coordinates are expressed in the base frame.

4.3.3 Polygonisation of the Toric Section

Everything that we have done up to now in Section 4.3 is valid for any relationship between ℓ_1 and ℓ_2. If $\ell_1 > \ell_2$, the vertex space as shown in Fig. 4.14(a) is a *ring torus*, the common form of torus that looks like a doughnut with a hole. If $\ell_1 = \ell_2$, the vertex space as shown in Fig. 4.14(b) is a *horn torus*. Finally, if $\ell_1 < \ell_2$, the vertex space as shown in Fig. 4.14(c) is a *spindle torus*. The spindle torus has an internal void that makes the workspace of a 6-$\underline{R}US$ parallel mechanism more intricate. It is partly because of such voids that discretisation methods for computing the constant-orientation workspace fail.

The relationship between ℓ_1 and ℓ_2 does not come into play in the problems of describing the algebraic equation of a torus or a toric section and the intersection between two toric sections. However, the ratio between these two radii is important in polygonising the toric sections. In practice, it is more common to see $\ell_1 < \ell_2$. Therefore, we will describe only the method for polygonising a cross-section of a spindle torus. Note, however, that polygonising a cross-section of a ring or horn torus is even simpler.

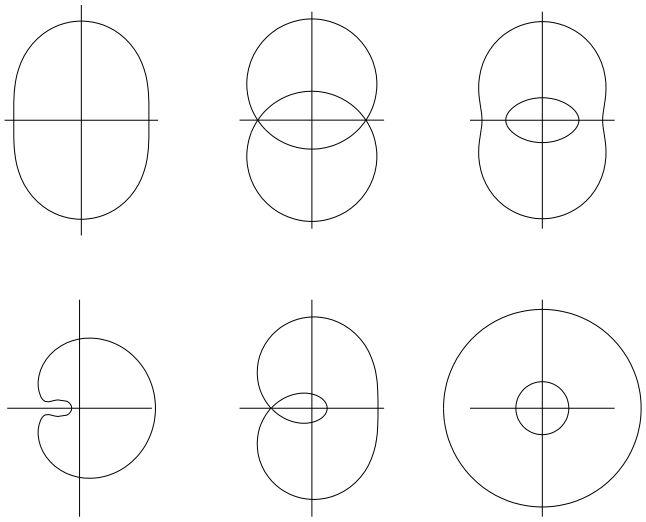

Figure 4.15: Various cross-sections of a spindle torus.

Figure 4.15 shows all basic types of shapes of the cross-sections of a spindle torus. We know that the sections, as considered in their natural frames, are always symmetric with respect to the $\hat{x}$ axis. The cross-sections have always a single exterior curve but some may have a single interior curve as well. While most forms can be easily polygonised, there is one rarely appearing shape, the one in the lower left corner, that requires some special attention. Let us refer to this particular shape as the *complex crescent shape*.

The first part of the algorithm for polygonisation of a toric section consists in computing the coefficients of the algebraic equation of the section in its natural frame, as described by Eq. (4.28). We also transform the coordinates of the intersection points, as found following the method of the preceding section, to the same natural frame. Then, if $z < 0$, we make it positive, $z = -z$, as well as the $\hat{x}$ coordinates of the intersection points. This mirror reflection with respect to the $\hat{y}$ axis is performed to ensure that the cavity of the complex crescent shape (in case it turns out later that we are dealing with such) is on the left. Note that this is true under the natural assumption that $\vartheta_i \in [0, \pi/2]$.

Next, we need to calculate the intercepts of the toric section with the $\hat{x}$ axis, i.e., set $\hat{y} = 0$ and solve

$$\hat{x}^4 + \hat{q}_3\hat{x}^2 + \hat{q}_6\hat{x} + \hat{q}_8 = 0. \tag{4.36}$$

The real solutions (maximum four) to the above equation should be ordered, i.e.,

$\hat{x}_1 \leq \hat{x}_2 \leq \hat{x}_3 \leq \hat{x}_4$. Based on this information we should now compute a centre defined by $\hat{x}_c$ which will be used for our ray discretisation method. If the number of real solutions of Eqs. (4.36) is equal to four, then we simply select $\hat{x}_c = (\hat{x}_2+\hat{x}_3)/2$. However, if $\hat{x}_2 = \hat{x}_3$, we move the centre slightly to the right, e.g., $\hat{x}_c = \hat{x}_c + 0.1(\hat{x}_4 - \hat{x}_3)/2$. Note that it is not possible to have all four solutions coinciding. Neither is it possible to have only one or three real solutions—complex solutions go in pairs. Similarly, if we have only two real solutions, then $\hat{x}_c = (\hat{x}_1 + \hat{x}_2)/2$. Finally, if there are no real solutions, then the toric section does not exist, i.e. the constant-orientation workspace does not exist at the current altitude.

Once we have calculated the centre $(\hat{x}_c, 0)$ for the toric section, we may directly obtain the maximum four vertical intercepts at $\hat{x} = \hat{x}_c$:

$$\hat{y}_1 = \frac{1}{2}\sqrt{-2\hat{q}_5 - 4\hat{x}_c^2 + 2\sqrt{\hat{q}_5^2 + 4(\hat{q}_5 - \hat{q}_3)\hat{x}_c^2 - 4\hat{q}_8}}, \tag{4.37}$$

$$\hat{y}_2 = \frac{1}{2}\sqrt{-2\hat{q}_5 - 4\hat{x}_c^2 - 2\sqrt{\hat{q}_5^2 + 4(\hat{q}_5 - \hat{q}_3)\hat{x}_c^2 - 4\hat{q}_8}}. \tag{4.38}$$

and $\hat{y}_3 = -\hat{y}_1$ and $\hat{y}_4 = -\hat{y}_2$, where $\hat{y}_1$ (if real) is the upper-most intercept that is part of the exterior contour, while $\hat{y}_2$ (if real) is the upper-most intercepts from the interior contour.

Let there be a line passing through the centre $(\hat{x}_c, 0)$ and making angle u with the $\hat{x}$ axis, i.e.,

$$s_u(\hat{x} - \hat{x}_c) - c_u\hat{y} = 0, \qquad u \in (0, \pi/2), \tag{4.39}$$

where $c_u \equiv \cos u$ and $s_u \equiv \sin u$. This line intersects the toric section in maximum four points which may be found by solving the following univariate quartic in $\hat{x}$ and substituting subsequently in Eq. (4.39) to find $\hat{y}$:

$$\begin{gathered}\hat{x}^4 - 4\hat{x}_c s_u^2\,\hat{x}^3 + (c_u^4\,\hat{q}_3 + s_u^2\,c_u^2\,\hat{q}_5 + 6s_u^4\,\hat{x}_c^2 + 2s_u^2\,c_u^2\,\hat{x}_c^2)\hat{x}^2 \\ +(c_u^4\,\hat{q}_6 - 2s_u^2\,c_u^2\,\hat{x}_c\,\hat{q}_5 - 4s_u^4\,\hat{x}_c^3)\hat{x} + c_u^4\,\hat{q}_8 + s_u^2\,c_u^2\,\hat{x}_c^2\,\hat{q}_5 + s_u^4\hat{x}_c^4 = 0.\end{gathered} \tag{4.40}$$

Finally, the algorithm for computing the polygon approximation of the toric section is as follows:

S1 Convert the list of intersection points to the list of angles $\mathbf{u}_{int}$, so that for each intersection point, there is a value in $\mathbf{u}_{int}$ for which the corresponding line passes

through that point. Render the elements of the list $\mathbf{u}_{int}$ in ascending order and eliminate any repeating values.

S2 Initialise one-dimensional arrays $\mathbf{E}_{left,x}$ and $\mathbf{E}_{left,y}$, as well as $\mathbf{E}_{right,x}$ and $\mathbf{E}_{right,y}$, which will contain the x and y coordinates of the left and right parts of the exterior contour. Note that by varying u in the range $(0, \pi/2)$, we will be able to obtain the lower-left and upper-right parts of the toric section, which after reflection will give us the whole toric section (Fig. 4.16). Assign $\hat{x}_1$ and 0 to respectively $\mathbf{E}_{left,x}$ and $\mathbf{E}_{left,y}$, and the rightmost horizontal intercept ($\hat{x}_2$ or $\hat{x}_4$) and 0 to respectively $\mathbf{E}_{right,x}$ and $\mathbf{E}_{right,y}$.

S3 If there are four, rather than just two, horizontal intercepts, then the toric section obviously has an interior contour. Therefore, initialise one-dimensional arrays $\mathbf{I}_{left,x}$ and $\mathbf{I}_{left,y}$, as well as $\mathbf{I}_{right,x}$ and $\mathbf{I}_{right,y}$, which will contain the x and y coordinates of the lower-left and upper-right parts of the interior contour. Assign $\hat{x}_2$ and 0 to respectively $\mathbf{I}_{left,x}$ and $\mathbf{I}_{left,y}$, and $\hat{x}_3$ and 0 to respectively $\mathbf{I}_{right,x}$ and $\mathbf{I}_{right,y}$.

S4 Initialise one-dimensional temporary arrays $\mathbf{E}_{1,x}$, $\mathbf{E}_{1,y}$, $\mathbf{E}_{2,x}$, $\mathbf{E}_{2,y}$, which will be used in case we have a complex crescent shape.

S5 Set the initial value of u to the first value from $\mathbf{u}_{int}$ or, for example, 0.01, whichever smaller. If a value from $\mathbf{u}_{int}$ has been used, then remove that entry from the list.

S6 Solve Eq. (4.40) for the current u. There should be either two or four real solutions, which need to be arranged in ascending order, $\hat{x}_{u,1} \leq \hat{x}_{u,2} (\leq \hat{x}_{u,3} \leq \hat{x}_{u,4})$.

S7 If there are only two horizontal intercepts, i.e., if we are dealing with a single contour, then two cases are possible. If there are two solutions to Eq. (4.40), then add $\hat{x}_{u,1}$ to $\mathbf{E}_{left,x}$ and the corresponding $\hat{y}_{u,1} = \tan u \, (\hat{x}_{u,1} - \hat{x}_c)$ to $\mathbf{E}_{left,y}$, as well as $\hat{x}_{u,2}$ to $\mathbf{E}_{right,x}$ and $\hat{y}_{u,2}$ to $\mathbf{E}_{right,y}$. Increment u with 0.04 unless the result is larger than the first element of $\mathbf{u}_{int}$, in which case assign the value of that element to u and remove the element from $\mathbf{u}_{int}$. If there are four solutions to Eq. (4.40), then we are dealing with a complex crescent shape, as shown in Fig. 4.16(b). Assign $\mathbf{E}_{1,x} = \mathbf{E}_{left,x}$ and $\mathbf{E}_{1,y} = \mathbf{E}_{left,y}$ and remove all values from $\mathbf{E}_{left,x}$ and $\mathbf{E}_{left,x}$. Add the four intersection points as $\hat{x}_{u,1}$ to $\mathbf{E}_{left,x}$, $\hat{x}_{u,4}$ to $\mathbf{E}_{right,x}$, $\hat{x}_{u,3}$ to $\mathbf{E}_{1,x}$, and $\hat{x}_{u,2}$ to $\mathbf{E}_{2,x}$, and similarly for the $\hat{y}_{u,i}$ values ($i = 1, 2, 3, 4$). Increment u with 0.01 unless the result is larger than the first element of $\mathbf{u}_{int}$, in which case assign the value of that element to u and remove the element from $\mathbf{u}_{int}$.

S8 If there are four horizontal intercepts, i.e., if we are dealing with two contours, simply add $\hat{x}_{u,1}$ to $\mathbf{E}_{left,x}$, $\hat{x}_{u,4}$ to $\mathbf{E}_{right,x}$, $\hat{x}_{u,2}$ to $\mathbf{I}_{left,x}$ and $\hat{x}_{u,3}$ to $\mathbf{I}_{right,x}$, and

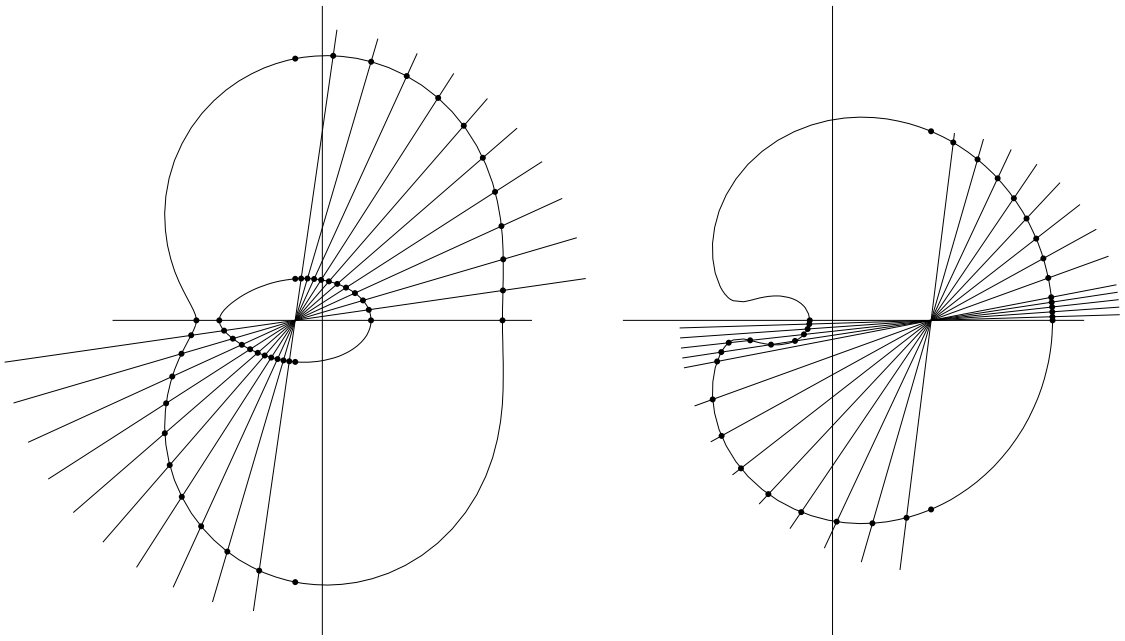

(a) (b)

Figure 4.16: Examples of polygonisation of a toric section.

similarly for the $\hat{y}_{u,i}$ values ($i = 1, 2, 3, 4$). Increment u with 0.04 unless the result is larger than the first element of $\mathbf{u}_{int}$, in which case assign the value of that element to u and remove the element from $\mathbf{u}_{int}$.

S9 Repeat steps 6 through 8 until $u < \pi/2$

S10 Finally add $\hat{x}_c$ and $\hat{y}_1$ to respectively $\mathbf{E}_{left,x}$ and $\mathbf{E}_{left,y}$, and if an inner contour exists, add $\hat{x}_c$ and $\hat{y}_2$ to respectively $\mathbf{I}_{left,x}$ and $\mathbf{I}_{left,y}$.

S11 In case a complex crescent shape was encountered, reverse the order of $\mathbf{E}_{2,x}$ as well as of $\mathbf{E}_{2,y}$, and assign $\mathbf{E}_{left,x} = \{\mathbf{E}_{1,x}, \mathbf{E}_{2,x}, \mathbf{E}_{left,x}\}$ and $\mathbf{E}_{left,y} = \{\mathbf{E}_{1,y}, \mathbf{E}_{2,y}, \mathbf{E}_{left,y}\}$.

S12 Create the one-dimensional lists:

$$\begin{aligned}
\mathbf{P}_{ext,x} &= \{\mathbf{E}_{left,x}, \text{reversed}(\mathbf{E}_{right,x}), \mathbf{E}_{right,x}, \text{reversed}(\mathbf{E}_{left,x})\}, \\
\mathbf{P}_{ext,y} &= \{\mathbf{E}_{left,y}, -\text{reversed}(\mathbf{E}_{right,y}), \mathbf{E}_{right,y}, \text{reversed}(\mathbf{E}_{left,y})\}, \\
\mathbf{P}_{int,x} &= \{\mathbf{I}_{left,x}, \text{reversed}(\mathbf{I}_{right,x}), \mathbf{I}_{right,x}, \text{reversed}(\mathbf{I}_{left,x})\}, \\
\mathbf{P}_{int,y} &= \{\mathbf{I}_{left,y}, -\text{reversed}(\mathbf{I}_{right,y}), \mathbf{I}_{right,y}, \text{reversed}(\mathbf{I}_{left,y})\}.
\end{aligned}$$

S13 Finally, if z was initially negative and made positive, then reflect the polygonised toric section, $\mathbf{P}_{ext,x} = -\mathbf{P}_{ext,x}$ and $\mathbf{P}_{int,x} = -\mathbf{P}_{int,x}$, and set back $z = -z$.

Once the polygon approximation of the toric section is found in the natural frame, a coordinate transformation should be applied to render the coordinates of the polygon as expressed in the base frame.

There are certainly many other possible algorithms for the polygonisation of the toric section, and ours is probably not the simplest one, particularly the part that deals with the complex crescent shape. Indeed, while for the spindle torus, the crescent shaped toric sections are very rare, for the other two types of tori, toric sections have usually a crescent shape. Thus, if dealing with a general toric section, a faster algorithm should be used.

4.3.4 Intersection of All Six Polygonised Toric Sections

Having all toric sections as polygons, external and possibly internal, we may use available planar Boolean algebra libraries to obtain the actual cross-section of the constant-orientation workspace at a given altitude. Once again, we have implemented all our algorithms in Matlab and therefore looked for such a Matlab toolbox. Probably the only free toolbox that can be used to perform Boolean algebra on polygons is the *SaGA* toolbox (Pankratov, 1996). The toolbox is professionally written following the well established principles of computational geometry but requires some slight modifications due to the old version of Matlab in which it is written and due to the lack of some special features necessary in our case.

With the help of the slightly modified *SaGA* toolbox, our Matlab program is capable of computing accurately each cross-section of the constant-orientation workspace in a matter of few seconds. Figures 4.17 and 4.18 show two examples of workspace slices (the ones in full colour) together with the six toric sections. The inner contours of the toric sections are drawn in dashed line. The points in red are the edges of the workspace cross-section and are from those obtained analytically by intersecting each pair of toric sections. Note the complex form of each cross-section and particularly the possibility of having more than a single area defining a cross-section. While we were unable to find a realistic example which features a void in the cross-section, this possibility is theoretically feasible. Therefore, a constant-orientation workspace with such a complex shape cannot be obtained by using a brute-force discretisation algorithm.

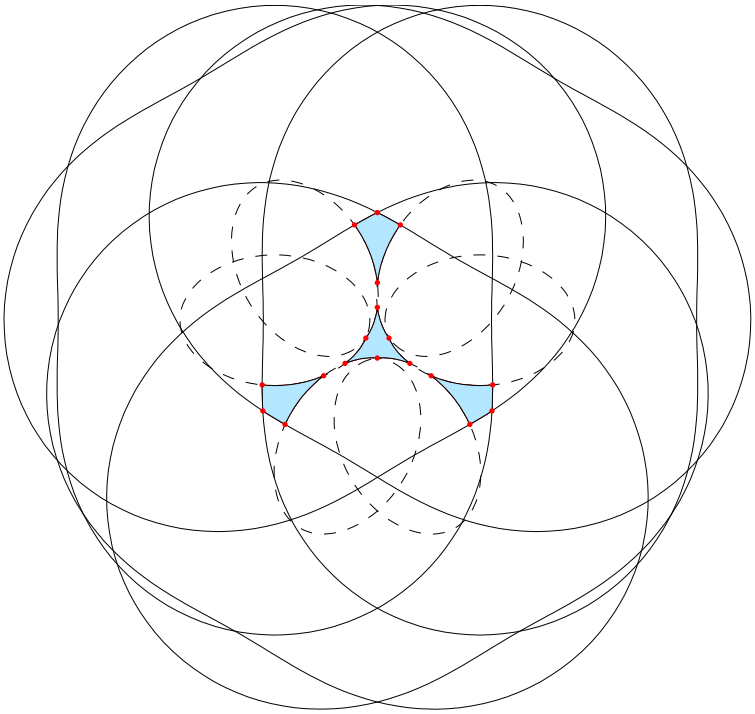

Figure 4.17: Example for the cross-section of the constant-orientation workspace showing four distinct areas.

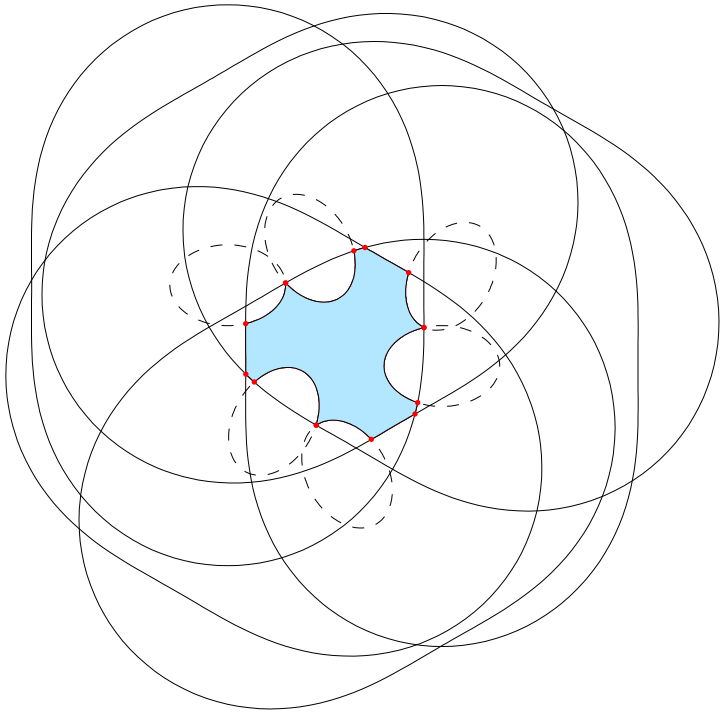

Figure 4.18: Example for the cross-section of the constant-orientation workspace having a complex shape.

Using a basic function of Matlab, the command `polyarea`, we are able to calculate the area of the workspace cross-sections. Integrating these areas along the whole height of the workspace yields a good approximation of the workspace volume.

4.3.5 Examples and Discussion

While the complete procedure for computing the edges and the horizontal cross-sections of the constant-orientation workspace is not trivial, we will not discuss it here in detail. Indeed, the most significant stages of this procedure were already outlined. Overall, for every orientation and design, we need to calculate the minimum and maximum altitude, so that for any altitude between them, all six toric sections exist. Then we need to discretise the range from the minimum to the maximum altitude and at each altitude, calculate the toric sections and the points of intersection between all pairs of toric sections, and finally compute the horizontal cross-section of the constant-orientation workspace. After (or before) all cross-sections are computed, the edges of the constant-orientation workspace may be computed following a simplification of the procedure previously described.

Four examples of the constant-orientation workspace of the 6-$\underline{R}US$ parallel mechanism whose data is given in Table 4.2.5 are presented in Figs. 4.19 through 4.21. Recall, that this time the mechanical limits on the range of the U joints are ignored.

Each of the examples was computed and plotted within less than a minute. Note that the combination of equally-spaced horizontal cross-sections and edges drawn in a different colour yields a very intuitive representation. This allows us to use a low resolution for the edges of the workspace—they no longer need to look like continuous curves—and thus reduce the computation time.

In both examples shown in Figs. 4.19 and 4.20, only the top halves of the constant-orientation workspace are drawn. Indeed, the actual constant-orientation workspace is composed of two separated parts. In practice however, only one of this parts will be usable, so special care should be taken not to consider both parts as in an optimisation procedure which computes the volume of the constant-orientation workspace. To do so, a simple constraint $z \geq z_{min}$ may be added. On the contrary, the two parts of the workspace unite into one for the two orientations for which the constant-orientation workspace is shown in Figs. 4.21(a) and 4.21(b). Therefore, an additional constraint $z \geq z_{min}$ is mandatory in order to ensure realistic results.

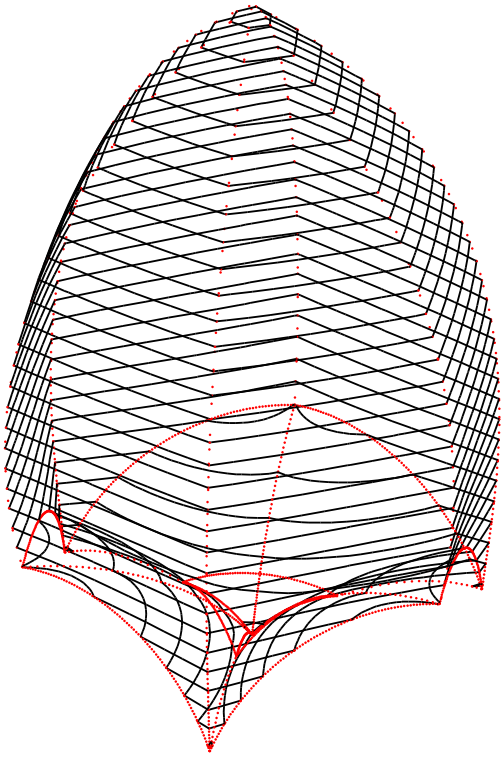

Figure 4.19: Constant-orientation workspace for the reference orientation.

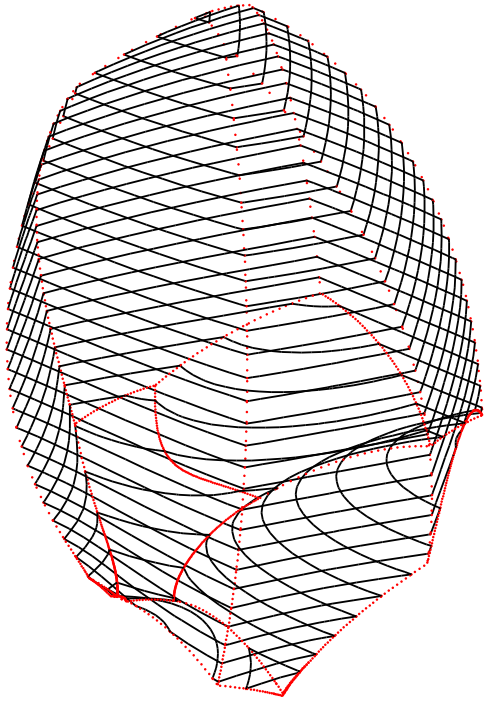

Figure 4.20: Constant-orientation workspace for $\phi = -150°$, $\theta = \sigma = 0°$.

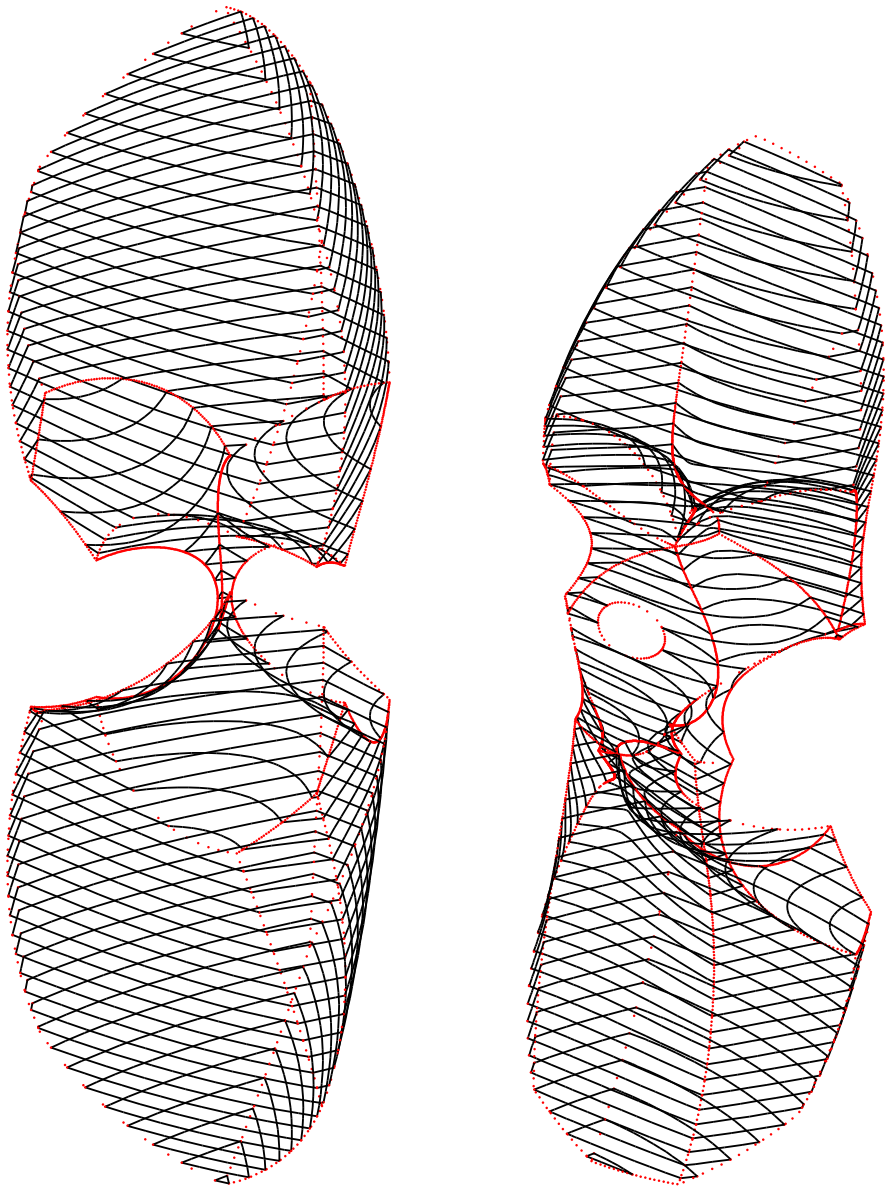

(a) (b)

Figure 4.21: Constant-orientation workspace for (a) $\phi = \theta = 0°$, $\sigma = 25°$ and (b) $\phi = \sigma = 0°$, $\theta = 30°$.

Finally, note the complex shape of the constant-orientation workspace shown in Fig. 4.21(b). The workspace has even a hole in it. Such a solid is almost impossible to compute and represent using a discretisation method. Thus, once again, we see the superiority of geometric methods as opposed to purely numerical ones.

4.4 Computing the Horizontal Cross-Sections of the Constant-Orientation Workspace and Singularity Surface of the Rotobot

We were able to propose intricate geometric methods for computing and visualising the constant-orientation workspace of general 6-$\underline{R}US$ parallel mechanisms. Unfortunately, however, a geometric study of the singularities of such general parallel mechanisms turned out to be impossible. Indeed, we saw that even the simple planar 3-$\underline{R}RR$ equivalent of the 6-$\underline{R}US$ parallel mechanism has extremely complex singularity loci. Recall that for a constant orientation, the curve that represents these singularity loci for all working modes is of degree 42. Furthermore, there is no polynomial that corresponds to the singularity loci of a single working mode. One can easily make a rough extrapolation of these results and foresee the unsurmountable complexity of the problem in the case of general 6-$\underline{R}US$ parallel mechanisms.

The situation is completely different with the *Rotobot* (Fig. 4.22). We were able to analyse in depth the complete kinematic geometry of this particular 6-$\underline{R}US$ parallel mechanism. Furthermore, some interesting results related to the singularities of the *Rotobot* were generalised for a larger class of 6-$\underline{R}US$ parallel mechanisms. Most importantly, a number of fascinating features of the *Rotobot* were discovered, among which, its workspace segmentation by working modes. Once again, it is the geometric approach that revealed these previously unknown kinematic properties.

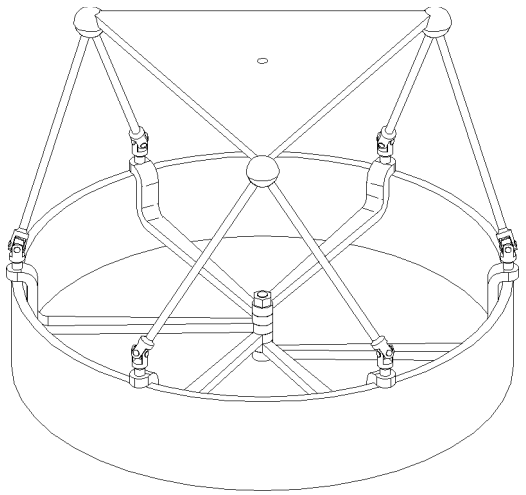

Figure 4.22: CAD model of the *Rotobot*.

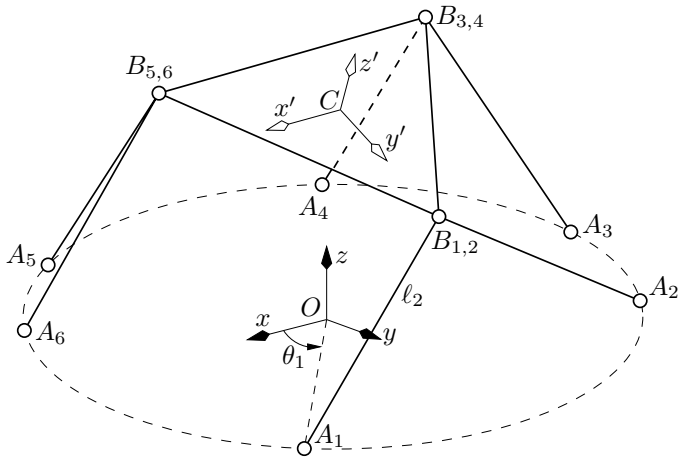

Figure 4.23: Schematic and notation of the *Rotobot*.

We will follow the notation for general 6-$\underline{R}US$ parallel mechanisms that was already introduced. All U joint centres, points A_i $(i = 1, \ldots, 6)$, move along the same circular trajectory referred to as *the track* whose centre is denoted by O. The centres of the spherical joints are pairwise coincident, i.e., $B_1 \equiv B_2$, $B_3 \equiv B_4$, and $B_5 \equiv B_6$. These centres form an equilateral triangle and lie on a circle of radius r_B and centre C.

Henceforth, we will use the term *adjacent* to refer to any two chains that have a common spherical joint centre. The same term will be applied to any of the corresponding elements of such two chains (e.g., points A_1 and A_2 are adjacent).

The lengths of all proximal links are equal and denoted by ℓ_1. The lengths of all distal links are also equal and denoted by ℓ_2. We select a fixed reference frame, called the *base frame*, with origin at O and axes x, y, and z, such that z is also the axis of all R joints and the track lies in the xy plane. We also select a *mobile frame* that is fixed to the mobile platform, with centre C and axes x', y', and z', such that all points B_i are in the $x'y'$ plane and the x' axis is parallel to B_3B_5 (Fig. 4.23).

Let the angle between the x axis and line OA_i be denoted by θ_i. This angle is *input variable* i and is controlled by the motor at R joint i. The mobile platform's position with respect to the base frame is defined by vector $\mathbf{p}$, while the platform orientation is described by a rotation matrix $\mathbf{R}$ that is defined by the *Tilt & Torsion angles*.

Finally, we will add the superscript $'$ to a vector when the latter is expressed in the mobile frame. No superscript will mean that the vector is expressed in the base frame. Finally, the vectors, expressed in the base frame, along lines OA_i, OB_i, and CB_i are respectively denoted by $\mathbf{r}_{OA_i}$, $\mathbf{r}_{OB_i}$, and $\mathbf{r}_{CB_i}$.

The solution to the inverse kinematic problem of the *Rotobot* is the same as for the general 6-$\underline{R}US$ parallel mechanism, with the simplification that all track frames coincide with the base frame. Thus, the input variables are determined uniquely from

$$\sin\theta_i = \frac{p_i y_{B_i} + x_{B_i}\delta_i\sqrt{\Gamma_i}}{\varrho_i^2} \equiv S_i, \quad \cos\theta_i = \frac{p_i x_{B_i} - y_{B_i}\delta_i\sqrt{\Gamma_i}}{\varrho_i^2} \equiv C_i, \tag{4.41}$$

$$\theta_i = \text{atan2}(S_i, C_i), \tag{4.42}$$

where $\varrho_i^2 = x_{B_j}^2 + y_{B_j}^2$,

$$\Gamma_i = x_{B_i}^2 + y_{B_i}^2 - p_i^2 \tag{4.43}$$

and

$$p_i = \frac{x_{B_i}^2 + y_{B_i}^2 + z_{B_i}^2 + \ell_1^2 - \ell_2^2}{2\ell_1}. \tag{4.44}$$

The variables x_{B_i}, y_{B_i}, and z_{B_i} are the coordinates of point B_i expressed in the base frame. Finally, recall that $\delta_i = \pm 1$ is the branch index.

The special thing about the *Rotobot* is directly related to the branch index and the whole issue of working modes. It all comes from the fact that the spherical joints are pair-wise coincident. Therefore, the two solutions to the inverse kinematic problem for each two coinciding vertices, e.g., B_1 and B_2, are the same. Since the corresponding U joint centres should not coincide, each chain should take one of the two solutions. In other words, the branch indices for each two adjacent chains should be different, i.e., $\delta_1 = -\delta_2$, $\delta_3 = -\delta_4$, $\delta_5 = -\delta_6$, while $\Gamma_1 = \Gamma_2$, $\Gamma_3 = \Gamma_4$, $\Gamma_5 = \Gamma_6$. Hence, there are only eight (instead of sixty four) working modes.

The fact that $\Gamma_j = \Gamma_{j+1}$ $(j = 1, 3, 5)$ guarantees that the singularity loci for the *Rotobot* and for any 6-$\underline{R}US$ parallel mechanism with pair-wise coincident S joints sharing the same tracks are the same for all working modes. This automatically means that these singularity loci can be represented by a polynomial. In fact, if the distal links are shorter than the proximal links ($\ell_2 < \ell_1$), as in the actual commercially available *Rotobot* by Hexel Corporation, there is only one working mode. Indeed, once such a mechanism is assembled, there is no way of changing the branch indices of the legs. If, however, $\ell_1 < \ell_2$, it is possible to change a working mode without disassembling the mechanism. This phenomenon gives rise to an interesting discussion on workspace segmentation.

4.4.1 Singularity Surfaces

The main equation that constitutes the inverse kinematic problem of the *Rotobot* is

$$\mathbf{r}_{A_iB_i} = \mathbf{r}_{OB_i} - \mathbf{r}_{OA_i}, \tag{4.45}$$

where $\mathbf{r}_{OB_i} = \mathbf{p} + \mathbf{R}\mathbf{r}'_{OB_i}$ and $\mathbf{r}_{OA_i} = \ell_1[\cos\theta_i, \sin\theta_i, 0]^T$. Squaring the above equation yields

$$\ell_2^2 = (\mathbf{p} + \mathbf{R}\mathbf{r}'_{OB_i} - \mathbf{r}_{OA_i})^T(\mathbf{p} + \mathbf{R}\mathbf{r}'_{OB_i} - \mathbf{r}_{OA_i}). \tag{4.46}$$

We may now proceed to differentiating Eq. (4.46) with respect to time:

$$\ell_2\mathbf{f}_i^T \left(\mathbf{v} + \dot{\mathbf{R}} \times \mathbf{r}'_{OB_i} - \ell_1\dot{\theta}_i \begin{bmatrix} -\sin\theta_i \\ \cos\theta_i \\ 0 \end{bmatrix} \right) = 0 \tag{4.47}$$

where $\mathbf{f}_i$ is the unit vector along proximal link i. Expressing $\ell_2\mathbf{f}_i$ as

$$\ell_2\mathbf{f}_i = \begin{bmatrix} x_{Bi} - \ell_1\cos\theta_i \\ y_{Bi} - \ell_1\sin\theta_i \\ z_{Bi} \end{bmatrix}, \tag{4.48}$$

and using the fact that $\dot{\mathbf{R}}\mathbf{r}'_{OB_i} = \dot{\mathbf{R}}\mathbf{R}^T\mathbf{r}_{OB_i} = \boldsymbol{\omega} \times \mathbf{r}_{OB_i}$, where $\boldsymbol{\omega}$ is the angular velocity of the mobile platform, and the fact that $\mathbf{f}_i^T(\boldsymbol{\omega} \times \mathbf{r}_{OB_i}) = (\mathbf{r}_{OB_i} \times \mathbf{f}_i)^T\boldsymbol{\omega}$, we obtain

$$\ell_2 \left[(\mathbf{r}_{OB_i} \times \mathbf{f}_i)^T, \mathbf{f}_i^T \right] \begin{bmatrix} \boldsymbol{\omega} \\ \mathbf{v} \end{bmatrix} = \ell_1(y_{B_i}\cos\theta_i - x_{B_i}\sin\theta_i)\dot{\theta}_i. \tag{4.49}$$

Finally, substituting $\sin\theta_i$ and $\cos\theta_i$ in the above equation with the expressions found in Eqs. (4.41), simplifying, and writing in matrix form gives us the final velocity equation:

$$\ell_2 \begin{bmatrix} (\mathbf{r}_{OB_1} \times \mathbf{f}_1)^T & \mathbf{f}_1^T \\ \vdots & \vdots \\ (\mathbf{r}_{OB_6} \times \mathbf{f}_6)^T & \mathbf{f}_6^T \end{bmatrix} \boldsymbol{\xi} = -\ell_1 \begin{bmatrix} \delta_1\sqrt{\Gamma_1} & & 0 \\ & \ddots & \\ 0 & & \delta_6\sqrt{\Gamma_6} \end{bmatrix} \dot{\boldsymbol{\theta}} \tag{4.50}$$

where $\boldsymbol{\xi} = [\boldsymbol{\omega}^T, \mathbf{v}^T]^T$ is the *twist* of the mobile platform, and $\dot{\boldsymbol{\theta}} = [\dot{\theta}_1, \dot{\theta}_2, \ldots, \dot{\theta}_6]^T$ is the vector of active joint rates. We will denote, as usual, the (Jacobian) matrices

multiplying the platform twist and the active joints rates with $\mathbf{Z}$ and $\mathbf{\Lambda}$, respectively. Thus, for every configuration, there is an equation

$$\mathbf{Z}\boldsymbol{\xi} = \mathbf{\Lambda}\dot{\boldsymbol{\theta}}, \tag{4.51}$$

which completely describes the velocity kinematics of the *Rotobot*.

Equation (4.51) can, therefore, be used to fully describe and classify the singularity configurations of the *Rotobot*. A general 6-$\underline{R}US$ parallel mechanism, as well as most parallel mechanisms, have two distinct types of singularities (Gosselin and Angeles, 1990). The first, or Type 1, occurs when matrix $\mathbf{\Lambda}$ is singular, while Type 2 corresponds to configurations where $\mathbf{Z}$ is singular.

The equation describing the instantaneous kinematics of the *Rotobot* was derived using the conventional approach of differentiations. However, we could have used reciprocal screws to directly obtain that equation, similarly to what we did for planar parallel mechanisms in Chapter 2. Indeed, for 6-$\underline{R}US$ parallel mechanisms, the reciprocal screws are the zero-pitch screws passing through the centres of the U and S joints in each leg, i.e., along the distal links. The rows of matrix $\mathbf{Z}$ are also the *Plücker coordinates* of the lines along the distal links (Merlet, 1989).

While in the planar case, a parallel mechanism was at a Type 2 singularity when the lines of the reciprocal screws intersect at one point or are all parallel, the situation in the spatial case is much more complicated. Merlet (1989) studied all possible scenarios in which a set of six reciprocal zero-pitch screws degenerate using Grassmann Geometry. He applied that classification to the study of the singularities of 6-DOF parallel mechanisms.

Ebert-Uphoff et al. (2000) studied geometrically the Type 2 singularity configurations for 6-DOF parallel mechanisms with three S joints at the mobile platform, such as our *Rotobot*. The authors classified the singularity configurations into several categories based on the relationship between the plane of the platform and three planes through the S joints. Their approach can be applied directly to the *Rotobot*, where the three planes will be the planes defined by the adjacent distal links. However, most of the groups for the particular design of the *Rotobot* represent very peculiar cases. Besides, the approach only gives a geometric insight and does not show how to obtain the singularity surfaces, which is our main task. Therefore, we will derive the expressions for the singularity surfaces by directly manipulating the Jacobian matrices.

4.4.1.1 Type 1 Singularity Surfaces

From the above, it follows that a Type 1 singularity occurs only if $\Gamma_i = 0$. As used in the transition from Eq. (4.49) to Eq. (4.50)

$$\mathbf{r}_{OB_i}^T \mathbf{r}_{OA_i}^{\perp} = -\ell_1 \delta_i \sqrt{\Gamma_i} \tag{4.52}$$

where $\mathbf{r}_{OA_i}^{\perp}$ is the vector obtained by rotating $\mathbf{r}_{OA_i}$ about the z axis by 90°. Hence, $\Gamma_i = 0$ when vector $\mathbf{r}_{OB_i}$, or equivalently, vector $\mathbf{f}_i$, is normal to the tangent to the track at point A_i.

The complete set of positions of point B_i that correspond to singularities of Type 1 forms a surface. From the description given in the previous paragraph, it can be easily seen that this surface is generated by sweeping a circle of radius ℓ_2, the *generatrix*, about a circle of radius ℓ_1, the *directrix* or, as we already call it, the track. The centre of the generatrix lies on the track while the axis of symmetry of the generatrix is tangent to the track. Such a surface is, of course, a *torus*.

Recall that this surface may have three distinctive shapes depending on the lengths of the proximal and distal links of the $\underline{R}US$ chain (Fig. 4.14). As we will see later, the case $\ell_2 \geq \ell_1$ makes the singularity and workspace analysis of the *Rotobot* much more intricate and ... intriguing. This is due to the existence of *self-intersection points* in the horn and spindle tori. Recalling the inverse kinematic problem of 6-$\underline{R}US$ parallel mechanisms, such self-intersection points correspond to configurations at which the inverse kinematics of the leg has infinitely many solutions.

For a given constant orientation of the mobile platform, the Type 1 singularity surfaces for point C may be obtained simply by translating the toroidal surfaces for each leg along the corresponding line B_iC. Naturally, there will be only three distinct Type 1 singularity surfaces for the *Rotobot*.

The volume enclosed by each of those surfaces is, of course, the *vertex space*. Formally, vertex space i is the set of all possible positions that may be attained by point C considering only the kinematic constraints of chain i and keeping the mobile platform at a constant orientation. It is important to note that the *spindle torus* has a lemon-shaped cavity. Thus, any horizontal cross-section of any such vertex space will be an *annulus*, i.e., the area enclosed by two concentric circles.

Finally, let us point out an interesting fact related to the singularities of general 6-$\underline{R}US$ parallel mechanisms with pair-wise coincident S joints and adjacent chains shar-

ing a common track. At a Type 1 singularity, at least one pair of adjacent distal (and proximal) links is coincident. In other words, at least two rows of matrix **Z** will be identical. Hence, Type 1 singularities, in such mechanisms, are also Type 2 singularities. The only exception may be at the above mentioned self-intersection points. Namely, a pose, at which one of points B_i is at a corresponding self-intersection point, corresponds to a Type 1 singularity. However, among the infinitely many possible placements for the corresponding two adjacent distal links, only some will lead to Type 2 singularities.

4.4.1.2 Type 2 Singularities

For a general 6-$\underline{R}US$ parallel mechanism, the inverse kinematic problem for each chain has two solutions, and hence, for the whole mechanism, it has sixty-four solutions. For a general 6-$\underline{R}US$ (or other, e.g., 6-$\underline{P}US$) parallel mechanism with pair-wise coincident S joints and adjacent chains sharing a common track, however, there is only one solution, since in each adjacent pair of chains, each chain corresponds to one of the two solutions of the inverse kinematic problem for that pair. This important property determines the nature of the Type 2 singularities for such mechanisms.

At the same time, when the distal links are longer than the proximal ones, the unique solution to the inverse kinematics of a 6-$\underline{R}US$ parallel mechanism with pair-wise coincident S joints and adjacent chains sharing a common track may happen to be in any of a total of eight working modes.

For a general 6-$\underline{R}US$ parallel mechanism, the singularity loci of Type 2 depend on the working mode of the mechanism. The problem with such parallel mechanisms is that the expression defining their Type 2 singularity loci is not polynomial (it contains radicals) and hence the singularities are difficult to study and represent. On the other hand, the advantage of such Type 2 singularities is that they may be modified without disassembling or reconfiguring the robot. Indeed, it is possible to change the branch index of one or more chains in order to change the Type 2 singularity loci and so be able to follow Type 2 singularity-free trajectories that are otherwise impossible for a given branch set.

For a 6-$\underline{R}US$ parallel mechanism with pair-wise coincident S joint centres and adjacent chains sharing a common track, it may be proven that the determinant of the Jacobian matrix **Z** is free of any radicals. In fact, for a constant orientation, the determinant reduces to a polynomial of degree eighteen in x, y, and z (in the case $\ell_1 = \ell_2$). This initially astonishing fact is actually quite obvious. Such a parallel mechanism is kinematically the same for any branch set for which $\delta_j \delta_{j+1} = -1$, $j = 1, 3, 5$.

Let us now focus on our *Rotobot* and determine its Type 2 singularity surfaces for a given orientation. Our task is quite simplified due to the fact that we need to specify only two Euler angles. Indeed, it is obvious that the Type 2 singularities remain the same when the mobile platform rotates about the z axis since the configuration of the *Rotobot* remains unchanged with respect to the mobile frame. It can be shown, again using a computer algebra system, that the Type 2 singularities of the *Rotobot* can be represented by a polynomial of degree 5 in x, y, and z (of degree 4 in x and y). The polynomial is, however, still too big (some two pages) to represent here.

In order to be able to describe in detail the derivation of the expression representing the Type 2 singularities we will limit ourselves to the case of the *redundant Rotobot*. (The procedure is almost the same as in the general case, though.) In other words, we will assume that the *Rotobot* is used with an axisymmetric tool along the mobile z' axis, such as a milling cutter or a laser beam. Thus, there will be no need to orient the mobile platform about the mobile z' axis and all required orientations of the mobile platform or, rather, all required directions of the axisymmetric tool may be realised by only one rotation. This rotation will be simply about the mobile x' axis at an angle θ.

Once the Jacobian $\mathbf{Z}$ is expressed in the variables x, y, z, and the parameters r_B (the platform radius), ℓ_1, ℓ_2, θ, ϱ_j, Γ_j, δ_j, (recall that $\varrho_j = \varrho_{j+1}$, $\Gamma_j = \Gamma_{j+1}$, and $\delta_j = -\delta_{j+1}$) we follow the procedure described below (in this section $j = 1, 3, 5$).

S1 Substitute the expressions $\delta_j\sqrt{\Gamma_j}$ with the parameters Δ_j.

S2 Obtain $\det \mathbf{Z}$. Its denominator is equal to $128\varrho_1^4\varrho_3^4\varrho_5^4$. Indeed, $\mathbf{Z}$ is not defined when point B_i lies on the z axis, i.e., when $\varrho_j = 0$. Eliminating this special case, we consider further only the numerator, $\mathcal{E}$. This numerator is a function of x, y, and z that cannot be generally factored and contains the three radicals $\delta_j\sqrt{\Gamma_j}$ (actually Δ_j) and the parameters ϱ_j^2.

S3 $\mathcal{E}$ can be factored to $\mathcal{E} = 9\ell_1^3 r_B^3 \Delta_1\Delta_3\Delta_5\mathcal{E}_1$, where $\mathcal{E}_1$ is an expression depending on x, y, z, r_B, ℓ_1, ℓ_2, θ, and ϱ_j, and cannot be factored. Indeed, recall that the Type 1 singularities which are represented by $\Delta_j = 0$ are also Type 2 singularities. Hence, we are interested only in $\mathcal{E}_1$.

S4 Substitute in $\mathcal{E}_1$ the expressions for $\varrho_j^2 = x_{B_j}^2 + y_{B_j}^2$:

$$\begin{aligned}
\varrho_1^2 &= x^2 + (y + \cos\theta\, r_B)^2,\\
\varrho_3^2 &= (x - r_B\sqrt{3}/2)^2 + (y - \cos\theta\, r_B/2)^2,\\
\varrho_5^2 &= (x + r_B\sqrt{3}/2)^2 + (y - \cos\theta\, r_B/2)^2.
\end{aligned}$$

S5 Now, $\mathcal{E}_1$ depends only on x, y, z, r_B, ℓ_1, ℓ_2, and θ, and may be factored to $96 r_B \varrho_1^2 \varrho_3^2 \varrho_5^2 (z - \sin\theta\, r_B/2)\mathcal{E}_2$, where ϱ_j^2 are actually the above left-hand expressions. The singularity for $z = \sin\theta\, r_B/2$ corresponds to the case where the horizontal side of the platform, B_3B_5, lies in the xy plane.

If the mobile platform is horizontal (or inverted, which however is practically impossible), i.e., if $\theta = 0$, then the singularity surfaces are a vertical cylinder, centred at the origin and of radius r_B, and the plane $z = 0$:

$$\mathcal{E}_2 = 8z^2(x^2 + y^2 - r_B^2) = 0. \tag{4.53}$$

Otherwise, the singularity surface defined by $\mathcal{E}_2$ for $\theta \neq 0$ is a complex-shaped quartic surface. However, each horizontal cross-section of that surface is a bicircular quartic that is symmetric about the x axis and the line $y = z\cot\theta$ (Fig. 4.24). This curve resembles the *spiric section*, also called *Perseus' spiric curve*. As we already mentioned, the spiric section is the curve obtained by intersecting a torus with a plane that is parallel to the axis of the torus.

To simplify the equation of the singularity loci, we perform the coordinate transformation $y = \hat{y} + z\cot\theta$ and after factoring out the constant $\csc\theta$, we obtain the final expression for the Type 2 singularity loci for a given z and $\theta \neq 0$:

$$\mathcal{Q} = (x^2 + \hat{y}^2)^2 + q_3 x^2 + q_5 \hat{y}^2 + q_8, \tag{4.54}$$

where

$$\begin{aligned}
q_3 &= 2\ell_2^2 - 2\ell_1^2 - r_B^2 + (2z^2 + 4z r_B \sin\theta)\csc^2\theta, \\
q_5 &= 2\ell_2^2 - 2\ell_1^2 - r_B^2 - 2z^2\csc^2\theta, \\
q_8 &= r_B^2(\ell_1^2 - \ell_2^2) + (\ell_1^2 - \ell_2^2)^2 + 2z^2(\ell_1^2 - \ell_2^2)\csc^2\theta - \\
&\quad z(2r_B\sin\theta - z)(r_B\sin\theta + z)^2\csc^4\theta.
\end{aligned}$$

Even though the above equation of the singularity curve is simpler than the more general bicircular quartic, the toric section, the curve still cannot be represented by a parametric equation or written in polar form. Therefore, we need to polygonise the curve as we already did for the toric section. Figure 4.24 shows all possible types of shapes that the bicircular quartic from Eq. (4.54) can take.

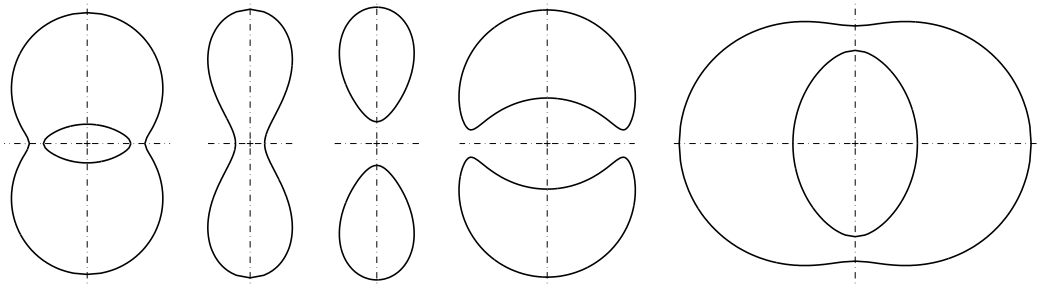

Figure 4.24: The types of shapes of the singularity loci (bicircular quartic).

The algorithm for the polygonisation of our bicircular quartic is similar to that for the toric section but slightly differs since the bicircular quartic of Eq. (4.54) is symmetric with respect to both the x and the new $\hat{y}$ axis. Furthermore, it seems that the curve has always at least two $\hat{y}$ intercepts. However, while we could not find any counterexample, we were unable to prove this fact theoretically. On the other hand, it was easy to show that the curve may have no x intercepts and be composed of two symmetric contours separated by the x axis.

Therefore, for the centre of the ray polygonisation method, one should simply select the origin of the coordinate frame, in case there is an equal number of x and $\hat{y}$ intercepts. If, however, there are no x intercepts, that centre should be selected somewhere between the two positive (or negative) $\hat{y}$ intercepts. Similarly, if there are no $\hat{y}$ intercepts, the centre should be selected somewhere between the two positive (or negative) x intercepts.

4.4.2 Constant-Orientation Workspace

The methodology for computing the constant-orientation workspace of a general 6-$\underline{R}US$ parallel mechanism was already described in detail. The workspace was visualised through its edges which were computed by analytical methods (Section 4.2). The other alternative of representing the workspace through its horizontal cross-sections was also explored for the case where no joint constraints are assumed (Section 4.3).

In this section, however, we deal mainly with the *Rotobot* design, and the emphasis is on obtaining simple formulations for the singularities and workspace for a constant orientation that can be used for optimisation purposes. In addition, our goal is to use the *Rotobot* design to demonstrate several new phenomena, rather than just provide a practical tool for analysing a particular parallel mechanism.

Hence, we choose to compute and visualise the constant-orientation workspace by horizontal slices. Firstly, the task is simpler, and, secondly, we need cross-sections and not edges in order to compute the volume of the workspace. The task of computing the workspace using a CAD system, as previously done (Bonev and Ryu, 1999b), is overruled due to the difficulty in representing some of the geometrical entities (a quartic singularity surface and three Bohemian domes) and the necessity for some extra tests involving the solution of the inverse kinematic problem. In our method, we will not consider the mechanical limits of the S and U joints. However, we will consider the inevitable constraint on the order of the U joints along the common circular track. This constraint is particularly interesting and can nicely be modelled geometrically. Once again, the geometric method will prove to be more effective than a numerical one.

4.4.2.1 Order of the U Joints Along the Track

If we were able to construct the *Rotobot* in such a way that the U joint centres A_i along the track could change their circular order, then all that would have been necessary to do is to find the intersection between all three vertex spaces. The latter task amounts to finding the intersection of three annular regions (Gosselin, 1990). Unfortunately, most feasible designs would restrain the order of the U joint centres along the circular track. In order to be able to easily model that physical constraint, we assume that *two or more* consecutive U joint centres can coincide but not pass over. Thus, in our case, points $A_1, A_2, \ldots, A_6$ should preserve their counter-clockwise order along the circular track.

For a given pose of the *Rotobot*, we may solve the inverse kinematic problem and generally know the values for all six input variables from Eq. (4.41). This is true if we choose to keep the branch index of each chain constant. However, as we will see later, two adjacent chains of the *Rotobot* may actually switch their branch indices simply by passing through a self-intersection singular point. Thus, by simply solving the inverse kinematic problem, we do not immediately know which of the two values in each of the three pairs of input variables corresponds to one or the other chain in the corresponding adjacent pair of chains.

Even though the problem of verifying whether six points along a circle are in a given order seems quite easy, its solution is a challenging task due to the fact that the points may coincide. This task is even further complicated by the fact that we do not differentiate between the two points in each of the three pairs. The following procedure is proposed:

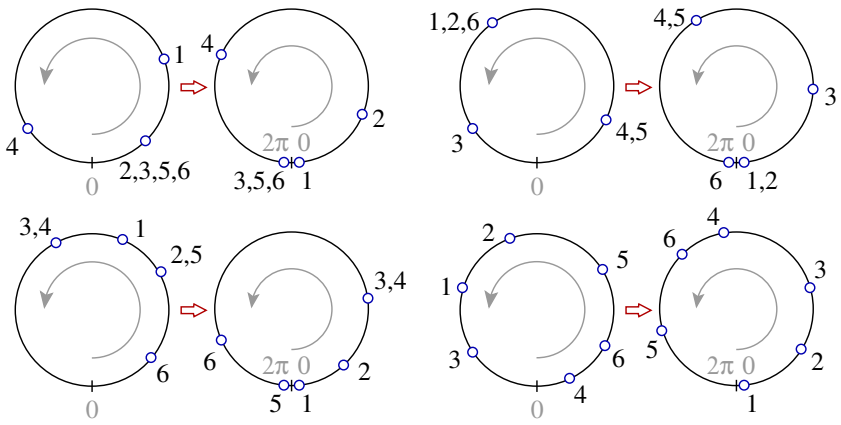

Figure 4.25: Four valid arrangements of the U joint centres.

S1 Form the ordered list $\boldsymbol{\vartheta} = \{\theta_1 + \pi, \ldots, \theta_6 + \pi\}$. Replace all elements that are equal to 2π by 0, so that $\boldsymbol{\vartheta} \in [0,\, 2\pi)$.

S2 Reduce the numeric precision of all elements to, say, three digits after the decimal point. This is done to ensure that theoretically equal elements are indeed identified as equal.

S3 If $\vartheta_2 < \vartheta_1$, then interchange the values of ϑ_2 and ϑ_1. If $\vartheta_2 \geq \max\{\vartheta_3, \ldots, \vartheta_6\}$ and $\vartheta_1 \leq \min\{\vartheta_3, \ldots, \vartheta_6\}$, then interchange (possibly again) the values of ϑ_2 and ϑ_1. This is done to ensure that, if possible, point 2 is immediately after point 1 in a counter-clockwise direction.

S4 Subtract ϑ_1 from all elements of $\boldsymbol{\vartheta}$. Add 2π to all elements, that have become negative to make $\boldsymbol{\vartheta} \in [0,\, 2\pi)$. If any of or both ϑ_5 and ϑ_6 are equal to zero, then replace the zero with 2π. If any of or both ϑ_3 and ϑ_4 are equal to zero and $\vartheta_2 \neq 0$, then replace the zero with 2π (Fig. 4.25).

S5 Is $\vartheta_2 \leq \min\{\vartheta_3,\, \vartheta_4\}$ and $\max\{\vartheta_3,\, \vartheta_4\} \leq \min\{\vartheta_5,\, \vartheta_6\}$?

If the above test is positive, then the order of the six points is valid and we may obtain the branch indices for each chain. In particular, $\delta_1 = -1$ if there was no interchange in the values of ϑ_1 and ϑ_2 in step 3; otherwise $\delta_1 = +1$. Similarly, $\delta_j = -1$ ($j = 3,\, 5$) if $\vartheta_j < \vartheta_{j+1}$; otherwise $\delta_j = +1$. (If $\vartheta_j = \vartheta_{j+1}$ or $\vartheta_j = \vartheta_{j+1} \pm 2\pi$, the branch indices δ_j and δ_{j+1} are irrelevant.)

If for some reasons we wish to—or are forced to (as in the case $\ell_2 < \ell_1$)—operate the *Rotobot* in a single working mode, the above procedure should be slightly modified. In particular, step 3 should be removed and steps 4 and 5 should be modified as follows:

S4' Subtract ϑ_1 from all elements of $\boldsymbol{\vartheta}$. To make $\boldsymbol{\vartheta} \in [0,\, 2\pi)$, add 2π to its negative elements. If $\vartheta_6 = 0$, set $\vartheta_6 = 2\pi$. If $\vartheta_i = 0$ and $\vartheta_{i-1} \neq 0$, set $\vartheta_i = 2\pi$ for $i = 3,\, 4,\, 5$.

S5' Is $\vartheta_2 \leq \vartheta_3 \leq \vartheta_4 \leq \vartheta_5 \leq \vartheta_6$?

4.4.2.2 Geometric Model for the *U* Joint Interference

The vertex space boundary, as previously defined, may be seen as the surface corresponding to all positions for the platform centre, for a given constant orientation of the mobile platform, for which two adjacent U joint centres are coincident. Inside the vertex space, the adjacent U joint centres are not interfering.

A similar geometric model exists to describe the positions of the platform centre for which two *neighbouring* U joint centres, i.e., $\{A_{j+1},\, A_k\}$, where $j = 1,\, 3,\, 5$ and $k = 3,\, 5,\, 1$ are coincident. Let the mobile platform has a given constant orientation and two of its neighbouring U joint centres, $\{A_{j+1},\, A_k\}$, are coincident and fixed to the track. Then, under these conditions, the platform centre can move along a circle, $\mathcal{C}$, whose plane is normal to B_jB_k. The radius of this circle is equal to the distance from A_k to line B_jB_k, i.e., $r_C = \sqrt{\ell_2^2 - 3r_B^2/4}$, and its centre is at a point obtained by translating point A_k along the constant vector $\mathbf{p}_k = -(\mathbf{r}_{CB_j} + \mathbf{r}_{CB_k})/2$.

Notice that the above remains true for any position of the coinciding U joint centres on the circular track. Hence, the complete set of positions of the platform centre for which two neighbouring centres are coincident is the *translation surface*, $\mathcal{B}_k$ obtained by sweeping circle $\mathcal{C}$, while its centre moves on the track circle and the plane of the circle remains parallel to vector $\mathbf{r}_{B_jB_k}$. Such a surface is a quartic and is referred to as a *Bohemian dome* (Weisstein, 2002), shown in Fig. 4.26. Its parametric equation is:

$$\mathcal{B}_k(u_k, v_k) = \mathbf{p}_k + \begin{bmatrix} r_C \cos\phi_k \cos u_k - r_C \sin\phi_k \cos\gamma_k \sin u_k + \ell_1 \cos v_k \\ r_C \sin\phi_k \cos u_k + r_C \cos\phi_k \cos\gamma_k \sin u_k + \ell_1 \sin v_k \\ r_C \sin\gamma_k \sin u_k \end{bmatrix} \tag{4.55}$$

where the coordinate $u_k \in [0, 2\pi]$ defines the horizontal circular *parallels* and $v_k \in [0, 2\pi]$ defines the inclined circular *parallels*, and ϕ_k and γ_k are respectively the azimuth and tilt angles defining vector $\mathbf{r}_{B_jB_k}$ as:

$$\mathbf{r}_{B_jB_k} = \mathbf{r}_{CB_j} - \mathbf{r}_{CB_k} = \sqrt{3} r_B \begin{bmatrix} \sin\phi_k \sin\gamma_k \\ -\cos\phi_k \sin\gamma_k \\ \cos\gamma_k \end{bmatrix}. \tag{4.56}$$

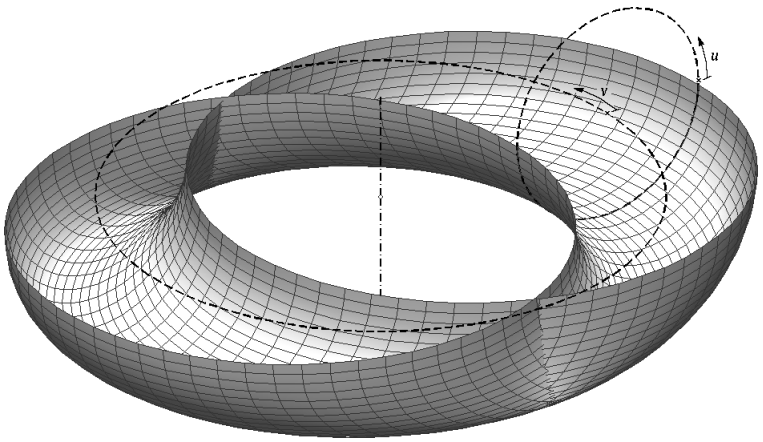

Figure 4.26: The lower half of a Bohemian dome surface.

Now, let us make the important observation that at the interior of the Bohemian dome $\mathcal{B}$, the two neighbouring U joint centres pass over and, therefore, are in interference. Hence, the platform centre should always be at the exterior of that surface.

For a given value of u_k, the corresponding horizontal circular parallel is of radius ℓ_1 and centre that can be directly obtained from Eq. (4.55). For a given height z, two values of u_k can be generally found. Hence, for a given height z, there are generally two circles. And it is the area enclosed by these two circles, excluding the area inside both of them (if the circles are intersecting as in Fig. 4.26), that corresponds to U joint interference and should be avoided. Note that for the heights $z_{k,min}$ and $z_{k,max}$ for which $u_k = \pm\pi/2$, there is only one circle, but neither of these circles limits the workspace area in any way. In other words, for $z \leq z_{k,min}$ and $z \geq z_{k,max}$ there is no interference between the two U joints.

Finally, let us study the relationship between the Bohemian dome surface for chains $j+1$ and k and the vertex spaces corresponding to those two chains (actually to pairs $\{j,\, j+1\}$ and $\{k,\, k+1\}$). By definition, the Bohemian dome should be inside both vertex spaces. The parametric equation of vertex space j is

$$\mathcal{V}_j(u_j, v_j) = \begin{bmatrix} \cos v_j(\ell_2 \cos u_j + \ell_1) \\ \sin v_j(\ell_2 \cos u_j + \ell_1) \\ \ell \sin u_j \end{bmatrix} - \mathbf{r}_{CB_j}, \tag{4.57}$$

where $u_j \in [0, 2\pi]$ and $v_j \in [0, 2\pi]$.

Using the parametric equations for $\mathcal{V}_j$, $\mathcal{V}_k$, and $\mathcal{B}_k$, it can be shown that $\mathcal{B}_k$ is not simply inside both vertex spaces but is tangent to their boundaries. This amazing ge-

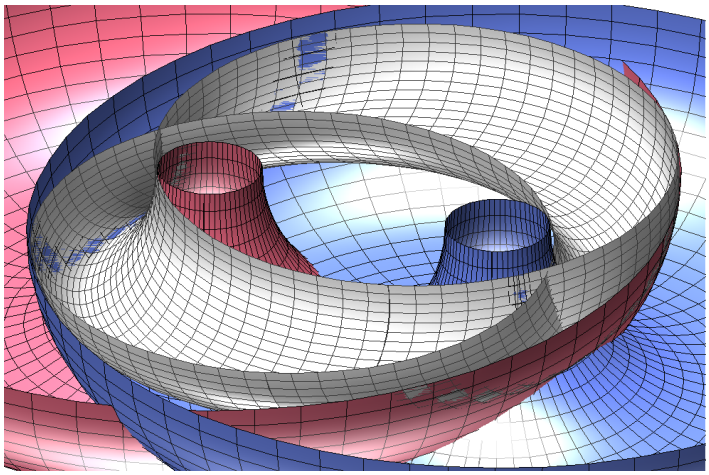

Figure 4.27: The lower halves of a Bohemian dome and the corresponding vertex spaces.

ometrical fact is demonstrated in Fig. 4.27, where the colour interfusion (the smudges) on the Matlab plot are due to the tangency between the surfaces. For a better representation, only the halves of the three entities are shown ($u \in [\pi, 2\pi]$).

An example of the cross-sections is given in Fig. 4.28. Basically, we have two pairs of concentric circles (from the vertex spaces) whose mean radius is ℓ_1, and two non-concentric circles of radius ℓ_1 (from the Bohemian dome). Each of the two non-concentric circles is tangent to all four concentric circles. The filled part is the area where the platform centre can move without causing interference between the two neighbouring U joint centres A_{j+1} and A_k.

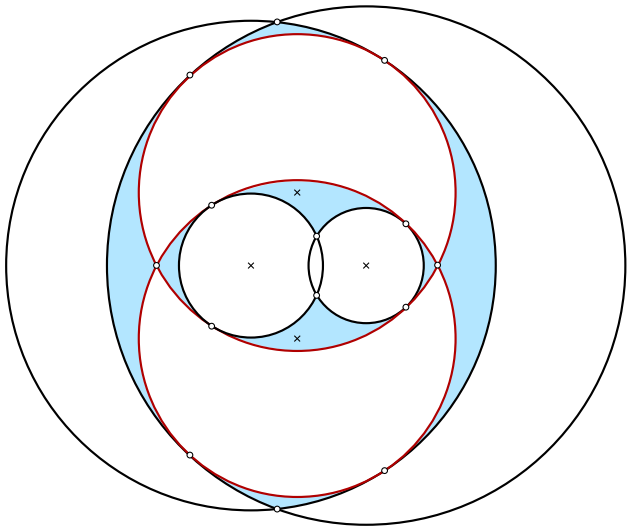

Figure 4.28: Cross-sections of a Bohemian dome and the corresponding vertex spaces.

4.4.2.3 Procedure for Computing the Workspace

We are finally ready to describe the computational procedure for computing the horizontal cross-sections of the constant-orientation workspace of the *Rotobot*.

For a given orientation, set the range $z \in (z_{min}, z_{max})$ for which all three vertex spaces exist and the distal links are always above the xy plane, where $z_{max} = \ell_2 - \max\{r_{CB_1,z}, r_{CB_3,z}, r_{CB_5,z}\}$ and $z_{min} = -\min\{r_{CB_1,z}, r_{CB_3,z}, r_{CB_5,z}\}$ ($r_{CB_j,z}$ are the z components of vectors $\mathbf{r}_{CB_j}$). Start decrementing z from z_{max} down to z_{min}. To achieve a better visual result, it is not recommended to use a fixed interval step. We use, for example, the law $z = z_{max} \cos w$, where $w \in (\cos^{-1} z_{min},\, 0)$.

For each z, we compute the centres and radii of all three pairs of concentric circles (the cross-sections of the vertex spaces—they exist for sure) and the centres of the maximum three pairs of non-concentric circles (the cross-sections of the Bohemian domes—some or all may be missing). This data is stored in maximum six structure objects, each divided into two. Each of these maximum twelve objects corresponds to a circle and contains fields for the geometrical data (centre and radius), the intersection points (as values in the range $[0, 2\pi]$), and the pairs of intersection points that define the boundary arcs of the workspace cross-section.

For each two pairs of concentric circles, we compute and store the maximum four intersection points. If, for those two pairs, there exists a Bohemian dome, we compute and store the maximum two points of intersection between the two non-concentric circles. Finally, we calculate the eight points of tangency (recall Fig. 4.28) and store them in the appropriate fields.

Next, we take each of the maximum three pairs of non-concentric circles, and for each pair, we take each of the non-corresponding vertex space concentric circles and each of the maximum two other pairs of non-concentric circles. For each pair of non-concentric circles and each pair of concentric or non-concentric circles, we compute the maximum eight (four times two) intersection points and store them in the appropriate field of each circle.

At this stage, we have computed all possible intersection points between the maximum twelve circles. We then sort in ascending order all maximum twelve lists containing the values that define the intersection points. If the list of a circle has none or only one value, its contents is replaced with the pair $\{0,\, 2\pi\}$. Otherwise, we copy the smallest value at the end of the list. In this way, the consecutive values in each list define the consecutive arcs composing the circle.

Finally, we proceed to checking which of the resulting arcs are part of the workspace boundary. For each of the maximum twelve circles, start testing each arc. Find the coordinates of the middle point of each arc. Then, solve the inverse kinematic problem. If some Γ_j ($j = 1, 3, 5$) is negative, then stop and start with the next arc. If all Γ_j are non-negative, then perform the tricky test on the order of the U joint centres. If the test is negative, then stop and start with the next arc. Otherwise, put the values defining the arc in the third field of the structure object and repeat the procedure with the next arc until all arcs have been tested.

When all valid arcs have been identified, we may construct the workspace boundary array. Discretise each arc into a finite number of sequential points, as pairs of $\{x, y\}$ coordinates, and put them into the array. If using Matlab, add the {`NaN`, `NaN`} pair after each arc list. Note that we do not sort the arcs to obtain the boundary as an ordered list of closed contours, which is needed if we wish to compute the area of the workspace cross-section.

The list is now ready to be plotted. We may discretise the bicircular quartic defining the Type 2 singularity loci and plot the parts that are inside the workspace.

N.B. For simplicity, we have considered that C is the point of interest, i.e., the tool-tip. Obviously, this is not always the case. However, since the mobile platform has a constant orientation, we only need to offset all of the results presented in this section if we are interested in another point of the mobile platform.

4.4.3 Examples and Discussion

The proposed methodology was implemented in Matlab 6, taking again advantage of its data structures and cell arrays. The computation time for the workspace is a few seconds only. Computing and plotting the whole singularity curves, as well, doubles the computation time. If instead, only the segments of the singularity curves inside the workspace are plotted, the computation time builds up to some 15 seconds.

We present several examples for several different designs that illustrate the ideas developed in this section. The first example, shown in Fig. 4.29 presents the constant-orientation workspace of the design that was chosen by Hexel Corporation for their commercially available prototype of the *Rotobot* ($\ell_1 = r_B = 500$ mm, $\ell_2 = 433$ mm). Their design has a much more simplified workspace computation due to the fact that

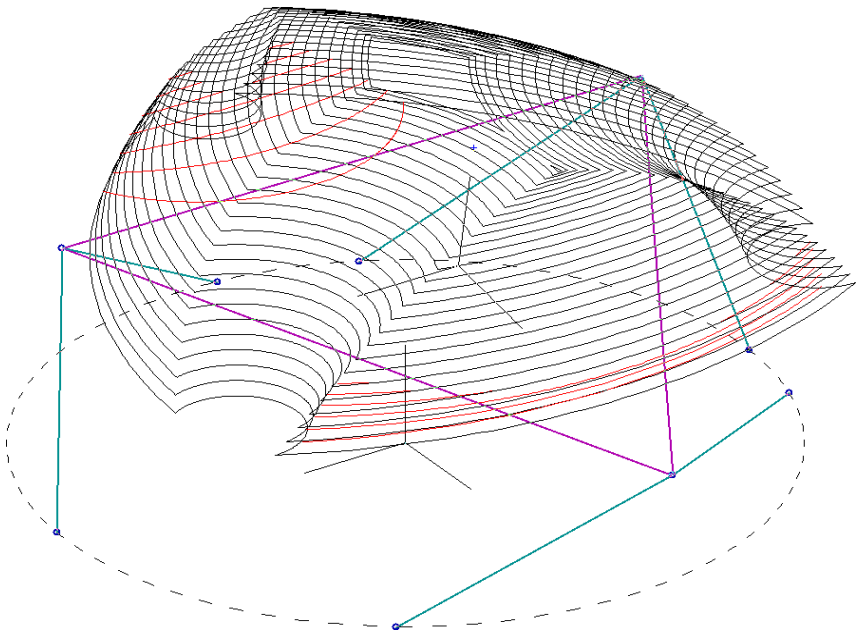

Figure 4.29: Constant-orientation workspace and singularity loci for a *Rotobot* design.

the distal links are shorter than the proximal links and the distance between two S joint centres is greater than twice the length of the distal links. These mechanical limits ensure respectively a constant working mode and no U joint interference. Even if the choice of the design was probably governed by the simplicity of the workspace computation, we should admit that the design seems to be quite optimal, with a "well-shaped" workspace that is almost singularity free.

Figure 4.29 shows the horizontal cross-sections of the workspace boundary (in black) and singularity loci (in red) for the orientation defined by $\theta = -10°$. The *Rotobot* is also shown at the position $x = -140$ mm, $y = -60$ mm, and $z = 380$ mm. Note that for this design, as well as for the others to come, the tool-tip for which all computations are made (shown as a small blue "+") is selected at $z' = 200$ mm.

The second example, shown in Fig. 4.30, refers to a design for which $\ell_1 = 500$ mm, $r_B = 300$ mm, and $\ell_2 = 650$ mm. The orientation of the mobile platform is defined by $\theta = 10°$ and the *Rotobot* is shown at the pose for which its tool-tip is at $x = y = 0$ and $z = 720$ mm. The constant-orientation workspace at this orientation is divided into six volumes, of which only the upper-most central three correspond to the branch set $\delta_j = -1$, $\delta_{j+1} = +1$ ($j = 1, 3, 5$). Note that for this working mode, the corresponding workspace is centrally located, while for the other working modes, the workspace volumes are far from the z axis.

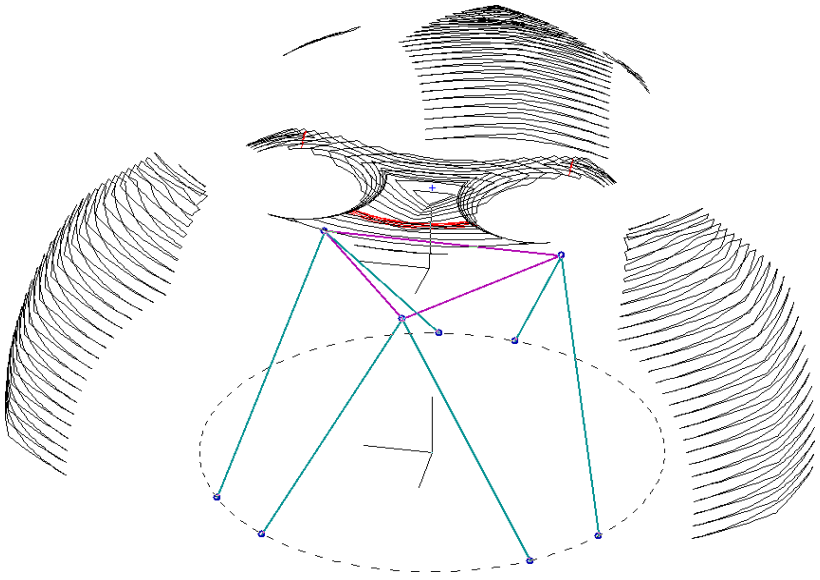

Figure 4.30: Constant-orientation workspace and singularity loci for a *Rotobot* design.

The final example, shown in Fig. 4.31, refers to a design for which $\ell_1 = 500$ mm, $r_B = 450$ mm, and $\ell_2 = 500$ mm. The orientation of the mobile platform is defined by $\theta = 0$ and the *Rotobot* is shown at the pose for which its tool-tip is at $x = y = 0$ and $z = 500$ mm. The constant-orientation workspace at this orientation is divided into four volumes, of which only the upper-most central one corresponds to the working mode $\delta_j = -1$, $\delta_{j+1} = +1$ ($j = 1, 3, 5$).

Based on these and many other examples, we conclude that the Type 2 singularity loci are scarce and close the the workspace boundary, and thus do not substantially limit the workspace. The optimisation of the *Rotobot* can, therefore, ignore the Type 2 singularity loci and focus of the constant-orientation workspace only. As the edges of the workspace boundary cross-sections represent arcs of circles, the areas of these cross-sections can be computed exactly. By integration, the volume of the whole workspace may further be obtained.

In view of design optimisation, we should mention the recent work of (Liu et al., 2002) on the design of general *Rotobot* parallel mechanisms with distinct S joints. However, with all the geometric tools proposed in this section, the optimisation of the *Rotobot* is a straightforward task that may be performed using a relatively brute-force approach since there are only two independent design variables, e.g., ℓ_2/ℓ_1 and r_B/ℓ_1.

Let us also mention that our study of the Bohemian dome surface may be useful in the analysis of other parallel mechanisms as well. For example, the workspace of

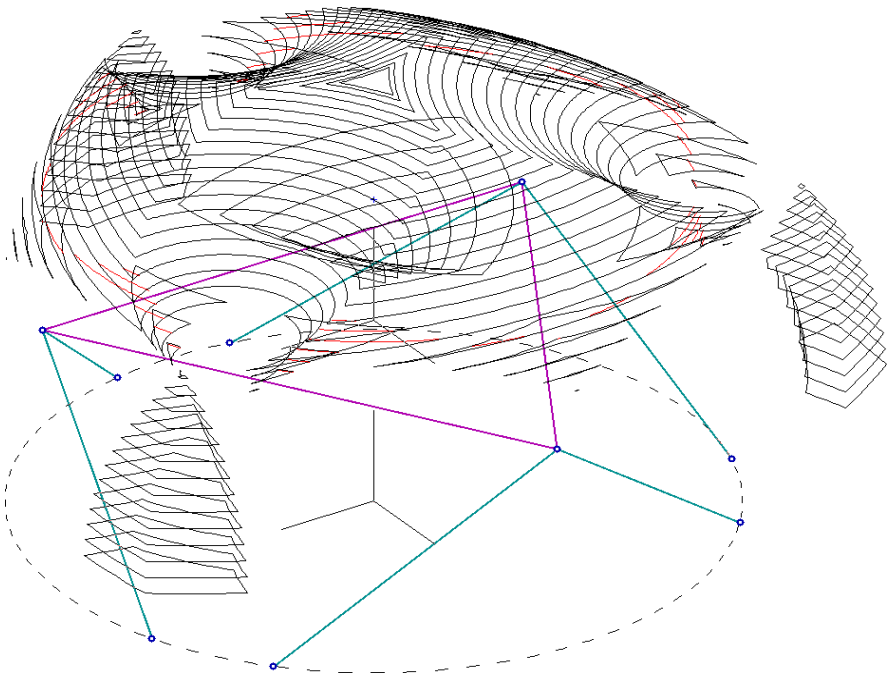

Figure 4.31: Constant-orientation workspace and singularity loci for a *Rotobot* design.

a novel parallelepiped parallel mechanism was recently found to be a Bohemian dome (Wu and Gosselin, 2002b).

The *Rotobot* is one of the best examples showing how only the use of a geometric method may lead to the complete understanding of the robot kinematics. Indeed, without using a geometric method, it is nearly impossible to realise that, in the case $\ell_2 \geq \ell_1$, there is an important phenomenon related to working modes. Without being aware of this phenomenon, one would, naturally, fix the working mode and thus reduce significantly the *Rotobot* workspace while, most probably, believing that the workspace is much larger.

Chapter 5

Conclusions

This thesis presents a rigorous and intuitive geometric approach to the kinematic analysis of parallel mechanisms. Unlike some previous works, the investigation is not based upon the extensive (and sometimes shortsighted) manipulation of algebraic equations and the frequent abuse of computer algebra systems. The often seen appendices with automatically generated unintelligible bulky equations have been rejected in favour of enlightening geometric illustrations and algorithms. Motion as incurred in mechanisms is a geometrical phenomenon, which is the reason why we speak of kinematic geometry. Kinematics of mechanisms should, therefore, be analysed geometrically.

Geometrical methods for the study of mechanisms are intuitive and provide an in-depth kinematics insight. They are especially useful at the design stage. Furthermore, geometry develops creativity as intuition is guided by unifying geometric principles.

Numerical methods are another alternative over analytical methods. But while numerical methods are general and may be applied to a wide class of different mechanisms, geometrical methods are more accurate and often prove to be much faster.

One of the simplest examples for the supremacy of geometrical methods is the problem of singularity analysis of 3-$\underline{R}RR$ planar parallel mechanisms with a pair of coincident platform R joints (Fig. 2.12, page 42). A brute-force manipulation of the determinant of the Jacobian matrix results in a polynomial of degree 42 which, because of its huge size, is almost impossible to factorise (even though, theoretically, this is possible). Thus, a study of this polynomial reveals nothing.

A numerical method, such as a simple discretisation method, would show, after long computations, that, for each orientation of the mobile platform and for a single working mode, the Type 2 singularity loci look like arcs of circles and a portion of some curve. If, by any chance, one plots these singularity loci for all working modes, then four complete circles and a close-loop curve would suddenly appear. Yet, those would not be smooth curves but thousands of scattered points that will take a long time to be computed and a whole lot of storage space.

In contrast, a geometrical approach immediately recognises the three scenarios that lead to Type 2 singularities—when the line along the lone distal link passes through the pair of coincident platform R joints, when the other two distal links are overlapping, or when they are fully stretched. These three scenarios are readily associated with two circles, another two circles, and a sextic, respectively. Moreover, these curves may be represented with parametric equations and, therefore, quickly and smoothly drawn. It can further be seen how they relate to the workspace boundaries, and how they are segmented corresponding to each of the eight working modes. Based on these findings, one may easily select the best design in order to maximise the workspace of the parallel mechanism.

Of course, the geometrical approach does not always eliminate the use of numerical methods. For example, the singularity loci for general 3-$\underline{R}RR$ planar parallel mechanisms which are represented by a curve of degree 48 can only be drawn using a discretisation algorithm. Nor does the geometrical approach always eliminate the use of algebra. For instance, the intersection points between a cyclide and a circle cannot be computed without the use of algebraic geometry. Geometry does not always make miracles but "it can often simplify, or even entirely eliminate, the subsequent steps in analysis" (Hunt, 1978). It is, therefore, crucial that the first step in the kinematic analysis of any parallel mechanism includes an overall geometric study of the problem.

5.1 Summary and Contributions of the Thesis

Our journey into the geometric analysis of parallel mechanisms starts naturally with a detailed investigation of the singularities of all possible 3-DOF planar fully parallel mechanisms (Chapter 2). And what better general approach to do that than the use of planar reciprocal screws. Since screw theory using three coordinates is not commonly used, we outline a detailed tutorial on the use of planar reciprocal screws for the analysis of the singularities of planar fully-parallel mechanisms.

Despite the recent increase in the popularity of screw theory, some remain reluctant to accept its advantages. The first of these is the systematic procedure of setting up directly the velocity equations and geometrically interpreting the singularities of a parallel mechanism. For Type 2 singularities of planar parallel mechanisms, for example, screw theory teaches us that the three lines along the three reciprocal screws should either be intersecting at one common point or parallel. To give a sense of the compactness of the reciprocal screw method, we have put it into contrast with the conventional way of deriving the velocity equations through differentiation, with respect to time, of the inverse kinematic equations.

The second advantage of using screw theory is the ability to correctly explain particular singularities such as configurations where the two passive R joints in an $R\underline{P}R$ chain coincide. There exist examples in the literature where such singularities are incorrectly classified based on a misleading analysis of the basic velocity equations. The problem is that at such singularities, the conventional input-output velocity equations are simply not valid, while screw theory can aid to set up the correct system of velocity equations.

One of the most important contributions of Chapter 2 is the systematic study of the kinematic geometry of all 3-DOF planar fully-parallel mechanisms. The results obtained in Chapter 2 are of great value to the designer looking for a 3-DOF planar parallel architecture. We propose some new simplified designs that have no Type 2 singularities, or other with singularities that are very easy to determine. The results could also be of value to support or reject general theories. For examples, among the various architectures, some give direct answers to questions such as whether Type 2 singularities divide the workspace into segments corresponding to each assembly mode. Finally, some examples are ideal candidates for a robot kinematics course exam. The singularity analysis of some mechanisms may take days to complete when incorrectly approached, yet require only minutes to outline when based on geometry.

In Chapter 3, we approach the constraint analysis of a special class of 3-DOF spatial parallel mechanisms. One of the major reasons for the complexity of the analysis of spatial mechanisms is the problem of orientation representation. Hence, we dedicate the first part of the chapter on a new type of Euler angles. The Tilt & Torsion angles, as we call them, have been previously used in biomechanics, but only recently have they been used to represent the orientation of the mobile platform of parallel mechanisms. We define these angles and summarise the numerous advantages that they offer for the analysis of spatial parallel mechanisms.

We saw that the use of the Tilt & Torsion angles is more intuitive, allows the representation of the orientation workspace under a nicely-shaped form, and reveals the particular symmetry of spatial parallel mechanisms when the torsion angle is equal to zero. We showed that the T&T angles are the best choice for most 6-DOF spatial parallel mechanisms and especially those for which the torsion capability is considered to be a redundant degree of freedom. In essence, the first part of Chapter 3 is a concise treatise on the use of T&T angles for spatial parallel mechanisms.

The most original contribution in Chapter 3 is, however, the analysis of a class of 3-DOF spatial parallel mechanisms with zero torsion. While none of the studied designs is new—in fact a lot of work has been done on most—these mechanisms have never been recognised before as members of the same class. In fact, it is not even clear whether all those researchers have reached the conclusion that the torsion of the mobile platform is always equal to zero. The key factor in our successful analysis is the use of T&T angles which allows us to directly obtain the simple equations relating the three constrained and three feasible degrees of freedom of the mobile platform.

The conclusion is once again in favour of geometry. When Euler angles are simply seen as a parametrisation of orientation, without any insight into their nature, one ends up with huge algebraic expressions and misses the exact nature of the motion of the analysed parallel mechanisms.

Finally, in Chapter 4, we approach the kinematic analysis of one of the most intricate 6-DOF parallel mechanisms—the 6-$\underline{R}US$ architecture. This chapter is abundant with geometry as we all know it—we construct general tori, intersect them with circles and planes, work with bicircular quartics, intersect and polygonise toric sections, work with translational surfaces. While most of the results in the previous two chapters could, theoretically, be obtained without even mentioning geometry, Chapter 4 could not even exist without it.

We first develop in Section 4.2 a geometrical method for the computation and representation of the edges of the constant-orientation workspace of general 6-$\underline{R}US$ parallel mechanisms. Not only do we cover the most general case, but we also consider the mechanical constraints on the U joints. For this purpose, we propose a method for obtaining the intersection of two general tori. The method is based on the analytic formulation of the problem of intersecting a cyclide with a circle.

Then, in Section 4.3, we ignore the constraints on the U joints and gain the capability of computing and representing the cross-sections of the constant-orientation workspace of general 6-$\underline{R}US$ parallel mechanisms. To achieve this, we define the equation of a toric section and propose an analytic method for computing the intersection points between two toric sections. Then, we propose an algorithm for polygonisation of each toric section.

Finally, in Section 4.4, we narrow down our investigation to the special *Rotobot* design which has pair-wise coincident S joint centres and one single common track for all U joints. While aimed at a very peculiar design, our study reveals interesting phenomena which appear in other parallel mechanisms as well. Basically, we propose a geometric method for the computation of the horizontal cross-sections of the constant-orientation workspace and the Type 2 singularity surface. The first major contribution is the description of a geometric model for the constraint on the circular order of the U joints along the track which was represented by three Bohemian dome surfaces. The second major result is the derivation of a bisymmetric bicircular quartic equation for the cross-sections of the Type 2 singularities. Based on our geometric study, we reveal the fact that the Type 2 singularities are the same for all working modes, but the workspace is segmented into parts that correspond to different working modes. Other interesting properties of the *Rotobot* have also been discussed. Apart from the very theoretical contributions, our method has the advantage that it may be easily incorporated into the optimisation of the *Rotobot* itself.

5.2 Directions for Future Work

One of the greatest benefits from using geometric methods in the kinematic analysis of parallel mechanisms is the gain of in-depth insight. It is, therefore, of no surprise that several new and interesting phenomena have been revealed during our study. Unfortunately, they are outside the scope of this thesis and require considerable efforts for

their proper study and generalisation. Herein, we suggest two main areas of continued investigation, which will require more advanced forms of the geometric approach used in this thesis.

5.2.1 Workspace Segmentation, Working Modes, and Assembly Modes

The workspace segmentation by working modes or by assembly modes is recognised at the very beginning of our thesis. We even delve, in some detail, into this mysterious phenomenon in Chapter 2, while still analysing the relatively simple planar parallel mechanisms. The phenomenon appears in a new light in the study of the spatial 6-DOF *Rotobot*. The more we study this problem and try to generalise the results, the more new peculiar cases appear.

The investigation of this phenomenon may look too theoretical to be of any practical value but we gave sufficient number of examples to demonstrate its practical importance. A complete understanding of the workspace segmentation, at least as appearing in a particular parallel mechanism, allows the optimised use of the workspace and the proper control of the mechanism.

As shown in Chapters 2 and 3, some parallel mechanisms have Type 2 singularities that depend on the particular working mode. Therefore, a hypothesis can be made that in order to make use of the whole workspace segmented by these dangerous singularities, the mechanism should be capable of switching working modes which, by definition, requires the passage through a less-menacing Type 1 singularity. But some examples suggested that it is probably impossible to switch working modes without encountering Type 2 singularities...

When mechanisms with multiple working modes have some mechanical limits as on the range of the actuated joints or the order of passive joints (as in the *Rotobot*), the workspace is segmented into parts corresponding to different working modes. Therefore, in order to maximise the use of the whole workspace, the mechanism should switch working modes by passing through a Type 1 singularity. But is it always possible to do that without passing through a Type 2 singularity?

Then, there is the old question of whether assembly modes are separated by Type 2 singularities. We saw that in some cases, as in the 2-DOF planar $\underline{P}RRR\underline{P}$ parallel

mechanism, this is true. But is it always true, at least for simple mechanisms as the planar ones? And what is the relation between assembly and working modes? Examples in Chapter 2 may fuel that discussion but a rigorous study of this problem has yet to be presented.

The issues discussed in the preceding paragraphs are all related to the design of some parallel mechanisms. But they are also important for the control of these mechanisms. Is it really that harmful to pass through a Type 2 singularity? Well, researchers in Germany have done that without any damage to their $\underline{P}RRR\underline{P}$ parallel mechanism (Hesselbach et al., 2002).

Undoubtedly, a geometrical study is the way to approach all those problems. It should not, however, be limited to the output space of the mechanism but, rather, investigate the motion of the mechanism in its configuration space.

5.2.2 Zero-Torsion 3-DOF Spatial Parallel Mechanisms

If the practical utility of a study on the issue of working modes is less evident to the general user of a parallel mechanism, the importance of 3-DOF spatial parallel mechanisms with zero-torsion is obvious.

To begin with, we all agree that 3-DOF spatial mechanisms allowing one translation and two rotations are useful for a wide range of applications. Indeed, the trend in parallel kinematic machines (PKMs) is the use of such mechanisms. There are multiple examples of commercially available PKMs based on such architectures. Such mechanisms are also used for telescope applications and micro-manipulation.

The translational degree of freedom is used to advance the mobile platform of the parallel mechanism, e.g., as in focusing, while the two rotational degrees are used to direct the axisymmetric tool. Clearly, these three basic degrees of freedom are the most important for applications requiring axisymmetric tools. The mechanisms may further be mounted on an XY stage to provide wide range of motion in x and y. Indeed, machine tools used in the aerospace industry are required to work on very large-area parts of relatively small thickness.

For most of the existing non-zero-torsion parallel mechanisms of this type, the relationship between the constrained and feasible degrees of freedom is extremely complicated. This leads to problems in the design of the mechanism and sets much higher

requirements on the control system of the mechanism. Therefore, it is of no doubt that having a constraint relationship as simple as $\sigma = 0$ is a great relief. Not surprisingly, nature has also "evolved" in this way, "designing" the human eye and the clavicle to work with zero torsion.

While the contribution of our thesis was to demonstrate, using the Tilt & Torsion angles, that certain parallel mechanisms are with zero torsion, we could not define the general rules for the synthesis of such mechanism. Therefore, one possible direction for research may be the synthesis of such zero-torsion mechanisms. Surely, such an endeavour should be based on the advanced geometric tools of screw theory.

Bibliography

Astanin, V., Duyunov, A., Smotritsky, G., and Usov, V., 2002, "The Modeling and Optmization System of Hexapod Layout," *Proceedings of the 3rd Chemnitz Parallel Kinematics Seminar*, Chemnitz, Germany, pp. 189–196.

Baerlocher, P., and Boulic, R., 2000, "Parameterization and range of motion of the ball-and-socket joint," *Proceedings of Avatars 2000*, Kluwer Academic Publishers.

Behi, F., Mehregany, M., and Gabriel, K.J., 1990, "A Microfabricated Three-Degree-of-Freedom Parallel Mechanism" *Proceedings of the 3rd IEEE Workshop on Micro Electro-Mechanical Systems*, Napa Valley, CA, USA, February, pp. 159–165.

Benea, R., 1996, "Contribution à l'étude des robots pleinement parallèles de type 6 R-RR-S," *Ph.D. Thesis*, Université de Savoie, Annecy, France, December.

Bonev, I.A., and Ryu, J., 1999a, "Orientation Workspace Analysis of 6-DOF Parallel Manipulators," *Proceedings of the ASME 1999 Design Engineering Technical Conferences*, Las Vegas, NV, USA, Paper No. DAC-8646.

Bonev, I.A., and Ryu, J., 1999b, "Workspace Analysis of 6-PRRS Parallel Manipulators Based on the Vertex Space Concept," *Proceedings of the ASME 1999 Design Engineering Technical Conferences*, Las Vegas, NV, USA, Paper No. DAC-8647.

Bonev, I.A., and Gosselin, C.M., 2001, "Singularity Loci of Planar Parallel Manipulators with Revolute Joints," *Proceedings of the 2nd Workshop on Computational Kinematics*, Seoul, South Korea, May 20–22, pp. 291–299 (http://www.parallemic.org/Reviews/Review001.html).

Buruncuk, K., and Tokad, Y., 1999, "On the Kinematic of a 3-DOF Stewart Platform," *Journal of Robotic Systems*, Vol. 16, No. 2, pp. 105–118.

Canfield, S.L., Ganino, A.J., Salerno, R.J., and Reinholtz, C.F., 1996, "Singularity and Dexterity Analysis of the Carpal Wrist," *Proceedings of the ASME Design Engineering Technical Conferences*, Irvine, CA, USA, Paper No. MECH-1156.

Canfield, S.L., Reinholtz, C.F., Salerno, R.J., and Ganino, A.J., 1997, "Spatial parallel-architecture robotic carpal wrist," U.S. Patent No. 5,699,695.

Carretero, J.A., Nahon, M.A., and Podhorodeski, R.P., 2000, "Workspace Analysis and Optimization of a Novel 3-DOF Parallel Manipulator," *IEEE Journal of Robotics and Automation*, Vol. 15, No. 4, pp. 178–188.

Chablat, D., and Wenger, P., 1998, "Working modes and aspects in fully parallel manipulators," *Proceedings of the 1998 IEEE International Conference on Robotics & Automation*, Leuven, Belgium, May, pp. 1994–1969.

Chang, T.-H., Inasaki, I., Morihara, K., and Hsu, J.-J., 2000, "The Development of a Parallel Mechanism of 5-D.O.F. Hybrid Machine Tool," *Proceedings of the Year 2000 Parallel Kinematic Machines International Conference*, Ann Arbor, MI, USA, September 13–15, pp. 79–86.

Chi, Y. L., 1999, "Systems and Methods Employing a Rotary Track for Machining and Manufacturing", WIPO Patent No. WO 99/38646.

Chrisp, A., and Gindy, N., 1999, "Parallel Link Machine Tools: Simulation, Workspace Analysis and Component Positioning," *Parallel Kinematic Machines: Theoretical Aspects and Industrial Requirements*, C. R. Boër, L. Molinari-Tosatti, and K. S. Smith (eds.), Springer-Verlag, pp. 245–256.

Chung, Y.-H., Choo, J.-H., and Lee, J.-W., 2001, "SenSation: A New 2 DOF Parallel Mechanism for Haptic Device" *Proceedings of the 2nd Workshop on Computational Kinematics*, Seoul, South Korea, May 20–22, pp. 45–56.

Daniali, H.R.M., Zsombor-Murray, P.J., and Angeles, J., 1993, "The Kinematics of 3-DOF Planar and Spherical Double-Triangular Parallel Manipulators," *Computational Kinematics*, J. Angeles et al. (eds.), Kluwer Academic Publishers, pp. 153–164.

Dunlop, G.R., and Jones. T.P., 1996, "Gravity Counter Balancing of a Parallel Robot for Antenna Aiming," *World Automation Congress*, Montpellier, France, Vol. 6, pp. 153–158.

Dunlop, G.R., and Jones, T.P., 1997, "Position Analysis of a 3-DOF Parallel Manipulator," *Mechanism and Machine Theory*, Vol. 32, No. 8, pp. 903–920.

Du Plessis, L.J., Snyman, J.A., and Smit, W.J., 2000, "A Configurationally Adjustable Planar Stewart Platform Machining Center with Feasible and Optimum Placement of Workspace Relative to Toolpath," *Proceedings of the ASME 2000 Design Engineering Technical Conferences*, Baltimore, MD, USA, September 10-13, Paper No. MECH-14088.

Durum, M.M., 1975, "Kinematic Properties of Tripode (Tri-pot) Joints," *ASME Journal of Engineering for Industry*, Vol. 978, pp. 708–713.

Ebert-Uphoff, I., Lee, J.-K., and Lipkin, H., 2000, "Characteristic Tetrahedron of Wrench Singularities for Parallel Manipulators with Three Legs," *Proceedings of the Symposium Commemorating the Legacy, Works, and Life of Sir Robert Stawell Ball*, Trinity College, Cambridge, UK.

Fichter, E.F., and Hunt, K.H., 1975, "The Fecund Torus, its Bitangent-Circles and Derived Linkages," *Mechanism and Machine Theory*, Vol. 10, pp. 167–176.

Gosselin, C.M., 1990, "Determination of the Workspace of 6-DOF Parallel Manipulators," *ASME Journal of Mechanical Design*, Vol. 112, September, pp. 331–336.

Gosselin, C.M., and Angeles, J., 1990, "Singularity Analysis of Closed-Loop Kinematic Chains," *IEEE Transactions on Robotics and Automation*, Vol. 6, No. 3, pp. 281–290.

Gosselin, C.M., Lavoie, E., and Toutant, P., 1992, "An Efficient Algorithm for the Graphical Representation of the Three-Dimensional Workspace of Parallel Manipulators," *Proceedings of the ASME 22nd Biennial Mechanisms Conference*, Scottsdale, AZ, USA, Vol. 45, pp. 323–328.

Gosselin, C.M., Lemieux, S., and Merlet, J.-P., 1996, "A New Architecture of Planar Three-Degree-Of-Freedom Parallel Manipulator," *Proceedings of the 1996 IEEE International Conference on Robotics and Automation*, Minneapolis, MN, USA, April, pp. 3738–3743.

Gosselin, C.M. and Wang, J., 1997, "Singularity Loci of Planar Parallel Manipulators with Revolute Actuators," *Robotics and Autonomous Systems*, Vol. 21, pp. 377–398.

Grassia, F.S., 1998, "Practical Parameterization of Rotations using the Exponential Map," *Journal of Graphics Tools*, Vol. 3, No. 3, pp. 29-48.

Hayes, M.J.D., 1999, "Kinematics of General Planar Stewart-Gough Platforms," *Ph.D. Thesis*, McGill University, Montreal, QC, Canada, September.

Hayes, M.J.D., and Husty, M., 2000, "Workspace Characterization of Planar Three-Legged Platforms With Holonomic Pairs," *Advances in Robot Kinematics*, J. Lenarčič and M.M. Stanišič (eds.), Kluwer Academic Publishers, The Netherlands, pp. 267–276.

Helmholtz, H.v., 1867, *Handbuch der physiologischen Optik*, Leipzig, Germany.

Hertz, R.B., and Hughes, P.C., 1998, "Kinematic Analysis of a General Double-Tripod Parallel Manipulator," *Mechanism and Machine Theory*, Vol. 33, No. 6, pp. 681–696.

Hesselbach, J., Helm, M.B., and Soetebier, S., 2002, "Workspace-Optimized Parallel Robot for Placing Tasks," *Proceedings of the 3rd Chemnitz Parallel Kinematics Seminar*, Chemnitz, Germany, pp. 697–713.

Hesselbach, J., and Raatz, A., 2000, "Pseudo-elastic Flexure-Hinges in Robots for Micro Assembly," *Proceedings of SPIE*, Vol. 4194, pp. 157–167.

Huang, T., Wang, J., and Whitehouse, D.J., 1999, "Closed Form Solution to Workspace of Hexapod-Based Virtual Axis Machine Tools," *ASME Journal of Mechanical Design*, Vol. 121, March, pp. 26–31.

Huang, Z., and Wang, J., 2000, "Instantaneous Motion Analysis of Deficient-Rank 3-DOF Parallel Manipulator by Means of Principal Screws," *Proceedings of the Symposium Commemorating the Legacy, Works, and Life of Sir Robert Stawell Ball*, Trinity College, Cambridge, UK.

Hunt, K.H., 1973, "Constant-Velocity Shaft Couplings: A General Theory," *ASME Journal of Engineering for Industry*, May, pp. 455–464.

Hunt, K.H., 1978, *Kinematic Geometry of Mechanisms*, Oxford University Press.

Hunt, K.H., 1983, "Structural Kinematics of In-Parallel-Actuated Robot-Arms," *ASME Journal of Mechanisms, Transmissions, and Automation in Design*, Vol. 105, December, pp. 705–712.

Hunt, K.H., 2000, "Don't cross-thread the screw," *Proceedings of a Symposium Commemorating the Legacy, Works, and Life of Sir Robert Stawell Ball*, Trinity College, Cambridge, UK.

Husty, M., 1996, "On the Workspace of Planar Three-Legged Platforms," *Proceedings of ISRAM World Congress of Automation*, Montpellier, France, pp. 1790–1796.

Husty, M., Hays, M.J.D., and Loibnegger, H., 1999, "The General Singularity Surface of Planar Three-Legged Platforms," *Advances in Multibody Systems and Mechatronics*, Duisburg, Germany, pp. 203–214.

Johnstone, J.K., 1993, "A New Intersection Algorithm for Cyclides and Swept Surfaces Using Circle Decomposition," *Computer Aided Geometric Design*, Vol. 10, No. 1, pp. 1–24.

Karger, A., and Husty, M., 1996, "On Self-Motions of a Class of Parallel Manipulators," *Recent Advances in Robot Kinematics*, J. Lenarčič and V. Parenti-Castelli (eds.), Kluwer Academic Publishers, pp. 339-348.

Korein, J.U., 1984, *A Geometric Investigation of Reach*, The MIT Press.

Kumar, V.R., 1992, "Instantaneous Kinematics of Parallel-Chain Robotic Mechanisms," *ASME Journal of Mechanical Design*, Vol. 114, No. 3, pp. 349–358.

Lambert, M., 1987, "Polyarticulated rectractile mechanism," U.S. Patent No. 4,651,589.

Lee, K.-M., and Shah, D.K., 1988, "Kinematic Analysis of a Three-Degree-of-Freedom In-Parallel Actuated Manipulator," *IEEE Journal of Robotics and Automation*, Vol. 4, No. 3, pp. 354–360.

Lenarčič, J., Stanišič, M., and Schearer, E., 2002, "Humanoid Humeral Pointing Kinematics," *Advances in Robot Kinematics*, J. Lenarčič and F. Thomas (eds.), Kluwer Academic Publishers, The Netherlands, pp. 79–88.

Li, J., Wang, J., Chou, W., Zhang, Y., Wang, and Zhang, Q., 2001, "Inverse Kinematics and Dynamics of the 3-RRS Parallel Platform," *Proceedings of the IEEE International Conference on Robotics & Automation*, Seoul, Korea, pp. 2506–2511.

Liu, X.-J., Wang, J., Gao, F., and Wang, L.-P., 2002, "Mechanism design of a simplified 6-DOF 6-RUS parallel manipulator," *Robotica*, Vol. 20, pp. 81–91.

Ma, O., and Angeles, J., 1992, "Architecture Singularities of Platform Manipulators," *Proceedings of the 1992 IEEE International Conference on Robotics and Automation*, Sacramento, CA, USA, April 11–14, pp. 1542-1547.

Mayer St-Onge, B., and Gosselin, C.M., 2001, "Logiciel d'aide á la conception de plates-formes de mouvement d'architecture parallèle," *Proceedings of the 2001 CCToMM Symposium on Mechanims, Machines, and Mechatronics*, Saint-Hubert, QC, Canada, June.

Merlet, J.-P., 1989, "Singular Configurations of Parallel Manipulators and Grassmann Geometry," *International Journal of Robotics Research*, Vol. 8, No. 5, pp. 45–56.

Merlet, J.-P., and Gosselin, C.M., 1991, "Nouvelle architecture pour un manipulateur parallèle à 6 degrés de liberté," *Mechanism and Machine Theory*, Vol. 2, No. 26, pp. 77–90.

Merlet, J.-P., 1994, "Détermination de l'espace de travail d'un robot parallèle pour une orientation constante," *Mechanism and Machine Theory*, Vol. 29, No. 8, pp. 1099–1113.

Merlet, J.-P., 1996, "Direct Kinematics of Planar Parallel Manipulators," *Proceedings of the 1996 IEEE International Conference on Robotics and Automation*, Minneapolis, MN, USA, April, pp. 3744–3749.

Merlet, J.-P., 1997, *Les robots parallèles*, 2nd ed., Hermès, Paris.

Mohammadi Daniali, H.R., Zsombor-Murray, P.J., and Angeles, J., 1995, "Singularity Analysis of Planar Parallel Manipulators," *Mechanism and Machine Theory*, Vol. 30, No. 5, pp. 665–678.

Mohammed, M.G., and Duffy, J., 1985, "A Direct Determination of the Instantaneous Kinematics of Fully Parallel Robot Manipulators," *ASME Journal of Mechanical Transmissions and Automation in Design*, Vol. 107, No. 2, pp. 226–229.

Murray, R.M., Li, Z., and Sastry, S.S., 1994, "A Mathematical Introduction to Robotic Manipulation," CRC Press.

Pankratov, K., 1996, "SaGA - Spatial and Geometric Analysis Toolbox," Massachusetts Institute of Technology, Cambridge, MA, USA, available online at http://puddle.mit.edu/~glenn/kirill/saga.html.

Patrikalakis, N.M., and Prakash, P.V., 1990, "Surface Intersections for Geometric Modeling," *ASME Journal of Mechanical Design*, Vol. 112, March, pp. 100–107.

Peruzzini, W., Ouellet, A., and Hui, R., 1995, "Design and Analysis of a Three-DoF Parallel Mechanism," *IFToMM Proceedings of the Ninth World Congress Theory Machines and Mechanisms*, Milan, Italy, pp. 2141–2145.

Phillips, J., 1984, *Freedom in Machinery. Vol. 1: Introducing Screw Theory*, Cambridge University Press.

Pierrot, F., Uchiyama, M., Dauchez, P., and Fournier, A., 1990, "A New Design of a 6-DOF Parallel Robot," *Journal of Robotics and Mechatronics*, Vol. 2, No. 4, pp. 308–315.

Podzorov, P.V., and Bushuev, V.V., 2002, "Synthesis of the Equipment on the Base of Parallel Kinematic Mechanism," *Proceedings of the 3rd Chemnitz Parallel Kinematics Seminar*, Chemnitz, Germany, pp. 861–882.

Raghavan, M., and Roth, B., 1995, "Solving Polynomial Systems for the Kinematic Analysis and Synthesis of Mechanisms and Robot Manipulators," *ASME Journal of Mechanical Design*, Vol. 117, June, pp. 71–79.

Satya, S.M., Ferreira, P.M., and Spong, M.W., 1995, "Hybrid Control of a Planar 3-DOF Parallel Manipulator for Machining Operations," *Transactions of NAMRI/SME*, Vol. XXIII, pp. 273–280.

Schönherr, J, 1998, "Bemessen, Bewerten und Optimieren von Parallelstrukturen," *Proceedings of Chemnitz PKM-Seminar*, Chemnitz, Germany, pp. 157–166.

Sefrioui, J., and Gosselin, C.M., 1995, "On the Quadratic Nature of the Singularity Curves of Planar Three-Degree-Of-Freedom Parallel Manipulators," *Mechanism and Machine Theory*, Vol. 30, No. 4, pp. 533–551.

Segre, C., 1884, "Étude des diffŕentes surfaces du 4e ordre à conique double ou cuspidale (générale ou décomposée) considérés comme des projections de l'intersection de deux variétés quadratiques de l'espace à quatre dimensions," *Mathematische Annalen*, Vol. 24, pp. 313–446.

Stefanini, C., Carrozza, M.C., Menciassi, A., and Dario, P., 1999, "Design and Experiments on an Orientable Platform with Unilateral Joints for Biomedical Applications," *International Workshop on PKM*, Milan, Italy, pp. 131–136.

Takeda, Y., Funabashi, H., and Ichimaru, H., 1997, "Development of Spatial In-Parallel Actuated Manipulators with Six Degrees of Freedom with High Motion Transmissibility," *JSME International Journal*, Series C, Vol. 40, No. 2, pp. 299–308.

Tischler, C.R., Hunt, K.H., and Samuel, A.E., 1998, "On Optimizing the Kinematic Geometry of a Dexterous Robot Finger," *International Journal of Robotics Research*, Vol. 17, No. 10, pp. 1055–1067.

Tsai, L.-W., 1999, *Robot Analysis: the Mechanics of Serial and Parallel Manipulators*, John Wiley & Sons.

Wahl, J., 2000, "Articulated tool head," WIPO Patent No. WO 00/25976.

Wang, J., and Gosselin, C.M., 1998, "Static Balancing of Spatial Six-Degree-of-Freedom Parallel Mechanisms With Revolute Actuators," *Proceedings of the ASME 1998 Design Engineering Technical Conferences*, Atlanta, GA, USA, Paper No. MECH-5961.

Wang, Y., 1999, "Workspace Analysis of a Novel Closed-Chain Manipulator," *MS Thesis*, Case Western Reserve University, Cleveland, OH, USA.

Weisstein, E.W., 2002, "Bohemian Dome," *Eric Weisstein's World of Mathematics*, (http://mathworld.wolfram.com/BohemianDome.html).

Wu, Y., and Gosselin, C.M., 2002, "Kinematic Analysis of Spatial 3-DOF Parallelepiped Mechanisms," *Advances in Robot Kinematics*, J. Lenarčič and F. Thomas (eds.), Kluwer Academic Publishers, The Netherlands, pp. 423–432.

Zabalza, I., Pintor, J.M., Ros, J., and Jimenez, J.M., 1999, "Evaluation of the 64 'Insensitivity' Positions for a 6-RKS Hunt-Type Parallel Manipulator," *Proceedings of the Tenth World Congress on the Theory of Machine and Mechanisms*, Oulu, Finland, June 20-24, pp. 1152–1157.

Zirn, O., Baldini, G., and Rutz, D., 1999, "Device for moving and positioning an object in plane" WIPO Patent No. WO 99/08832.

Zlatanov, D., Fenton, R.G., and Benhabib, B., 1994, "Singularity Analysis of Mechanisms and Robots via a Motion-Space Model of the Instantaneous Kinematics," *Proceedings of the 1994 IEEE International Conference on Robotics and Automation*, San Diego, CA, USA, May 8-13, pp. 980–985.

Zlatanov, D., Fenton, R.G., and Benhabib, B., 1994, "Analysis of the Instantaneous Kinematics and Singular Configurations of Hybrid-Chain Manipulators," *Proceedings of the ASME 23rd Biennial Mechanisms Conference*, DE-Vol. 72, Minneapolis, MN, USA, September 11–14, pp. 467–476.

Zlatanov, D., Bonev, I.A., and Gosselin, C.M., 2002, "Constraint Singularities of Parallel Mechanisms," *Proceedings of the 2002 IEEE International Conference on Robotics and Automation*, Washington, D.C., USA, May 11-15.

Zlatanov, D., Bonev, I.A., and Gosselin, C.M., 2002, "Constraint Singularities as C-Space Singularities," *Advances in Robot Kinematics*, J. Lenarčič and F. Thomas (eds.), Kluwer Academic Publishers, The Netherlands, pp. 183–192 (http://www.parallemic.org/Reviews/Review008.html).